High Pressure Investigations of Structural, Electronic, and Topological Quantum Phase Transitions in Strong Spin Orbit Coupling Systems

A Thesis

Submitted for the Degree of

Doctor of Philosophy

By

V. RAJAJI

CHEMISTRY AND PHYSICS OF MATERIALS UNIT

JAWAHARLAL NEHRU CENTRE FOR ADVANCED SCIENTIFIC RESEARCH

BANGALORE – 560 064, INDIA.

FEBRUARY 2019

Dedicated to

Amma, Appa, Thambi, Rooplavathi (Wife) and
Rithul Advik (Son)

DECLARATION

I hereby declare that the matter embodied in this thesis entitled "**High Pressure Investigations of Structural, Electronic, and Topological Quantum Phase Transitions in Strong Spin Orbit Coupling Systems**" is the result of the investigations carried out by me at the Chemistry and Physics of Materials Unit, Jawaharlal Nehru Centre for Advanced Scientific Research (JNCASR), Bangalore, India, under the supervision of Professor Chandrabhas Narayana and that it has not been submitted elsewhere for the award of any degree or diploma.

In keeping with the general practice in reporting scientific observations, due acknowledgements have been made whenever the work described is based on the findings of other investigators. Any omission which might have occurred by oversight or error in judgement is regretted.

_____

(V. Rajaji)

CERTIFICATE

I hereby certify that the matter embodied in this thesis entitled **"High Pressure Investigations of Structural, Electronic, and Topological Quantum Phase Transitions in Strong Spin Orbit Coupling Systems"** has been carried out by Mr. V. Rajaji at the Chemistry and Physics of Materials Unit, Jawaharlal Nehru Centre for Advanced Scientific Research (JNCASR), Bangalore, India under my supervision and that it has not been submitted elsewhere for the award of any degree or diploma.

_____

Prof. Chandrabhas Narayana

(Research Supervisor)

ACKNOWLEDGEMENTS

I take this great opportunity to acknowledge people who have inspired, motivated and supported me throughout Ph.D both in my academic and personal life.

First and foremost I extend my sincere gratitude to my Research supervisor Prof. Chandrabhas Narayana for giving me an opportunity to work with him and also to be a part of the fantastic scientific environment JNCASR. I sincerely thank him for being receptive to my ideas, giving immense support, all the help in both professional and personal life, enormous freedom in the workplace, fruitful discussions, and the belief he had in me. I had the fantastic opportunities to work with him closely during the synchrotron visits and learned many things from him. Apart from a scientist, it has been a pleasure to work with a very energetic, humble, friendly, and well behaved human being. I would cherish the memory of working with him forever and will be following all of his positive things in my career. Thank you very much sir.

I want to thank Bharat Ratna Prof. C. N. R. Rao for his never-ending enthusiasm for science. He continues to be a source of inspiration for many of us.

I would like to thank all of my collaborators Prof. Umesh V. Waghmare (JNCASR), Prof. Sebastian C. Peter (JNCASR), Prof. Kanishka Biswas (JNCASR), Prof. Swapan K. Pati (JNCASR), Dr. S. Karmakar (BARC, Mumbai), Prof. V. Kanchana (IIT Hyderabad), Dr. Sorb (Ex. Postdoc, JNCASR), Dr. Boby Joseph (Elettra, Italy), Mr. Saurav Ch. Sarma,, Dr. Koushik Pal, Dr. Pallavi S. Malavi (BARC), Mr. Utpal Dutta (BARC), Mr. Subodha Sahoo (BARC) , Dr. Sharma S. R. K. C. Yamijala, Ms. Raagya Arora, Dr. U. Subbarao, Mr. P. Halappa, Ms. Janaky, Dr. Satya N. Guin, Mr. Subhajit Roychowdhury, Prof. R. N. Kini (IISER, Trivandrum), Dr. M. Kanagaraj, Prof. Ranjan Datta (JNCASR), Dr. R. S. Joshya, Mr. B. Vishal, Dr. Soumyabrata Roy and P. C. Sreeparvathy (IIT Hyderabad). I have learned a lot from the scientific discussions which we had. Particularly, I would like to thank Dr. Sorb

who has introduced the high pressure techniques present in our lab (LSL - Light Scattering Lab) to me.

I would also like to take this opportunity to thank Dr. Boby Joseph (Elettra), Dr. Paolo Lotti (Elettra), and Dr. Arpan Bhattacharya (KEK, Japan), for the user support and various help during synchrotron measurements. In particular, I thank Dr. Boby Joseph who has extended us a very friendly, and lively scientific environment in the synchrotron measurements (24/7) at Xpress beamline, Elettra, Trieste, Italy. Also, he has been excellent in instrument handling, various scientific discussion, and critical corrections of the manuscript and have learned many things from him. Thank you Boby.

I am pleased to acknowledge Prof. Isaac. F. Silvera (Harvard University, USA) for his outstanding course in GIAN program at IISER Kolkata and learned the conceptual aspect of nuts and bolts of high pressure science during this program. Sir, your passion, dedication, and directional work (metallic hydrogen) towards the high-pressure science over a very long period, inspires me a lot.

I would like to thank the faculties of CPMU and NCU for their various help. I sincerely thank Prof. Chandrabhas Narayana, Prof. Umesh V. Waghmare, Prof. G.U. Kulkarni, Prof. S.M. Shivaprasad, and Prof. T. N. Guru Row (IISc) for their wonderful courses.

Certainly, I have spent more than two-thirds of my Ph.D. life in my lab (LSL) with my lab mates. I would like to express my immense pleasure in thanking the amazing lab mates (past and present); Dr. Srinu, Dr. Partha, Dr. Soumik, Dr. Gayatri, Dr. Dhanya, Dr. Sorb, Shantanu, Priyank, Divya, Priyanka Jain, Kamali, Janaky, Jyothi, Dr. Prajit, Dr. Sayan Mandol, Dr. Amit, Prince, Anjana and Kazi. I sincerely thank all of them for the various academic and personal interactions which have made an enjoyable stay during my Ph.D. We had lots of fun together, and they have always kept a conducive environment which has helped me a lot. Thank you guys; I shall

always remember you as a fantastic memory. I thank Jilin Rachel who spent a few months (as a project student) with me in the lab and for baring my scientific curiosity. A special thanks to Divya, Janaky, and Dr. Kamali for the critical reading of my thesis.

I would also like to thank my batch mates, and friends at JNCASR. Few of them need special mention. They are Manjeet, Pawan, Aditya, Anand, Raagesh, Dr. Gopalakrishnan, Dr. Kiruthika, Dr. Summayya Kouser, Dr. Dasari, Dr. Ankush, Vybhav and Srinath. I thank all of them for their support, encouragement and their valuable time spent with me.

It's my pleasure to thank all of my wonderful friends, and seniors from my school, B.Sc, M.Sc, and M.Phil days. Special thanks to Dr. Sivadasan, Mr. Joseph Prabagar, Dr. Abuthagir for the wonderful scientific discussions.

I express my heartfelt thanks to all the academic, technical, non-technical, library, hostel, and computer lab staff members of JNCASR.

I have been very fortunate to be taught by many good teachers during my schools, B.Sc, M.Sc and M.Phil days and I thank all of them. I sincerely acknowledge the Tagore Arts College (TAC) campus, Pondicherry where I studied the bachelor and masters and spent six years of my academic life. Also, I would like to thank IGCAR, Kalpakkam, where I have spent one and half years as project student and JRF, and this place gave me a huge breakthrough in my career and changed my approach to science. I sincerely thank Dr. Janaki ad Dr. Bharathi for giving the opportunity to work in IGCAR and for their scientific motivation. Special thanks to madam (Dr. Janaki) who is really a disciplined scientist and this quality of her inspiring me a lot.

I had immense admiration to my role model Bharat Ratna Dr. A.P.J. Abdul Kalam Sir, who inspires me a lot in my personal life. I sincerely thank my outstanding physics teacher Prof. S.V.M. Sathyanarayana (Pondicherry University) who has

influenced me in a big way and are the main motivation to choose science as my career from M.Sc onwards.

I acknowledge DST and DST-SERB for the financial support to the various synchrotron trips [Elettra (Italy), KEK, Photon factory (Japan), PETRA (Germany)] and Gordon Research Conference, USA.

My special thanks to Madam (Mrs. Shobha Chandrabhas), and Ms. Sushmitha for their affection and excellent hospitality they extended during several occasion.

Most importantly, I would like to take this very special opportunity to thank my loving family members who have been giving me endless support and unconditional love. First, I thank my mother (Mrs. Suseela Vincent) and father (Mr. Vincent) who worked as a coolie (labour) and through their very hard and painful work, they enriched me as an educated person. I thank my lovable brother Ragadevan for his constant support and encouragement. Special thanks to my in-laws family for their various help and support during my Ph.D.

Finally, my sincere and deepest appreciation to my wife (Rooplavathi) who has been very supportive and encouraging in all circumstances for more than a decade and very fortunate to have her in my life. Besides, I thank my wife for her patience, understanding, unbelievable and unconditional love, and she has been always celebrating each of my achievement as her's. Importantly, I thank my lovely son (Rithul Advik) who has given me the time to complete my Ph.D commitments. I dedicate this work to all of my family members.

Table of Contents

2. Experimental techniques

Part I Pressure induced topological quantum phase transitions

3. Phonon signatures of multiple topological quantum phase transitions in compressed $TlBiS_2$

4. Switching of the topologically non-trivial and trivial quantum phase transitions in compressed 1T-$TiTe_2$

PREFACE

Pressure is one of the fundamental thermodynamic parameters which is clean and very effective tool to study material properties. It alters the interatomic bond distances, forces, volume, density, effective hybridization, electronic structure, and, consequently, material intrinsic characteristics. Raman scattering and synchrotron X-ray diffraction (XRD) are the efficient and versatile probes to study the structural and electronic transitions induced by external stimuli such as pressure. This thesis utilizes high pressure Raman scattering and synchrotron XRD techniques to investigate and understand the pressure induced electronic and structural phase transitions in strong spin orbit coupling materials. This thesis is divided into eight chapters. Each work chapter includes a topical introduction and motivation on the problem which is being addressed.

Chapter 1 gives a brief discussion about the general aspects of Raman scattering, XRD and the fundamental excitations which affect the phonons. Also, high pressure effects on materials and Raman spectra are discussed. Further, brief overview of the equation of state, types of structural and electronic phase transitions and the scope of the present thesis are covered. Chapter 2 describes the experimental details which include the design and working principle of Raman setup, and the methods of doing high pressure experiments. Also, brief overview of the typical powder XRD experiments at the synchrotron and Xpress beamline, Elettra, Trieste, Italy has been given.

The work chapters are divided into two parts. Part I comprises of pressure induced topological quantum phase transitions (TQPT) in $TlBiS_2$ and 1T-$TiTe_2$. Chapter 3 presents high pressure Raman and synchrotron XRD studies on $TlBiS_2$. In this chapter, we show the evidence of two isostructural electronic transitions deduced from the unusual electron-phonon coupling (A_{1g} and E_g phonons) at ~0.5 GPa and ~1.8 GPa observed in the Raman scattering measurements. Our first principles density functional theory based electronic band structure, topological invariant Z_2 and mirror Chern number n_M calculations reveal that the phonon anomalies at ~0.5 GPa and ~1.8 GPa are related to the topological insulator and topological crystalline insulator (TCI) transitions, respectively. Both high pressure Raman and powder synchrotron XRD

confirm a reversible first order structural phase transition of the rhombohedral phase above 4 GPa.

Chapter 4 deals with the effect of high pressure on transition metal chalcogenide 1T-$TiTe_2$, a prominent layered 2D system. Here, we have explored the topologically non-trivial and trivial quantum phase transitions at ~2 GPa and ~4 GPa with evidence of the minima in *c/a* ratio concomitant with the phonon linewidth anomalies of E_g and A_{1g} modes. Between ~4 GPa and ~8 GPa, a transformation from an anisotropic 2D layer to a quasi-3D crystal network is noticed, which occurs due to increased interlayer Te-Te interactions (bridging) by the charge density overlap. In addition, we observed a reversible first-order structural phase transition from a trigonal ($P\bar{3}m1$) to monoclinic ($C2/m$) phase above 8 GPa.

Part II is based on the investigations of pressure induced structural and isostructural electronic transitions such as electronic topological transition, the semiconductor to metal transition in InTe, $AgBiSe_2$ and Sb_2S_3 compounds. In Chapter 5, we have investigated Raman scattering and synchrotron XRD measurements on InTe compound. The pressure induced a semiconductor-to-metal transition in InTe is deduced from the phonon anomalies of A_{1g} and E_g modes along with the decrease and anomaly in Raman intensities at ~3.6 GPa. In distinct pressure regime, the presence of strong anharmonic phonon-phonon interactions and electron-phonon interactions are noticed from phonons' peculiar behavior. Our Raman scattering experiments up to ~19 GPa reveals the pressure induced structural transitions (B37 → B1 → B2) in InTe.

Chapter 6 deals with the pressure dependent structural and vibrational study of $AgBiSe_2$. From our study, we found that pressure induced a weakly first-order structural phase transition from hexagonal (α-$AgBiSe_2$) to rhombohedral (β-$AgBiSe_2$) at ~0.7 GPa. In the rhombohedral phase, we observed the electronic topological transition at ~2.8 GPa, followed by a semiconductor to metal transition at ~7.0 GPa, from the changes observed in the Raman measurements. In Chapter 7, we have studied the pressure dependence of Raman scattering on Sb_2S_3. The electronic topological transition is evidenced in the wide band gap semiconductor Sb_2S_3 (E_g = 1.7-1.8 eV) at ~4 GPa from the softening of phonon modes A_g^2, A_g^3, and B_{2g} and a sharp anomaly in their line widths.

Chapter 8 concludes the thesis with a brief summary and future prospects originating from this thesis.

List of publications relevant to this thesis

1. **V. Rajaji**, Raagya Arora, Saurav Ch. Sarma, B. Joseph, Umesh V. Wagmare, Sebastian C. Peter, and Chandrabhas Narayana *"Phonon signatures of multiple topological quantum phase transitions in compressed $TlBiS_2$: A combined Experimental and theoretical study" (Under review in Phys. Rev. B).* (**Chapter 3**)

2. **V. Rajaji**, Utpal Dutta, P. C. Sreeparvathy, Saurav Ch.Sarma, Y. A. Sorb, B. Joseph, Subodha Sahoo, Sebastian C. Peter, V. Kanchana, and Chandrabhas Narayana, *"Structural, vibrational, and electrical properties of 1T-$TiTe_2$ under hydrostatic pressure: Experiments and theory" Phys. Rev. B **97**,085107 (2018).* (**Chapter 4**)

3. **V. Rajaji**, Koushik Pal, Saurav Ch.Sarma, B. Joseph, Sebastian C. Peter, Umesh V. Waghmare, and Chandrabhas Narayana, *"Pressure induced band inversion, electronic and structural phase transitions in InTe: A combined Experimental and theoretical study" Phys. Rev. B **97**, 155158 (2018).* (**Chapter 5**)

4. **V. Rajaji**, Pallavi S. Malavi, Sharma S. R. K. C. Yamijala, Y. A. Sorb, Utpal Dutta, Satya N. Guin, B. Joseph, Swapan K. Pati, S. Karmakar, Kanishka Biswas, and Chandrabhas Narayana, *"Pressure induced structural, electronic topological, and semiconductor to metal transition in $AgBiSe_2$" , Appl. Phys. Lett. **109**, 171903 (2016).* (**Chapter 6**)

5. Y. A. Sorb, **V. Rajaji**, P. S Malavi, U. Subbarao, P. Halappa, S. C Peter, S. Karmakar and C. Narayana, *"Pressure-induced electronic topological transition in Sb_2S_3" J. Phys.: Condens. Matter **28**, 015602 (2016).* (**Chapter 7**)

Chapter 1

Introduction

1.1 Historical background

The study of light and its interaction with matter has fascinated the scientific field right from its discovery. In 1864, James Clerk Maxwell established the electromagnetic (EM) theory of light, which couples the electricity and magnetism [1]. Importantly, he proposed that light is an EM wave which travels at the speed of about 3 x 10^8 m/s. This is considered as the greatest advancement in the field of light. Remarkably, in 1887, the German physicist Heinrich Hertz showed the existence of EM waves experimentally and thus created fascination about light in many other physicists. In 1924, French physicist Louis de Broglie gave the idea of dual nature of light (i.e., wave and particle) and this hypothesis was subsequently proved in many experiments. Light exhibits many interesting properties such as reflection, transmission, absorption, scattering, interference, diffraction, polarization, *etc*. When light interacts with matter, it can undergo any of these phenomena. In this thesis, we have used the scattering and diffraction-based experiments such as inelastic light scattering (Raman Spectroscopy) and X-ray Diffraction (XRD). Hence, we briefly review the history of scattering and diffraction of light.

Historically, scattering was first accounted by Leroy Tyndall, who observed the scattering of light from particles suspended in transparent fluids [2]. In 1871, British physicist Lord Rayleigh explained the blue color of the sky as an effect of elastic (i.e., without a change in frequency) scattering [3]. He suggested that the amount of scattering is inversely proportional to the fourth power of the wavelength, for the objects whose dimensions are smaller than the wavelength of the radiation. According to Rayleigh's law, the scattering objects can be electrons, atoms, molecules, *etc*. Another kind of elastic scattering is Mie scattering [4], in which the particle sizes (e.g. aerosol particles) are larger than the wavelength of the light. In 1922, the inelastic scattering of light by long wavelength elastic sound waves was theoretically predicted by Brillouin [5]. Shorty later, in 1923, Austrian physicist Adolf Smekal developed the theory of inelastic light scattering using a system with two quantized energy levels [6]. In 1928, Sir C. V. Raman and his student K. S. Krishnan experimentally observed the inelastic scattering of light in liquids [7-9]. They referred it to as '*A new type of secondary radiation*' and later on, this phenomenon was named '*Raman effect'*. Raman effect was considered to be an optical analog of the Compton effect in molecular

systems. Sir C. V. Raman won the Noble prize in 1930 for this discovery of inelastic scattering of light. It is important to mention here that soon after Raman's discovery, Russian scientists Grigory Landsberg and Leonid Mandelstam independently observed the same phenomenon in crystals [10].

An important property of the wave nature of light is diffraction, which refers to the slight bending of light as it passes around the edge of an object. Historically, the diffraction of light was observed for the first time by Francesco Maria Grimaldi who has also gave the name diffraction from the Latin word *diffringere.* It means 'to break into pieces' thus indicating the breaking of light in different directions. After that, a Scotland scientist James Gregory observed the diffraction patterns caused by a bird feather which was considered as the first diffraction grating. Soon after this, many scientists like Thomas Young, Augustin-Jean Fresnel, Christiaan Huygens, *etc*, contributed to the concept of diffraction. The discovery of XRD by Max von Laue (1912) revolutionized the field of the solid-state crystallography. In 1912–1913, William Lawrence Bragg, established the Bragg's law, which relates the observed scattering to the reflections from evenly spaced lattice planes within the crystal [11, 12]. It is well known that, physicists William Lawrence Bragg and his father William Henry Bragg contributed a lot to the field of crystallography (based on XRD) and were awarded the Nobel Prize in Physics (1915). With advancements in technology, it is now possible to study (using XRD) more complicated two and three-dimensional structures (in solid state) and also the structures of many biological molecules including proteins, vitamins, and nucleic acids such as DNA.

In this chapter, we will briefly present an overview about the theory of Raman scattering (classical and quantum theory), various concepts used in the thesis such as high-pressure phenomena, pressure effects on Raman spectra, phonon-phonon interactions, electron-phonon coupling, equation of state, types of phase transitions, probing the phase transition, and finally a scope of the thesis.

1.2 Raman scattering

When a monochromatic light of frequency υ_i is incident on a sample (gas, liquid or solid), a small part of the light will be scattered along different directions in addition to phenomenon like transmission, reflection, absorption, *etc*. Scattered light can be

identified to have elastic and inelastic components. The elastic component with no change in frequency with respect to the incident light is known as Rayleigh scattering (elastic scattering). If there is a change in the frequency with respect to the incident light, then it is known as Raman scattering (inelastic scattering). Further, there are two components in Raman scattering, 1. Stokes lines and 2. Anti-Stokes lines. The Stokes lines have a lower energy, and the anti-Stokes have a higher energy than the incident radiation. Since the Stokes line lies on the low frequency side with respect to incident light, [i.e., the changes in frequency is negative ($-\Delta\nu$)], resembles the Stokes shift found in luminescence. Hence, they are referred to as Stokes-Raman lines.

Raman is non-destructive and has good flexibility in sampling arrangements when compared to many other spectroscopy techniques. Historically, the first Raman experiment was performed using direct Sun light as the source, filter to get a component of the visible spectra, lens to converge the light, telescope objective and eye or camera as the detector. However, with the development of the laser, monochromator, and optical components, nowadays Raman spectroscopy has been widely used in many fields such as physics, chemistry, biology, art, archeology, *etc*. In the subsequent section, we will briefly describe the classical and quantum theory of Raman scattering.

1.2.1 Classical theory

When an EM wave is incident on a molecule, the polarization of the medium takes place with respect to the electric field direction. The strength of the induced polarization (P) is directly proportional to the applied electric field E. That is,

$$\mathrm{P} = \alpha \mathrm{E} \tag{1.1}$$

where α is the constant of proportionality and is called polarizability of the molecule. Mathematically α is a tensor with nine components (in a Cartesian coordinate system). In general, it is an intrinsic property of the material that mainly depends on the nature of its bonds.

The time-varying electric field component of the incident EM wave is expressed as,

$$\mathrm{E} = E_i \cos 2\pi \upsilon_i \mathrm{t} \tag{1.2}$$

where υ_i and E_i are the frequency and amplitude of the incident EM wave, respectively. The time-dependent induced dipole moment is given by,

$$P = \alpha E_i \cos 2\pi\upsilon_i t \tag{1.3}$$

During the molecular vibration of the frequency υ_n, consider Q is the displacement of the respective atoms about their equilibrium position. In case of the harmonic approximation, Q can be expressed as,

$$Q = Q_0 \cos 2\pi\upsilon_n t \tag{1.4}$$

here Q_0 represents the maximum displacement about the equilibrium position. When the displacements associated with molecular vibrations are sufficiently small, the polarizability α can be approximated by the Taylor series with the normal coordinate Q as,

$$\alpha = \alpha_0 + \left(\frac{\partial\alpha}{\partial Q}\right) Q + \ldots\ldots\ldots \tag{1.5}$$

where α_0 is the molecular polarizability of the vibrational mode at the equilibrium position. Neglecting the higher order terms in the Taylor series and substituting the Eqs. 1.5 and 1.4 into Eq. 1.3, we get,

$$P = \left[\alpha_0 + \left(\frac{\partial\alpha}{\partial Q}\right) Q_0 \cos 2\pi\upsilon_n t\right] E_i \cos 2\pi\upsilon_i t \tag{1.6}$$

$$P = \alpha_0 E_i \cos 2\pi\upsilon_i t + \left(\frac{\partial\alpha}{\partial Q}\right) Q_0 E_i \cos 2\pi\upsilon_i t \cos 2\pi\upsilon_n t \tag{1.7}$$

Using the below trigonometric identity,

$$[2 \cos\theta_1 * \cos\theta_2 = \cos(\theta_1 + \theta_2) + \cos(\theta_1 - \theta_2)]$$

The Eq. 1.7 reduces into,

$$P = \alpha_0 \cos 2\pi\upsilon_i t + \frac{1}{2}\left(\frac{\partial\alpha}{\partial Q}\right) Q_0 E_i \left[\cos 2\pi(\upsilon_i + \upsilon_n)t + \cos 2\pi(\upsilon_i - \upsilon_n)t\right] \tag{1.8}$$

Thus, the induced dipole moment consists of three different frequency components, namely υ_i, $(\upsilon_i + \upsilon_n)$ and $(\upsilon_i - \upsilon_n)$ for every vibration of the molecule with frequency, υ_n. The scattered frequency υ_i represents the elastic scattering (Rayleigh scattering) in which there is no exchange of momentum and energy between the

molecule and the incident EM wave. The other two frequency components ($\upsilon_i + \upsilon_n$) and ($\upsilon_i - \upsilon_n$) are generally considered as inelastic scattering (Raman scattering). Here, the increase of scattered frequency ($\upsilon_i + \upsilon_n$) is referred to as 'anti-Stokes scattering' and the decrease of scattered frequency ($\upsilon_i - \upsilon_n$) is referred to as 'Stokes scattering'. When the $\left(\frac{\partial \alpha}{\partial Q}\right) \neq 0$ in Eq. (1.8), then the contribution will exist for the Stokes and anti-Stokes scattered light for the frequency υ_n also called as Raman active vibration. Hence, the mode will show stronger (weaker) intensity for a huge change (small change) in the polarizability. Though the classical theory described above predicts the Raman frequencies and selection rule, it fails to give the accurate intensities. Thus, it becomes necessary to invoke the quantum mechanical picture to describe the scattering cross-section which accurately calculates the Raman intensities.

1.2.2 Quantum theory

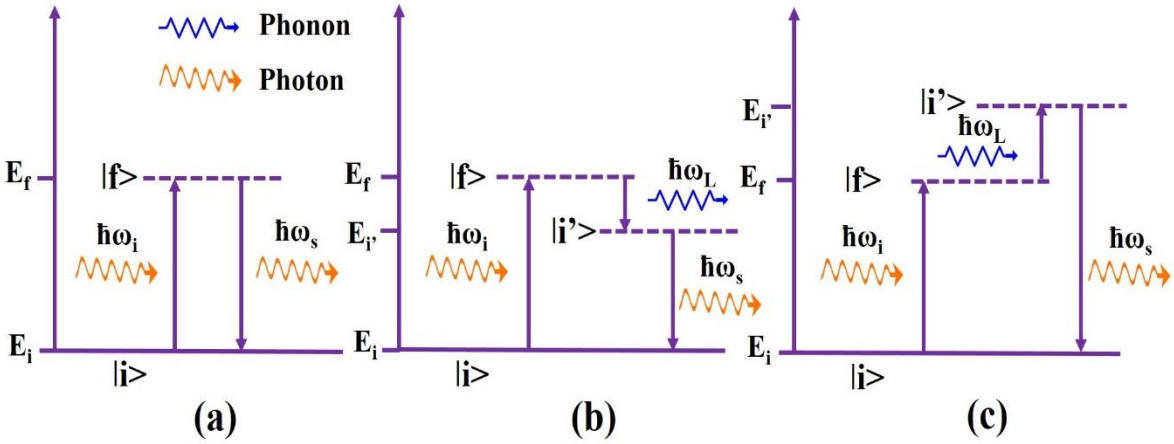

FIG. 1.1 Schematic diagram of the (a) Rayleigh, (b) Stokes and (c) anti-Stokes Raman scattering.

In quantum mechanical treatment, the Raman scattering phenomena can be explained using third order time-dependent perturbation theory [13-15]. In the Raman process, the interaction between the photons and phonon is mediated by an electron. To be precise, Raman scattering involves a three-step process which is explained as below:

1) The incident photon ($\hbar\omega_i$) excites the electron from the ground state $|i>$ to a virtual state (intermediate state) $|f>$ and hence an electron-hole pair is created.

2) The virtual state $|f>$ goes to another state $|i'>$ due to the creation (Stokes process) or annihilation (anti-Stokes process) of a phonon in the lattice with an energy $\hbar\omega_L$.

3) Finally, the electron in the state $|i'>$ recombines with the hole in the state $|i>$ thus emitting a Raman scattered photon ($\hbar\omega_s$).

The schematic of the three-step Raman process is shown in Figs. 1.1 (a)-(c). The combination of the above three processes gives the scattering cross section using the third order perturbation theory as below [13];

$$\hat{e}_s.\xi.\,\hat{e}_i \sim \frac{<i|H_{ep}|i'><i'|H_{eph}|f><f|H_{ep}|i>}{(E_{i'}-\hbar\omega_i)(E_f-\hbar\omega_s)} \tag{1.9}$$

here, H_{ep} and H_{eph} represent the Hamiltonian terms which describe the electron-photon interaction and the electron-phonon interaction, respectively. E_i, E_f and E_i' are energy levels associated with the states $|i>$,$|f>$, and $|i'>$ respectively. ξ is the Raman tensor and $\hat{e}_i$ and $\hat{e}_s$ are the unit polarization vectors of incident and scattered light, respectively. Similarly, ω_i, and ω_s, are frequencies of the incident and scattered photon, while ω_L indicates the frequency of the phonon. For the normal Raman scattering process, the virtual state need not be a real electronic state. Hence, the normal Raman process is weaker than the fluorescence. But, when the frequency of the incident light is closely matched with the real electronic state, the scattering cross section will be very large and possibly enhanced by a factor of 10^6. This phenomenon is called resonance Raman scattering.

The differential scattering cross section in terms of the solid angle $d\Theta$ with a frequency between ω_s and $\omega_s + d\omega_s$ can be written for the Stokes process as, [14]

$$\frac{d^2\sigma}{d\Theta d\omega_s} = \upsilon V \frac{\hbar\omega_s^4}{2N\omega_i c^4} |\hat{e}_s.\xi.\,\hat{e}_i|^2 \,(n(\omega)+1)\, g_i(\omega) \tag{1.10}$$

Similarly, for the anti- Stokes process,

$$\frac{d^2\sigma}{d\Theta d\omega_s} = \upsilon V \frac{\hbar\omega_s^4}{2N\omega_i c^4} |\hat{e}_s.\xi.\,\hat{e}_i|^2 \, n(\omega)\, g_i(\omega) \tag{1.11}$$

here, N indicates the number of oscillators, $g_i(\omega)$ is the line shape response function (generally considered to be Lorentzian function), $n(\omega) = \left[e^{\frac{\hbar\omega_L}{2K_BT}}\right]^{-1}$ is the Bose-Einstein (BE) thermal population factor for the phonons and V is the sample volume. BE factor clearly describes that the phonon population in the excited state is lesser than the ground state and hence Stokes lines must be of higher intensity than the anti-Stokes line. The intensity is directly proportional to the differential scattering cross section. Therefore, from Eqs. 1.10 and 1.11, we can show that:

$$\frac{I_{Stokes}}{I_{anti-Stokes}} = \left[\frac{\omega_i-\omega_L}{\omega_i+\omega_L}\right]^4 e^{\frac{\hbar\omega_L}{K_BT}} \tag{1.12}$$

Using the Eq. 1.12, we can calculate the *in-situ* sample temperature (non-contact method) by measuring the intensity of the Stokes and anti-Stokes spectral lines [16].

From the Eqs. 1.10 and 1.11, scattering efficiency is dependent on three factors.

(i) Incident light frequency (ω_i)

In the Raman process, the frequencies of the incident (ω_i) and scattered (ω_s) light differ very little; hence we can say that scattering intensity increases as ω_i^3. It is noteworthy that here the Raman scattering intensity violates the general frequency dependence of radiation (i.e., intensity is proportional to ω^4).

(ii) Scattering volume (V)

Generally, the light penetration depth (d) of the material is calculated by relation ($d = \frac{\lambda_i}{\kappa}$), where λ_i is the wavelength of the incident light, and κ is the absorption coefficient. Here, scattering volume increases with an increase in the penetration depth d in an opaque sample, and therefore scattering efficiency can be improved by increasing the λ_i. It is important to note that, the scattering intensity depends on both λ_i and ω_i^3. But, if you increase the λ_i, ω_i^3 decreases drastically and thus no advantage can be gained.

(iii) Polarization configuration ($\hat{e}_s.\xi.\hat{e}_i$) (scattering geometry)

The polarization configuration ($\hat{e}_s.\xi.\hat{e}_i$) factor plays a significant role. The scattering intensity is directly proportional to the polarization of the incident and scattered light. The components of the scattering tensor will be decided by the crystal symmetry and also the symmetry of the specific vibrational mode. By varying the polarization geometry and changing the orientation of the sample, we can choose the particular set of components in the scattering tensor ξ that contributes to Raman intensity. In fact, this third factor gives the polarization selection rule which is helpful in the assignment of Raman mode for the crystalline samples. The Raman tensor for the different point groups and polarization selection rules are listed elsewhere in the great detail [15, 17-19].

From the above discussion, it is clear that the experimental conditions need to be optimized to get the maximum Raman intensity with respect to the above three points.

1.3 High pressure effects on materials

Physical properties of materials are strongly dependent on temperature and pressure. All applied research involves the understanding of the pressure and temperature dependence of their physical properties with a view to preparing the material to operate in a mechanically strained environment and induce the expected properties in different thermodynamic conditions. Pressure is one of the fundamental thermodynamic parameters which is effective and cleaner compared to other parameters like temperature. For instance, the pressure changes of 10 GPa in Si produces a volume decrease of 5 %, whereas the total temperature induced volume change from ~ 0 K to melting is only 1.8% [20]. In fact, for the softer molecular solids (lower bulk modulus), this volume change with pressure is even greater. Therefore, the effect of temperature is subtler than pressure. Besides, pressure induces only the volume changes whereas the temperature changes the phonon populations along with the volume changes, and therefore the pressure perturbation is much cleaner.

Pressure is the effect of a force applied on per unit surface area. So, the application of a huge amount of force on a small area will generate high pressure. With the help of a simple diamond anvil cell (DAC), we can generate the pressure up to ~ 5

megabars (500 GPa) on the sample size of < 10 μm. To ascertain this, recently, metallization of hydrogen at ~ 495 GPa has been shown with the help of optical measurements using DAC [21], which is considered as a holy grail problem of the high-pressure science. The DAC is the most versatile tool as diamonds are transparent to a wide spectrum of EM wavelengths including X-rays, visible and IR light. Hence we can perform various studies [22] such as XRD, Raman scattering, photoluminescence, resistivity, infrared absorption, optical reflectivity, *etc*.

Generally, the appropriate utilization of high pressure techniques in material science is broadly divided into three categories; 1. To understand the pressure dependent phenomena of the materials (like structural phase transition, phase stability, *etc*.), 2. To synthesis a new class of materials, which are not commonly seen at ambient conditions. Super hard materials like synthetic diamond, cubic boron nitride, and superconducting materials are synthesized using high pressure techniques [23, 24]. For example, recently, the new allotrope of Si, Si_{24} [space group (SG): *Cmcm*] was discovered at P ~ 10 GPa and T ~ 800°C, which has a quasi-direct bandgap near 1.3 eV [25] and hence expected to have photovoltaic applications. 3. To induce novel properties in a material such as metallization, superconductivity, topological quantum phase transition, *etc*. For example, recently, a sharp drop in the electrical resistance (using four-probe measurements) was observed around 260 K at P ~ 190 GPa for $LaH_{10\pm x}$ (where x varies between +2 and -1) [26], which brings a twist in the high temperature superconducting field. It is noteworthy that, pressure dependent phenomena are reversible (most of the time), but for the DAC laser heating experiments (high pressure high temperature conditions), they are irreversible.

1.3.1 Pressure units and its significance

The SI unit of pressure is Pascal (Pa), defined as a force of one Newton per square meter. Pascal is a very small pressure unit, for example, the standard atmospheric pressure is 101325 Pa. Another common practical unit of pressure is a bar which is given by 1 bar = 10^5 Pa = 10^6 dynes / cm^2. The average atmospheric pressure at the surface of the earth is 1 atm = 1.01325 bar. In high pressure science, pressure units of kbar, MPa, and GPa are generally used (1 kbar = 0.1 GPa = 100 MPa). Here it is important to mention that for solid materials consisting of ionic, covalent, and

electrostatic bonds, significant changes can be noticed only in a pressure range of GPa. But, in case of molecular solids, a few MPa is enough to induce significant changes. It is interesting to note the lower and higher pressure regions of the earth. The pressure experienced at the bottom of the deepest ocean (Mariana Trench) is about 1,086 bars, and the pressure at the center of the earth is about 3.6 Mbar (maximum pressure).

1.3.2 Methods for generating high pressure

There are two major categories of high pressure generation, i.e., Static and Dynamic methods. Here, we briefly discuss these two methods.

(a) Static method

The static methods give purely hydrostatic pressure conditions and do not change the temperature at all. In this method, sufficient time is available to attain thermodynamic equilibrium under isothermal conditions. Using the piston cylinder, the tungsten carbide (WC) cell, the diamond anvil cell (DAC), and the cubic press method, hydrostatic pressure can be achieved. Recently, with the advent of the DAC, the range of pressure in static experiments has been increased up to ~5 Mbar.

(b) Dynamic method

The dynamic methods provide changes in the pressure as well as the temperature. The shockwave [27] and ultrasonic techniques are the generally used in dynamic methods. A shock wave is a disturbance propagating at supersonic speed in a material, which is produced by an impact of a projectile on the sample or by the detonation of an explosive in contact with it. During the shockwave interaction, the system is not in equilibrium, hence an extremely rapid rise in pressure, density and temperature is observed.

In this thesis, we have applied static pressure using DAC up to ~22 GPa (maximum pressure) at room temperature conditions for studying the strong spin orbit coupling materials.

1.4 Pressure effects on Raman spectra

The Raman mode parameters such as frequency, linewidth, and intensity are generally very sensitive to the applied pressure. The changes in the Raman mode parameters indicate many types of transitions. We will be discussing briefly how the Raman profile changes under pressure.

(a) Raman frequency changes under pressure

As the pressure decreases the volume of the unit cell, in turn decreases the interatomic distance. For the case of a simple diatomic molecule, vibrational frequency is directly proportional to the square root of the spring constant (i.e., bond stiffness). Hence, the vibrational frequency is expected to increase upon lattice compression. Mathematically, Gruneisen parameter (**γ**) quantifies the changes in the frequency of the vibrational mode as a function of the unit cell volume and is given below [28].

$$\gamma = -\frac{\partial \ln \omega}{\partial \ln V} \tag{1.13}$$

$$\gamma = -\frac{1}{\beta}\frac{\partial \ln \omega}{\partial P} \tag{1.14}$$

where ω is the frequency of the vibrational mode, and β is the isothermal volume compressibility. The γ plays an important role in understanding the pressure (or temperature) dependence of elasticity. It takes positive values for the three-dimensional crystals, but negative for some cases such as soft modes, and negative thermal expansion materials [29]. Mention must be made that, γ is strongly dependent on compressibility, hence takes different values for different compressions such as uniaxial, biaxial and hydrostatic. In this thesis, Gruneisen parameters are calculated for various materials (under hydrostatic pressure) and will be discussed in the following chapters.

(b) Raman linewidth changes under pressure

Generally, Raman linewidth is inversely proportional to the lifetime of the phonons (an important physical quantity) for crystalline materials. During the increase in pressure, a systematic increase in the linewidth of the Raman peak is expected from

the quantum uncertainty principle ($\Delta E.\Delta t \geq \hbar/2$). However, in many cases very anomalous behaviors are reported. Since pressure can also change the phonon density of states (in addition to bond length changes) and thus can increase or decrease certain types of interactions between excitations present in the material. Therefore, if the phonon couples with the excitations, then its lifetime will be modified accordingly. It is important to mention that some of the pioneering works on the linewidth of a Raman mode were studied for the zinc blend structure semiconducting systems like Si, Ge, and SiC [30,31]. In these materials, the observed systematic increase in linewidth upon the increase in pressure was understood as the anharmonic decay of a phonon into phonons of different energies. Recently, the pressure dependent Raman linewidth studies on ambient 3D topological insulator materials like Bi_2Te_3, Bi_2Se_3, and Sb_2Te_3 compounds showed the lifting of the Fermi resonance [32]. We have observed similar behavior in the $AgBiSe_2$ compound and will be discussed in Chapter 6. It is noteworthy that pressure- induced disorder and amorphization phenomenon give rise to unusually large linewidths.

(c) Raman intensity changes under pressure

The intrinsic strength of the Raman intensity comes from the net changes in the polarizability (i.e., derivative of polarizability) during a vibration. In most of the experiments, the decreasing intensity of Raman modes is observed for increasing pressure [33, 34]. This can be explained by scattering losses due to heterogeneities induced by pressure gradients and changes in the absorption coefficient. Since Raman scattering is a light based technique, Raman intensity is very sensitive to the types of electronic states of matter. For example, metals show relatively weaker Raman intensity than insulators or semiconductors. It is mainly because the increase of density of states, increases the number of conduction electrons, which would screen the incident electromagnetic light. Consequently, this will affect the Raman scattering cross section in the case of a metal. We have also observed interesting pressure dependent Raman intensity behavior during electronic transitions, and that will be discussed in Chapters 5 and 6.

1.5 Various interactions which affect phonons

Phonon is a quantized lattice energy. In solids, phonons are not independent and often interact with other particles and quasiparticles such as the electrons, magnons and even with other phonons. For example, temperature and pressure induced frequency changes in Raman spectra cannot be explained by the harmonic model. Here, we will discuss the effect of anharmonic interactions and electron-phonon coupling on Raman modes. This discussion will be useful in understanding the pressure dependence of the Raman mode parameters in Chapters 3 to 7.

1.5.1 Phonon-phonon interactions (anharmonicity)

In harmonic approximations, phonons are considered independent, and the distribution of phonon states does not vary with time. This is not true in case of real crystals. Also, the phenomena like thermal expansion, pressure and temperature variations of elastic constants and compressibility cannot be explained by the harmonic model [33]. To understand the anharmonicity, we first describe the simplest case, i.e., temperature induced anharmonicity model. Based on the Balkanski *et al*. theoretical work [16], the temperature dependence of the Raman frequency (ω) and linewidth (Γ) for the cubic anharmonic model is given by,

$$\omega(T) = \omega_0 + CT + B_1\left(1 + \frac{2}{e^{\hbar\omega/2K_BT} - 1}\right) \quad (1.15)$$

$$\Gamma(T) = \Gamma_0 + B_2\left(1 + \frac{2}{e^{\hbar\omega/2K_BT} - 1}\right) \quad (1.16)$$

where, ω_0 and Γ_0 are the intrinsic (T = 0 K) frequency and linewidth of the phonon respectively. B_1 and B_2 are the cubic anharmonic constants and C is the thermal expansion coefficient. Here, CT is the implicit frequency shift caused by temperature which is determined by the thermal volume expansion. The third term in Eq. 1.15 is an explicit contribution from the thermal population of vibrational levels. The zone center optical phonon can decay into two phonons of different energy (see Fig. 1.2) and these decay channels broaden the Raman linewidth, and this phenomenon is mathematically accounted for the second term of Eq. 1.16. The anharmonic decay of an optical phonon into a pair of phonons should follow the conservation of energy and wave vectors. For

example, Fig. 1.2 represents the conservation of energy {$\upsilon_{acosutic}$ (q= π/a) = ½ [υ_{optic} (q= 0)]} and wave vectors {(q_{optic} = 0) = [($q_{acoustic}$ = π/a) + ($q_{acoustic}$ = -π/a)]} [33].

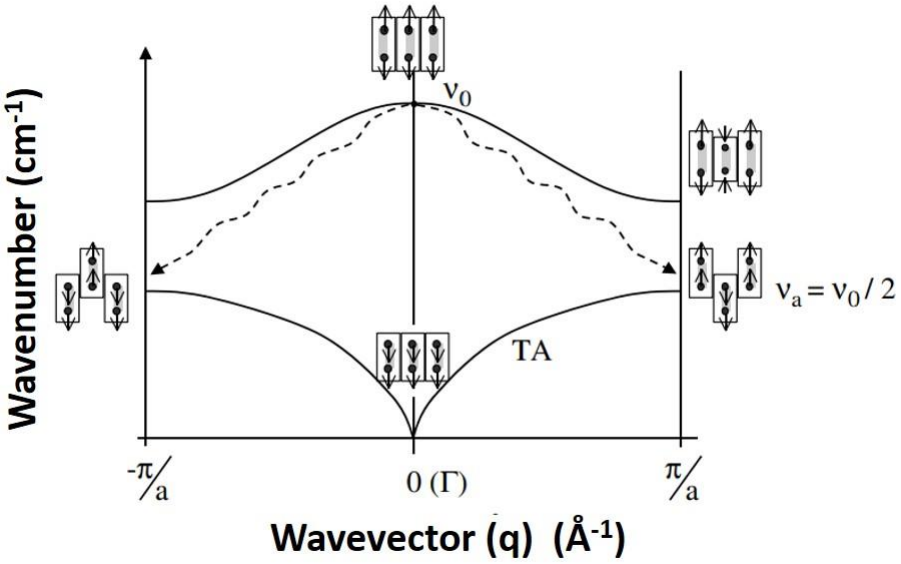

FIG. 1.2 Schematic representations of an optical phonon decay into two acoustic phonons. (This picture is adopted from Ref. [33]).

According to a theoretical work developed by R.A. Cowley, the perturbation (e.g. pressure) dependent phonon frequency (ω) is given below, [35,30]

$$\omega = \omega_0 + \Delta\,(\omega) \tag{1.17}$$

where Δ(ω) represents the anharmonic contribution due to phonon-phonon interactions, i.e., the real part of the phonon self-energy and ω_0 indicates the harmonic frequency (intrinsic). The full width at half maximum (FWHM, 2Γ) of the optical phonon at zero temperature for anharmonic interactions is given by [30,35],

$$2\Gamma\,(\omega) = \frac{\pi}{\hbar^2} \sum_{q,i_1,i_2} |E_3(q,i_1,i_2)|^2\, \delta(\omega - \omega_{i_1}(q) - \omega_{i_2}(q)) \tag{1.18}$$

where, anharmonic matrix element E_3 is representing the Fourier transform of the third derivative of the total energy per unit cell volume with respect to the phonon displacements and the indices i_1, i_2 run over the different phonon branches. The re-normalization of the phonon frequency due to the anharmonic phonon-phonon

interactions at zero temperature (cubic and quadratic force constants) is given by two contributions, [i.e., $\Delta^{(3)}(\omega)$ and $\Delta^{(4)}(\omega)$] [30,35]

$$\Delta(\omega) \simeq \Delta^{(3)}(\omega) + \Delta^{(4)}(\omega) \tag{1.19}$$

The Hilbert transform of Γ (imaginary part of the phonon self-energy) gives the $\Delta^{(3)}(\omega)$,

$$\Delta^{(3)}(\omega) = -\frac{2}{\pi} P_1 \int_0^{\infty} \frac{\omega' \Gamma(\omega')}{(\omega'^2 - \omega^2)} d\omega' \tag{1.20}$$

$$\Delta^{(4)}(\omega) = \frac{12}{\hbar} \sum_{q,i_1} E_4(q, i_1) \tag{1.21}$$

where P_1 indicates the Cauchy principal part of the integral, E_4 is the Fourier transform of the quartic anharmonic force constant, and the summation sign indicates the energy shift due to the interaction of the zone-center optical phonon with a phonon of wave-vector q in the i_1^{th} branch.

Temperature changes the average position of the atoms and creates a non-equidistance in the energies of these levels. Hence it affects the phonon population associated with each normal mode and thereby the phonon occupation number. In the case of a pressure change, equilibrium distance between the atoms changes and consequently the restoring force and the phonon density of states are modified. Even though the origin of the deformation induced by these two external perturbations (T and P) are different, the phonon density of states is a critical parameter, because pressure changes its form and temperature changes the phonon population [33]. In both cases, the changes in the unit cell dimension (or lattice parameters) and phonon frequencies are attributed to the anharmonicity of the potential. Hence the pressure and temperature induced changes of Raman frequency and Raman linewidth are attributed to the decay of optical phonons into two or three phonons of different energy [33]. It is important to point out, for a perfect crystal, even at zero temperature (0 K), the lifetime of the phonon is finite, due to the anharmonic decay. This decay rate can be probed via the linewidth of a Raman mode (which is inverse of the phonon lifetime).

1.5.2 Electron-phonon interactions

In solids, electron-phonon interaction or electron-phonon coupling (EPC) is one of the most fundamental and common interactions. It plays an important role in the dynamic processes such as resistivity, thermal conductivity, superconductivity, excited state dynamics, Raman spectra, phonon dispersions, *etc*. For example, EPC is the pairing glue in conventional low-temperature superconductors [36] and this kind of electron-phonon interactions is schematically represented in Fig. 1.3.

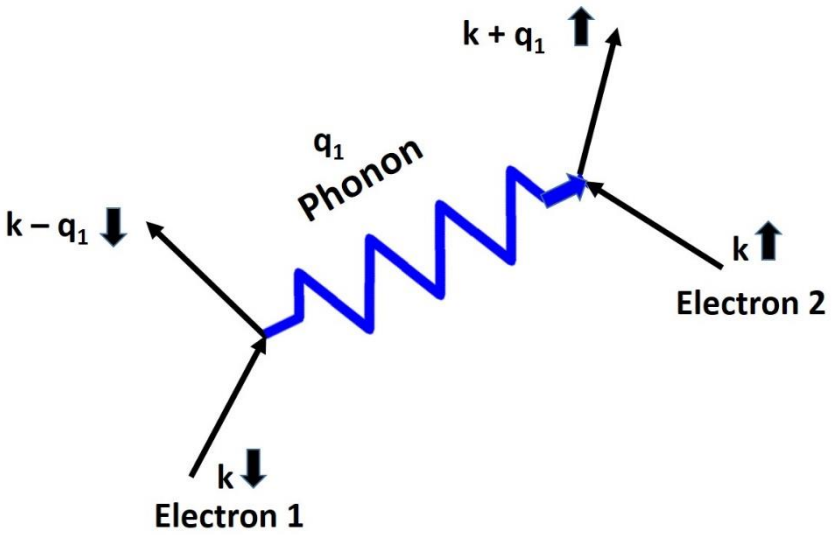

FIG. 1.3 Schematic diagram of a typical electron-phonon coupling for the case of phonon-mediated superconductivity. Here, electron 1 collides with the lattice creating a phonon with a wave vector q_1 and gets scattered with a wave vector $k-q_1$. Electron 2 absorbs the phonon and scatters with wave vector $k+q_1$. The wave vectors k and q_1 are vector quantities.

Based on the time-dependent perturbation theory (here the phonon is treated as a dynamic quantity and oscillating at a frequency ω_L), the phonon self-energy with wave vector q and frequency ω_L is given by [37-39],

$$\sum(q_L, \omega_L + i\delta) = \frac{2}{N_k} \sum_{k,i_1,i_2} \frac{\left|g^L_{ki_1,(k+q_1)i_2}\right|^2 (f_{ki_1} - f_{(k+q_1)i_2})}{E_{k_{i_1}} - E_{(k+q_1)_{i_2}} - (\hbar\omega_L + i\delta)} \qquad (1.22)$$

where, the numerical factor 2 represents the spin degeneracy, k is the Bloch wave vector of a specific electronic state, N_k is the number of k vectors; i_1, i_2 indicate the band indices and f_{ki_1} and $f_{(k+q_1)i_2}$ are the Fermi-Dirac distribution functions.

$g^{L}_{ki_1,(k+q_1)i_2}$ gives the matrix element of the electron-phonon coupling between the energy states $E_{k_{i_1}}$ and $E_{(k+q_1)_{i_2}}$ associated with wave functions $\Psi_{k_{i_1}}$ and $\Psi_{(k+q_1)_{i_2}}$ respectively.

For a perfect crystal which is having strong electron-phonon interaction, the EPC term mainly contributes to the linewidth of the phonon mode. The EPC contribution to the linewidth of a phonon mode is given by the Fermi golden rule [40,38],

$$\Gamma_L = \frac{4\pi}{N_k} \sum_{k,\, i_1, i_2} \left| g^{L}_{ki_1,\,(k+q_1)i_2} \right|^2 \left(f_{ki_1} - f_{(k+q_1)i_2} \right) * \delta\left(E_{k_{i_1}} - E_{(k+q_1)_{i_2}} + \hbar\omega_L \right) \quad (1.23)$$

where δ is the Dirac delta function. The Eq. 1.22 and Eq. 1.23 clearly illustrate us that the EPC term $g^{L}_{ki_1,(k+q_1)i_2}$ plays an essential role in determining the phonon frequency and linewidth.

Generally, the linewidth of the Raman peak is contributed by anharmonicity and EPC. Therefore, $\Gamma = \Gamma^{\text{anharmonic}} + \Gamma^{\text{EPC}}$. Here $\Gamma^{\text{anharmonic}}$ is determined by the phonon-phonon interactions (higher order terms in the interatomic potential) and is inherent. For the case of higher electronic carrier systems (e.g. metal) the Γ^{EPC} term dominates. The electron states contributing to EPC should follow the energy and momentum conservation laws. Mostly, EPC is contributed by electrons in the vicinity of the Fermi levels [40]. In the case of an insulator $\Gamma^{\text{EPC}} \sim 0$. For instance, in $HgBa_2Ca_3Cu_4O_{10+\delta}$, the softening of A_{1g} mode at 240 cm^{-1} below the superconducting transition temperature (T_c = 123 K) was observed and accompanied by a linewidth broadening within a rather narrow temperature interval [41]. These are the effects of phonon renormalization effects due to EPC. The broadening of Raman G band in graphite, graphene and G$^-$ peak in the single wall carbon nanotubes are due to the existence of strong EPC [40,42]. In fact, in InTe compound, two distinct pressure regions of the anharmonic and EPC domination are identified and will be discussed in Chapter 5.

1.6 X-ray Diffraction (XRD)

XRD is a powerful non-destructive analytical technique widely used in the structural identification and characterization of crystalline solids. X-rays are the part of an EM spectrum having the wavelength from 0.01 to 100 nm corresponding to energies in the range 100 eV to 100 keV. This X-rays wavelength is comparable to the unit-cell dimensions (interatomic spacing) of crystals and therefore it diffracts well. This technique is based on detecting the scattered intensity of an X-ray beam hitting the sample as a function of diffraction angle, and wavelength (or energy). The XRD pattern of a specific material is its fingerprint for a particular phase (structure). Hence, from both the angles and relative intensity of a diffraction pattern, we can generate a three-dimensional picture of the density of electrons within the crystal structure.

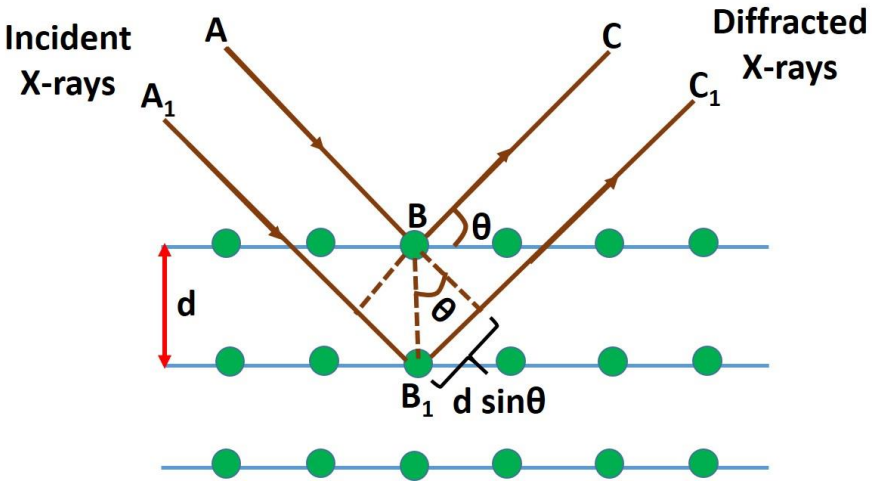

FIG. 1.4 Schematic diagram for the Bragg's law of diffraction. The path length difference between the two X-rays (i.e., ABC and $A_1B_1C_1$) is $2d\sin\theta$. In the case of constructive interference, this path difference is equal to an integral multiple of the wavelength of the radiation ($n\lambda$).

The basic principle behind XRD is the Bragg's Law of diffraction, and the schematic representation of the Bragg law is shown in Fig. 1.4. When X-rays are incident on the crystal, reflected X-rays are produced (or elastically scattered) by the atomic electrons at certain angles. For the waves (reflected X rays) to interfere constructively, the difference in their travel path must be equal to integral multiples of

the wavelength. Bragg established a general relationships between the Bragg angle, wavelength, and interplanar spacing, is known as Bragg's Law (given below) [43]:

$$2d\sin\theta = n\lambda \quad (1.24)$$

where, n is the order (n=1, 2, 3…), λ is the wavelength of the incident X-rays, d is the interplanar spacing of the crystal, and θ is the angle of incidence (Bragg angle). From the Eq. 1.24, it is well known that XRD can be measured using two different methods, 1. Angle-dispersive (varying the angle θ and keeping λ as constant) and 2. Wavelength dispersive (varying the wavelength λ and keeping angle θ as constant). It is noteworthy that the diffraction angle (2θ) is the angle between the incident primary beam and the diffracted beam. The maxima of the scattered intensity at particular $2\theta_{hkl}$ corresponds to a particular lattice spacing d_{hkl}. All possible diffraction directions of the lattice should be attained due to the random orientation of the powdered material by scanning the sample through a range of 2θ angles. In the case of polycrystalline samples (ideal), the individual microcrystalline grains are contributing equally with all possible orientations, and therefore X-ray is scattered symmetrically around the primary beam into discrete diffraction cones.

When a hydrostatic pressure is applied to a crystals, the volume of the unit cell decreases according to thermodynamics. From the XRD measurements under pressure, we can get the volume of a unit cell and thereby the equation of state (P vs. V) can be analyzed. In high pressure studies, EOS is extremely useful for the identification of structural phase transitions. In the next section, we will briefly discuss the important equation of states related to high-pressure crystallography.

1.6.1 Equation of state (EOS)

An EOS is a thermodynamic equation relating the pressure (P), temperature (T), volume (V), *etc*. It is helpful in characterizing the state of matter under a given set of physical conditions and generally applicable to gases, fluid mixtures, and solids. In thermodynamics, one of the simplest EOS is the ideal gas law, $PV = nRT$, where R is the gas constant (R = 8.31451 J K^{-1} mol^{-1}) and n is the number of moles. This EOS works well for gases at low pressures and moderate temperatures.

In contrast to the gaseous state, EOS takes a more complex form in solids due to the existence of various kinds of bonding and interaction potentials between the atoms. Many equations have been proposed for solids [44,45], and we will discuss below the most commonly used EOS in high pressure physics. All EOS are mathematically developed from a number of assumptions. There is no perfect thermodynamic basis for identifying the correct form of the EOS for solids. Therefore, the validity of EOS (as well as its assumption) can only be tested in terms of its ability to reproduce the experimental data. In this thesis, we have used Murnaghan EOS and Birch-Murnaghan EOS, and therefore we briefly present the details of these EOS as below.

(a) Murnaghan EOS

The bulk modulus (B) (or incompressibility) of the solid can be deduced from the Hooke's law which is given below;

$$B = -V\left(\frac{\partial P}{\partial V}\right) \tag{1.25}$$

where $\partial P/\partial V$ represents the partial derivative of pressure with respect to volume. Generally, the bulk modulus is the measure of the ability of a material to withstand volume changes when subjected to uniform compression.

Eq. 1.25 is the simplest isothermal EOS for a solid and is valid only for pressure ranges P < B and for a constant B. However, in reality, when a solid is compressed, it becomes more difficult to compress further which is mainly due to inter-atomic repulsions. Therefore, the larger compressions need a new expression for which the bulk modulus B linearly increases with pressure.

$$B = B_0 + B_0' P \tag{1.26}$$

Here, B_0 is the bulk modulus at ambient pressure and $B_0' = \left(\frac{\partial B}{\partial P}\right)_{P=0}$ is the first order pressure derivative of B. Murnaghan gave this assumption and it holds good for many materials in the pressure range $0 < P < B/2$ [44]. The integration of Eq. 1.26 leads to Murnaghan EOS [45,46].

$$P(V) = \frac{B_0}{B_0'} \left[\left(\frac{V}{V_0} \right)^{-B_0'} - 1 \right] \quad (1.27)$$

Murnaghan EOS empirically works well for the ambient pressure bulk modulus B_0 up to about 10% compression through P-V relations.

(b) Birch-Murnaghan EOS (BM EOS)

BM EOS is one of the finite strain based approaches. This EOS is derived, based on the assumption that Helmholtz free energy (strain energy) of a solid undergoing compression can be expressed as a Taylor series of the Eulerian finite strain, f_1 [47,45].

$$f_1 = \frac{1}{2} \left[\left(\frac{V}{V_0} \right)^{-\frac{2}{3}} - 1 \right] \quad (1.28)$$

From the standard derivation, third order BM EOS is given by,

$$P(V) = \frac{3B_0}{2} \left[\left(\frac{V_0}{V} \right)^{\frac{7}{3}} - \left(\frac{V_0}{V} \right)^{\frac{5}{3}} \right] \left\{ 1 + \frac{3}{4} (B_0' - 4) \left[\left(\frac{V_0}{V} \right)^{\frac{2}{3}} - 1 \right] \right\} \quad (1.29)$$

here, V_0 is the volume at ambient pressure, V is the deformed volume, B_0 is the bulk modulus, and B_0' is the derivative of the bulk modulus with respect to pressure. This isothermal EOS is widely used in high pressure science and work well for fairly high pressure regions. From the knowledge of the coefficients from the EOS and V_0, we can calculate (predict) the density, volume and bulk modulus of the system for any pressure.

1.7 Phase transitions

In condensed matter, the phase is a homogenous quantity of matter with a characteristic chemical composition and atomic arrangement. For the given chemical composition, a solid system can exist in many different crystallographic arrangements (or phases). Based on the thermodynamic parameters (pressure, temperature, *etc.*) and alloy composition, different phases attain an equilibrium state (stable). Also, if we tune these parameters (driving forces), a phase transformation (transitions) occurs from one

stable phase to another. For a given set of thermodynamic variables, minimization of the overall Gibbs free energy (G= H-TS) is the basic principle of phase transitions. Here H is the enthalpy, S is the entropy and T is the temperature. The studies of phase stability and phase transitions are very important and have significance in technological applications. As it is relevant to the present thesis, types of phase transitions such as structural and isostructural electronic transitions will be discussed in the following sections.

1.7.1 Structural phase transitions

The transformation of one crystal structure (symmetry) to another structure is called a structural phase transition in solids. During the structural phase transitions, the electronic or spin configuration also changes. Hence, structural phase transitions are accompanied by changes in physical properties such as thermal, electrical, magnetic, ferroelectric, *etc*. Austrian and Dutch theoretical physicist Paul Ehrenfest classified the phase transitions into two orders (or types) based on the behavior of the Gibbs free energy as a function of other thermodynamic variables [48]. In the first order phase transition, the change in the Gibbs free energy is zero ($\Delta G = 0$), but the first derivative of Gibbs free energy is discontinuous $\left[\Delta\left(\frac{\partial G}{\partial X}\right)_{X=T,P} \neq 0\right]$. The first derivatives of Gibbs free energy are given below as,

$$\left(\frac{\partial \mathrm{G}}{\partial \mathrm{P}}\right) = \mathrm{V} \tag{1.30}$$

$$\left(\frac{\partial \mathrm{G}}{\partial \mathrm{T}}\right) = -\mathrm{S} \tag{1.31}$$

For second order phase transitions, the first derivative of Gibbs free energy is continuous whereas the second derivative of Gibbs free energy is discontinuous $\left[\Delta\left(\frac{\partial^2 G}{\partial X^2}\right)_{X=T,P} \neq 0\right]$. The second derivative of Gibbs free energy is given below as,

$$\left(\frac{\partial^2 \mathrm{G}}{\partial P^2}\right)_T = -\frac{1}{V}\left(\frac{\partial \mathrm{V}}{\partial \mathrm{P}}\right)_T = \beta \tag{1.32}$$

$$\left(\frac{\partial^2 \mathrm{G}}{\partial T^2}\right)_P = -\,\mathrm{T}\left(\frac{\partial \mathrm{S}}{\partial \mathrm{T}}\right)_P = -\,C_P \tag{1.33}$$

$$\left(\frac{\partial^2 \mathrm{G}}{\partial \mathrm{P}\,\partial \mathrm{T}}\right) = \frac{1}{V}\left(\frac{\partial \mathrm{V}}{\partial \mathrm{T}}\right)_P = \alpha \tag{1.34}$$

where β is the compressibility, C_P is the heat capacity, and α is the thermal expansivity. The second order transitions are also called as 'gradual, smeared or diffuse' transitions.

In 1951, Buerger classified the structural phase transitions into two types based on the mechanistic approach [49]. They are 1) displacive and 2) reconstructive transformations. The cooperative and homogenous movement of a large number of neighboring atoms, leads to a change in the crystal structure which are called displacive transformations (or diffusionless transformations). In this process, the movements (i.e., changes in bond length, bond angle, *etc*) are lesser than the interatomic distance. Typical examples are the Martensitic transformation in steel and shape memory alloys. Reconstructive transformations occur through the breaking and formation of bonds in a structure. During this kind of phase transitions, atoms move from parent to product phase by diffusional jumps and usually involve large atomic displacements (10-20 % of distortion in the lattice). The phase transition of graphite to diamond under high temperature and high pressure conditions is a typical example of reconstructive transitions. Generally, the volume change of 1 to 5% leads to a significant overlap of orbitals between the atoms in a material, which show drastic changes in the electronic, and magnetic properties and structural phase transitions. But, superhard materials may be an exception for this expected behavior. Typical examples for the pressure induced phase transitions are given below. The III-VI semiconducting compounds such as TlSe show a reversible first-order phase transition from TlSe I (tetragonal) to TlSe II (CsCl cubic) at 21 GPa [50]. Tetradymite semiconducting family compounds such as Bi_2Se_3, Bi_2Te_3, and Sb_2Te_3 undergo a pressure-induced first-order structural phase transitions from rhombohedral (SG: $R\bar{3}m$) to monoclinic (SG: $C2/m$) phase at a pressure above 7 GPa [32]. We have explored the pressure induced first-order phase transitions in InTe, $AgBiSe_2$, $TlBiS_2$, and $TiTe_2$ which will be discussed in the following chapters.

1.7.2 Isostructural phase transitions

A phase transition in which no change occurs in the symmetry of the crystalline lattice is referred to as an isostructural phase transitions. Most of such transitions are driven by the behavior of electrons in the solid and are accomplished with or without volume collapse. For example, cubic perovskite $PbCrO_3$ evidences an isostructural phase transition at ~ 1.6 GPa with a ~ 9.8 % volume collapse [51]. Similarly, pressure induced superconductivity has been observed in Bi_2Te_3 with T_c of ~3 K between 3 to 6 GPa, and its ambient structure (SG: $R\bar{3}m$) is stable up to 7 GPa [52]. Further, an orthorhombic perovskite $RFeO_3$ (R= Pr, Eu, Lu) shows a reversible first-order isostructural phase transition around 50 GPa with the volume decrease of about 5% [53]. It is primarily driven by the transition from high spin to low spin state of Fe^{3+}. In this thesis, we are mainly concerned with the pressure induced semiconductor to metal transitions, electronic topological transitions, and topological quantum phase transitions. So, here, we briefly discuss such types of isostructural electronic transitions.

1.7.2.1 Semiconductor to metal transition

According to band theory of solids, materials can be majorly classified into three electronic states (1) insulators, (2) semiconductors, and (3) conductors. In case of an insulator, the valence band and conduction bands are separated by a large band gap, whereas semiconductors have a small band gap between the valence and conduction bands. Metals show an overlapping of the valence and conduction bands.

As the pressure alters the band gap, it may change the electronic states of matter. A variety of semiconductor to metal conversion mechanisms has been observed under application of pressure. For example, transition metal dichalcogenides MoS_2 is a semiconductor (bandgap ~ 1.2 eV) at ambient conditions. But, it undergoes a pressure induced metallization at ~ 19 GPa and is mainly caused by the structural distortion via the layer sliding from $2H_c$–MoS_2 to the $2H_a$–MoS_2 [54]. Further, $MoSe_2$ shows pressure induced metallization above 27 GPa without any structural transition [55]. Though MoS_2 and $MoSe_2$ show highly similar chemical and structural environments (SG: $P6_3/mmc$), $2H_c$–$2H_a$ sliding is not observed in $MoSe_2$. This is because the 4p orbitals of Se^{2-} are more delocalized than 3p orbitals of S^{2-} and hence strong interlayer interactions

are established which prevent the sliding process [55]. The semiconductor to metal transition is observed at ~5 GPa in InTe due to the changes in oxidation state from In^{1+} and In^{3+} to In^{2+} via the first order structural phase transition from tetragonal to cubic phase [56]. However, our recent first principle calculations reveal that metallization occurs in the tetragonal phase (at ~ 3.6 GPa) itself without a change in the oxidation state. Therefore, it is also possible to get the semiconductor to metal transition by only increasing the density of states without changing the crystal structure and oxidation state. This kind of semiconductor to metal transition has been observed in InTe and $AgBiSe_2$ compounds, which will be explained in Chapters 5 and 6. Further, it is not necessary that the semiconducting system should show a metallic state under pressure. This is because the increase or decrease in band gap is mainly determined by the bonding or antibonding orbitals under pressure. So naturally, the situation in which there is an increase in band gap will not lead to the metallization. Hence, it is important to note that a semiconductor to metal conversion under pressure is not a common process and it is material specific.

1.7.2.2 Electronic topological transition (ETT)

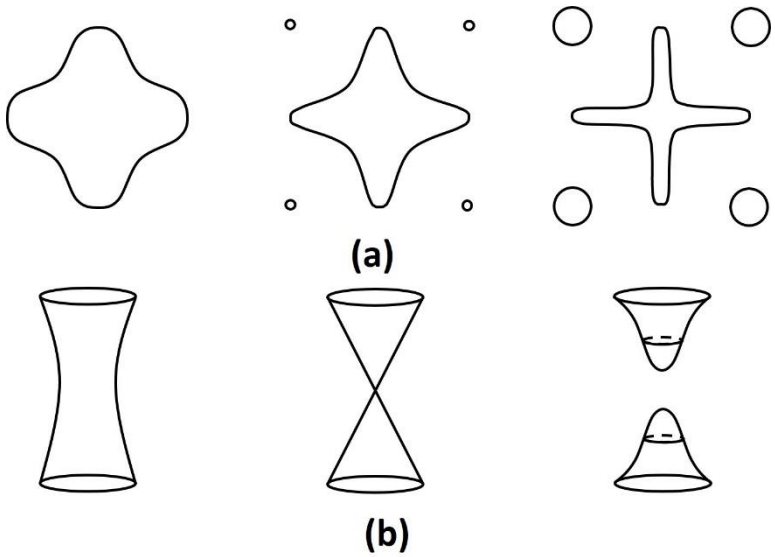

FIG. 1.5 Schematic diagram of the typical ETT. (a) The appearance of new voids and (b) Fermi surface neck disruption. (The schematic is adopted from Ref. [58])

ETT is mainly caused by the drastic changes in the topology of electronic Fermi surface [57,58]. It is also called Lifshitz transition [57]. Thermodynamically, ETT is a second order isostructural transition without volume collapse and with no change in its

Wyckoff positions. The application of hydrostatic pressure varies the unit cell volume and consequently electron density of states, Fermi surfaces size and its shape. The external perturbations like pressure, chemical doping, temperature, *etc*., in metals or degenerate semiconductors, may lead to the crossing of van Hove singularity (band extremum in the density of states) through the Fermi level and strong redistribution of electrons occurs near the Fermi surface [58]. Hence, Fermi surface can undergo different types of topological transition (changes) like appearance and disappearance of voids, formation and disruption of a neck, depending on the type of critical point passing through the Fermi surface [58]. The schematic representation of the appearance of voids and disruption of Fermi surface neck are shown in Fig. 1.5 [58]. Due to ETT, electrons near the Fermi surface show some peculiar kinetic and thermodynamic characteristics [59]. Since transport properties strongly depend on the density of states near Fermi level; it can show significant changes during ETT. Recently, it was experimentally shown that the tetradymite semiconducting compounds A_2B_3 (A= Bi, Sb, and B = Se, Te, S) exhibit pressure induced ETT around 3–5 GPa [32,60]. The transverse-optical (E_{2g}) phonon mode of Zn metal shows the occurrence of an ETT at ~10 GPa through electron-phonon coupling anomalies via changes in Raman linewidth [61]. In this thesis, ETT has been explored through phonon and transport anomalies in $AgBiSe_2$ and Sb_2S_3 compounds which will be discussed in Chapters 6 and 7.

1.7.2.3 Topological quantum phase transition (TQPT)

TQPT is an iso-structural second order transition which arises as a consequence of non-adiabatic band inversion occurring at the time reversal invariant momenta points (TRIM) with a parity change (odd/even). In this process, topological invariant quantity Z_2 changes from $Z_2 = 0$ (conventional insulator) to $Z_2 = 1$ (topological insulator) [63-65]. Mathematically, Z_2 is calculated as the product of the parities at the TRIM points of the Brillouin zone. Generally, four Z_2 topological invariants (υ_0; $\upsilon_1\upsilon_2\upsilon_3$) are used to classify the 3D topological insulator [63]. If the system has $\upsilon_0 = 1$, then it is called a strong topological insulator. When the system has $\upsilon_0 = 0$, then it will be further classified by the values of υ_1, υ_2, and υ_3. For instance, $\upsilon_0 = 0$ and υ_1, υ_2, $\upsilon_3 \neq 0$ represents a weak topological insulators and Z_2 (0;000) represents the normal insulator. The process of TQPT is represented in Fig. 1.6.

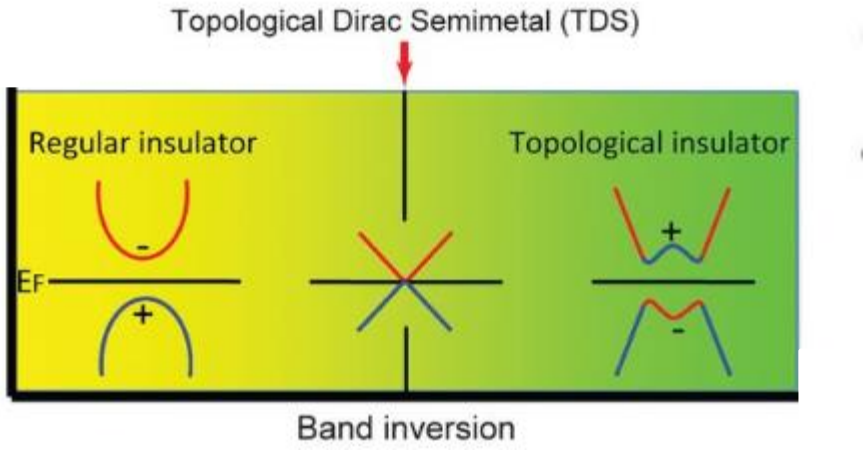

FIG. 1.6 Schematic of the TQPT process. Here, the + and – signs represent the even and odd parity of the bands at the TRIM point, respectively. The driving force for a TQPT process is the tuning (achieved either by chemical substitution or pressure) of the SOC strength. (The picture is adopted from Ref. [62]).

Generally, TQPT can be driven by spin orbit coupling (SOC) strength which can be tuned either by chemical substitution or strains. For instance, tuning of the strength of the SOC via chemical substitution in $TiBi(S_{1-x}Se_x)_2$,[66] and $Pb_{1-x}Sn_xSe$ systems[67] cause TQPT. The hydrostatic pressure (strain) induced TQPT has been experimentally observed in systems like BiTeI, Sb_2Se_3, and BiTeBr compounds [38,68,69]. The observation of TQPT is rare, and only a few materials show this property. In this thesis, TQPT has been explored in $TlBiS_2$ and 1T-$TiTe_2$ compounds at relatively low pressure regions which will be discussed in Chapters 3 and 4. Here we would like to emphasis that, even though TQPT and ETT are named as topological transitions, they are different phenomena and have no connection between them.

1.8 Probing the phase transitions

In this thesis, we have extensively used Raman scattering and synchrotron XRD measurements for probing the structural and isostructural electronic transitions. Raman scattering is a local, sensitive and an effective technique for detecting various types of phase transitions. Typical Raman spectra contain the information such as peak position 'ω' (frequency), full width at half maximum (Γ) and the intensity (A). The parameters ω, Γ and A are very sensitive to symmetry and environment of the system; hence any

changes under perturbation would immediately influence it. Particularly, Raman mode's frequency (ω) is the thermodynamic order parameter which is sensitive to the type of the structural phase transition (whether 1st or 2nd order) under perturbation. The appearance and disappearance of Raman active modes and changes in the slope of the frequencies $\left(\frac{d\omega}{dP}\right)$ indicate the type of phase transition. For instance, small changes in $\left(\frac{d\omega}{dP}\right)$ might be an indicator for the second order or weakly first order phase transitions. The sharp discontinuities in the frequency plot (P vs. ω) could be an indicator for the first order phase transition. Generally, Raman linewidth (Γ) contains information about the phonon-phonon anharmonic interactions, electron-phonon interactions, spin-phonon interactions, *etc.* (as discussed in the Section 1.5). However, a disordered and nanocrystalline phase shows a broader linewidth in Raman spectra. Also, Raman intensity (A) can be extensively used to identify the structural and electronic phase transitions. It is well known that XRD gives a detailed structural information. Here, the volume of the unit cell is the order parameter, which will be used to identify the types of phase transitions. For example, the sharp discontinuity and gradual small slope change in volume indicate the first and second order structural phase transitions respectively. In addition to this, lattice parameters (*a*, *b*, and *c*), axial ratio, bond angle, and bond length also signature the various phase transitions.

1.9 Scope of the thesis

Recently, there has been an increased research interest in the high pressure studies of strong SOC materials because they exhibit exotic features such as TQPT, ETT, semiconductor to metal transitions, structural phase transitions, and superconductivity. Among these, materials undergoing TQPT and topological insulators (TI) are strongly driven by SOC strength and have fascinated the high-pressure research for over a decade. TI is a new kind of electronic state of matter which has spin polarized conducting states at its surface and insulating states in its bulk. The existence of time reversal symmetry gives the protection to the topological surface states against non-magnetic impurities or defects [63]. TIs have potential applications in spintronics and quantum computation devices. Apart from these, TIs also offer a useful platform for realizing quantum particles like Majorana Fermions in a condensed matter system [63]. The theoretical prediction of TI made in HgTe/CdTe quantum wells

[two dimensional (2D)] [70] were subsequently observed experimentally [71]. Soon after this discovery, TI in 3D bulk materials (various strong SOC systems) have been theoretically predicted [72] and found using angle resolved photo emission spectroscopy (ARPES) at ambient conditions [73-75]. Interestingly, some narrow band gap materials (at ambient conditions) with strong SOC can be tuned to a TI by external strain (pressure) [64,68]. This process is known as TQPT (as discussed in Section 1.7.2.3). Even though strong SOC is the primary factor for the observation of TQPT, many of the existing strong SOC systems do not show TQPT either at ambient/high-pressure conditions. This suggests that TQPT is not a straightforward formalism and therefore more experimental work is necessary to get a better understanding.

Another important electronic transition, ETT is caused by changes in the topology of the Fermi surface (i.e., fermiology) which has been observed in strong SOC materials under hydrostatic compression. Apart from studies for fundamental science, ETT is one of the technologically important phenomena because of its ability to enhance the thermoelectric (TE) power [59,76,77]. Similarly, the pressure induced semiconductor to metal transition is another interesting phenomenon, which is caused by the charge density redistribution during overlapping of atomic orbitals. Hence, understanding as well as exploring the novel electronic transitions such as TQPT, ETT, and the semiconductor to metal transitions in a strong SOC system are rich in condensed matter physics and thus constitute the core of this thesis.

In this thesis, we have used high pressure Raman scattering and Synchrotron XRD to study five different strong SOC materials, namely, $TlBiS_2$, 1T-$TiTe_2$, InTe, $AgBiSe_2$, and Sb_2S_3. The strong motivation and background of all these materials are described in their respective chapters with appropriate reasoning. Now, here we briefly describe the important results of the studies on these materials.

1. $TlBiS_2$: Pressure induced topologically trivial and non-trivial quantum phase transitions are observed through phonon linewidth of A_{1g} and E_g mode in $TlBiS_2$. We also observed a first order pressure induced a structural phase transition at ~4 GPa in both Raman and synchrotron XRD measurements.
2. 1T-$TiTe_2$: We have explored the pressure induced topologically non-trivial and trivial quantum phase transitions, 2D to quasi 3D conversion and structural

phase transition from trigonal (SG: $P\bar{3}m1$) to monoclinic (SG: $C2/m$) phase in $TiTe_2$.

3. InTe: We have explored the pressure induced band inversion, semiconductor to metal transition and structural phase transition in InTe using Raman scattering measurements.
4. $AgBiSe_2$: Pressure induced a weakly first-order structural transition from trigonal to rhombohedral phase is observed in $AgBiSe_2$ at relatively lower pressure regions using Raman and synchrotron XRD measurements. Besides, pressure induced ETT and semiconductor to metal transition have been found in β-$AgBiSe_2$ (rhombohedral phase) at higher pressure regions.
5. Sb_2S_3: We have explored the pressure induced ETT in Sb_2S_3 compound using Raman scattering measurements.

1.10 Bibliography

1. M. J. Clerk, *A dynamical theory of the electromagnetic field*, Philosophical Transactions of the Royal Society of London **155**, 459 (1865).
2. J. Tyndall, Phil. Mag **37,** 384 (1869).
3. L. Rayleigh, Phil. Mag **41,** 447 (1871).
4. G. Mie, Ann. Phys., Lpz **330,** 377 (1908).
5. L. Brillouin, Ann. Phys. (Paris) **17,** 88 (1922).
6. A. Smekal, Die Naturwissenschaften **11,** 873 (1923).
7. C. V. Raman, Indian J. Phys. **2,** 387 (1928).
8. C. V. Raman and K. S. Krishnan, Nature **121,** 501 (1928).
9. C. V. Raman, Nature **121,** 619 (1928).
10. G. S. Landsberg and L. I. Mandelstam, Naturwiss **16,** 557 (1928).
11. W. L Bragg, Nature. **90**, 2250 (1912).
12. W. L Bragg, Proceedings of the Cambridge Philosophical Society **17**, 43 (1913).
13. M. Cardona, *Light scattering in solids I: Introductory concepts, Topics in Applied Physics,* Vol 8, Springer-Verlag Berlin Heidelberg New York (1982).
14. M. Cardona, and G. Guntherodt, *Light-Scattering in Solids II: Basic Concepts and Instrumentation, Topics in Applied Physics,* Vol 50, Springer-Verlag Berlin Heidelberg New York (1982).

15. R. Loudon, Adv. Phys. **50**, 813 (2001).
16. M. Balkanski, R. F. Wallis, and E. Haro, Phys. Rev. B **28**, 1928 (1983).
17. D. W. Feldman, J. Parker, W. J. Choyke, and L. Patrick, Phys. Rev. **170**, 698 (1968).
18. D. W. Feldman, J. H. Parker, W. J. Choyke, and L. Patrick, Phys. Rev.**173**, 787 (1968).
19. A. S. Barker, and R. Loudon, Rev. Mod. Phys. **44**, 18 (1972).
20. B. A. Weinstein, and R. Zallen, *Pressure-Raman effects in covalent and molecular solids*, Light Scattering in Solids IV, Topics in Applied Physics, Vol 54, Springer, Berlin, Heidelberg, p. 463 (1984).
21. R. P. Dias, and I. F. Silvera, Science **355**, 715 (2017).
22. A. Jayaraman, Rev. Mod. Phys. **55**(1), 65 (1983).
23. P. F. McMillan, Nat. Mater. **1**, 19 (2002).
24. Z. Hiroi, and M. Takano, Physica C **29**, 235 (1994).
25. D. Y. Kim, S. Stefanoski, O. O. Kurakevych, and T. A. Strobel, Nat. Mater. **14**, 169 (2015).
26. M. Somayazulu, M. Ahart, A. K. Mishra, Z. M. Geballe, M. Baldini, Y. Meng, V. Struzhkin, and R. J. Hemley arXiv:1808.07695 (2018).
27. L. Davison, and R. A. Graham, Phys. Rep. **55,** 255 (1979).
28. M. Blackman, Proc. Phys. Soc. B **70**, 827 (1957).
29. K. Wang, and R. R. Reeber, Appl. Phys. Lett. **76**, 2203 (2000).
30. A. Debernardi, C. Ulrich, M. Cardona, and K. Syassen, Phys. Status Solidi b **223,** 213 (2001).
31. C. Ulrich, A. Debernardi, E. Anastassakis, K. Syassen, and M. Cardona, Phys. Status Solidi B **211**, 293 (1999).
32. F. J. Manjon, R. Vilaplana, O. Gomis, E. P. Gonzalez, D. S. Perez, V. M. Borras, A. Segura, J. Gonzalez, P. R. Hernandez, A. Munoz, C. Drasar, V. Kucek, and V. M. Sanjose, Phys. Status Solidi B **250**, 669 (2013).
33. G. Lucazeau, J. Raman Spectrosc. **34**, 478 (2003).
34. D. Olego, and M. Cardona, Phys. Rev. B **25**, 1151 (1982).
35. R. A. Cowley, J. Physique **26**, 659 (1965).
36. J. Bardeen, Science **181,** 1209 (1973).
37. M. Lazzeri, and F. Mauri, Phys. Rev. Lett. **97**, 266407 (2006).

38. A. Bera, K. Pal, D. V. S. Muthu, S. Sen, P. Guptasarma, U. V. Waghmare, and A. K. Sood, Phys. Rev. Lett. **110**, 107401 (2013).
39. S. Pisana, M. Lazzeri, C. Casiraghi, K. S. Novoselov, A. K. Geim, A. C. Ferrari, and F. Mauri, Nat. Mater. **6**, 198 (2007).
40. M. Lazzeri, S. Piscanec, F. Mauri, A. C. Ferrari, and J. Robertson, Phys. Rev. B **73**, 155426 (2006).
41. V. G. Hadjiev, X. Zhou, T. Strohm, M. Cardona, Q. M. Lin, and C. W. Chu, Phys. Rev. B **58**, 1043 (1998).
42. S. Piscanec, M. Lazzeri, J. Robertson, A. C. Ferrari, and F. Mauri, Phys. Rev. B **75**, 035427 (2007).
43. B. D. Cullity, *Elements of X-ray Diffraction*, second edition, Addison-Wesley Publishing Company Inc, Reading, Massachusetts, (1978).
44. O. L. Anderson, *Equations of state of solids for geophysics and ceramic science*, Oxford University Press, Oxford, UK (1995).
45. R. J. Angel, *Equations of State*, Reviews in Mineralogy and Geochemistry, volume 41 (1), p. 35, (2000).
46. F. D. Murnaghan, Natl. Acad. Sci. USA, **30**, 244 (1944).
47. F. Birch, Phys. Rev. **71**, 809 (1947).
48. G. Jaeger, *The Ehrenfest Classification of Phase Transitions: Introduction and Evolution*, Archive for History of Exact Sciences **53** (1), 51 (1998).
49. M.J. Buerger, *Phase Transformations in Solids*, John Wiley, 1951.
50. G. B. Demishev, S. S. Kabalkina, and T. N. Kolobyanina, Phys. Status solidi a **108,** 89 (1988).
51. W. Xiao, D. Tan, X. Xiong, J. Liu, and J. Xu, Proc. Natl. Acad. Sci. USA **107**, 14026 (2010).
52. J. L. Zhang, S. J. Zhang, H. M. Weng, W. Zhang,L. X. Yang, Q. Q. Liu, S. M. Feng, Wang, R. C.Yu, and L. Z. Cao, Proc. Natl Asso. Soc. **108,** 24 (2011).
53. G. K. Rozenberg, M. P. Pasternak, W. M. Xu, L. S. Dubrovinsky, S. Carlson, and R. D. Taylor, Europhys. Lett. **71**, 228 (2005).
54. A. P. Nayak, S. Bhattacharyya, J. Zhu, J. Liu, X. Wu, T. Pandey, C. Jin, A. K. Singh, D. Akinwande, and J.F. Lin, Nat. Commun. **5**, 3731 (2014).

55. Z. Zhao, H. Zhang, H. Yuan, S. Wang, Y. Lin, Q. Zeng, G. Xu, Z. Liu, G. K. Solanki, K. D. Patel, Y. Cui, H. Y. Hwang, and W. L. Mao, Nat. Commun. **6**, 7312 (2015).
56. S. Pal, D. N. Bose, S. Asokan, and E. S. R. Gopal, Solid State Commun. **180**, 753 (1991).
57. M. Lifshitz, Sov. Phys. JETP **11**, 1130 (1960).
58. Y. M. Blanter, M. I. Kaganov, A. V. Pantsulaya, and A. A. Varlamov, Phys. Rep. **245**, 159 (1994).
59. D. A. Polvani, J. F. Meng, N. V. Chandra Shekar, J. Sharp, and J. V. Badding, Chem. Mater. **13**, 2068 (2001).
60. R. Vilaplana, D. Santamaría-Pérez, O. Gomis, F. J. Manjón, J. González, A. Segura, A. Muñoz, P. Rodríguez-Hernández, E. Pérez-González, V. Marín-Borrás, V. Muñoz- Sanjose, C. Drasar, and V. Kucek, Phys. Rev. B **84**, 184110 (2011).
61. H. Olijnyk, A. P. Jephcoat, D. L. Novikov, and N. E. Christensen, Phys. Rev. B **62**, 5508 (2000).
62. Z. K. Liu, B. Zhou, Y. Zhang, Z. J. Wang, H. Weng, D. Prabhakaran, S.K. Mo, Z. X. Shen, Z. Fang, X. Dai, Z. Hussain, and Y. L. Chen, Science **343**, 864 (2014).
63. M. Z. Hasan and C. L. Kane, Rev. Mod. Phys. **82**, 3045 (2010).
64. M. S. Bahramy, B. J. Yang, R. Arita, and N. Nagaosa, Nat. Commun. **3**, 679 (2012).
65. W. Li, X. Y. Wei, J. X. Zhu, C. S. Ting, and Y. Chen, Phys. Rev. B **89**, 035101 (2014).
66. T. Sato, K. Segawa, K. Kosaka, S. Souma, K. Nakayama, K. Eto, T. Minami, Y. Ando, and T. Takahashi, Nat. Phys. **7**, 840 (2011).
67. P. Dziawa, B. J. Kowalski, K. Dybko, R. Buczko, A. Szczerbakow, M. Szot, E. Łusakowska, T. Balasubramanian, B. M. Wojek, M. H. Berntsen, O. Tjernberg, and T. Story, Nat. Mater. **11**, 1023 (2012).
68. X. Xi, C. Ma, Z. Liu, Z. Chen, W. Ku, H. Berger, C. Martin, D. B. Tanner, and G. L. Carr, Phys. Rev. Lett. **111**, 155701 (2013).
69. A. Ohmura, Y. Higuchi, T. Ochiai, M. Kanou, F. Ishikawa, S. Nakano, A. Nakayama, Y. Yamada, and T. Sasagawa, Phys. Rev. B **95**, 125203 (2017).

70. B. A. Bernevig, T. L. Hughes, and S.C. Zhang, Science **314** (5806), 1757 (2006).
71. M. König, S. Wiedmann, C. Brüne, A. Roth, H. Buhmann, L. W. Molenkamp, X.L. Qi, and S.C. Zhang, Science **318**, 766 (2007).
72. H. Zhang, C.X. Liu, X.L. Qi, X. Dai, Z. Fang, and S.C. Zhang, Nat. Phy. **5**, 438 (2009).
73. Y. Xia, D. Qian, D. Hsieh, L. Wray, A. Pal, H. Lin, A. Bansil, D. Grauer, Y. S. Hor, R. J. Cava, and M. Z. Hasan, Nat. Phys. **5**, 398 (2009).
74. Y. L. Chen, J. G. Analytis, J. H. Chu, Z. K. Liu, S. K. Mo, X. L. Qi, H. J. Zhang, D. H. Lu, X. Dai, Z. Fang, S. C. Zhang, I. R. Fisher, Z. Hussain, and Z. X. Shen, Science **325**, 178 (2009).
75. D. Hsieh, Y. Xia, D. Qian, L. Wray, F. Meier, J. H. Dil, J. Osterwalder, L. Patthey, A. V. Fedorov, H. Lin, A. Bansil, D. Grauer, Y. S. Hor, R. J. Cava, and M. Z. Hasan, Phys. Rev. Lett. **103**, 146401 (2009).
76. N. V. Chandra Shekar, D. A. Polvani, J. F. Meng, and J. V. Badding, Phys.B **358**, 14 (2005).
77. S. V. Ovsyannikov, V.V. Shchennikov, G.V. Vorontsov, A.Y. Manakov, A.Y. Likhacheva, and V. A. Kulbachinskii, J. Appl. Phys. **104**, 053713 (2008).

Chapter 2

Experimental techniques

This chapter provides a brief overview of the various experimental techniques used in present thesis.

2.1 Raman spectrometer

Raman scattering is a weak process (only one photon is getting Raman scattered for every 10^7 incident photons) [1]. To get a good quality Raman spectrum (necessary for detailed analysis) from this weak process, one needs to use high throughput and high signal to noise ratio spectrometer. In recent times, with the technical development in optical components (laser source, monochromator, *etc*.) and electronic components (CCD detector), commercial spectrometers provide the high-quality Raman spectrum. However, commercial modern Raman instruments are expensive and do not have the flexibility in modification required for different kind of experiments. To overcome such difficulties, we have fabricated a home-built Raman spectrometer [2,3] in our laboratory, and used for various experiments. Particularly, in this thesis, we have used this custom-built Raman spectrometer, for studying the high-pressure Raman scattering measurements on $AgBiSe_2$, InTe, and Sb_2S_3 compounds. Similarly, the commercial Raman spectrometer such as WiTec (UHTS600) and LabRAM HR Evolutions are utilized for studying the high-pressure Raman on 1T-$TiTe_2$ and $TlBiS_2$ compounds respectively. Though the designs are different, the working principle remains the same for our custom-built and commercial spectrometers. So, in the next section, we would like to discuss the design, principles, and performance of the custom-built Raman spectrometer. The details of the commercial spectrometer are found elsewhere [4,5].

2.1.1 Design and performance of the custom-built Raman spectrometer

Figure 2.1 shows the schematic of the custom-built micro-Raman spectrometer [2]. The setup consists of the linearly polarized 532 nm line from a solid state, diode pumped, frequency doubled Nd-YAG (Neodymium-doped Yttrium Aluminum Garnet) continuous wave laser (model GDLM-5015 L, Photop Suwtech Inc., China) as the excitation source. The total output power of this laser is ~ 18 mW. In our setup, the collection optics of the Raman microscope consist of the double port (Y-IDP), modular focusing unit (LV-IM), universal epi-illuminator (LV-U EPI 2), sextuple nosepiece (C-N), eyepiece lens (CFI 10x) and a trinocular tube (Y-TF2) all from NIKON, Japan. Using the L-shaped metal holder (home-built), the complete Raman microscope is mounted to the optical table as shown in Fig. 2.2.

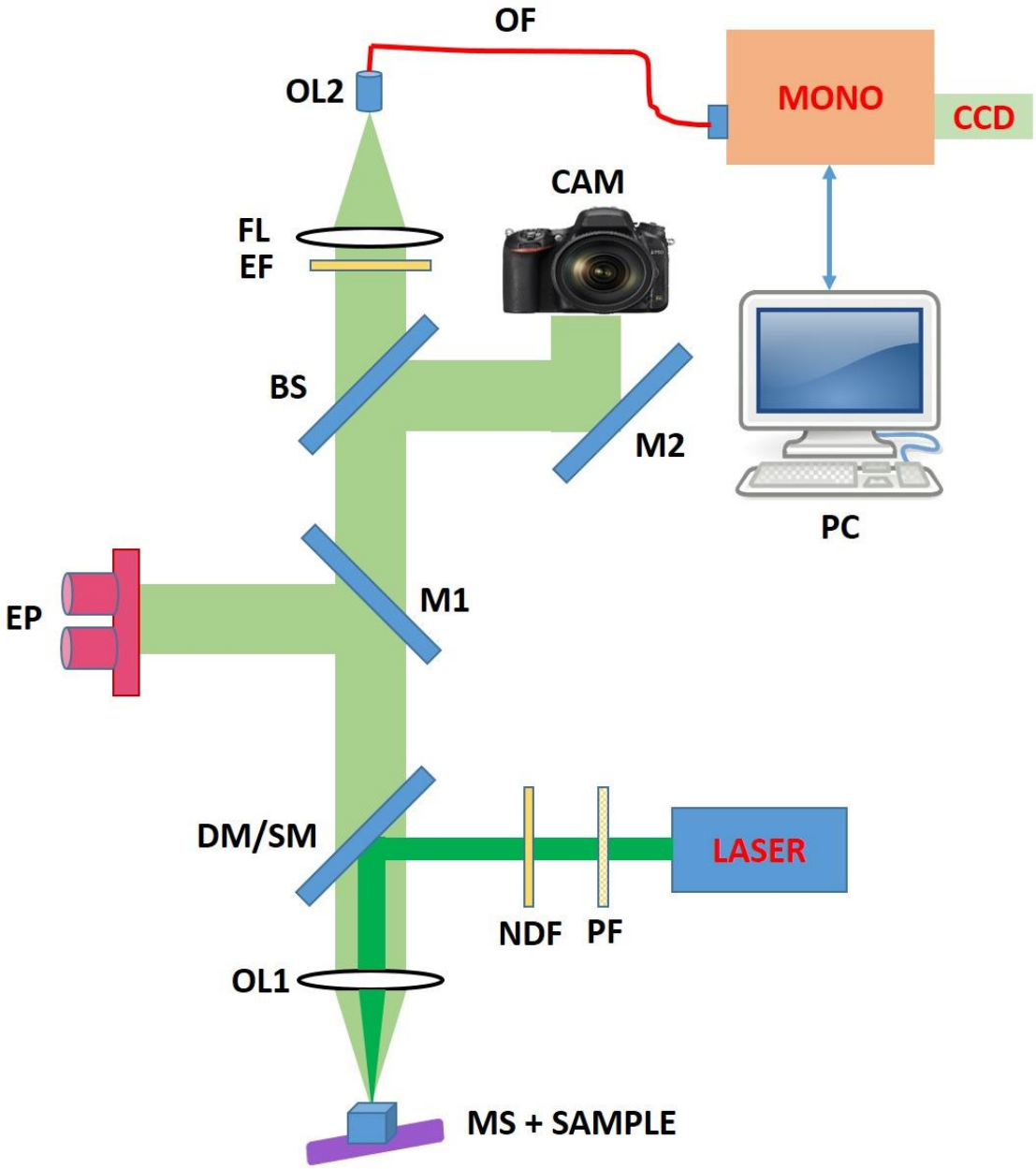

FIG. 2.1. Schematic of the custom -built micro-Raman spectrometer: PF – Plasma filter, NDF - Neutral density filter, DM – Dichroic mirror, SM- special mirror, OL1 and OL2- Objective lenses, MS- Micrometer stage, M1– Movable mirror, M2 – Mirror, EP – Eyepiece, BS – Movable beam splitter, CAM – Camera, FL- Focusing lens, EF- Edge filter, MONO – Monochromator, OF- Optical fiber, CCD – Charge-coupled device, PC – personal computer.

Initially, the monochromatic laser beam (532 nm) passes through the plasma filter (PF) (LL01-633-12.5, Semrock) followed by neutral density filters (NDF). The PF

removes the plasma lines generated in a laser, and NDF reduces the power of the incident beam to desired levels. Generally, a high-power density can damage the samples and hence we need to allow appropriate laser power onto the sample, with the help of NDF. We have variable NDFs such as 10%, 20%, 50%, and 75% transmission of incident light intensity. Further, all these filters can be moved manually in and out of the beam path depending on the desired intensity. Generally, for a normal sample, Raman can be done with only a few mW or sometimes less than one mW power. In this thesis, we have studied chalcogenide samples, and all of them undergo lased induced damage even for a few mW of power. After passing through the NDF, the laser light is incident on a special mirror (SM)/ dichroic mirror (DM) placed at 45° to the path of the light inside the epi-fluorescent microscope. One of the slots in this microscope has a holder for DM or SM. The SM was designed by us and fabricated by Acexon technologies, Singapore. The SM contains the Ag coating of 2-3 mm diameter at the center of a 25.2 x 35.6 (± 0.2) mm fused silica substrate of 1.1 mm thickness. This Ag coating was exclusively used to reflect the laser light. After getting reflected from SM, the beam is directed onto the sample through an infinity corrected microscope objective lens (OL1). The typical OL (NIKON company) used for all the high-pressure experiments was an infinity corrected 20X magnification objective with a numerical aperture (NA) and a long working distance (WD) of 0.33 and 24 mm, respectively. However, the revolving sextuple nosepiece can potentially host the six OLs using six different slots. One can choose the appropriate OL depending on their experimental requirements (working distance, depth of focus, scattering efficiency, *etc*.).

By bringing the movable mirror M1 into the light path, we can view the sample and focus the laser spot with the help of an eyepiece. Also, a camera (CAM) is used for capturing the optical pictures by engaging the movable beam splitter (BS). The back-scattered light (Raman and Rayleigh scattered light) from the sample is collected by the OL1 and then directed on to the edge filter (EF) (LP03-532RS-25, Semrock) which blocks most of the Rayleigh light. Further, using the OL2 (NIKON L Plan 20X, 0.33 NA, WD 24 mm), the collected light is then focused onto the optical fiber (OF) (200 μm multimode single core optical fiber with a bandpass range of 400-1000 nm). This optical fiber was f-number matched to the entrance mirror of the monochromator (MONO) of focal length 550 mm (Jobin-Yvon, Triax 550, Instruments SA, Inc., NJ,

USA). Liquid nitrogen cooled charge coupled device (CCD) (Spectrum One) detector is attached to this monochromator.

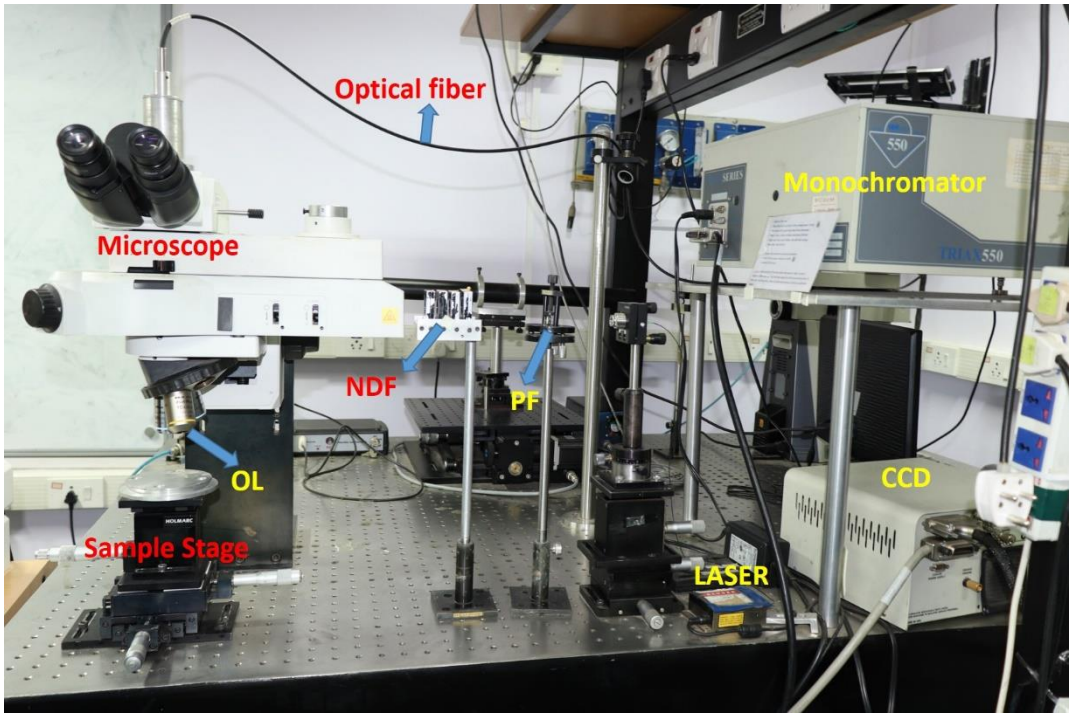

FIG. 2.2 Photograph of the custom-built micro Raman spectrometer.

Three different gratings (groove density) are available in our monochromator (TRIAX 550): 1. Holographic 1800 grooves/mm, 2. Blazed reflection type 1200 grooves/mm (500 nm blaze) and 3. 900 grooves/mm (450 nm blaze). Depending on the requirement of spectral resolution and window (spectral range), one can choose any of the above. The light was focused onto the monochromator through the entrance slit, which was dispersed by the motorized diffraction grating to be focused onto the CCD. To reduce the readout noise (or dark counts) and improve the signal to noise ratio, CCD is cooled using liquid nitrogen. The attached CCD is made of a rectangular two-dimensional array (1024 x 128) of pixels. Labspec software program installed on the personal computer controls the data acquisition and the spectrometer. For instance, we can control (using Labspec software) parameters such as slit width, the exposure time of the CCD (controlled by the shutter), the spectral range for the spectrum (determined by the angle of the diffraction grating), the pixels used on the CCD for data collection, *etc*.

Our microscope set up does not include any specific sample stage. So, we can adopt different types of the experimental setup in this free area under the OL. We have

used micrometer stages (MS) to place the sample. The vertical movement of the stage helps to focus the sample. The available large area permits us to place the diamond anvil cell (DAC) on this micrometer stages to perform *in-situ* high pressure Raman measurements. The picture of an actual customized micro-Raman spectrometer set up is shown in Fig. 2.2.

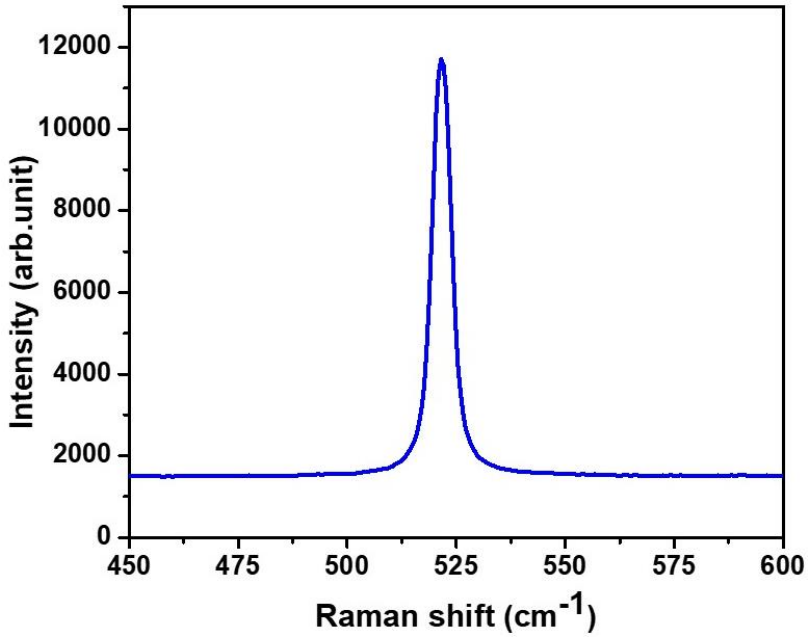

FIG. 2.3. Raman spectrum of Silicon.

The first-order Raman spectrum of crystalline silicon [6] sample is recorded (λ = 532 nm) at ambient conditions using our custom-built Raman spectrometer as shown in Fig. 2.3. This spectrum was collected using an entrance slit width of 200 μm, 1800 grooves/mm grating, laser power at the sample as 12 mW and 50X (NA = 0.45) OL. From the Fig. 2.3, it is obvious that a very high throughput (~10,500 counts/10 seconds) is achieved in our setup. The Si signal can be used for aligning the spectrometer optics for maximum throughput. Also, this Si sample's Raman frequency was used for a quick calibration check. However, accurate calibration is always done using the emission lines from Neon [7] and Krypton lamps (Oriel instruments, Newport) whenever required.

Our custom-built spectrometer has some drawbacks. The anti-Stokes part of the Raman spectrum cannot be measured due to the use of EF. Moreover, this EF has the Rayleigh cut off frequency around 80 cm^{-1}. Hence, low-frequency Raman modes

cannot be observed with this current set up. But this problem can be avoided by using a notch filter. Although the DM provides better throughput in this setup, peaks at lower frequency Raman shifts are masked by strong Rayleigh background.

2.2 High pressure techniques and components

The main idea of generating high pressure is based on the simple definition of pressure P (given below).

$$P = \frac{F}{A} \tag{2.1}$$

where F is the force applied perpendicular to an area A. From Eq. 2.1, there are two critical factors (F and A) influencing the high-pressure generation. A large force applied to a small area through an opposed anvil device will generate high pressure, and this is a commonly used strategy. For instance, the typical force of a few kN applied on a square micrometer area will result in a pressure in the order of GPa. In fact, we can increase the pressure by just increasing the force. But, increasing the applied force may exceed the threshold of compressive strength of the anvils and consequently would lead to failure of the anvils. Therefore, anvils with smaller faces are required for achieving high pressures. This is the basic reason for using small size diamond tips in diamond anvil cell for high pressure generation, and this device revolutionized the high-pressure science [8-10].

2.2.1 Diamond anvil cell (DAC)

DAC is a simple, powerful and most used tool for the investigations of matter under extreme conditions. The working principle of DAC is shown in Fig. 2.4. The first DAC was developed by Weir *et al*. [in the NBS (National Bureau of Standards) laboratory] and Van Valkenberg [9] for generating high-pressure conditions. Before the invention of the DAC, Percy W. Bridgman carried out the high-pressure research using large volume press and was awarded a Nobel Prize (1946) in Physics for his contribution [11]. Diamonds are used in the DAC because of their hardness and transparent nature to a wide frequency range of the electromagnetic spectrum (X-ray, visible light, γ ray, and most of the infrared and ultraviolet region). Therefore, DAC can be used to study a wide range of materials' properties under high pressure at *in-situ*

conditions. Importantly, DAC allows the possibility of many kinds of experimental techniques under high-pressure such as Raman and IR spectroscopy, X-Ray diffraction (XRD), optical absorption, *etc*. [12,13]

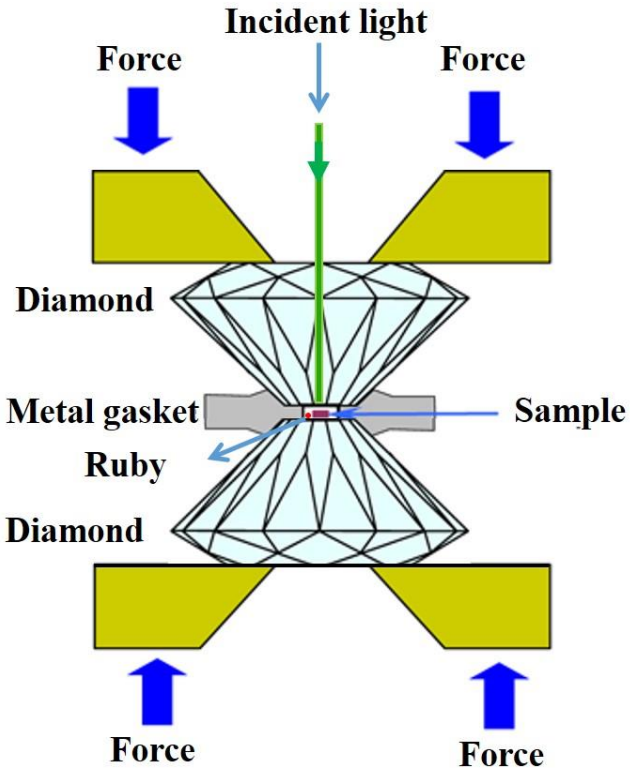

FIG. 2.4. The **s**chematic and working principle of the DAC.

The DAC is composed of two opposed diamond anvils and it creates high pressure by trapping the sample between polished culets of two diamonds inside metal gaskets. Due to this specific configuration, a small force is enough to create extremely large pressures in the sample chamber. Based on the mechanisms of generating force and anvil alignment method, different kinds of DAC have been designed. There are five major types of DACs used for high pressure generation [12,14-18].

1. NBS Cell

2. Basset Cell

3. Mao-Bell Cell

4. Syassen-Holzapfel Cell or Membrane Cell

5. Merrill-basset Cell

In this thesis work, we have used a Mao-Bell [16] type DAC (fabricated in house), and Membrane DAC (from BETSA, France) for performing the high-pressure Raman experiments. Also, for high pressure synchrotron XRD experiments at Xpress beamline (Elettra, Trieste, Italy), Mao Bell cell was used. Therefore, in the next section, we will discuss the salient features of the Mao Bell and membrane DAC.

2.2.2 Mao-Bell Diamond anvil cell

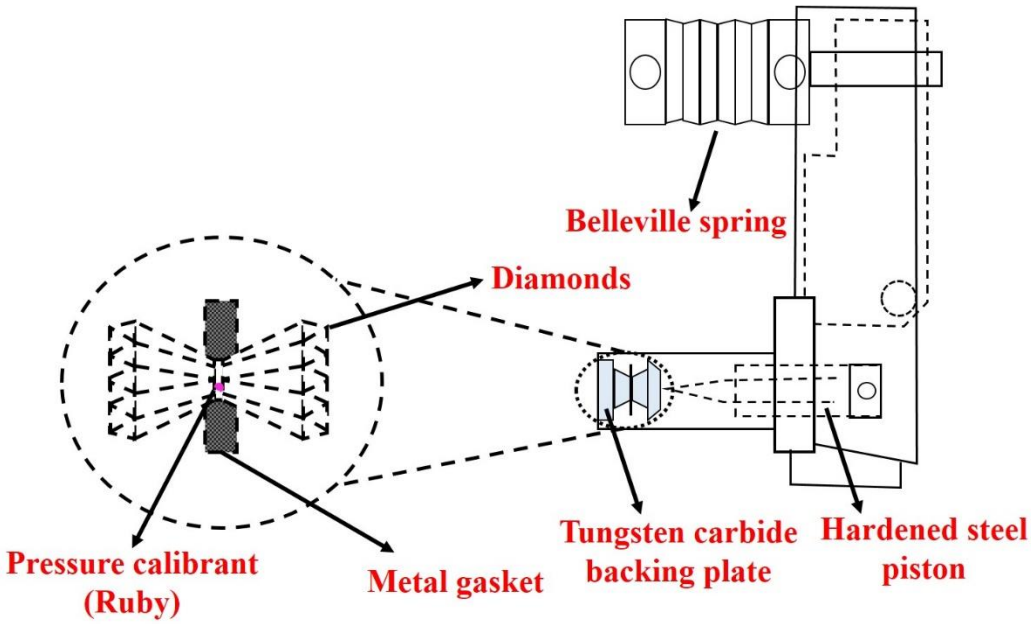

FIG. 2.5 Schematic diagram of the Mao Bell DAC.

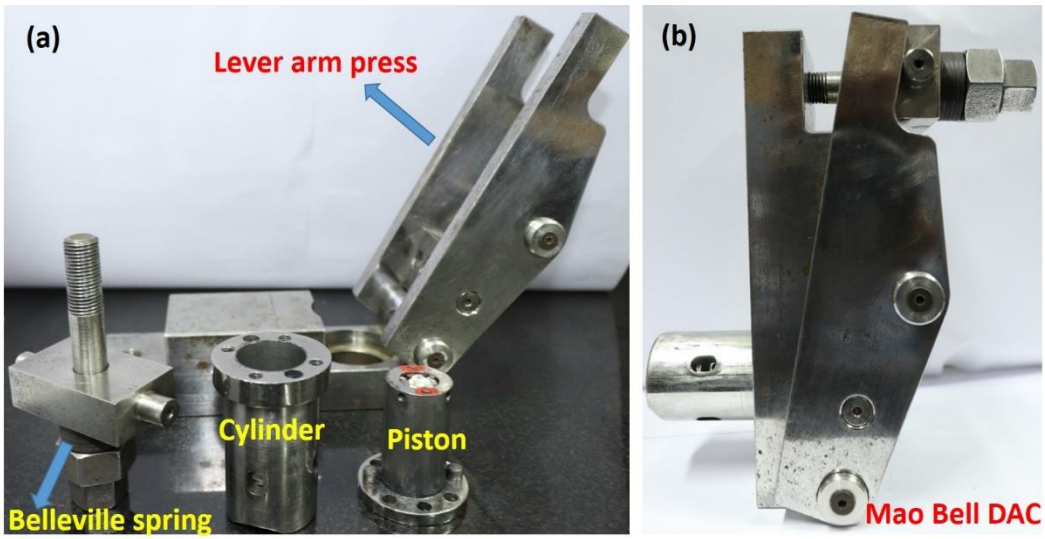

FIG. 2.6 (a) Photograph of the Mao Bell DAC components and (b) assembled Mao Bell DAC set up.

The schematic of the homemade Mao Bell DAC used in this thesis is shown in Fig 2.5. The basic components are, i) diamonds mounted on tungsten carbide rockers, ii) hardened stainless steel lever arm based on a nutcracker or scissor mechanism, iii) piston-cylinder assembly, iv) a lead screw with Belleville spring to squeeze the lever, and v) hardened stainless steel gaskets to hold the sample in between the anvils. The actual photograph of the Mao Bell DAC used is shown in Fig. 2.6 (a) and (b). The detailed view (individual components) of the DAC is shown in Figure 2.6 (a).

The piston, cylinder, and the screw are made of hardened stainless steel. The piston and cylinder assembly (with mounted diamond on each of it) are held facing each other by a lever arm mechanism. The longer arm at the lever arm press is held together by a screw with Belleville spring washers, and the shorter arm has the piston and cylinder assembly. By tightening the screw (with the Belleville spring), we can increase the pressure of the cell.

2.2.3 Membrane Diamond anvil cell (MDAC)

The schematic of the MDAC used in this thesis is shown in Fig. 2.7. The basic components of MDAC are, i) diamonds glued to the flat shaped lower and upper rockers (backing plates), ii) stainless steel gas membrane (diaphragm), to push the piston against the cylinder when gas is filled in it, and iii) guidance dowel to hold and align the piston inside the cylinder. The guidance dowel is replaced by a guide screw and notch in some specific designs. Here, the MDAC utilized in this thesis has similar guide screw-notch arrangement which facilitates to lock piston over cylinder in only one way. Figure 2.8 represents the actual photograph of MDAC used for the present thesis.

This MDAC comfortably fits under our customized Raman set up for the pressure-dependent Raman scattering experiments as shown in Fig. 2.8 (b). A pneumatic drive system (PDS) is used to control the pressure of the experiment. PDS consists of a gas (helium) cylinder (up to 200 bar capacity) which is directly connected to the MDAC as shown in Fig. 2.8 (c). When the stainless-steel gas membrane is fill up with the helium gas, it bulges and pushes the piston against the cylinder and thereby generates the high pressure inside the cell. The membrane act like a spring that expands when exposed to pressure. Using this MDAC, pressure can be controlled precisely in

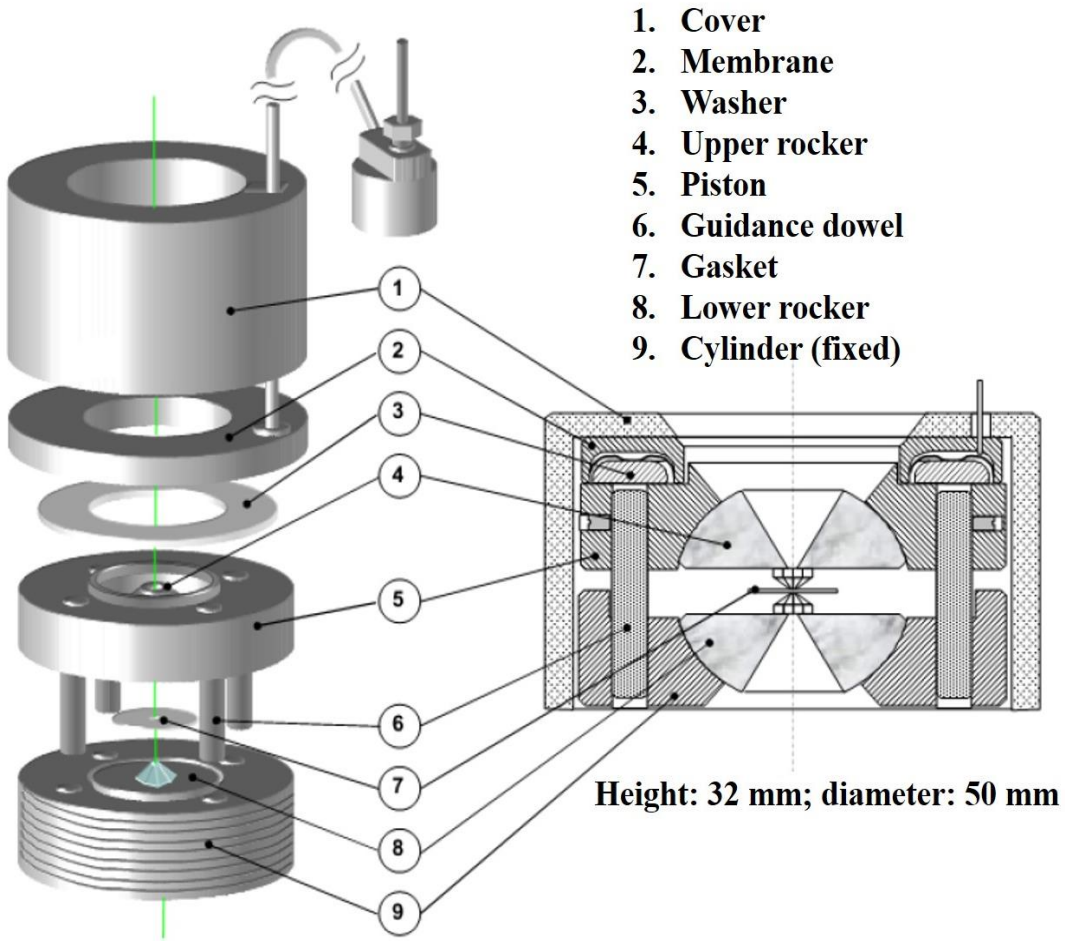

FIG. 2.7 Schematic diagram of the MDAC. This picture is adopted from the website www.betsa.fr.

steps as small as 0.1 GPa. The main difference between Mao Bell DAC and MDAC is based on the pressure generation method. In the case of Mao Bell DAC, it is achieved mechanically (pistons or screws) while MDAC it is pneumatic.

The maximum pressure generated in a high-pressure cell majorly depends on the culet size of the diamonds used, alignment of the anvils, type of anvils, the hardness of the material which makes the cell body and backing plates are made from, gasket material to confine the sample, *etc*. In the next section, each of these factors and pressure calibration are discussed in brief.

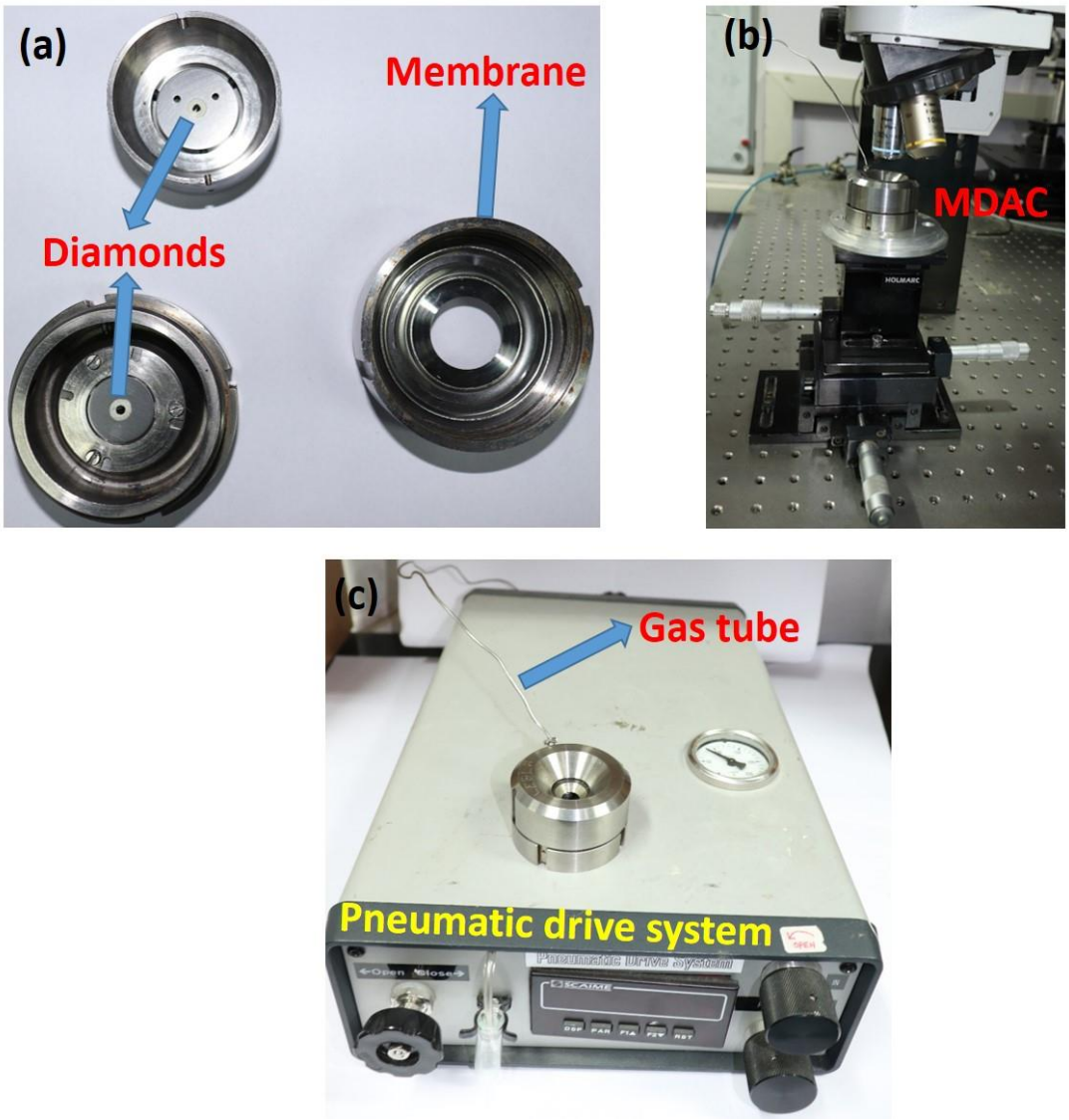

FIG. 2.8 (a) Photograph of the MDAC components, (b) assembled MDAC set up under Raman microscope and (c) MDAC connected to PDS.

2.2.4 Diamonds

The appropriate diamond selection is the first step in fabricating an anvil. The 4Cs (i.e., cut, color, clarity and carat) rate the quality of diamonds and plays a deterministic role in the outcome of the high-pressure experiments. Generally, gem quality diamonds with brilliant, and modified brilliant cut are used as anvils. Diamonds are majorly classified into two types, namely type I and type II. According to the level and type of their chemical impurities, it is further classified into type Ia, Ib, IIa, and IIb. Type I diamonds (with more nitrogen impurities) have very strong absorption in the mid IR region. It has two strong absorption regions, around 2000 cm^{-1} and 1000 - 1350

cm^{-1}, respectively. But, type IIa diamonds are pure which has the clean window below 2000 cm^{-1} allowing IR measurements in the DAC. However, it is expensive and hence are sparingly used in ultra-high-pressure experiments. Also, based on their optical transparencies, type IIa diamonds are mainly utilized for IR spectroscopy, while type I diamonds are used for Raman spectroscopy and XRD studies. It is important to mention that all the diamonds have an intense first order Raman line at 1332 cm^{-1} (F_{2g} mode), which prevents the spectrum reliability in the regions around 1300-1360 cm^{-1}. In general, diamonds with small culet diameter (<100 μm) are required for the megabar pressure experiments. An approximate formula to calculate the maximum achievable pressure (P_{max}) using DAC with culet diameter d_1 is given below, [19]

$$P_{max}(GPa) = \frac{12.5}{[d_1(mm)]^2} \tag{2.2}$$

The stress applied on the backing plates is directly influencing d_1, and thus the maximum achievable pressure. The size of the culet should be much smaller than the table of the anvil, because low pressure applied onto the table of the anvil is intensifies the pressure on the culet. The pressure intensification is controlled by the ratio of the area of the table to that of the culet. In this thesis, we have used type Ia ((100) oriented) modified Brilliant cut (purchased from Almax Easylab), 400 μm size culet based diamonds for Mao Bell DAC. For MDAC, we have used the type Ia [(100) oriented] Boehler-Almax design 85° modified Brilliant cut (purchased from Almax Easylab), 400 μm size culet diamonds.

2.2.5 Backing plates

The material supporting the diamonds (or backing plates) is one of the important factors for attaining the maximum pressure. For instance, when the stress on the backing plate exceeds the plastic deformation limit, then the diamonds get misaligned and further causing its breakage. Mostly, tungsten carbide and boron carbide materials are utilized for mounting the diamond. In our Mao Bell DAC, a hemisphere and a disk-shaped backing plates (made of the tungsten carbide) are used. For MDAC also, we have used the similar tungsten carbide based disk-shaped flat backing plates. The tapered holes are created on the backing plates for increasing the solid angle subtended on the diamonds, which helps in increasing the collection angle

for both Raman scattering and XRD. Further, the culet of the diamond anvil is exactly centered on this tapered hole of the backing plate. Before mounting the diamond, the top surface of the backing plate is polished well using diamond suspension liquid (Buehler's MetaDi). The diameter of the tapered hole should not be greater than about one-third of the diameter of the diamond's table. But, at the same time, to view the anvil culet faces during alignments, the diameter of the tapered hole should always be greater than the diameter of the culets of the diamonds. Normally, the holes are cut with a conical angle. However, the large conical angle [18] weakens the backing plate.

2.2.6 Diamond alignment

The careful alignment of the diamond's culets is the most important and critical part (or step) of the high-pressure experiments with the DAC. The diamond culet surface must be aligned lateral and parallel to each other to avoid the gasket deformation and breakage of the diamonds. Depending on their mode of operation and design, different DAC required different alignment procedures. We adopt the following procedures for the perfect alignment of our Mao Bell DAC. Initially, the piston is inserted into the cylinder taking care not to touch the diamonds, and this assembled set is placed on a V-block. With the help of the holes (the four holes in the perpendicular directions) in the wall of the cylinder, the diamonds are viewed under the optical microscope. Now, estimation of the offset of the culets along X and Y directions can be made by reducing the gap between the two anvils as close as possible (but not touched). The four set screws in the ports of the cylinder wall are used for adjustments (movement of the culets). The repeated adjustments of the culets in both the X and Y directions are made until the lateral alignment gets perfect. The screw on the bottom of the cylinder is used to align the angular orientation of the culets. The final alignment of the culets is checked by light fringe technique (Newton's rings). To check this fringe alignment, the piston is inserted into the cylinder very carefully (without banging into each other) in the vertical direction. The interference fringe patterns are observed from the top of the cylinder through the optical microscope. The observation of the zero fringe conditions (i.e. single dark) covering the whole culet confirms that the culets are aligned in parallel. We need to check if the lateral alignment is still perfect, if not we need to move the diamonds in the X and Y directions. This fringe technique is a highly reliable and unique signature of the perfect alignment of DAC. The pressure

distribution will be uniform in the case of perfect alignment. In contrast, the appearance of the color fringes or dark striations suggest that the culets are not parallel to each other. It is important to note that the complete alignment of the culets should be checked in every pressure cycle and frequently.

For the case of MDAC, we have adopted the following steps. Initially, both the diamond culets are perfectly matched along X and Y directions by adjusting the three set screws located on the piston wall. Then, the parallelism of the culet surfaces is achieved by adjusting the screws on top of the cylinder. To confirm the perfect alignment, we have used the same Newton's ring method, like the case of Mao Bell DAC.

2.2.7 Gaskets

The gasket introduction in between the two diamond anvils has an important purpose. i) It acts as the chamber which confines the sample, the pressure transmitting medium and pressure calibrant. ii) It extrudes around the diamonds on compression and acts as a supporting ring for the diamond culets. Hence the gaskets are protecting the diamonds from touching each other. Usually, the gaskets are commonly made of a hard material like hardened stainless steel (T301), tungsten, rhenium, inconel, and copper-beryllium alloy. Tungsten and rhenium are more robust and extensively used in Mbar range high-pressure/high-temperature experiments. But, stainless steel gaskets are cheap, readily available, and quite easy to drill. The gasket should be pre-indented prior to the experiment to the thickness corresponding to the desired maximum pressure. As the gasket work hardens while pre-indenting it helps to avoid the plastic deformation (hole deformation) during the experiment and hence prevents the premature failure of the diamonds. The indented gasket has a characteristic crater-like shape which perfectly holds the diamonds and guarantees support. After the pre-indentation procedure, a hole should be drilled at the center of the indented area. Because of the pre-indentation, it is easier to center the actual chamber for drilling purpose. Generally, the size of the hole should be one-third of the culet size [20]. There is an equal and opposite force acting inwards between the surface of the culet and gasket materials. This gives the stability to the gasket. In the case of the thickness of gasket being large, the outward destabilizing force will be larger than the inward stabilizing force, and hence leads to the elongation

of the gasket hole [20,21]. On the other hand, in the case of the small thickness of the gasket, the destabilizing outward force is smaller than the inward stabilizing force, and thereby shrinkage of the gasket hole happens. It is very crucial to observe the shape of the gasket hole, in each pressure step at the experiment. If the hole starts to expand asymmetrically, it means that the diamonds are approaching each other (i.e., gasket failure) and hence the experiment should be terminated. In this thesis, for most of the experiments, we have used stainless steel gaskets (T301) of the initial thickness of ~ 250 μm which is pre-indented to a thickness of ~ 60 μm. We have drilled a hole of ~ 150 μm using micro drill equipment with the aid of miniature drill bit (Tungsten carbide based) at the center of pre-indented area. For instance, the hole of ~ 150 μm is drilled at the center of the gasket pre-indented to a thickness of 60 μm is shown in Fig. 2.9.

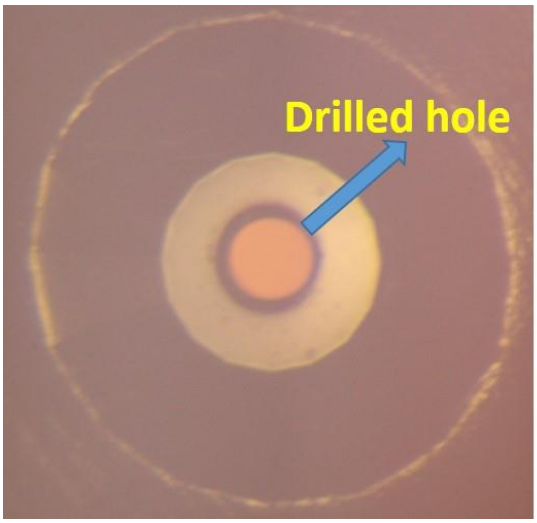

FIG. 2.9 Photograph of the drilled hole in a pre-indented gasket.

2.2.8 Pressure transmitting medium (PTM)

The PTM permits the homogeneous distribution (hydrostatic pressure) of stress inside the gasket-embedded sample chamber. In principle, PTM can be a solid, liquid or gas but in any case, they must be inert to the sample. Various fluid based PTMs have been reported to provide good hydrostatic pressure conditions [22-24]. A mixture of methanol and ethanol in the ratio of 4:1 is commonly used as a PTM which maintain the hydrostaticity up to 10.5 GPa at room temperature [23]. Further, when diluted with small amount of distilled water, the PTM of methanol: ethanol: water is in the 16:3:1

ratio, extends the hydrostatic limit of the mixture to 14.5 GPa [12]. Similarly, H_2O, isopropyl alcohol, and silicone oil give the hydrostatic conditions up to ~5 GPa, ~ 4 GP and ~ 12 GPa respectively. These fluids solidify beyond their hydrostatic limits and become quasi-hydrostatic and then non-hydrostatic (at very high-pressure range) [25]. In the case of solid PTM, usually, alkali-halides are the easiest to use. For instance, sodium chloride and silver iodide give the hydrostatic pressure up to ~ 7 GPa. Inert gases like He and Ne give hydrostatic pressures up to ~70 GPa and ~ 16 GPa respectively. These inert gas PTMs are the most reliable and consequently preferential for the use in high pressure experiments, but difficult to work with it (mostly requires cryogenic loading device). In this thesis, we have used the mixture of methanol: ethanol in the ratio of 4:1 as PTM for all the high-pressure Raman and synchrotron XRD experiments.

2.2.9 Pressure measurement

A reliable and accurate pressure gauge is essential for all high-pressure experiments. The ruby fluorescence method is the widely used pressure calibration technique [26] in the DAC. Ruby is Al_2O_3 doped with Cr^{3+} and it does not undergo any phase transition under pressure ranges up to ~ Mbar at room temperature conditions. The fluorescence signal of the Ruby is very strong and composed by two narrow lines (R_1, and R_2) [27]. The R_1 and R_2 lines appear at ~ 694.2 nm and ~ 692.7 nm respectively. These lines originates from the lifting of the degeneracy of the d-orbitals of the Cr^{3+} ion by the octahedral coordination of the oxygen atoms due to crystal field theory proposed for this geometry. Precisely, the change in the electron states from the ground to the metastable $4A_2 \rightarrow 2E$ of Cr^{3+} in the distorted octahedral coordination emit these lines (R_1 and R_2) [28]. Under pressure, the position of the R_1 and R_2 peaks shift to a longer wavelength. Mainly, the wavelength shift of the R_1 line is used for pressure calibration under static high-pressure conditions [28]. Under hydrostatic pressure, R_1 and R_2 lines redshift equally and hence there is no change in the separation between them. The Fig. 2.10 represents the pressure dependence of the Raman shift of the Ruby lines for typical pressure values.

Pressure can be determined from the wavelength of the R_1 line using the formula, [29]

$$P\ (GPa) = \frac{1904}{B}\left[\left(1 + \frac{\Delta\lambda}{\lambda_0}\right)^{B} - 1\right] \tag{2.3}$$

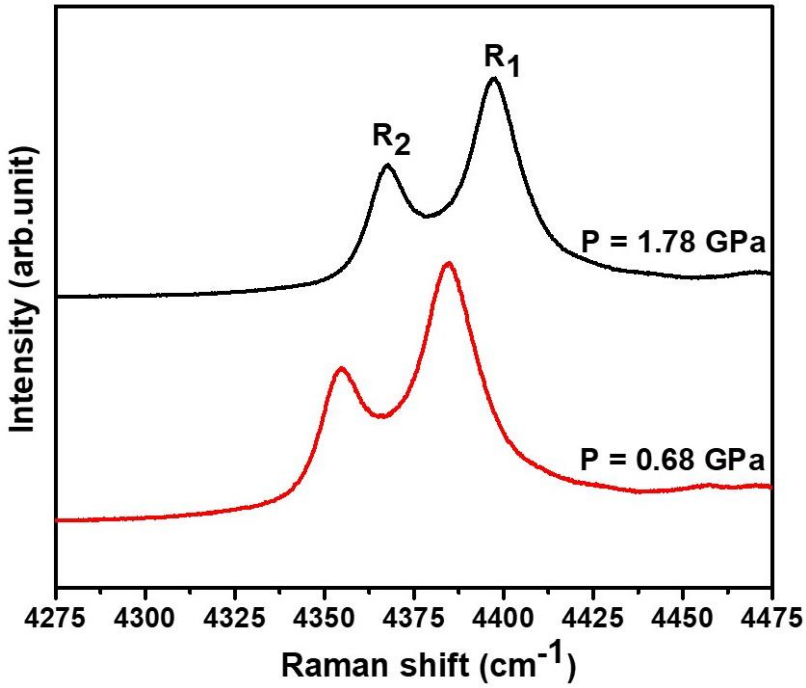

FIG. 2.10 Typical Raman shift of the Ruby peaks as a function of hydrostatic pressure. The wavelength used for this Raman spectrum is λ = 532 nm.

where, $\Delta\lambda = \lambda_p - \lambda_0$ is the difference between the wavelength at a pressure P and ambient pressure, and B is empirically determined coefficients. B= 7.665 and 5 for quasi-hydrostatic and non-hydrostatic conditions respectively. Using Ruby pressure calibration method, the precision of the pressure can be achieved to the order of ± 0.03 GPa. The precision of the pressure measurement depends on the degree of crystallinity, size, shape, and importantly annealing of the ruby crystals to remove the residual strains when the ruby particles are made into spheres using ball milling. Ruby can be well detected even from a very small (~ 10 μm diameter) sphere because of the large strength of its signal. This is helpful in safely placing the Ruby in the gasket hole without altering the measurement. Further, the broadening of the R_1 and R_2 spectra clearly indicate the substantial non-uniformity of stress [27] over the dimension of the ruby chip. In this thesis, we have used the ruby fluorescence method for *in situ* pressure

calibration of Raman and synchrotron XRD experiments. A ruby sphere of size ~ 10 – 20 μm is loaded in the sample chamber together with the sample and PTM.

2.3 Synchrotron X-ray diffraction

Synchrotron radiation is electromagnetic energy produced by accelerating charged particles (e.g., electrons and ions) approaching the speed of light [30]. According to classical electrodynamics, any charged particle which is accelerated in a straight-line path or moves in a curved path will radiate electromagnetic energy.

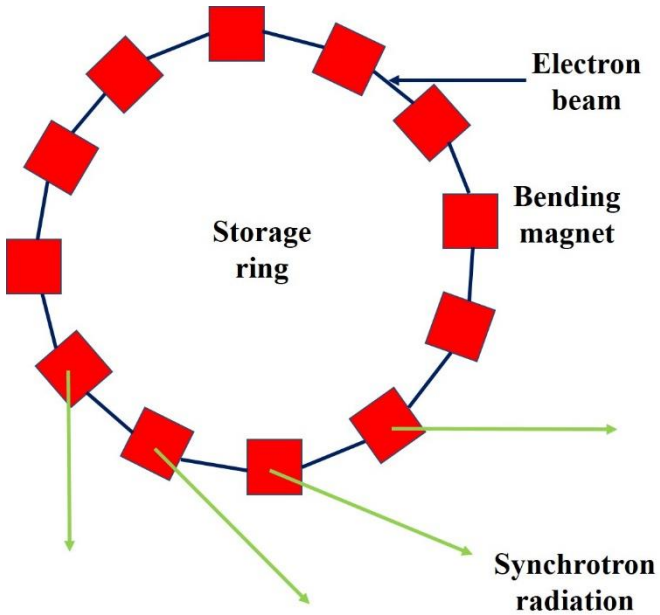

FIG. 2.11 Schematic of the typical synchrotron radiation source.

The schematic of the synchrotron radiation principle is shown in Fig. 2.11. Initially, the high energy electrons are first accelerated close to the speed of light (relativistic), and then injected to the storage ring that is guided by arrays of magnets which constrain the relativistic electron beam to move in a circular path. Consequently, electromagnetic radiation is produced tangential to the curved orbit of accelerated electrons. The straight sections of the storage ring consist of essential devices (called 'insertion devices') for monitoring, focusing and steering the electron beam to maintain a stable and predictable orbit. For this purpose, wigglers and undulators are used in the straight section [31,32]. The curved section contains the bending magnets which bend the electron beam and effectively generates a sweeping searchlight pattern of photons. The synchrotron radiation mainly depends on the energy of electrons in the storage ring

and the curvature of their path. Thus, to have higher energy of the emitted X-rays, greater electron energy in the storage ring is needed.

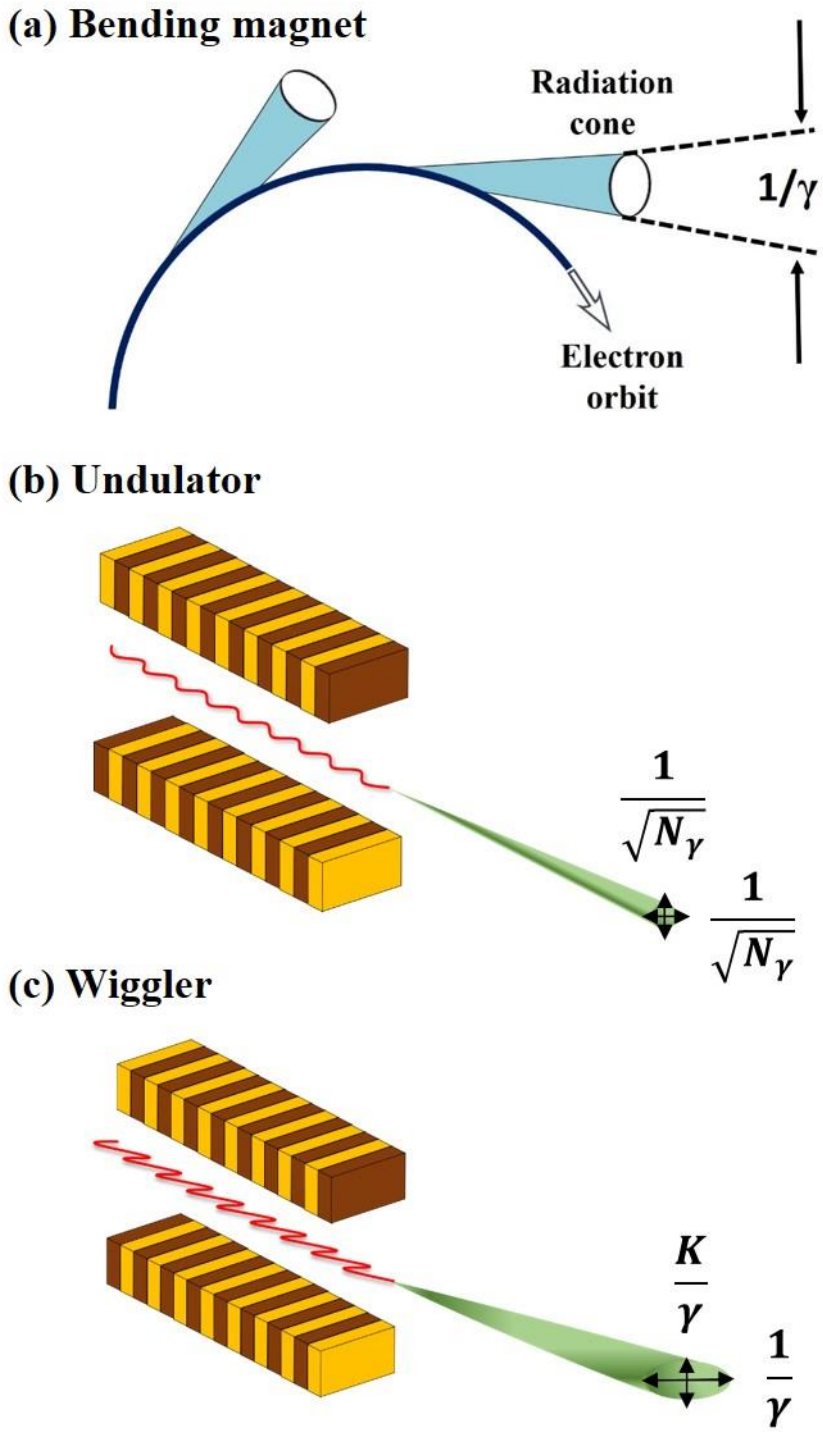

FIG. 2.12. Radiation from (a) bending magnets, (b) undulator and (c) wiggler. In this, K (maximum angle of electron oscillations in the horizontal plane) is around 20 for the wiggler. The number of period N is around 5. The schematic is adopted from [32].

The synchrotron storage rings contain bunches of electrons that are circulating at constant energy $\gamma = \frac{E_e}{mc^2}$. Here, c is the velocity, m is the mass of the charged particle and E_e is the rest mass electron energy. Generally, the radiation emitted from the relativistic charged particle (moving in a circular orbit) is tightly directed into cones of radiation. Mathematically, this cone angle is inversely proportional to γ. Typical synchrotron radiations are extracted from bending magnets [Fig. 2.12(a)] or in the insertion devices such as undulators [Fig. 2.12(b)] or wigglers [Fig. 2.12(c)] [32] are shown in Fig.2.12. In the case of insertion devices, an alternating magnetic field (dipoles are arranged with alternating polarity) forces the electrons to move in the oscillating paths rather than moving in a straight line.

The amplitude of the oscillations from a wiggler is large, and the radiation from different wigglers adds incoherently. Hence, wiggler can emit intense radiation over a wide spectral range and is closely like a bending magnet. However, this kind of broad spectral feature has a major disadvantage because most scientific experiments usually only require a very narrow range of wavelengths. So, most of the unused wiggler radiation gives unwanted heat within the optical devices. But in the case of undulator, the small-amplitude oscillations from the passage of a single electron emits a coherent addition of the radiation from each oscillation which leads to a higher brightness and series of sharp peaks [33]. Therefore, the main difference in the performance of these two devices (wigglers and undulators) arises from the difference in the amplitude of the electron's oscillations in the horizontal plane as shown in Fig. 2.12(b) and (c). It is noteworthy that wigglers are kept in higher magnetic fields (controls the cone's open angle) than undulators.

Synchrotron radiation has many advantages than the conventional laboratory-based tube X-ray sources. The most notable one is the brilliance (the number of photons emitted per second per unit solid angle). The brilliance of the X-ray beam from the standard synchrotron sources is four (first generation synchrotrons) to twelve (third generation synchrotrons) orders of magnitude higher than that from a conventional laboratory X-ray source. Another important advantage is the tunability of the energy (e.g., from far IR to hard X-rays) to the experimental requirements [34]. However, the standard laboratory X-ray tube provides just a few characteristic wavelengths depending on its target material (Mo-K_α with λ = 0.71073 Å and Cu-K_α with λ =

1.54184 Å are the most commonly used). Generally, for high-pressure diffraction experiments, shorter wavelength (e.g., $\lambda \sim 0.5$ Å) is preferred as it allows for a conical section to contain a much wider 2θ range. In the next subsection, we will provide a very brief description of the Xpress beamline, at Elettra synchrotron radiation, Trieste which is extensively used for the studies presented in this thesis.

2.3.1 Xpress - high pressure powder diffraction beamline

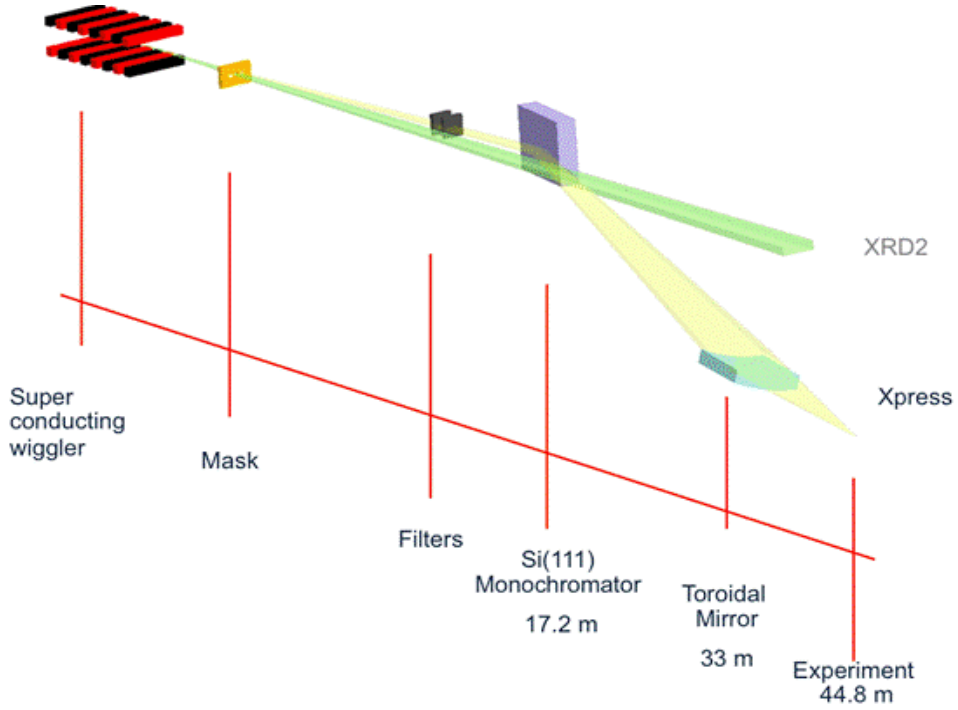

FIG. 2.13. Schematic of the Xpress beamline. Here, XRD2 beamline (next to Xpress beamline) is sharing the SCW.

The schematic outline of the beamline is shown in Fig. 2.13. A photograph of the end station of the Xpress beamline together with a schematic diagram explaining the main components are shown in Fig. 2.14. The Xpress beamline provides a high photon flux at a fixed energy of 25 keV which is ideal for high pressure powder experiments using DAC [35]. A multipole superconducting wiggler (SCW) is the source of the beamline. Liquid nitrogen cooled Si(111) single crystal hosted in the splitter chamber intercepts the X-ray beam from the SCW. The monochromator directs the X-ray beam to the focusing mirror at a fixed energy of 25 keV. The focusing mirror

is Pt coated to achieve 80% reflectivity at 25 keV and is a 1.4 m long torus, kept at 2.9 mrad grazing angle.

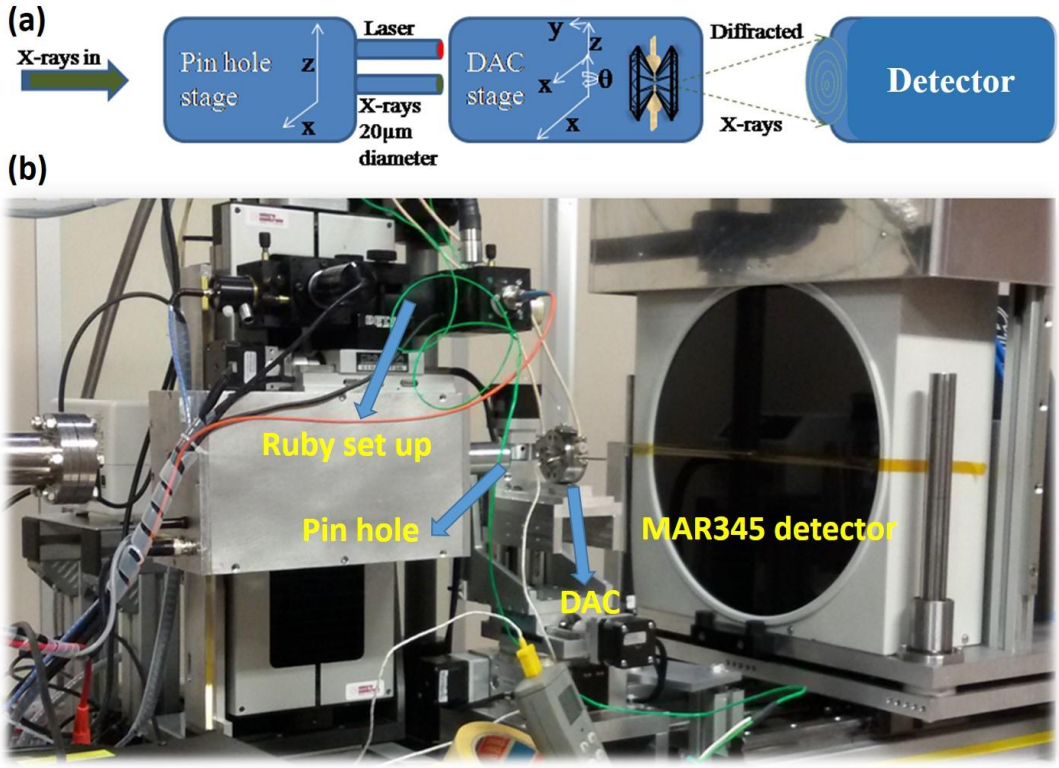

FIG. 2.14. (a) Block diagram of the synchrotron high pressure XRD set up at Xpress beamline and (b). Photograph of the Xpress beamline set up.

Finely focused beam from this mirror is further optimized by collimators (200 - 20 µm in diameter pin holes) which gives an intense and well-defined monochromatic beam with minimum divergence for the diffraction experiments. An image plate detector MAR345 is used to record the XRD patterns of the samples under pressure from inside DAC. Further, this MAR345 detector is placed in a special stage which allows the controllable linear movement along the beam direction at two fixed vertical positions. A ruby fluorescence microscope is connected side by side to the pinhole stage which helps to estimate the accurate measurements of the sample's pressure (Fig. 2.14). Xpress beamline has a friendly graphical user interface permitting an easy setting-up of the beamline as well as data collection parameters [35,36,37].

2.4 Bibliography

1. W. Hayes, Contemp. Phys. **16,** 69 (1975).
2. G. V. P. Kumar, and C. Narayana, Curren. Sci. **93**, 778 (2007).
3. G. Kavitha, S. R. C. Vivek, A. Govindaraj, and C. Narayana, Proc.Indian Acad. Sci. Chem. Sci. **115**, 689 (2003).
4. https://www.witec.de/products/spectroscopic-system/
5. http://www.horiba.com/in/scientific/products/raman-spectroscopy/raman-spectrometers/raman-microscopes/hr-evolution/labram-hr-evolution-17309/
6. J. H. Parker, D. W. Feldman, and M. Ashkin, Phys. Rev. **155,** 712 (1967).
7. S. B. Kim, R. M. Hammaker, and W. G. Fateley, Appl. Spect. **40,** 412 (1986).
8. C. E. Weir, E. R. Lippincott, A. Van Valkenburg, and E. N. Bunting, J. Res. Natl. Bur. Stand. **63 A,** 55 (1959).
9. W. A. Bassett, High Pres. Res. **29,** CP5 (2009).
10. J. C. Jamieson, A. W. Lawson, and N. D. Nachtrieb, Rev. Sci. Instrum. **30,** 1016 (1959).
11. https://www.nobelprize.org/prizes/physics/1946/bridgman/facts/
12. A. Jayaraman, Rev. Mod. Phys. **55,** 65 (1983).
13. A. Jayaraman, and S. K. Sharma, Curren. Sci. **74,** 308 (1998).
14. W. A. Bassett, T. Takahash, and P. W. Stook, Rev. Sci. Instrum. **38,** 37 (1967).
15. G. Huber, K. Syassen, and W. B. Holzapfel, Phys. Rev. B **15,** 5123 (1977).
16. H. K. Mao, and P. M. Bell, Carnegie Inst. Washington Yearbook **77,** 904 (1975).
17. G. J. Piermarini, and S. Block, Rev. Sci. Instrum. **46,** 973 (1975).
18. L. Merrill, and W. A. Bassett, Rev. Sci. Instrum. **45,** 290 (1974).
19. D. J. Dunstan, and I. L. Spain, J. Phys. E: Sci. Instrum. **22,** 913 (1989).
20. D. J. Dunstan, Rev. Sci. Instrum. **60**, 3789 (1989).
21. L.Spain, and D. J. Dunstan, J. Phys. E: Sci. Instrum. **22**, 923 (1989).
22. S. J. You, L. C. Chen, and C. Q. Jin, Chinese Phys. Lett. **26,** (2009).
23. S. Klotz, J. C. Chervin, P. Munsch, and G. Le Marchand, J. Phys. D : Appl. Phys. **42,** 075413 (2009).

24. G. J. Piermarini, S. Block, and J. D. Barnett, J. Appl. Phys. **44,** 5377 (1973).
25. A. Jayaraman, Rev. Sci. Instrum. **57,** 1013 (1986).
26. D. Barnett, S. Block, and G. J. Piermarini, Rev. Sci. Instrum. **44,** 1 (1973).
27. R. A. Forman, G. J. Piermarini, J. Dean Barnett, and S. Block, Science **176,** 284 (1972).
28. Syassen, High Press. Res. **28,** 75 (2008).
29. H. K. Mao, P. M. Bell, J. W. Shaner, and D. J. Steinberg, J. Appl. Phys. **49,** 3276 (1978).
30. S. Doniach, and, H. Winick, Synchrotron Radiation Research, Plenum Press: NewYork (1980).
31. W. Clegg, J. Chem. Soc., Dalton Trans. 3223 (2000).
32. J. A. Nielsen, and D. McMorrow, Elements of modern x-ray physics, John Wiley and Sons, UK (2011).
33. H. Winich, Synchrotron Radiation Sources: A primer, World Science (1994).
34. V. K. Pecharsky, P. Y. Zavalij, Fundamentals of Powder Diffraction and Structural Characterization of Materials, Springer Science + Business Media, Inc., New York (2005).
35. B. Joseph, M. Polentarutti, P. Lotti, N.K. Varshney, G. Bais, S.M. Sharma, D.D. Sarma, A. Lausi, Xpress: A dedicated high pressure powder diffraction facility, Elettra Highlights, Pages 130-131 (2015-2016).
36. B. Joseph, A. Lausi, N.K. Varshney, G. Bais, M. Polentarutti, S. M. Sharma, Nanoscale excitations in emergent materials, NEEM-2015, Superstripes press, Rome, pages 53-54 (2015), ISBN 9788866830450.
37. http://www.elettra.eu/elettra-beamlines/xpress.html

Part I

Pressure induced topological quantum phase transitions

Chapter 3

Phonon signatures of multiple topological quantum phase transitions in compressed $TlBiS_2$

The author's main contribution in this chapter is the core research idea, performing the high pressure Raman and synchrotron XRD measurements on $TlBiS_2$ sample and analyzing the data. To execute this research problem, we have collaborated with Prof. Sebastian C. Peter's group, JNCASR, Bangalore for sample synthesis and Prof. Umesh V. Waghmare's group, JNCASR, Bangalore for the first principles theoretical calculations.

V. Rajaji, Raagya Arora, Saurav Ch. Sarma, B. Joseph, Umesh V. Wagmare, Sebastian C. Peter, and Chandrabhas Narayana *"Phonon signatures of multiple topological quantum phase transitions in compressed $TlBiS_2$: A combined experimental and theoretical study"*(under review in *Phys. Rev. B*).

3.1 Introduction

Recently a new state of quantum matter known as topological insulators has received a great deal of attention due to their potential applications in spintronics, quantum computing, and thermoelectric energy conversion devices [1]. The description of TQPT has been discussed in Chapter 1 (section 1.7.2.3). Due to its technological importance, a considerable number of materials have been theoretically predicted as a topological insulator under high pressure. However, a direct experimental detection of band inversion with the high-pressure setup is challenging to perform. For example, angle-resolved photoemission spectroscopy (ARPES) is the most direct tool to probe the nontrivial electronic band inversion [2,3]. But ARPES measurements under pressure have not been implemented yet due to the experimental difficulties. However the indirect evidence of TQPT can be obtained from a combination of transport, synchrotron x-ray diffraction (XRD), and Raman linewidth anomalies [4-8]. Electron-phonon coupling is the basic mechanism for detecting the indirect signatures of TQPT (or band inversion) through optical phonons via Raman spectroscopy. Mathematically, Raman linewidth is directly proportional to the square of the energy-resolved electron-phonon matrix elements [9], and hence the dynamics of electron-phonon coupling will be strongly replicated at full width at half maximum (FWHM) [6,7]. Especially for a centrosymmetric space group, long-wavelength optical phonons (q = 0) couple to electrons either through commutation or anticommutation with an electronic parity operator and hence effectively capture the changes in topological invariants via linewidth [9]. Though an axial (*c/a*) ratio as a function of pressure is expected to give the relative compressibility (isotropic or anisotropic), fluctuations in an electronic density due to band inversion cause anomalies in it (*c/a* ratio) [4,5].

For instance, combined synchrotron powder XRD and infrared spectroscopy measurements on BiTeI [space group (SG) *P*3*m*1, band gap E_g = 0.38 eV] revealed a correlation between band gap closing and band inversion with a minimum of *c/a* ratio in the pressure range 2.0–2.9 GPa [4,10]. Interestingly, a phonon linewidth anomaly (unusual electron phonon coupling) of the E mode at ~3.0 GPa has been observed during TQPT in BiTeI [7]. Furthermore, an unusual increase in the inner Fermi surface shape and curvature changes of the outer Fermi surface shape have been noticed from Shubnikov–de Haas oscillations measurements during the TQPT in BiTeI [11].

Similarly, TQPT has been claimed in Sb_2Se_3 (SG *Pnma*, E_g = 1 eV) at ∼2.5 GPa by studying the vibrational phonon and electrical resistivity anomalies together with first-principles calculations [6,8], though there is also an alternate interpretation suggested [12]. Recently, Ohmura *et al.* showed that bismuth tellurihalide BiTeBr (SG $P3m1$, E_g = 0.55 eV) undergoes a TQPT at 2.5–3.0 GPa using resistivity and synchrotron XRD measurements under pressure [5]. The above examples provide the strong basis for using such indirect methods (XRD and Raman scattering) to study pressure-induced TQPT in strong spin-orbit coupling (SOC) systems and provide relevant information.

Another interesting class of materials are called as topological crystalline insulators (TCI) [13, 14], where the gapless surface states are protected by mirror symmetry. These materials are different from topological insulators in which the time reversal symmetry protects the surface states and hence the protection of surface states for TCI perseveres even when time-reversal symmetry is broken. The presence of mirror symmetry in the crystal structure of a material results in the presence of planes in the Brillouin zone (BZ) that are mirror symmetric. Therefore, mirror symmetry protected Dirac cones arise in the surface electronic structure. TCIs are characterized by a non-zero mirror Chern number. The individual Chern numbers C_{+i} and C_{-i} are defined on a mirror-invariant plane. The mirror Chern number [13] defined as $n_M = (C_{+i} - C_{-i})/2$ can be used as a topological invariant for TCI. A TCI supports an even number of Dirac cones and band inversions in sharp contrast to a topological insulator characterized by odd number of band inversions. The first TCI phase experimental [15] observation was made in SnTe, which were earlier theoretically [16] predicted.

The narrow band gap tetradymite semiconductors Bi_2Se_3 (band gap E_g = 0.30 eV), Bi_2Te_3 (E_g = 0.12 eV) and Sb_2Te_3 (E_g = 0.28 eV) crystallize in rhombohedral structure (space group SG: $R\bar{3}m$) and are 3D topological insulator at ambient conditions with surface states consisting of a single Dirac cone at the Γ point of the BZ [17-19]. In the tetradymite semiconductors family, the Sb_2Se_3 is having the larger band gap (E_g ~ 1 eV) and lesser SOC strength than remaining members (Bi_2Se_3, Bi_2Te_3, and Sb_2Te_3). There are no topologically non-trivial states present at ambient conditions in Sb_2Se_3. It is well known that the thermodynamic parameter pressure *P* can tune the strength of the SOC and also the band gap. Interestingly, hydrostatic pressure induced band inversion with parity change at Γ point in the Sb_2Se_3 compound has been theoretically predicted

[20] and then subsequently phonon anomalies are noticed at ~2.5 GPa [6]. Similarly, thallium based III-V-VI_2 ternary chalcogenides $TlBiSe_2$ (E_g = 0.28 eV) and $TlBiTe_2$ (E_g = 0.11 eV) crystallize in rhombohedral structure (SG: $R\bar{3}m$) and are 3D topological insulator at ambient conditions [21]. In this family, $TlBiS_2$ (E_g = 0.42 eV) is having relatively higher band gap and lesser SOC than $TlBiSe_2$ and $TlBiTe_2$ compounds. Under the application of external strain, the TQPT is theoretically predicted in the $TlBiS_2$ system [22]. The above two examples (tetradymite semiconductors and thallium based III-V-VI_2 ternary chalcogenides) illustrate the interplay between the crystal symmetry, band gap, and SOC. In other words, when the compound of 3D topological insulator family shares the same crystal and electronic structure, but lacks the band gap and SOC, and then pressure can serve as an ideal external tool to induce the band inversion in it.

Thallium based III-V-VI_2 ternary chalcogenide $TlBiS_2$ is the narrow band gap semiconducting material and has significant interest on the aspect of thermoelectric and topological properties under different conditions [22]. Even though $TlBiS_2$ share the same crystal structure (SG: $R\bar{3}m$) as tetradymite compounds (Bi_2Se_3, Bi_2Te_3, and Sb_2Te_3), there is a considerable difference exists between them. The tetradymite semiconductors consist of quintuple layers stacking along the *c* axis, and each quintuple layers are separated by weak Van der Waals type interactions and therefore it is a quasi 2D nature. In $TlBiS_2$, each Tl (or Bi) layer is sandwiched between the two S layers. But, strong coupling exists between the two layers and makes it intrinsically 3D natures [22, 23]. Recently, it is observed that the substitution of Se (x~0.5) at S site [$TlBi(S_{1-x}Se_x)_2$], leading to the formation of a single Dirac cone at the Γ point [24]. Here, the substituted Se (i) increases the effective SOC strength of $TlBiS_2$ compound without changing the crystal structure, and (ii) decreases the band gap. Consequently non-trivial topological phase transition (Z_2 = 1) is observed in [$TlBi(S_{1-x}Se_x)_2$] at ambient pressure. This interesting chemical approach strongly stimulated us to perform the high pressure studies on $TlBiS_2$. Because, the substitution of Se is analogous to the externally applied pressure which can also possibly tune the effective hybridization, the relative strength of the SOC, bandgap and topological invariant Z_2. To support our intuition further, recently, first principles theoretical calculations predicted the topologically non-trivial phases in rhombohedral phase (SG: $R\bar{3}m$) of $TlBiS_2$ under different strain effects

(uniaxial, biaxial and hydrostatic strains) [22]. However, to the best of our knowledge, to date, there is no strain dependent experimental work available on the $TlBiS_2$ compound in the literature. Also, we would like to mention here that the hydrostatic pressure is effective, well controlled and experimentally easily accessible strain using the diamond anvil cells (DAC). Hence, it will be interesting to explore the possibility of hydrostatic pressure tuned topological phase transitions in $TlBiS_2$ using Raman scattering complemented with the synchrotron XRD measurements and first principles theoretical calculations.

In this chapter, we have investigated the pressure dependent structural and vibrational properties of the rhombohedral phase of $TlBiS_2$ compound using *in situ* synchrotron XRD and Raman scattering measurements respectively. Combined Raman and synchrotron XRD results indicate that the rhombohedral phase shows the structural stability up to ~4.0 GPa and beyond which the first-order structural phase transition takes place. Further, two isostructural electronic transitions are observed from phonon (E_g and A_{1g}) anomalies at ~0.5 GPa and ~1.80 GPa and corroborated with our first principle theoretical calculations to TQPT (Z_2 = 1) and TCI (n_M = 2) transitions respectively. Finally, the significance of the obtained results is discussed in connection with other known pressure induced topological materials.

3.2 Experimental details

The pure phase of $TlBiS_2$ was synthesized by adding the stoichiometric amount of Tl powder (purity >99.99%), Bi shots (purity >99.99%) and S powder (purity >99.99%) in a 9 mm diameter quartz tube. The quartz tube was flame-sealed under the vacuum of 10^{-3} Torr, achieved with the help of a rotary pump, to prevent oxidation during the sealing process. The temperature was raised to 900 ^oC within 5 h, held at that temperature for 4 days and then cooled to room temperature in 10 h. No reaction with the quartz tube was observed. Grey $TlBiS_2$ solid was obtained after the reaction. The weight losses of the final material were found to be less than 1%. The synthesized polycrystalline $TlBiS_2$ was then subjected to vertical Bridgeman method for single crystal growth. $TlBiS_2$ powder was again vacuum-sealed in a 9 mm diameter quartz tube and introduced into the dual zone vertical Bridgeman furnace. Zone 1 was heated to 900 ^oC in 10 h and held at that temperature for 2 days. Zone 2 was

simultaneously heated to 700 ^oC in 68 h and held there till the reaction ends. The movement controller was slowly lowered from Zone 1 to Zone 2 with a velocity of 6 mm/h for a total distance of 750 mm. Small single crystals of ~1 mm size were obtained after the reaction. Phase identity and purity of the sample were determined by powder XRD study, which was carried out with the Xpress beam line, Elettra synchrotron using the wavelength (λ = 0.50070 Å).

Raman spectra were recorded using LabRam HR evolution (Horiba) micro Raman spectrometer in the backscattering geometry (180˚). This commercial Raman spectrometer equipped with a solid-state four level laser (Nd:YAG, wavelength λ =532 nm), 800 mm focal length monochromator, and Peltier cooled CCD detector. The resolution of the spectrometer is about ~0.6 cm^{-1} for the grating of 1800 groves per mm and 200 μm entrance slit width. The *in situ* high pressure Raman scattering measurements were carried out using a typical Mao Bell DAC with the culet size of 400 μm. The stainless steel (T301) was used as a gasket material, and it was pre-indented to the thickness of about 60 μm. The pressure was determined by the ruby fluorescence method [25]. The methanol:ethanol (4:1) mixture was used as the pressure transmitting medium (PTM) which maintains the hydrostatic condition up to 10.5 GPa [26]. The typical accumulation time of each spectrum was about 25 minutes. The laser power was kept at a lower value (<0.5 mW) which prevents the sample from laser induced damage and oxidation.

The *in situ* high pressure XRD measurements were performed using Mao Bell DAC at Xpress beamline of the Elettra synchrotron radiation facility, Trieste, Italy. The wavelength (λ) of the synchrotron radiation used is ~ 0.50070 Å. The MAR-345 imaging plate detector is used for the present experiment. Initially, the sample to detector distance was calibrated with a LaB_6 sample and found to be ~271.38 mm. The gasket preparation, pressure calibration and PTM used are the same as above mentioned in the case of high pressure Raman scattering experiments. Typical accumulation time for each collected synchrotron XRD pattern is 10 minutes. The collected two dimensional (2D) diffraction image patterns were converted to one dimensional (1D) patterns (intensity vs. 2θ) using the fit2D software [27]. The Le Bail method fitting of the powder XRD patterns was performed using the FullProf software [28].

3.3 Computational methods

Our first-principles theoretical calculations are based on density functional theory (DFT) employing the Quantum ESPRESSO (QE) code [29]. We used a generalized gradient approximation (GGA) [30] to the exchange-correlation energy functional as parametrized by Perdew, Burke, and Ernzerhof (PBE) [31]. The projector augmented wave (PAW) potentials [32] with valence configuration $4f^{14}\ 6s^2\ 6p^1\ 5d^{10}$, $4f^{14}\ 6s^2\ 6p^3\ 5d^{10}$ and $4d^{10}\ 5s^2\ 5p^2$ were adopted for Tl, Bi and S respectively. Electronic wave functions and charge density were represented in plane wave basis sets truncated with cut-off energies of 55 Ry and 550 Ry respectively. The discontinuity in occupation numbers of electronic states was smeared using a Fermi-Dirac distribution function with broadening of k_BT = 0.003 Ry and integrations over BZ were sampled on a uniform 6x6x6 mesh of k-points. In the simulation of pressure-dependent properties, we used scalar-relativistic PAW potentials to optimize the structure with respect to lattice constants and atomic coordinates. The structure was optimized to minimize the enthalpy, H = E + PV at a given pressure. Atomic coordinates of these optimized structures were used as the initial structure for further optimization using fully-relativistic potentials. Effects of SOC were included in our calculations of the electronic structure through the use of fully relativistic potentials [33], while we used scalar-relativistic PAW potentials in the calculation of phonons. Electronic spectrum was determined at Bloch vectors along high symmetry lines (Γ - L - Z - F - Γ - Z) in the BZ. Lattice dynamical properties were determined using density functional linear response (called as density functional perturbation theory [34]) as implemented in the QE package [29]. To obtain phonon dispersion, dynamical matrices were obtained on a 2x2x2 q-points grid in the BZ. We Fourier interpolated these dynamical matrices to obtain the phonon dispersion along high symmetry lines (Γ - L - Z - F - Γ - Z) in the BZ. To determine the bulk electronic topology of $TlBiS_2$, we used Z2PACK code [35] to determine the Z_2 topological invariants and mirror Chern number (n_M). This code uses hybrid Wannier functions [36, 37] and employs the ideas of time reversal polarization in the determination of the Z_2 invariants.

3.4 Results

3.4.1 Ambient characterization

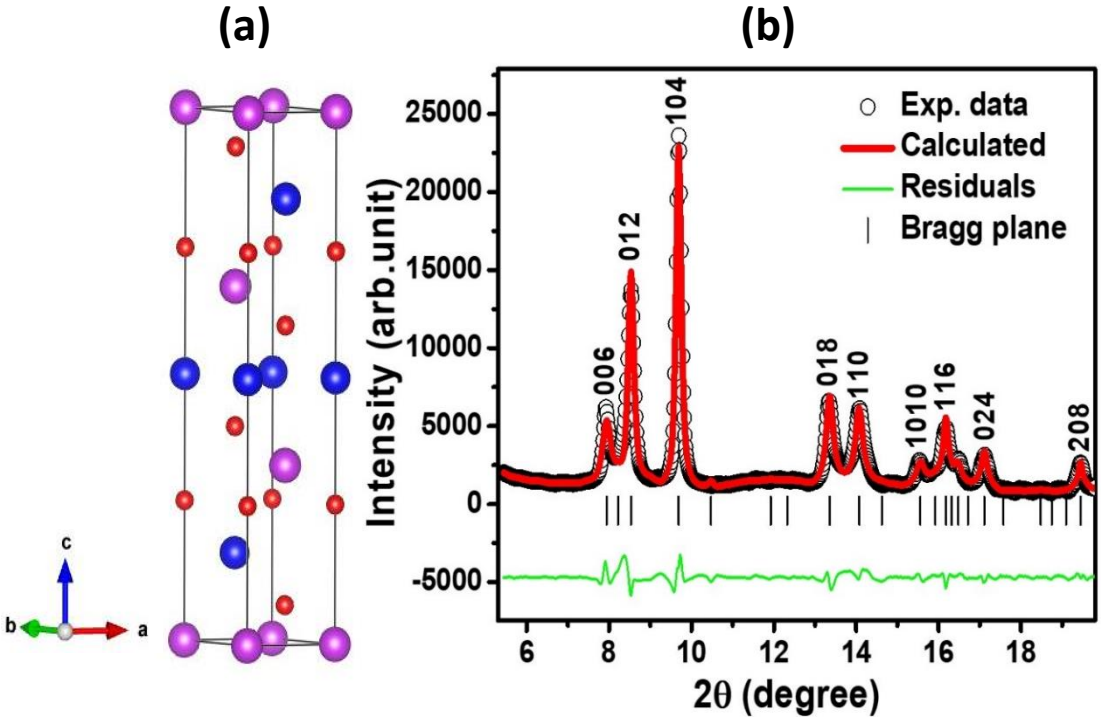

FIG. 1. (a) Unit cell of the hexagonal (supercell) phase of $TlBiS_2$ (violet, blue, and red spheres represents the Tl, Bi, and S atoms repectively) and (b) Rietveld refinement of the XRD pattern for $TlBiS_2$ at ambient conditions (λ = 0.50070 Å).

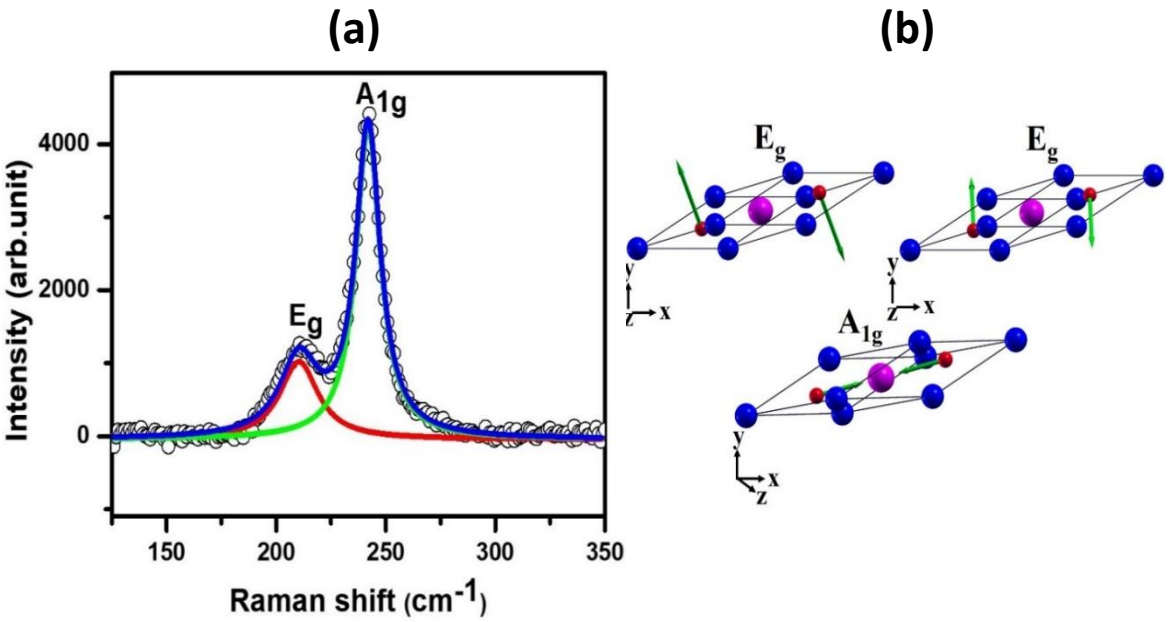

FIG. 2. (a) Experimental Raman spectrum of $TlBiS_2$ at an ambient conditions, and (b) visualization of the atomic displacement patterns for the E_g and A_{1g} modes obtained from calculations.

At ambient conditions, $TlBiS_2$ adopts the rhombohedral structure with Tl^{1+}, Bi^{3+}, and S^{2-} atoms occupying 3*a*, 3*b*, and 6*c* Wyckoff sites respectively. The schematic of the unit cell of $TlBiS_2$ is shown in the Fig. 1(a). In this centrosymmetric structure, both Bi and Tl site act as the inversion center. The Rietveld refinement of the ambient XRD pattern of $TlBiS_2$ is shown in the Fig. 1(b). The calculated lattice parameters are *a* = 4.1083 Å, *c* = 21.8660 Å, and *V* = 319.61 $Å^3$ which agrees well with the previous literature [38]. The refined atomic fractional coordinates of Tl, Bi and S are (0,0,0.5), (0,0,0) and (0,0,0.2624) respectively. Here the only free positional fractional coordinate is *z* of the S atom, and it controls the hybridizations between the two layers.

According to group theoretical analysis, the rhombohedral structure (D_{3d}^5) of $TlBiS_2$ compound has 12 zone center phonon modes:

$$\Gamma = A_{1g}+3A_{2u}+3E_u+E_g$$

Here, there are two Raman active modes ($A_{1g}+E_g$) and four infrared (IR) active modes ($2A_{2u}+2E_u$). The acoustic phonon $\Gamma_{acoustic} = A_{2u} + E_u$. The subscript g and u represents the *gerade* and *ungerade* mode respectively. Based on our DFT based phonon mode calculations, the observed Raman mode at ~211 cm^{-1} and ~242 cm^{-1} [see Fig. 2(a)] are assigned to E_g and A_{1g} symmetry respectively. The schematic of displacement patterns for phonon modes is shown in the Fig. 2(b). The comparison between the experimental and theoretical phonon frequencies are given in the Table I.

TABLE I. Raman mode assignment of the rhombohedral phase of $TlBiS_2$.

Raman mode	**Experimental frequency (cm^{-1})**	**Theoretical frequency (cm^{-1})**
E_g	211	200
A_{1g}	242	234

3.4.2 X-ray diffraction measurements under pressure

Typical XRD patterns of $TlBiS_2$ at selected pressure values up to ~6.00 GPa are shown in the Fig. 3. As evident from Fig. 3, the rhombohedral structure of $TlBiS_2$ is stable up to ~ 4.00 GPa. After that, the appearance of new Bragg peaks above ~4.00 GPa indicat-

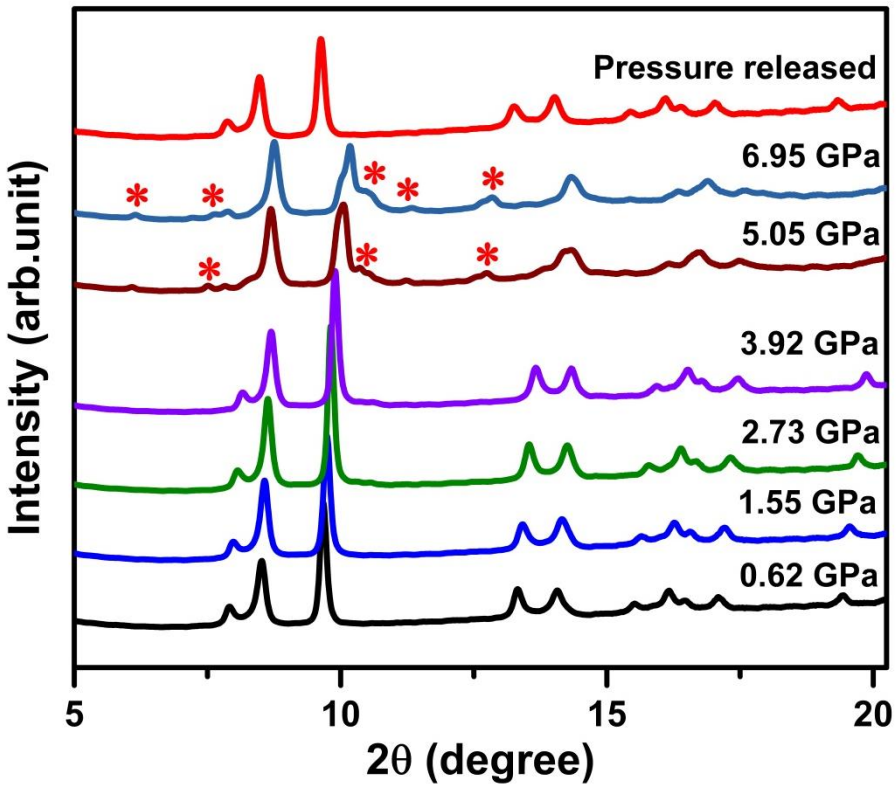

FIG. 3. Pressure dependence of the synchrotron XRD patterns (λ= 0.50070 Å) of $TlBiS_2$ at selected pressure values. The red color asterisk symbol represents the appearance of new peaks.

es the structural phase transition. The structural phase transition is fully reversible upon decreasing pressure to ambient condition (see Fig. 3). The main emphasis of the present work is only on the investigation of possible topological transition in the rhombohedral phase of $TlBiS_2$. Therefore, the detailed study of pressure induced structural phase transitions in $TlBiS_2$ compound is the future interest of our group. The presence of strong texture affects the obtained XRD patterns; hence we could not do the full Rietveld refinement reliably. However, we have done the Le Bail method fitting of the obtained XRD patterns (for each pressure values) which gives the accurate unit cell parameters (*a*, *c*, and *V*). Figures 4(a) and 4(b) represents the Le Bail fit of the synchrotron XRD pattern at ~1.55 GPa and ~3.92 GPa respectively. The pressure dependence of the lattice parameters (*a* and *c*) are shown in the Fig. 5(a). The monotonic decrease in *a* and *c* are observed under pressure up to ~4.0 GPa. The pressure dependence of the unit cell parameters (*a* and *c*) are fitted by Murnaghan

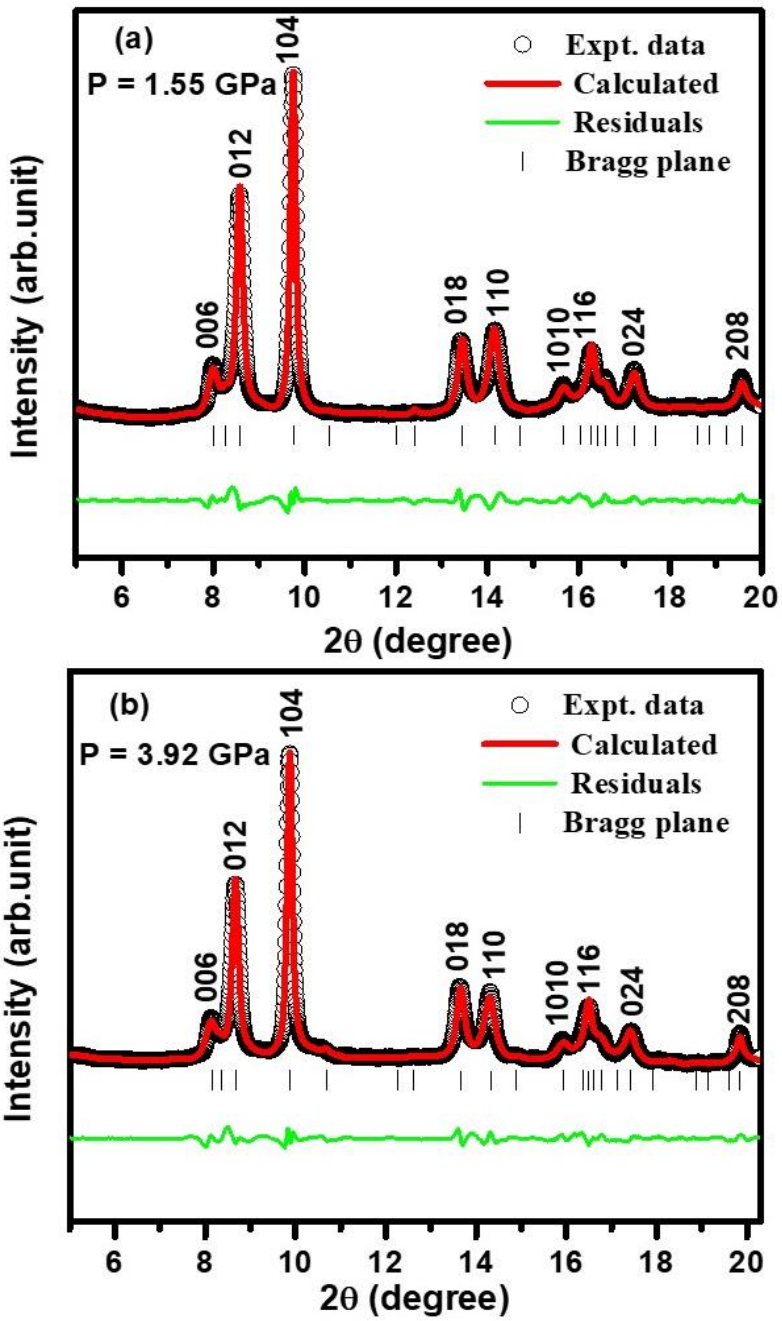

FIG. 4. Le Bail fit to the synchrotron XRD patterns (λ= 0.50070 Å) of $TlBiS_2$ at (a) 1.55 GPa and (b) 3.92 GPa.

equation of state (EOS) [39] using EOSfit7 software and the fit yields the linear compressibility of *a* axis K_a (or K_b) = 9.25 x 10^{-3} GPa^{-1} and that of *c* axis, K_c = 9.58 x 10^{-3} GPa^{-1}. The obtained values of linear compressibility suggesting us that lattice parameter *a* and *c* are having more or less similar compressibility (isotropic nature), which is consistent with the 3D nature of $TlBiS_2$ crystal structure. Further, the

systematic decreasing trend in *c/a* ratio under pressure was observed [see the inset of Fig 5(a)]. Mention must be made that there is no anomaly found in lattice parameters (*a* and *c*) and *c/a* ratio within the experimental accuracy. The pressure dependent unit cell volume data is best fitted (see Fig. 5(b)) up to ~ 4.00 GPa by Murnaghan EOS [39] (discussed in Chapter 1) and the fit yields V_0 = 319.584 $Å^3$, bulk modulus B_0 = 37.65 GPa and B_0' = 5.7. Here, the obtained value of bulk modulus (B_0 = 37.66 GPa) for $TlBiS_2$ is lower than tetradymite semiconductors [Bi_2Se_3 (B_0 = 53 GPa) [40], and Sb_2Te_3 (B_0 = 54.7 GPa) [41], and hence $TlBiS_2$ is relatively softer.

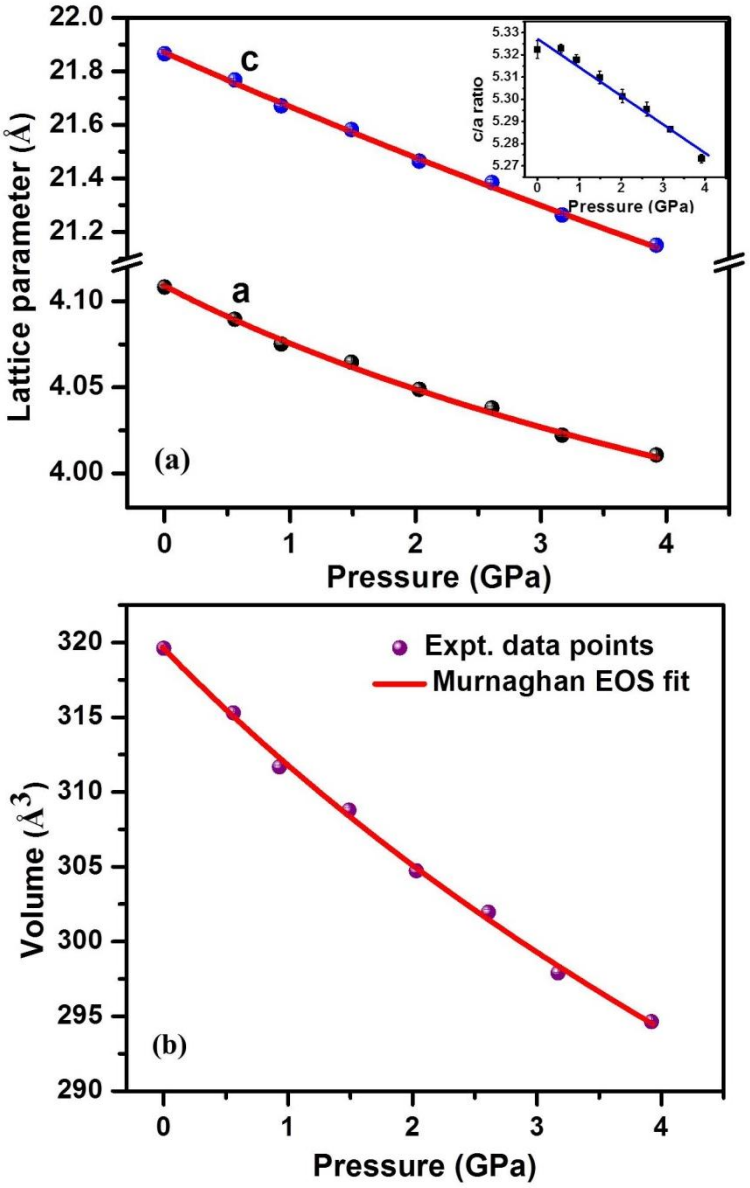

FIG. 5. (a) Pressure dependence of the lattice parameters (*a* and *c*) of $TlBiS_2$. The inset shows the *P* vs. *c/a* ratio. (b). Pressure vs. Volume of $TlBiS_2$. The red and blue solid line represents the Murnaghan EOS fit and guide to the eye respectively.

3.4.3 Raman scattering measurements under pressure

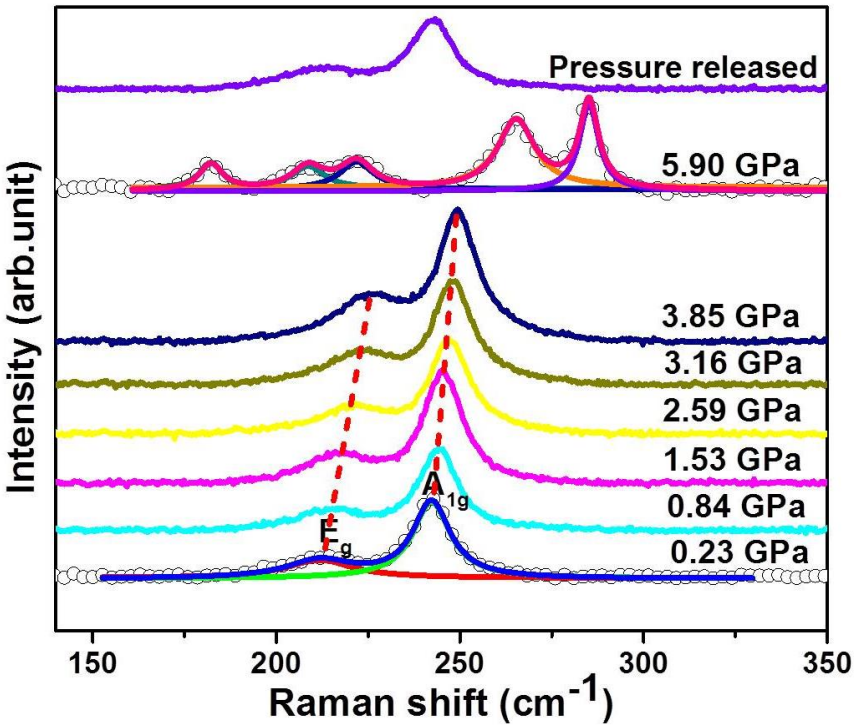

FIG. 6. Experimental Raman spectrum of $TlBiS_2$ at different selected pressures up to ~5.9 GPa.

Raman spectroscopy is a local sensitive technique which can be extensively used for studying the structural, electronic and topological transitions in the system [6,40,42,43]. So, to explore the lattice dynamical properties of the rhombohedral phase of $TlBiS_2$ compound, we have carried out the high pressure Raman scattering measurements up to ~6.0 GPa. Figure 6 represents the pressure evolution of the Raman spectrum of $TlBiS_2$ up to ~6.0 GPa. As the pressure increases, the intensity of both the modes' (E_g and A_{1g}) is increased. After ~ 4 GPa, the appearance of five new Raman peaks and disappearance of rhombohedral phase Raman active peaks (E_g and A_{1g}) indicates the structural phase transitions. Raman mode's frequency is the thermodynamic order parameter which is particularly sensitive to the type of the structural phase transition (whether 1^{st} or 2^{nd} order) under perturbations (discussed in Chapter 1). Hence, to get the more insight about this structural transition, we have analyzed the pressure dependent phonon mode frequencies up to ~6.0 GPa and plotted in Fig. 7. The sharp discontinuity at ~4.0 GPa in Fig. 7 confirms the first order structural phase transition in $TlBiS_2$ which is consistent with the XRD results. Figures

8(a) – 8(d) shows the pressure dependence of the A_{1g} and E_g modes (only the rhombohedral phase) of $TlBiS_2$ single crystal. Generally, the systematic hardening (increasing frequency) of phonon modes is expected under hydrostatic lattice compression. Here, both the modes (A_{1g} and E_g) hardening up to ~4.0 GPa with the significant change in its slope at ~1.80 GPa. The pressure dependence behavior of both the phonon modes (E_g and A_{1g}) is fitted using a linear equation for two different pressure regions (0-1.8 GPa and 1.8-4.0 GPa). The pressure coefficients and Gruneisen parameter (γ) are listed in Table II, and it can be observed that apparent changes in the pressure coefficient (a_1) of A_{1g} mode (2.5 cm^{-1} GPa^{-1} and 1.7 cm^{-1} GPa^{-1}) and E_g mode (4.0 cm^{-1} GPa^{-1} and 3.3 cm^{-1} GPa^{-1}) between 0-1.8 GPa and 1.8 GPa - 4.0 GPa regions.

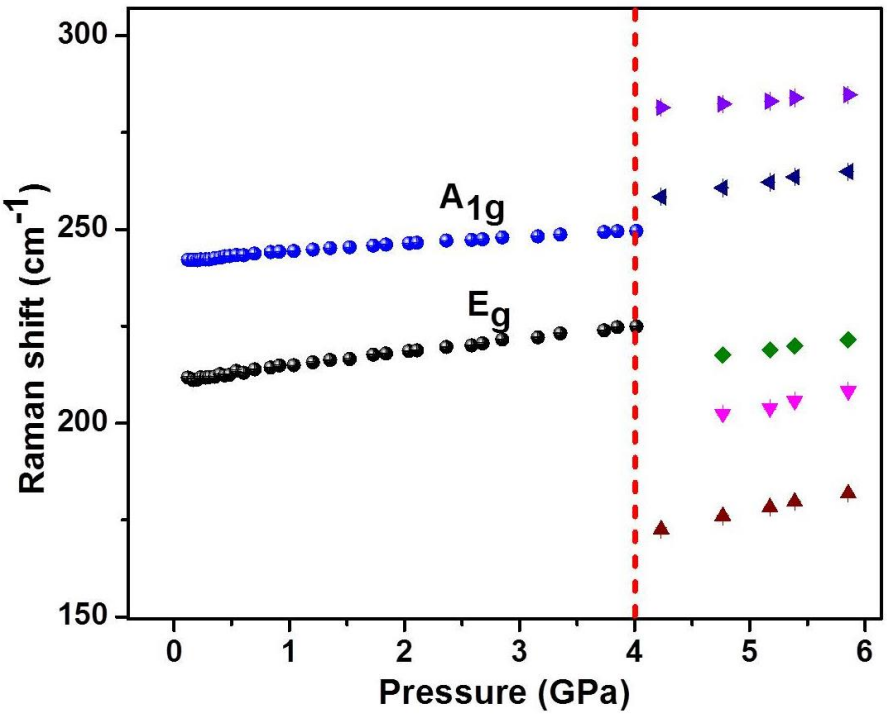

FIG. 7. Pressure dependence of the various phonon modes of $TlBiS_2$ up to ~6 GPa. The vertical dashed lines indicate the structural phase transition.

Generally, Raman linewidth is inversely proportional to the life time of the phonons for the crystalline materials. Hence, the linewidth of the Raman active phonon modes will give important information about the interactions existing in the solid system. For instance, electron-phonon, spin-phonon, and phonon-phonon coupling existing in the crystalline material and has been identified by Raman linewidth analysis [44-46]. So, to get the more detail about $TlBiS_2$, we have carefully analyzed the

linewidth as a function of pressure and represented in Figs. 8(c) and 8(d). During the increase in pressure, systematic increase in the linewidth of the Raman peak is expected from quantum uncertainty principle. However, we had observed an unusual behavior. The full width at half maximum (FWHM) of the E_g peak decreases up to ~1.8 GPa with the change in slope at ~0.5 GPa (see Fig. 8(c)). After that, the FWHM of the E_g peak increases with pressure up to ~4.0 GPa. The FWHM of A_{1g} peak almost remains constant up to ~0.5 GPa, and further, it increases with pressure. The trend in the FWHM has been reproducible over multiple experimental runs. Since the $TlBiS_2$ shows the rhombohedral phase stability (as clearly observed in synchrotron XRD results) up to ~4.0 GPa, the obtained linewidth anomalies cannot be due to the structural phase transition. So, the linewidth anomalies of A_{1g} and E_g mode at ~0.5 GPa and ~1.8 GPa indicates the isostructural electronic transition in $TlBiS_2$.

TABLE II. Experimental values of the Raman mode (E_g and A_{1g}) frequencies and its pressure coefficients at both ambient pressure and ~1.80 GPa which is obtained from fits to the data using the linear equation $\omega(P) = \omega(P_0) + a_1.(P - P_0)$. Here, $a_1 = (\frac{d\omega}{dP})$ represents the pressure coefficients (slope of the curve). The Gruneisen parameters γ are obtained by using the relation $\gamma = (\frac{B}{\omega(P0)} \times \frac{\partial\omega}{\partial P})$, where B represents the bulk modulus of $TlBiS_2$ (B_0 = 37.65 GPa).

Raman mode	**Pressure regions (GPa)**	**Mode frequency $\omega(P_0)$ (cm^{-1})**	**a_1 (cm^{-1} GPa^{-1})**	**Gruneisen parameter γ**
E_g	0 – 1.8	210.8±0.1[a]	4.0±0.1[a]	0.71
E_g	1.8 – 4.0	211.8±0.2[b]	3.3±0.1[b]	0.59
A_{1g}	0 – 1.8	241.7±0.1[a]	2.5±0.1[a]	0.39
A_{1g}	1.8 – 4.0	243.1±0.1[b]	1.7±0.0[b]	0.26

[a] Estimated at ambient pressure (P_0 = 1atm), [b] Estimated at P_0 = 1.80 GPa

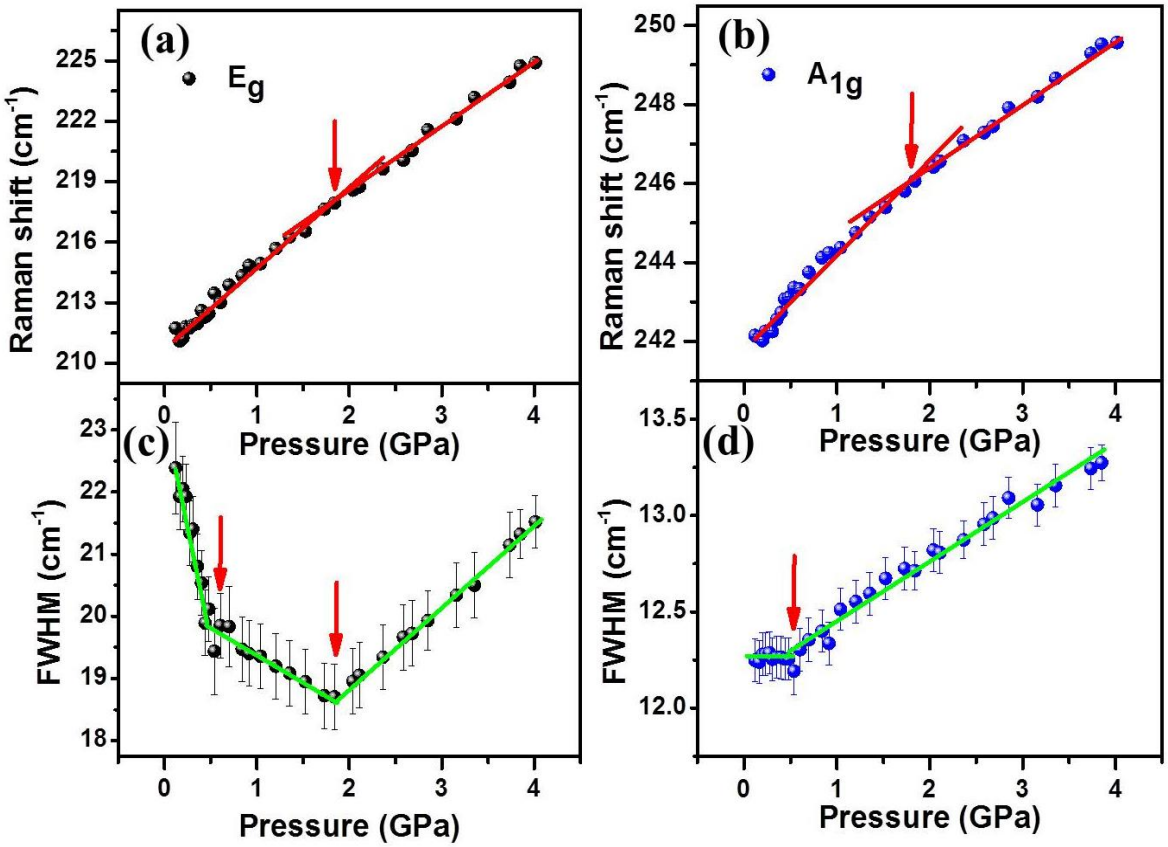

FIG. 8. (a) Pressure dependence of the frequency of A_{1g} and (b) E_g mode of $TlBiS_2$. (c) P vs. FWHM of E_g mode and (d). FWHM of A_{1g} mode. The error bars are obtained from Lorentzian fitting. The solid red and green line indicates the linear fitting and guide to the eye respectively. The red arrow represents the isostructural electronic transitions.

3.4.4 Theoretical calculations

To understand the experimentally observed Raman anomalies (isostructural transitions) at ~0.5 GPa and ~1.8 GPa, we used first-principles calculations to simulate the rhombohedral phase (SG: $R\bar{3}m$) of $TlBiS_2$ as a function of pressure. Our estimates of the optimized lattice constants of $TlBiS_2$ are a = 7.74 Å and angle α = 31.03°, which are within the typical GGA errors of experimental lattice parameters (a = 7.67 Å, α = 31.09°). The calculated internal parameter characterizing the positions of the S atoms is z = 0.261. Electronic band structure of $TlBiS_2$ calculated including spin-orbit

interaction at the optimized lattice constants reveals a direct bandgap of 0.10 eV. Band gap estimated here is slightly lower than the experimental band gap of 0.42 eV, which

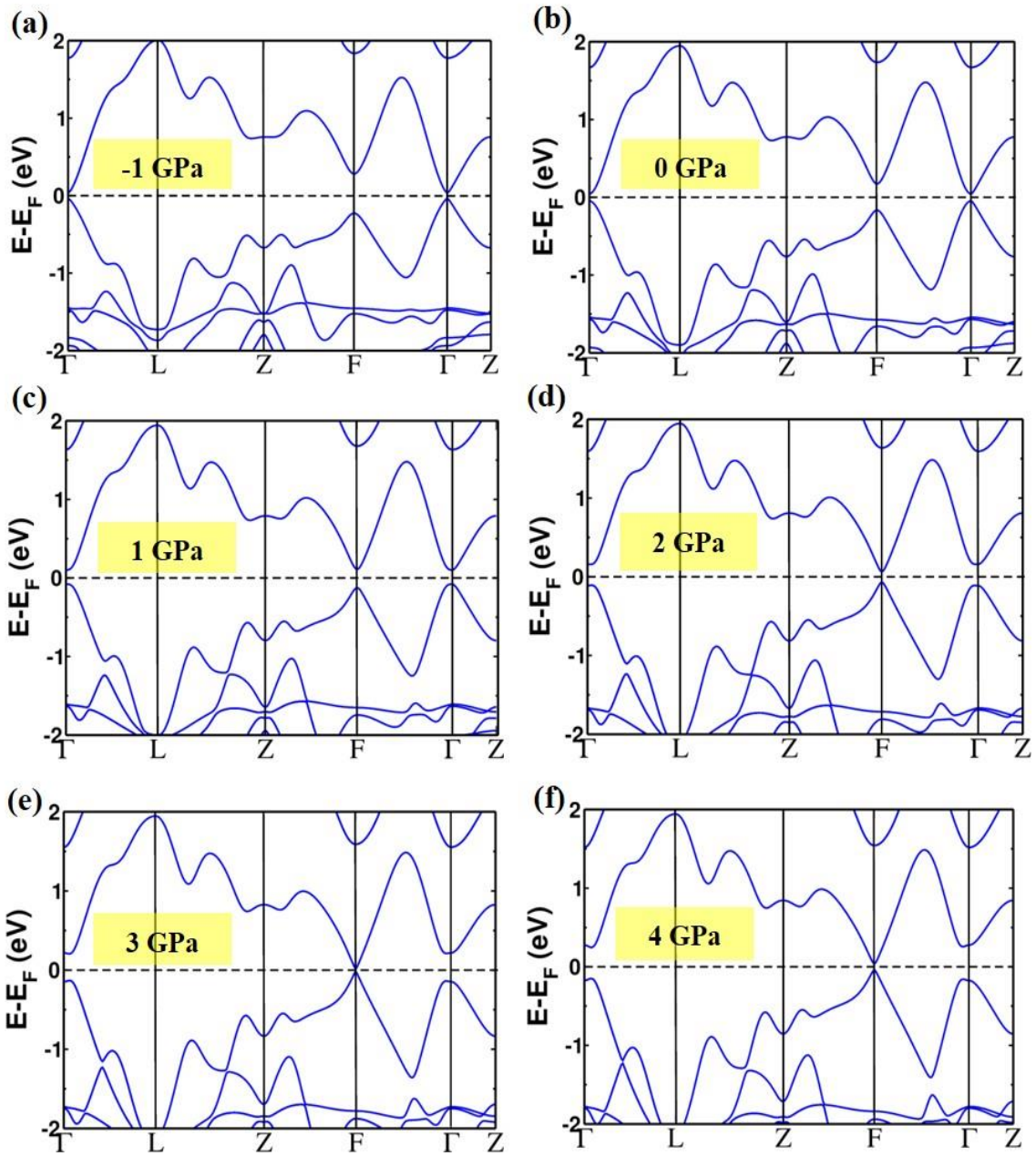

FIG. 9. (a) – (f) Electronic band structure of $TlBiS_2$ are calculated with SOC at different hydrostatic pressures (from -1 GPa to 4 GPa). Band inversion takes place at the Γ and F points in the BZ as a function of pressure near P_c^{Γ} = -0.4 GPa and P_c^{F} = 3.6 GPa, respectively.

is typical of DFT calculations of band gaps. The electronic structure of $TlBiS_2$ exhibits valleys at the Γ and F points of the BZ. The valence band maximum (VBM) at the Γ valley has higher energy than the VBM at the F valley [see Fig. 9(b)], whereas the conduction band minima (CBM) at the Γ valley is lower in energy than the CBM at the F valley. Band gaps estimated using optimized lattice constants (ambient pressure) at Γ and F points are 0.09 eV, and 0.33 eV respectively [see Fig. 9(b)]. Further, in the electronic band structure of the $TlBiS_2$ system ($R\bar{3}m$ phase), the conduction bands are dominated by p orbitals of Bi and Tl and the valence bands are dominated by the p orbitals of S.

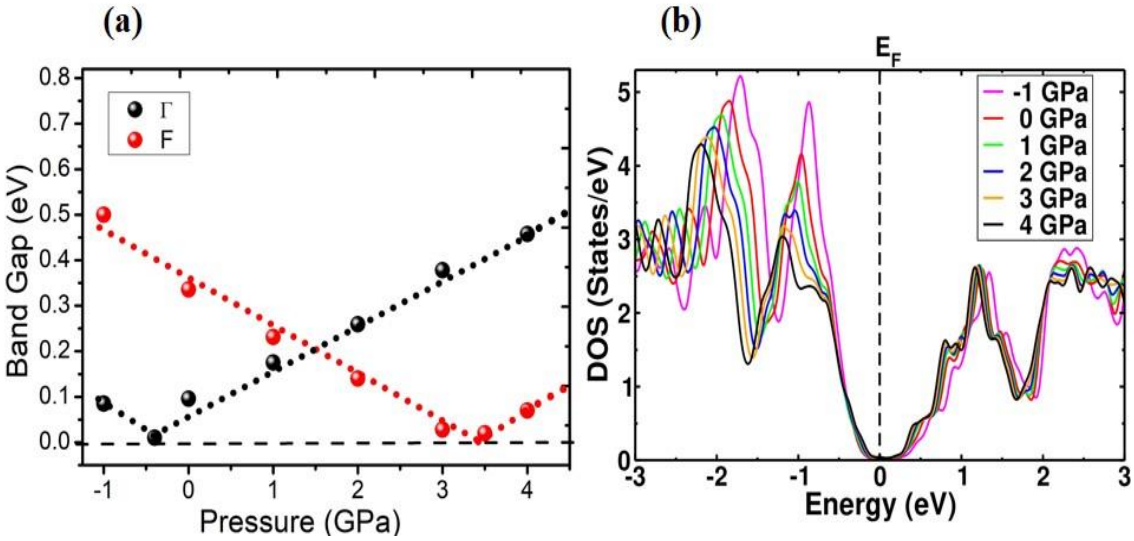

FIG. 10. (a) Evolution of band gap with hydrostatic pressure at Γ and F points showing the opening and closing of gaps at the critical pressures (P_C^{Γ} and P_C^{F}). (b) Electronic density of states of $TlBiS_2$ calculated with SOC at different hydrostatic pressures.

With increasing hydrostatic pressure, the CBM and VBM in both the valleys come closer and cross each other resulting in inversion of bands. A close examination of the electronic structure reveals that the critical pressures (P_c^{Γ} and P_c^{F}) marking band inversions at the Γ and F points are different. With increasing pressure from -1 GPa to 4 GPa, the energy gap at the Γ point first closes and then reopens at close to P ~ 0 GPa, and similar behavior is found at F point with a critical pressure close to P~ 3 GPa [see Fig. 10(a)]. These values of critical pressures (P_c^{Γ} and P_c^{F}) differ from previous calculations [22], primarily because of differences in estimated lattice constants due to different pseudopotentials, and exchange correlation functionals. Further, the pressure

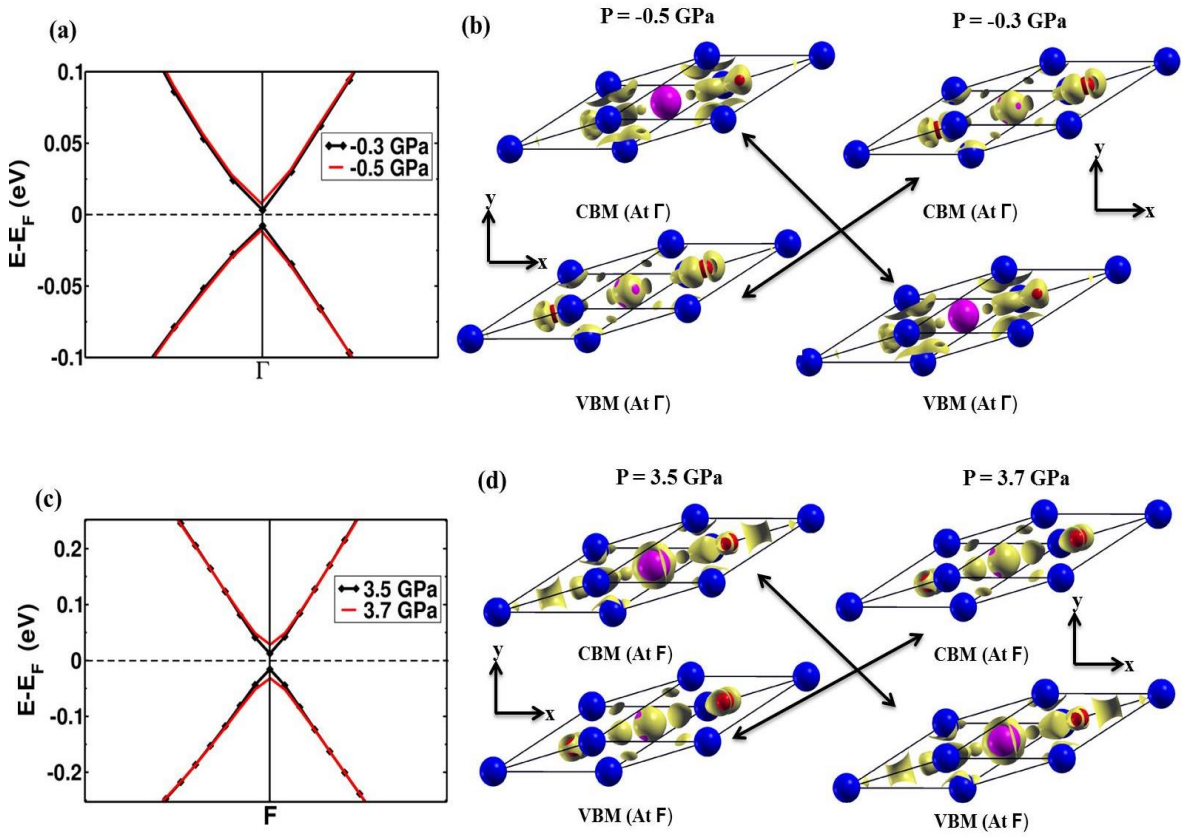

FIG. 11. Electronic structures of rhombohedral $TlBiS_2$ around the (a) Γ point and the (c) *F* point showing the band inversion between the top valence and lowest conduction bands as a function of hydrostatic pressures. (b) Isosurfaces of charge densities associated with VBM and CBM before and after the band inversion at the Γ point and the (d) *F* point reveal that the band inversion at Γ takes place in between -0.3 GPa and -0.5 GPa (i.e., -0.5 < P_c^{Γ} < -0.3 GPa, hence P_c^{Γ} ~ -0.4 GPa at Γ point), whereas the band inversion at the *F* point occurs in between 3.5 and 3.7 GPa (i.e., 3.5 < P_c^{F} < 3.7 GPa, P_c^{F} ~ 3.6 GPa at F point).

evolution of electronic density of states (DOS) is indicating the semiconducting nature of $TlBiS_2$ up to ~4.0 GPa (see Fig. 10(b)). At the Γ point, the band inversion occurs in between -0.5 and -0.3 GPa (i.e., -0.5 < P_c^{Γ} < - 0.3 GPa, hence P_c^{Γ} ~ -0.4 GPa) and it is evident in the isosurfaces of charge densities [see Fig. 11(b)] associated with VBM and CBM at -0.3 and -0.5 GPa. On the other hand, the band gap separating the VBM and CBM at the F point is higher than the gap between them at the Γ point, hence higher pressure is required for the band inversion to occur at F point. Examining the isosurfaces of charge densities associated with VBM and CBM at the F point [see Fig.

11(d)] at 3.5 and 3.7 GPa, it is clear that band inversion at the F point occurs in between 3.5 and 3.7 GPa (i.e., 3.5 < P_c^F < 3.7 GPa, hence P_c^F ~ 3.6 GPa).

3.5 Discussion

A TQPT is typically indicated by the crossing of valence and conduction bands at the critical pressures (P_c^Γ and P_c^F). To verify the change in topology due to band inversion, we determined the strong Z_2 topological index using a robust, quantitative and exact method as employed in the Z2PACK code [35]. The strong Z_2 topological invariant (υ_0) of $TlBiS_2$ calculated at -0.5 GPa and -0.3 GPa is $\upsilon_0 = 0$ (normal insulator) and $\upsilon_0 = 1$ (topological insulator) respectively. Thus Z_2 topological index confirms the change in electronic topology and establishes the non-trivial band topology of $TlBiS_2$ at pressures greater than P_c^Γ ~ -0.4 GPa. We find that the topological invariants calculated at -1, 0, 1, 2, and 3 GPa (υ_0 = 0, υ_0 =1, υ_0 =1, υ_0 =1 and υ_0 =1 respectively), are consistent with the above mentioned band inversion picture. To probe the effect of second band inversion which occurs at F point on the electronic topology we examined the Z_2 topological invariant at 3.5 GPa and 3.7 GPa. $TlBiS_2$ changes from a strong topological insulator at 3.5 GPa ($\upsilon_0 = 1$) to a system with trivial topology at 3.7 GPa ($\upsilon_0 = 0$). Thus, the Z_2 topological index based argument confirms a trivial phase resulting from even number of band inversions at the TRIM points (above 3.6 GPa).

The even number of band inversions is an indicator of the TCI phase. In our system, the band gap closes and reopens with an even number of inversions between the two extreme pressures (-0.4 GPa and 3.6 GPa). This implies that even though the phase above 3.6 GPa cannot be a Z_2 topological insulator, we obtain a TCI phase driven by the mirror symmetry of the hexagonal lattice. Hence we have calculated the mirror Chern number (n_M) as a function of pressure. The mirror Chern number (n_M) of $TlBiS_2$ calculated at 3.5 GPa and 3.7 GPa is n_M=1 and n_M=2 (TCI) respectively. Thus n_M confirms the change in electronic topology and establishes the non-trivial band topology of $TlBiS_2$ with respect to TCI phase characterized by n_M =2 at pressures greater than 3.6 GPa. In summary, ongoing from -0.5 GPa to -0.3 GPa the odd number of inversions occurring at Γ point results in a change of Z_2 topological invariant from 0 to 1. At pressures greater than 3.6 GPa i.e. following the second band inversion a total even number of inversions (3 from F and 1 from Γ) results in n_M =2 and Z_2

topological index 0. The comparison between invariant quantities Z_2 and n_M are shown in the Table III.

TABLE III. Mirror Chern number (n_M) and Z_2 topological index of $TlBiS_2$ calculated at 3.5 GPa and 3.7 GPa. The second band inversion at F around P_Γ^C ~ 3.6 GPa results in a TCI phase characterized by n_M=2 and ν_0=0 (trivial with respect to Z_2 topological insulators).

Pressure (GPa)	**Z_2 Topological index**	**Mirror Chern number (n_M)**
3.5	1	1
3.6	0	2

The experimentally observed Raman signatures of multiple isostructural electronic transitions are closely consistent with our DFT theoretical prediction. Therefore, we attribute the linewidth anomalies of A_{1g} and E_g mode at ~0.5 GPa to the non-trivial TQPT which is a consequence of band inversion at Γ of the BZ. Similarly, the phonon anomalies at ~ 1.8 GPa can be attributed to TCI phase as a consequence of even number of band inversion (3 from F and 1 from Γ) of the BZ. In both the band inversions (Γ and A points), VBM characters (dominated by S p orbitals) are exchanged with CBM characters (dominated by p orbitals of Bi and Tl). During the exchange of the orbital characters, the charge gets redistributed between VBM and CBM which further modulates the electronic structure. Consequently, here Raman active phonon (E_g and A_{1g}) life time is getting affected, which reflect the unusual electron-phonon coupling at ~ 0.5 GPa and ~ 1.8 GPa in Raman linewidth. Note that there is a small difference between the experimental (0.5 GPa and 1.8 GPa) and theoretical critical pressure values (-0.4 GPa and 3.6 GPa). This difference in the critical pressure values can arise from the various factors such as temperature, the typical error in calculated lattice parameters and band gaps (depends on the pseudo potential and exchange correlation functional), *etc*. In fact, many high pressure experiments present the mismatches of the critical pressure values with first principle theoretical calculations [45,46] that could mainly originate from various approximations used in the theoretical approach. For example, theoretical calculations

predict the transition pressure of band inversions at L and A point of the BZ in 1T-$TiTe_2$ at ~0.88 GPa, and ~3.40 GPa, however experimentally phonon anomalies are noticed at ~ 2.0 GPa and ~4.0 GPa respectively [46]. Similarly, in BiTeI, the topological phase transition points (as a consequence band inversion at A points) are calculated to be 1.7 GPa and 4.1 GPa corresponding to the calculation based on local density approximations (LDA) and GGA respectively [47]. But, experimentally observed transition point is ~2.0-2.9 GPa [4]. These two above examples demonstrate the commonly observed mismatch between the high pressure experimental and theoretical transition pressure values. However, we have clearly seen two isostructural electronic transitions through Raman phonon anomalies at ~0.5 GPa, and ~1.8 GPa within the stability range of the rhombohedral symmetry of $TlBiS_2$ compound and the transition pressure values qualitatively agree with the DFT based theoretical predictions (-0.4 GPa and 3.6 GPa).

Even though the non-trivial topological phase of $TlBiS_2$ was predicted at 0 GPa (ambient condition), ARPES measurements reveal that $TlBiS_2$ is a direct band gap semiconductor (E_g = 0.42 eV) and is topologically trivial (Z_2 = 0) at ambient condition [24]. The obvious reason for this contradiction is the under estimation of the band gap using GGA. So, the direct observation (using ARPES) [24] of the band gap (E_g = 0.42 eV) clearly suggesting that first band inversion has to occur at above 0 GPa and consistent with our experimental results. Therefore, the applied pressure increases the effective strength of the SOC, decreases band gap and at a critical pressure point (~0.5 GPa) a phase transition takes place from topologically trivial to nontrivial state as a consequence of the first band inversion at the Γ point. Further, the evolution of electronic structure with hydrostatic pressure corroborates that $TlBiS_2$ remains as a direct band gap semiconductor up to 4 GPa and has bulk calculated band gaps of 0.10, 0.17, 0.14, 0.03, 0.07 and 0.19 eV for pressures of 0, 1, 2, 3 and 4 GPa respectively. At pressure P ~ 2 GPa, we observe a shift in the CBM and VBM at the Γ to those at the F point. With increasing hydrostatic pressure, the Fermi level [marked with the dashed horizontal black line in Figs. 9(a) - 9(f)] does not cross the top valence band and bottom conduction band indicating that $TlBiS_2$ does not undergo a semiconductor to metal phase transition.

The pressure dependent electronic band structure (calculated) of $TlBiS_2$ reveals that there is no overlap near the Fermi energy across any other directions of the BZ, except two successive band inversions at Γ and F point. This feature might be very interesting because the electronic contribution from the band inversions (only) can be understood in detail by transport measurements. It is noteworthy that, four consecutive bands inversions are predicted in 1T-$TiTe_2$ under hydrostatic pressure [48], and experimentally two band inversions are claimed by phonon and electrical transport anomalies [46]. However, in 1T-$TiTe_2$, the electronic bands are crossing over other direction of the BZ (in addition to band inversion points) near the Fermi energy which makes the system quite difficult to deal with transport tools for only studying the topological contributions. So, here the successive band inversions and clean band structure (under pressure evolution) make the $TlBiS_2$ system unique and it is material specific. Hence, the $TlBiS_2$ compound could be an ideal candidate for exploring much exciting physics behind topology, and its effect in multiple properties. Conclusively, the two isostructural electronic transitions at ~0.5 GPa and ~1.80 GPa are evidenced from unusual electron-phonon coupling and attributed to non-trivial TQPT and TCI transition respectively, based on first principles theoretical calculations. Further, the larger atomic mass (Tl and Bi), the narrow band gap semiconducting nature of $TlBiS_2$ compound (up to ~4.0 GPa) and multiple band inversions (topological phase transitions) can be expected to give a good thermoelectric performance under pressure. Besides, the existence of topological states ($Z_2 = 1$) in $TlBiS_2$ at relatively low pressure regions from 0.5 GPa to 1.8 GPa (experimentally accessible pressure regions), hence this system may be useful for next generation spintronic and thermoelectric devices operating in the mechanically strained environment. Finally, we hope our interesting results will stimulate research interest on $TlBiS_2$, particularly for Shubnikov de Haas oscillation measurement under pressure [11] which may provide further insight into observed TQPT.

3.6 Conclusions

In summary, a combination of high pressure Raman scattering and synchrotron diffraction measurements confirms that $TlBiS_2$ undergoes a first order structural phase transition at ~4.0 GPa. Furthermore, the A_{1g} and E_g phonon linewidth anomalies at ~0.5 GPa and ~1.8 GPa are observed due to unusual electron-phonon coupling in the

rhombohedral phase of $TlBiS_2$. We have attributed the two isostructural electronic transitions at ~0.5 GPa and ~1.80 GPa respectively to the non-trivial TQPT (Z_2 = 1) and TCI (n_M = 2) transitions based on our first principles theoretical calculations. More precisely, applied hydrostatic pressure systematically tunes the electronic states of $TlBiS_2$ from a normal semiconductor at ambient conditions to a topological insulator ~0.5 GPa and then to a TCI at ~1.8 GPa. We are sure that our results will motivate further research interest in $TlBiS_2$ on the aspect of quantum oscillations measurements under pressure.

3.7 Bibliography

1. M. Z. Hassan and C. L. Kane, Rev. Mod. Phys. **82**, 3045 (2010).
2. Y. L. Chen, J. G. Analytis, J. H. Chu, Z. K. Liu, S. K. Mo, X. L. Qi, H. J. Zhang, D. H. Lu, X. Dai, Z. Fang, S. C. Zhang, I. R. Fisher, Z. Hussain, and Z. X. Shen, Science **325**, 178 (2009).
3. D. Hsieh, Y. Xia, L. Wray, D. Qian, A. Pal, J. H. Dil, J. Osterwalder, F. Meier, G. Bihlmayer, C. L. Kane, Y. S. Hor, R. J. Cava, and M. Z. Hasan, Science **323**, 919 (2009).
4. X. Xi, C.Ma, Z. Liu, Z. Chen,W. Ku, H. Berger, C.Martin, D. B. Tanner, and G. L. Carr, Phys. Rev. Lett. **111**, 155701 (2013).
5. A. Ohmura, Y. Higuchi, T. Ochiai, M. Kanou, F. Ishikawa, S. Nakano, A. Nakayama, Y. Yamada, and T. Sasagawa, Phys. Rev. B **95**, 125203 (2017).
6. A. Bera, K. Pal, D. V. S. Muthu, S. Sen, P. Guptasarma, U. V. Waghmare, and A. K. Sood, Phys. Rev. Lett. **110**, 107401 (2013).
7. Yu. S. Ponosov, T. V. Kuznetsova, O. E. Tereshchenko, K. A. Kokh, and E. V. Chulkov, JETP Lett. **98**, 557 (2013).
8. P. P. Kong, F. Sun, L. Y. Xing, J. Zhu, S. J. Zhang, W. M. Li, Q. Q. Liu, X. C. Wang, S. M. Feng, X. H. Yu, J. L. Zhu, R. C. Yu, W. G. Yang, G. Y. Shen, Y. S. Zhao, R. Ahuja, H. K. Mao, and C. Q. Jin, Sci. Rep. **4**, 6679 (2014).
9. K. Saha, K. Légaré, and I. Garate, Phys. Rev. Lett. **115**, 176405 (2015).
10. Y. Chen, X. Xi, W. Yim, F. Peng, Y. Wang, H. Wang, Y. Ma, G. Liu, C. Sun, C. Ma, Z. Chen, and H. Berger, J. Phys. Chem. C **117**, 25677 (2013).
11. J. Park, K. H. Jin, Y. J. Jo, E. S. Choi, W. Kang, E. Kampert, J. S. Rhyee, S. H. Jhi, and J. S. Kim, Sci. Rep. **5**, 15973 (2015).

12. I. Efthimiopoulos, J. Zhang, M. Kucway, C. Park, R. C. Ewing, and Y. Wang, Sci. Rep. **3**, 2665 (2013).
13. J. C. Y. Teo, L. Fu, and C. L. Kane, Phys. Rev. B **78**, 045426 (2008).
14. L. Fu, Phys. Rev. Lett. **106**, 106802 (2011).
15. Y. Tanaka, Z. Ren, T. Sato, K. Nakayama, S. Souma, T. Takahashi, K. Segawa, and Y. Ando, Nat. Phys. **8**, 800 (2012).
16. T. H. Hsieh, H. Lin, J. Liu, W. Duan, A. Bansil, and L. Fu, Nat. Commun. **3**, 982 (2012).
17. H. Zhang, C.X. Liu, X. L. Qi, X. Dai, Z. Fang and S.C. Zhang, Nat. Phys. **5**, 438 (2009).
18. Y. Xia, D. Qian, D. Hsieh, L. Wray, A. Pal, H. Lin, A. Bansil, D. Grauer, Y. S. Hor, R. J. Cava and M. Z. Hasan, Nat. Phys. **5**, 398 (2009).
19. D. Hsieh, Y. Xia, D. Qian, L. Wray, F. Meier, J. H. Dil, J. Osterwalder, L. Patthey, A. V. Fedorov, H. Lin, A. Bansil, D. Grauer, Y. S. Hor, R. J. Cava and M. Z. Hasan, Phys. Rev. Lett. **103**, 146401 (2009).
20. W. Liu, X. Peng, C. Tang, L. Sun, K. Zhang and J. Zhong, Phys. Rev. B **84**, 245105 (2011).
21. Y. L. Chen, Z. K. Liu, J. G. Analytis, J. H. Chu, H. J. Zhang, B. H. Yan, S. K. Mo, R. G. Moore, D. H. Lu, I. R. Fisher, S. C. Zhang, Z. Hussain and Z. X. Shen, Phys. Rev. Lett. **105**, 266401 (2010).
22. Q. Zhang, Y. Cheng and U. Schwingenschlögl, Sci. Rep. **5**, 8379 (2015).
23. R. J. Cava, H. Ji, M. K. Fuccillo, Q. D. Gibson and Y. S. Hor, J. Mater. Chem. C **1** , 3176 (2013).
24. T. Sato, K. Segawa, K. Kosaka, S. Souma, K. Nakayama, K. Eto, T. Minami, Y. Ando and T. Takahashi, Nat. Phys. **7**, 840 (2011).
25. J. C. Chervin, B. Canny and M. Mancinelli, High Pressure Res. **21**, 305 (2001).
26. S. Klotz, J. C. Chervin, P. Munsch and G. L. Marchand, J. Phys. D: Appl. Phys. **42**, 075413 (2009).
27. A. P. Hammersley, S. O. Svensson, M. Hanfland, A. N. Fitch and D. Hausermann, High Pressure Res. **14** , 235 (1996).
28. J. Rodríguez-Carvajal, Physica B **192**, 55 (1993).

29. Quantum-ESPRESSO is a community project for high-quality quantum-simulation software, based on density-functional theory, and coordinated by P. Giannozzi. See http://www. quantum-espresso.org and http://www.pwscf.org.
30. X. Hua, X. Chen and W. A. Goddard, Phys. Rev. B **55**, 16103 (1997).
31. J. P. Perdew, K. Burke and M. Ernzerhof, Phys. Rev. Lett. **77**, 3865 (1996).
32. G. Kresse and D. Joubert, Phys. Rev. B **59**, 1758 (1999).
33. A. Dal Corso, Comput. Mat. Sci. **95**, 337 (2014).
34. S. Baroni, S. de Gironcoli, A. Dal Corso and P. Giannozzi, Rev. Mod. Phys. **73**, 515 (2001).
35. D. Gresch, G. Autès, O. V. Yazyev, M. Troyer, D. Vanderbilt, B. A. Bernevig and A. A. Soluyanov, Phys. Rev. B **95**, 075146 (2017).
36. A. A. Soluyanov and D. Vanderbilt, Phys. Rev. B **83**, 235401 (2011).
37. J. Bhattacharjee and U. V. Waghmare, Phys. Rev. B **71**, 045106 (2005).
38. C. L. Teske, and W. Bensch, Acta Cryst. E **62**, i163 (2006).
39. F. D. Murnaghan, Proc. Nat. Acad. Sci. USA **30**, 244 (1944).
40. R. Vilaplana, D. Santamaría-Pérez, O. Gomis, F. J. Manjón, J. González, A. Segura, A. Muñoz, P. Rodríguez-Hernández, E. Pérez-González, V. Marín-Borrás, V. Muñoz-Sanjose, C. Drasar and V. Kucek, Phys. Rev. B **84**, 184110 (2011).
41. M. Yanmei, L. Guangtao, Z. Pinwen, W. Hui, W. Xin, C. Qiliang, L. Jing and M. Yanming, J. Phys.: Condens. Matter **24**, 475403 (2012).
42. V. Rajaji, S. Janaky, Saurav Ch. Sarma, Sebastian C. Peter, and Chandrabhas Narayana (Accepted in J. Phys.: Condens. Matter – doi: 10.1088/1361-648X/ab01bb).
43. V. Rajaji, K. Pal, S. C. Sarma, B. Joseph, S. C. Peter, U. V. Waghmare and C. Narayana, Phys. Rev. B **97**, 155158 (2018).
44. M. Cardona, High Pressure Res. **24**, 17 (2004).
45. V. Rajaji, P. S. Malavi, S. S. R. K. C. Yamijala, Y. A. Sorb, U. Dutta, S. N. Guin, B. Joseph, S. K. Pati, S. Karmakar, K. Biswas and C. Narayana, Appl. Phys. Lett. **109**, 171903 (2016).
46. V. Rajaji, U. Dutta, P. C. Sreeparvathy, S. C. Sarma, Y. A. Sorb, B. Joseph, S. Sahoo, S. C. Peter, V. Kanchana and C. Narayana, Phys. Rev. B **97**, 085107 (2018).

47. M. S. Bahramy, B. J. Yang, R. Arita and N. Nagaosa, Nat. Commun. **3**, 679 (2012).
48. Q. Zhang, Y. Cheng and U. Schwingenschlögl, Phys. Rev. B **88**, 155317 (2013).

Chapter 4

Switching of the topologically non-trivial and trivial quantum phase transitions in compressed 1T-$TiTe_2$

The author's main contribution in this chapter is the core research idea, performing the high pressure Raman and synchrotron XRD measurements on 1T-$TiTe_2$ sample and analyzing the data. To execute this research problem, we have collaborated with Prof. Sebastian C. Peter's group, JNCASR, Bangalore for sample synthesis, Dr. S. Karmakar's group, BARC, Mumbai for electrical transport measurements and Prof. V. Kanchana's group, IIT Hyderabad for first the principles theoretical calculations.

V. Rajaji, Utpal Dutta, P. C. Sreeparvathy, Saurav Ch.Sarma, Y. A. Sorb, B. Joseph, Subodha Sahoo, Sebastian C. Peter, V. Kanchana, and Chandrabhas Narayana, *"Structural, vibrational, and electrical properties of 1T-$TiTe_2$ under hydrostatic pressure: Experiments and theory" Phys. Rev. B* **97**,085107 (2018).

4.1 Introduction

Titanium-based transition-metal dichalcogenides (TMDs) TiX_2 (X = Te, Se, and S) crystallize in layered hexagonal structure (SG $P\bar{3}m1$, No. 164) which shows exotic properties such as charge density wave, superconductivity, *etc* [1,2]. Among these $TiTe_2$ has recently received significant interest due to its series of topological transitions under moderate pressures and potential usage in information processing [3,4]. The unit cell of 1T-$TiTe_2$ consists of stacks of hexagonal close packed layers of Ti metal atoms sandwiched between two adjacent layers of Te atoms and in each layer, the Ti atom is octahedrally surrounded by six Te atoms. It has predominately weak van der Waals-type interlayer bonding forces along the *c* axis and strong intralayer covalent bonds along the *ab* plane. First principles calculations based on density functional theory (DFT) predicted a series of pressure-induced transitions between topologically trivial and non-trivial phases related to the band inversions at different points (L, M and Γ) of the Brillouin zone in $TiTe_2$ [4]. This remarkable theoretical prediction strongly motivated us to explore the pressure-induced topological changes in $TiTe_2$ compound through XRD, Raman scattering, and electrical transport measurements. The basic idea of using the Raman scattering and synchrotron XRD to study the topological phase transitions has been discussed in Chapter 3 (section 3.1). Also, the introduction and importance of TQPT has been discussed in Chapters 1 (section 1.7.2.3) and 3 (section 3.1).

In this chapter, we present the structural, vibrational and electrical transport properties of 1T-$TiTe_2$ under hydrostatic compression. The synchrotron XRD, Raman scattering, and electrical transport anomalies show signatures of the two iso-structural electronic transitions at ~ 2 GPa and ~ 4 GPa in the 1T phase, which we have attributed to the non-trivial TQPT and the trivial metallic transition, respectively, based on a recent theoretical report [4]. Further, the applied pressure switches the 2D layered material (anisotropic) to an isotropic 3D crystal above ~ 4 GPa through charge density overlapping between the interlayer Te atoms along the *c* axis. The experimental evidence of isotropic 3D behavior (constant *c/a* ratio) was explained using first-principles theoretical calculations. This is followed by the 1T phase undergoing a pressure-induced structural transition from trigonal (SG $P\bar{3}m1$) to monoclinic (SG $C2/m$) phase at ~ 8 GPa. Finally, the theoretically calculated pressure-dependent

electronic band structure and Fermi surface show the occurrence of an electronic topological transition (ETT) at 9 GPa (close to the experimental value ~8 GPa) in the 1T phase.

4.2 Experimental details

The 1T phase of $TiTe_2$ was synthesized by mixing 0.1579 g of titanium shots (99.99 %, Alfa Aesar) and 0.8420 g of tellurium shots (99.99 %, Alfa Aesar) in a 9 mm diameter quartz tube. The tube was flame-sealed under a vacuum of 10^{-3} Torr, achieved with the help of a rotary pump, to prevent oxidation during heating. The tube was then placed in a vertically aligned tube furnace and heated to 800 °C over a period of 8 h to allow proper homogenization. Subsequently, the temperature was kept constant for 6 days. Finally, the system was allowed to cool to room temperature over a period of 10 h. No reaction with the quartz tube was observed. A black polycrystalline $TiTe_2$ was formed.

Raman spectra were recorded using a WITec micro Raman spectrometer (UHTS600) in the backscattering geometry (180°). The Raman spectrometer was equipped with a diode-pumped frequency-doubled Nd:YAG solid state laser (wavelength λ = 532 nm), 600 mm focal length monochromator, and Peltier air-cooled CCD detector. The spectral resolution was about ~ 0.5 cm^{-1} for a grating of 2400 lines per mm. The *in situ* high-pressure Raman scattering measurements were performed using a membrane-type diamond anvil cell (MDAC) with a culet size of 400 μm. The procedures of gasket preparation, PTM and pressure calibration is the same as discussed in Chapters 2 and 3 (section 3.2). The accumulation time of each Raman spectrum was about 5 minutes. A lower value of laser power (< 0.5 mW) was maintained to avoid the risk of heating and oxidation of the samples.

The *in situ* high-pressure synchrotron XRD experiments were carried out using a Mao-Bell type DAC with diamonds having a culet size of 400 μm. The synchrotron XRD measurement and analysis details are the same as discussed in Chapter 3 (section 3.2). Further, pressure-dependent electrical resistance was measured up to ~ 16 GPa at room temperature with the standard quasi-four probe method using a miniature DAC and an ac-resistance bridge in combination with fine gold electrodes fabricated on the diamond culet. The sample and electrodes were insulated from the metal gasket using

an insulation layer of Al_2O_3 and epoxy mixture. The sample pressure was measured with the *in situ* ruby fluorescence method at room temperature [5]. Powdered NaCl was used as the PTM which not only maintains quasi-hydrostaticity but also keeps the electrodes in good contact with the sample.

4.3 Computational method

The calculations were carried out within the frame work of DFT implemented in the CASTEP and WIEN2k packages [6,7]. The experimental parameters are considered as an input, and the structure was optimized using the Broyden- Fletcher-Goldfarb-Shanno (BFGS) minimization scheme [8]. The optimized structure was used to calculate the bonding and electronic structure properties, which was performed using the WIEN2k package with the generalized gradient approximation of Perdew, Burke, and Ernzerhof (GGA-PBE) functional [9]. Considering the presence of heavy elements we have included spin-orbit coupling in the calculations. A dense k mesh of 39× 39×19 was used and all the calculations were performed with the optimized lattice parameters with an energy convergence criterion of 10^{-6} Ry per formula unit. Raman spectra were calculated with the CASTEP package.

4.4 Results

4.4.1 Characterization of $TiTe_2$ at ambient conditions

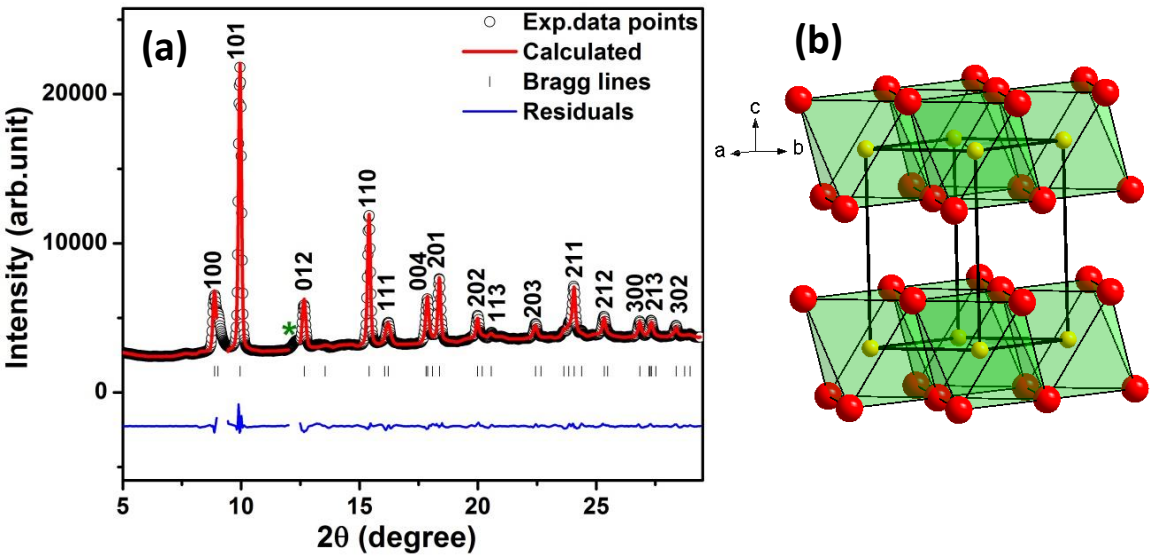

FIG. 1 (a) Rietveld refinement of the synchrotron XRD pattern of 1T-$TiTe_2$ at ~ 0.36 GPa and (b) schematics of the unit cell of 1T-$TiTe_2$. The yellow and red spheres represent the Ti and Te, respectively.

The Rietveld refinement of the XRD pattern for the $P\bar{3}m1$ structure (referred to as the 1T phase) as shown in Fig. 1(a). The calculated cell parameters and volume at ~ 0.36 GPa are a = 3.76416 Å, c = 6.46711 Å and V = 79.355 $Å^3$ respectively, which show good agreement with the 1T phase of the previous report at ambient conditions [10,11]. The typical unit cell for the 1T structure is shown in Fig. 1(b). There are three atoms in the unit cell of 1T-$TiTe_2$, where Ti^{4+} and Te^{2-} atoms occupy 1*a* and 2*d* Wyckoff sites, respectively. Further, the presence of a small elemental Te has been detected in the synchrotron pattern and is indicated by green asterisk symbols in Fig. 1(a). We have carefully excluded the Te regions during the refinements.

According to group-theoretical analysis, the layered 1T structure of $TiTe_2$ has nine vibrational modes at the gamma point of the phonon dispersion curve [12,13];

$$\Gamma = E_g + A_{1g} + 2E_u + 2A_{2u}$$

where, the *gerade* (E_g and A_{1g}) and *ungerade* (E_u and A_{2u}) modes represent the Raman-active and IR-active phonon modes, respectively. In this centro-symmetric structure, the doubly degenerate E_g mode (symmetric in-plane bending) represents the atomic vibrations along the ab plane whereas the A_{1g} mode (symmetric out of plane stretching) represents the atomic vibrations parallel to the *c* axis as shown in Fig. 2.

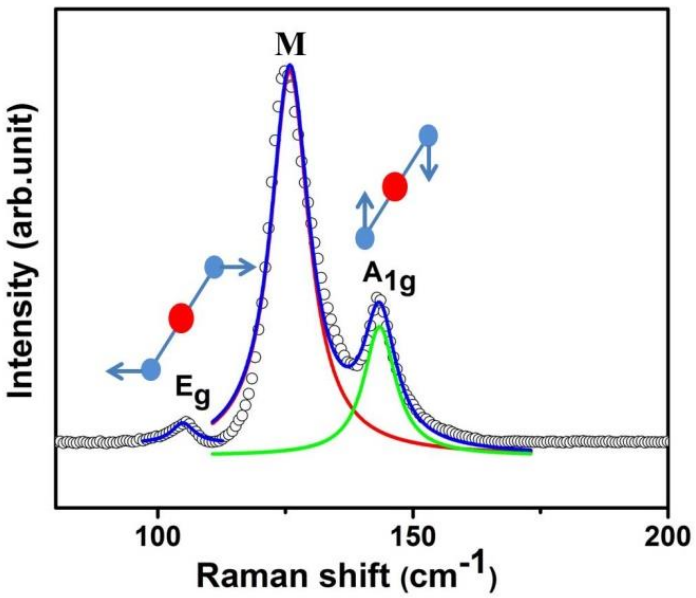

FIG. 2. Raman spectrum of 1T-$TiTe_2$ at ambient conditions.

TABLE I. The assignment of the Raman modes for 1T-$TiTe_2$.

Raman mode	Experimental frequency (cm^{-1})			Theoretical frequency (cm^{-1})		
	This work	Ref.14[a]	Ref.3[b]	This work	Ref.13	Ref.12
E_g	105	102	-	100	105	99.1
M	126	-	124	-	-	-
A_{1g}	143	145	145	140	150	145.1

[a] single crystal, [b] few layers

Raman modes were fitted using the Lorentzian line shape function. Based on our theoretical calculation and the existing literature, the phonon modes at ~ 105 cm^{-1} and ~ 143 cm^{-1} are assigned to E_g and A_{1g} symmetry respectively [12-14]. However, we observed an additional strong mode at ~126 cm^{-1}, named the M mode. This mode was seen in a few layers of $TiTe_2$ grown as a thin film by Khan *et al*., and was attributed to E_g symmetry [3]. This assignment seems to be unreliable since a polarization-dependent study on single crystals confirmed that the selection rule allowed two Raman-active modes (E_g and A_{1g}) and its energies are ~102 cm^{-1} and ~145 cm^{-1}, respectively [14]. Recent accurately calculated vibrational modes of $TiTe_2$ closely match with our assignment [12]. Hence this M mode could be a zone-folded Raman-active mode and has been observed in proto type 1T phase layered TMD materials at different conditions [15-17]. However, the polarization and temperature dependent behavior of this mode (M) in the few layers may give more insight into this mode, which is the subject of future interest. The detailed comparative analysis of vibrational energies for the 1T-$TiTe_2$ compound is shown in Table I.

4.4.2 Synchrotron XRD measurements under pressure

In situ high-pressure synchrotron XRD measurements were carried out up to ~16 GPa and the representative XRD plots for selected pressures are shown in Fig. 3. The systematic increase in the Bragg peaks to higher diffraction angle (2θ) is consistent with the compression of the unit cell. Furthermore, the appearances of new Bragg peaks at ~ 12.0 GPa indicate structural transition. However, the onset of the phase transition point can be traced to ~ 8 GPa via the (101) Bragg peak analysis (by peak fit-

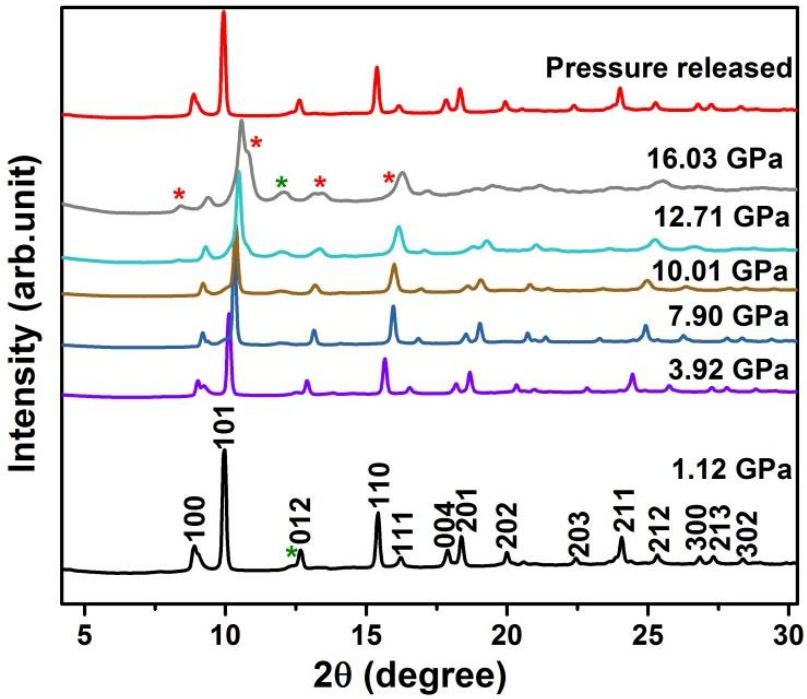

FIG. 3. Pressure evolution of the synchrotron XRD patterns of $TiTe_2$ at selected pressure values. The red asterisk symbol represents the appearance of new Bragg peaks at higher pressure regions.

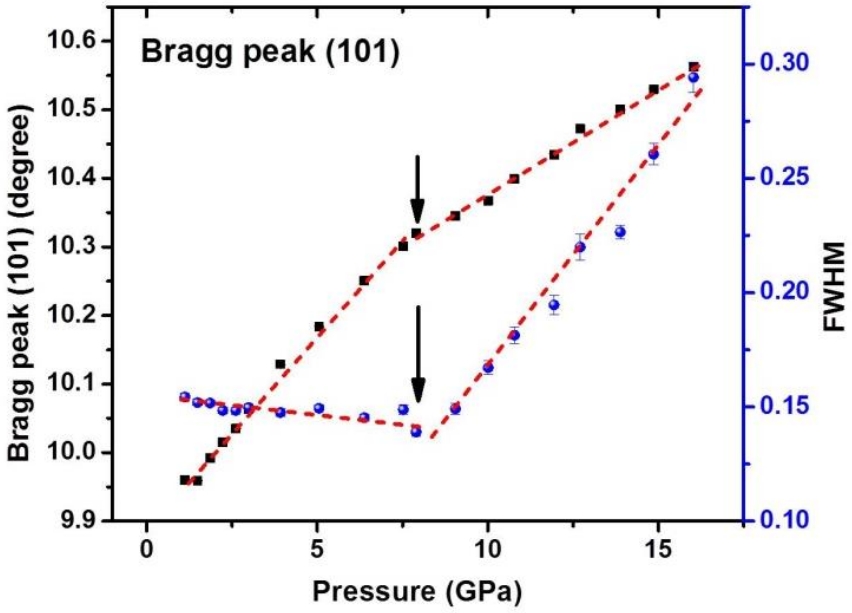

FIG. 4 Pressure dependent angle (2θ) and FWHM of (101) Bragg peak for the 1 T phase. The black arrow at ~ 8 GPa indicates the onset of structural phase transition.

ing) as shown in Fig. 4. By comparing our XRD patterns (Fig.3) with proto type compounds such as $IrTe_2$ and ZrS_2 (CdI_2 type structure), we found that $TiTe_2$ follows

an identical structural sequence to $IrTe_2$ and ZrS_2 under high-pressure [18,19]. Notably, a distinct splitting of the (101) Bragg peak observed in $TiTe_2$ is exactly in agreement with $IrTe_2$ and ZrS_2 [18,19]. Even though a new high-pressure phase appears in $TiTe_2$, the ambient phase coexists up to ~ 16.0 GPa, the maximum pressure reached in this study. The structural evolution of the Te phase (shown as the green asterisk in Fig. 3) under pressure is well established; hence a discussion on the high-pressure phases of Te was excluded in the whole pressure range of this study.

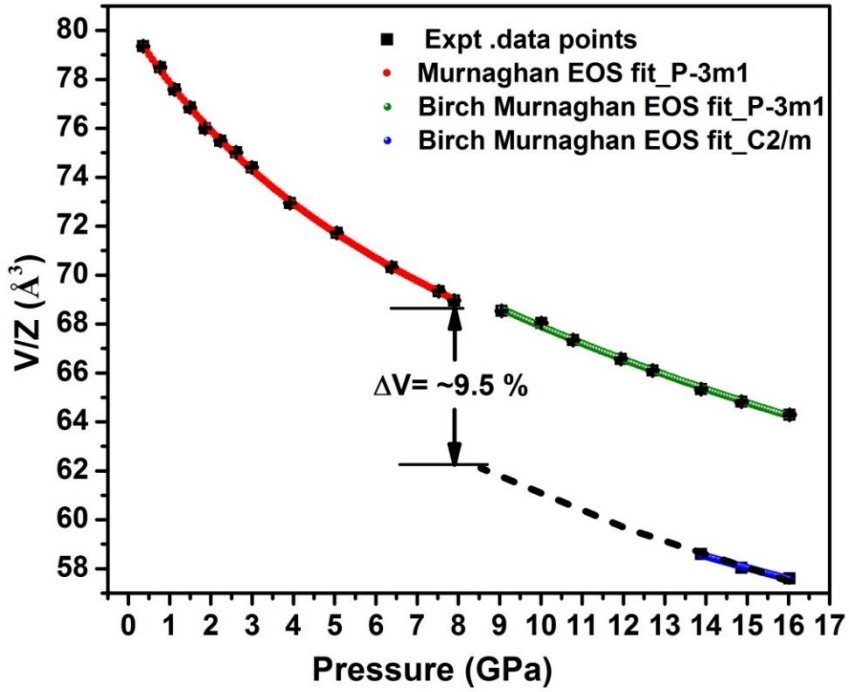

FIG. 5. EOS fit for the 1T-$TiTe_2$ phase to the pressure versus volume per formula unit (V/Z) data. The black dotted line represents the extrapolated curve for the monoclinic *C*2/m phase. The volume drop of ~9.5 % has been observed during the structural phase transition.

In the 1T phase, the only free atomic position is the *z* coordinate of the Te ions which defines the Te(1) – Te(2) contact distance. The lattice parameters and atomic coordinates are refined using the FullProf software [20] for each XRD pattern up to 8 GPa. After ~ 8 GPa, due to the complexity of the mixed phases, we analyzed the 1T phase of $TiTe_2$ using Powd and Dicvol software [21], which provides only the unit cell parameters (*a*, *b*, *c*) and volume (*V*). Figure 5 represents the systematic decrease in volume of the unit cell up to ~ 16 GPa. Notably, an apparent change is observed at ~ 8 GPa, which further ascertain the phase transition. The pressure-volume data best fit the

equation of state (EOS) into two different regions using the Murnaghan EOS and third-order Birch-Murnaghan EOS respectively [discussed details in Chapter 1]. For instance, the Murnaghan EOS was used to fit the pressure region up to ~ 8 GPa and the fit yields V_0 = 80.34 Å^3, bulk modulus B_0 = 28.60 GPa and B_0' = 7.19. In the mixed phase regions (8 – 16 GPa), the 1T phase was fitted with the third-order Birch Murnaghan EOS, and the fit gives V_0 = 79.26 Å^3, bulk modulus B_0 = 40.73 GPa and B_0' = 6.02. After the phase transition, B_0 increases from 28.60 GPa to 40.73 GPa suggesting that the high-pressure 1T phase has lesser compressibility than ambient conditions.

The pressure dependence of the normalized lattice parameters (a/a_0, c/c_0) is plotted in Fig. 6. Though a/a_0 and c/c_0 decrease systematically under pressure up to ~ 16 GPa, a clear anomaly in a/a_0 at ~ 8 GPa is observed. Figure 7(b) represents the pressure versus c/a ratio of 1T-$TiTe_2$. Initially, the c/*a* ratio decreases from 1.718 to 1.690, implying that the *c* axis is more compressible than the *a* axis which is usually expected for anisotropic layered crystals due to the weak van der Waals interlayer forces along the *c* direction. Interestingly, two inflection points are noticed in the 1T phase at ~ 2 GPa and ~ 4 GPa. Here, we would like to emphasize that a similar trend was reported in the pressure ranges 2.0 – 2.9 GPa and 2.5 – 3.0 GPa in BiTeI and BiTeBr, respectively and these changes were interpreted as the signature of TQPT [22,23].

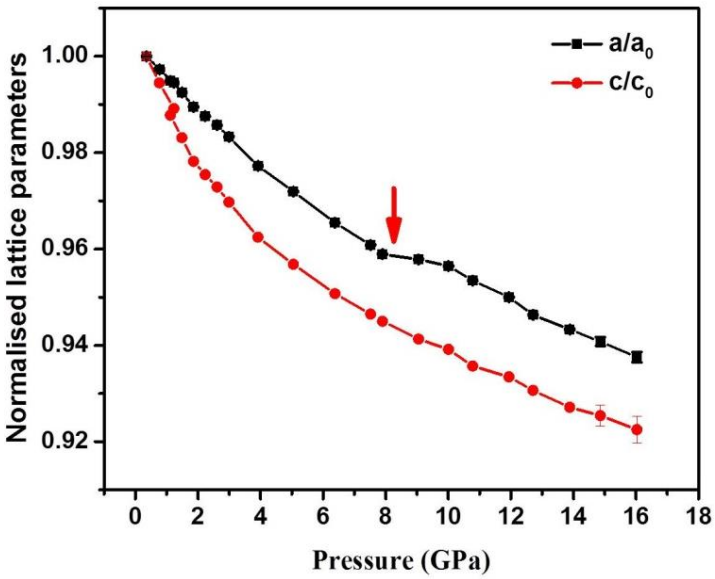

FIG. 6 Pressure dependence of the normalized lattice parameters for 1T-$TiTe_2$ phase. The solid red arrow at ~8 GPa indicates structural phase transition.

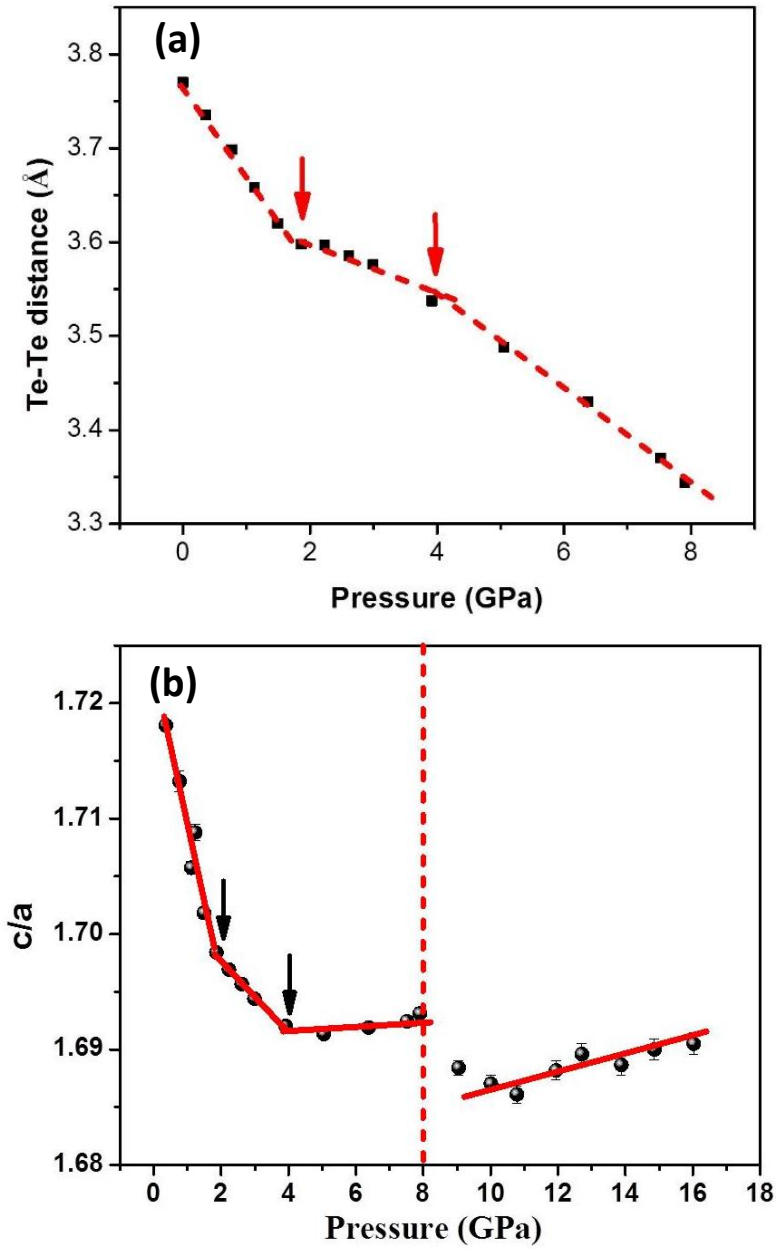

FIG. 7(a) Pressure versus Te(1)-Te(2) contact distance for 1T- $TiTe_2$ up to 8 GPa, and (b) pressure dependence of the *c/a* ratio for 1T-$TiTe_2$. The solid red and black arrows at ~2 GPa and ~4 GPa indicate isostructural anomalies (transitions) due to charge density redistribution. The red vertical dotted lines signify structural phase transition.

To get more insight about *c/a* ratio anomalies, the pressure-dependent Te(1) – Te(2) contact distance is plotted in Fig. 7(a). As seen from Fig. 7(a), it shows two distinct anomalies in the 1T phase region at ~ 2 GPa and ~ 4 GPa. But after 4 GPa, the *c/a* ratio surprisingly turns out to be almost pressure invariant which suggests that the compressibilities of both the lattice parameters (*a* and *c*) are similar. A plausible cause

for this behavior could be because the lower threshold level of the Te(1) – Te(2) anionic contact distance is reached and strong charge repulsion (Coulomb) is built up between the interlayers. Hence this constant behavior of the *c/a* ratio under pressure hints at the isotropic nature. So, the pressure switches the 2D layered 1T-$TiTe_2$ into a quasi-3D network like feature from 4 GPa to 8 GPa, and a similar observation has been made in $MoSe_2$ [24]. This change in axial compressibility is directly related to the fluctuations in the charge density distribution along the different directions, as we discuss in more detail below (theoretical results). In the pressure region 4 – 8 GPa, a huge amount of strain is developed inside the sample. In order to relax the strain, the 1T phase undergoes a structural phase transition. Evidently, the discontinuity in *c/a* ratio at ~ 8 GPa indicates the structural transition and further it increases with pressure. Therefore, in the 1T phase, initially the *a* axis is stiffer than the *c* axis and after the structural transition, *c* axis is stiffer than the *a* axis.

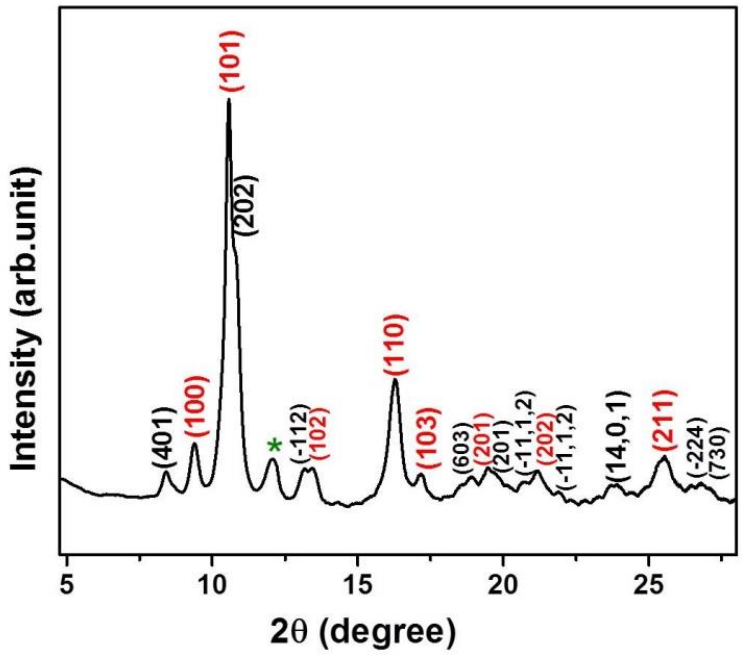

FIG. 8 The representative indexing of the mixed phases ($P\bar{3}m1$ and $C2/m$) at ~13.9 GPa. The red and black color Bragg planes denote the $P\bar{3}m1$ and $C2/m$ phase respectively. The green asterisk indicates the high pressure phase of Te.

$IrTe_2$ also undergoes a pressure-induced structural transformation from $P\bar{3}m1$ to $C2/m$ at ~ 5 GPa [18]. Due to the poor data quality and complexity of the mixed phase, we could not refine this phase through the Rietveld method from ~ 8 GPa onwards.

However, we have indexed the XRD pattern at ~ 13.90 GPa with the monoclinic *C*2/*m* space group using the Powd and Dicvol software [21] as shown in Fig. 8. The indexed values for the monoclinic unit cell at ~ 13.90 GPa are a = 17.3666 Å, b = 3.5545 Å, c = 5.6966 Å, β = 91.17°, V = 351.57 $Å^3$, Z = 6 and V/Z = 58.60 $Å^3$, which agree well with the similar proto type system, $IrTe_2$ [18]. The volume change of ~ 9.5 % (when we extrapolate the volume data of the high-pressure phase to ~ 8 GPa) is observed during the structural transition which confirms the first-order nature of the transition (see Fig. 5). Mention must be made of the V/Z values of the monoclinic phase (*C*2/*m*), which very well agree with the V/Z trend of $P\bar{3}$m1 phase as shown in Fig. 5. During the indexing of the monoclinic *C*2/*m* phase, the *b* axis is considered as the unique axis, and the lattice parameters of the indexed pattern for three different pressure values. Upon releasing pressure, the high-pressure phase is transformed back to the ambient 1T phase indicating reversibility of the transition. The study of detailed pressure-induced structural changes with atomic coordinates is beyond the scope of the present work, and will be the future interest of our group.

4.4.3 Raman scattering measurements under pressure

To shed light on the observed isostructural anomalies (*c/a* ratio) and phase transitions in $TiTe_2$, Raman spectroscopy measurement under pressure was employed up to ~ 13.7 GPa. The pressure evolutions of Raman spectra of $TiTe_2$ are shown in Figs. 9(a) and 9(b). As the pressure increases, the intensity of the E_g mode increases, whereas the intensity of the M and A_{1g} modes are decreasing. However, the overall intensity of all the phonon modes is observed to be drastically decreased above ~ 8.0 GPa. As evident from Fig. 9(b), the appearance of a new Raman mode at ~ 10.97 GPa (named the N mode) confirms the structural phase transition and the presence of the E_g and A_{1g} modes at higher pressures confirms the phase coexistence (mixed phase), which is consistent with the XRD results. After ~ 13.7 GPa, the peaks become very broad and difficult to deconvolute from the background. During the depressurization, the system came back to initial phase (1T), which suggests the observed transition is reversible.

The pressure-dependent Raman shift of the E_g, A_{1g}, M and N modes is shown in Fig. 10(a). In general, the phonon modes are expected to harden (blue shift) during the

hydrostatic lattice compression. But, Fig. 10(a) shows that the behaviors of all the modes are anomalous and we can identify four distinct pressure regions. To elucidate this we have fitted in each region A_{1g} and E_g modes using linear equations, and the fitting parameters [slope a_1 and intercept $\omega(P_0)$] are summarized in Table II.

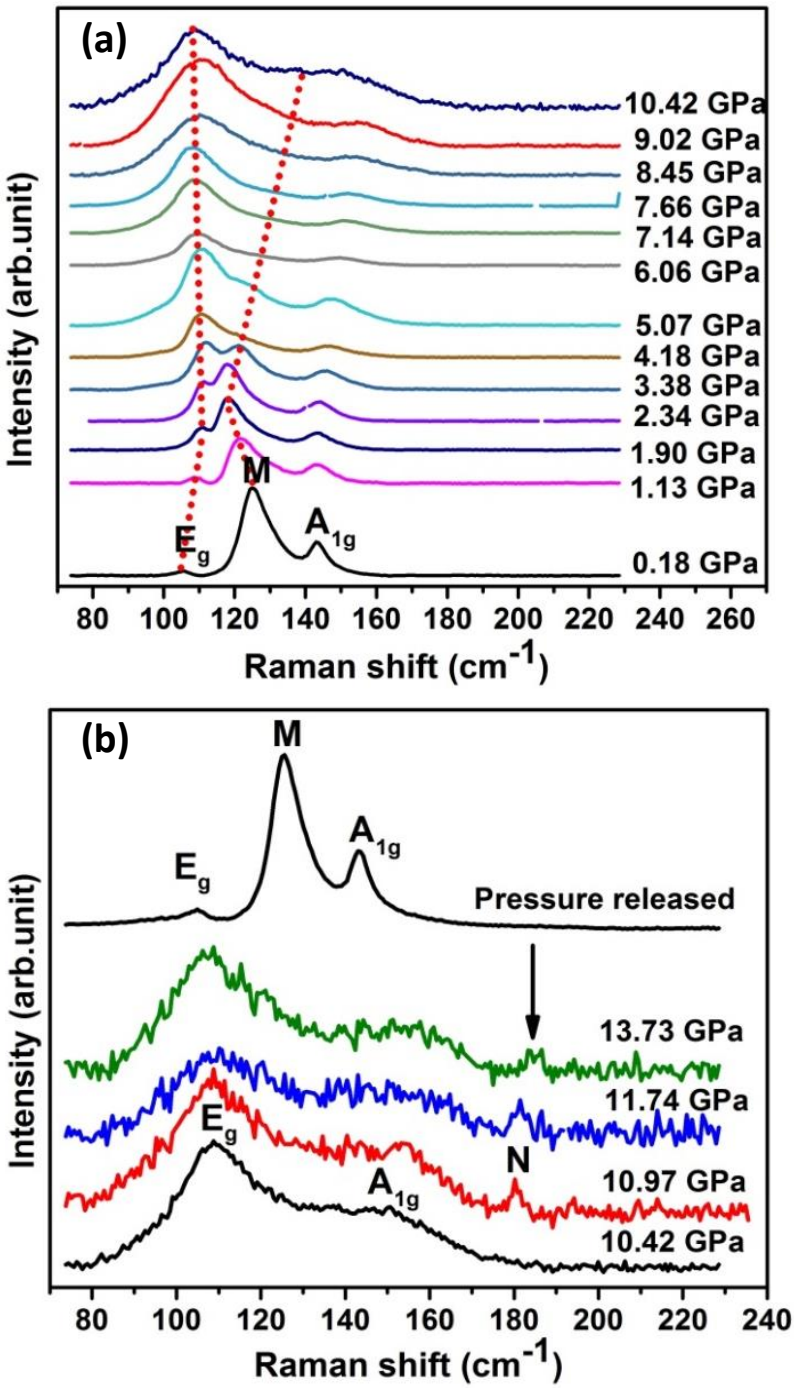

FIG. 9. (a) The representative Raman spectra of $TiTe_2$ at relatively low pressure regions and (b) at high-pressure regions and depressurized ambient Raman spectrum.

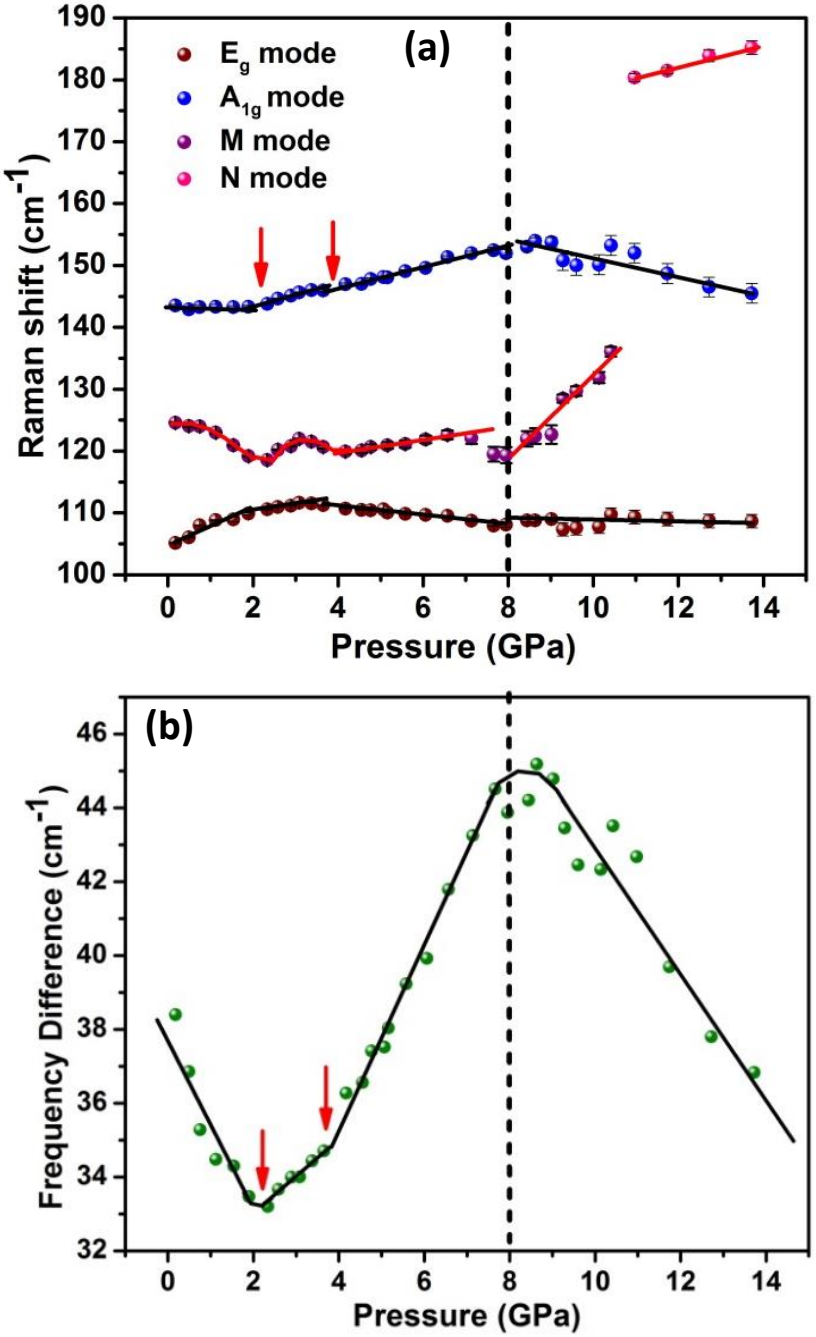

FIG. 10. (a) Pressure versus Raman shift of phonon modes (A_{1g}, M, E_g and N) of $TiTe_2$. The solid black line represents the linear fit, and the red line represents a guide to the eye. (b) Pressure versus frequency difference (A_{1g} - E_g) between the A_{1g} and E_g modes of $TiTe_2$. The solid red arrows at ~ 2 GPa and ~ 4 GPa represent the isostructural electronic transitions. The solid and vertical dotted lines represent guide to the eye and structural phase transition, respectively.

TABLE II. Pressure dependence behavior of various Raman-mode frequencies and Gruneisen parameters (γ) of 1T-$TiTe_2$. The pressure coefficients for 1T-$TiTe_2$ were fitted [25] using $\omega(P) = \omega(P_0) + a_1.(P - P_0)$. The Gruneisen parameters γ are determined by using the relation $\gamma = (\frac{B}{\omega(P0)} \times \frac{\partial\omega}{\partial P})$, where B represents the bulk modulus.

Raman Mode	$\omega(P_0)$ (cm^{-1})	a_1 (cm^{-1} GPa^{-1})	γ
E_g	105.1 ± 0.6 [a]	3.07 ± 0.67 [a]	0.84
	109.3 ± 0.7[b]	0.65 ± 0.24[b]	0.17
	113.6 ± 0.4 [c]	-0.68 ± 0.07[c]	-0.17
	106.5 ± 2.2[d]	0.20 ± 0.02[d]	0.08
A_{1g}	143.4 ± 0.1 [a]	-0.10 ± 0.01 [a]	-0.03
	140.2 ± 0.6[b]	1.69 ± 0.20[b]	0.34
	139.5 ± 0.6[c]	1.70 ± 0.10[c]	0.35
	165.9 ± 2.9[d]	-1.46 ± 0.27[d]	-0.36

[a] Estimated at room pressure (P_0 = 1atm), [b] Estimated at P_0 = 1.89 GPa,
[c] Estimated at P_0 = 4.1 GPa, [d] Estimated at P_0 = 7.95 GPa.

The A_{1g} mode softens slightly up to ~2 GPa and thereafter it starts to harden up to ~ 8 GPa with a small change in slope at ~4 GPa, while, the E_g mode shows hardening up to 4 GPa with a clear change in slope at ~ 2 GPa followed by softening till 8 GPa. Upon further compression, the frequency of the E_g mode and the newly appeared N mode starts to increase, while the A_{1g} mode begins to soften up to ~ 14 GPa, which is the maximum pressure achieved in Raman study. The frequency of the zone-folded Raman mode M exhibits very interesting high-pressure behavior. It shows two parabolic pressure dependencies with two distinct points of inflection at ~ 2 and ~ 4 GPa, beyond which it slowly hardens up to ~ 8 GPa. After the phase transition, the M mode shows significant hardening with pressure. Notably, over the pressure range between 0 – 2 GPa and also between 4 – 8 GPa, the pressure dependencies of the A_{1g} and E_g modes show opposite behaviors.

The drastic softening of the E_g mode (a_1 = – 0.68 cm^{-1}/GPa) and hardening of the M mode from ~4 GPa to ~ 8 GPa hint at the structural instability and plausible reason for the impending structural phase transition. The slope change of the A_{1g} and E_g

modes at ~8.0 GPa is attributed to the onset of structural phase transition from trigonal ($P\bar{3}m1$) to monoclinic ($C2/m$). The intensity and linewidth of the N mode is smaller compared to that of the A_{1g} and E_g modes. This could be the reason we did not observe the appearance of the N mode at the onset pressure (~8 GPa) of the structural transition. However, once its intensity evolves under pressure, it comes out above 10.97 GPa. To get more insight, the frequency difference between the A_{1g} and E_g modes is plotted as a function of pressure and represented in Fig. 10(b). The plot illustrates four different regions, which substantiate the analysis of the pressure dependence of the A_{1g} and E_g modes. The maximum in frequency difference ($A_{1g} - E_g$) at ~8 GPa represents the structural phase transition, whereas the two minima at ~2 GPa and ~4 GPa signify the isostructural anomalies.

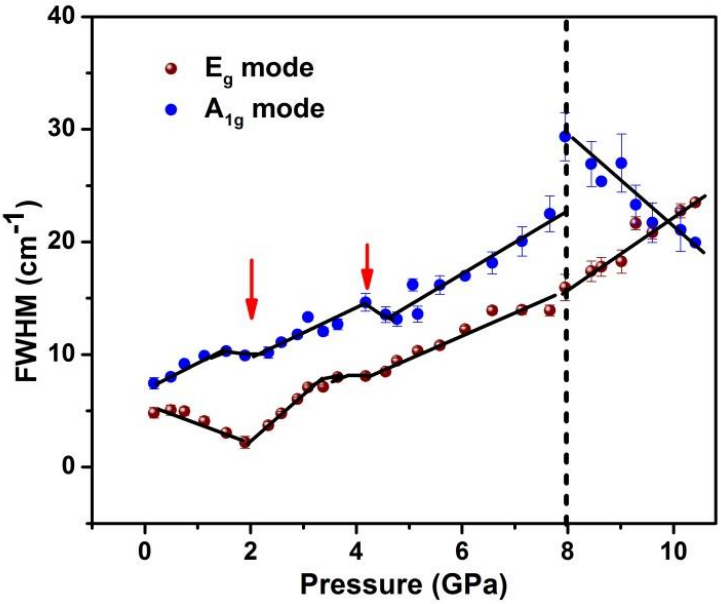

FIG. 11. Pressure dependence of FWHM of A_{1g} and E_g modes for $TiTe_2$. The solid red arrows at ~ 2 GPa, and ~ 4 GPa indicate the isostructural electronic transitions. The solid and vertical dotted lines represent a guide to the eye and structural phase transition, respectively.

We have carefully analyzed the FWHM of the A_{1g} and E_g modes and these are shown in Fig. 11. It should be noted that the nature of PTM limits the accuracy of information about intrinsic linewidth of the sample beyond the hydrostatic limit. Since the methanol: ethanol (4:1) mixture gives only the hydrostatic pressure limit up to ~ 10.5 GPa, the linewidth of the phonon modes has been analyzed below 10.5 GPa [26]. It is normally seen that as we increase the pressure, there is an increase in linewidth of

phonon modes. However, the FWHM of the E_g mode decreases under pressure up to ~ 2 GPa, followed by an increase up to ~ 10.5 GPa with anomalous behaviors at ~ 4 GPa and ~ 8 GPa. It is noteworthy that a similar pressure-induced decrease in linewidth of the E and E_g modes was observed in BiTeI and A_2B_3 (A = Bi, Sb and B= Te, Se, and S) series compounds during the TQPT at 3 – 4 GPa and ETT at 3 – 4 GPa respectively [25,27,28]. In contrast, the A_{1g} linewidth increases up to 8 GPa with significant anomalies at ~ 2 GPa and ~ 4 GPa, followed by a decrease up to 10.5 GPa with a discontinuity observed during the phase transition at ~ 8.0 GPa. After the structural transition, the decreasing trend in linewidth of the A_{1g} phonon mode could be due to decrease of electron-phonon coupling in the monoclinic *C*2/m phase. The zone-folded Raman mode M shows increasing linewidth behavior under pressure up to ~ 11 GPa, which is the expected behavior for any phonon. More importantly, evidence of an unusual electron-phonon coupling from the linewidth anomalies (A_{1g} and E_g) at ~ 2 GPa and ~ 4 GPa further confirms the isostructural ($P\bar{3}m1$) transitions, which could possibly be originated from electronic state modulation under pressure. Finally, the pressure-dependent frequency and linewidth behavior of both the A_{1g} and E_g modes suggests two isostructural transitions and a structural transition, which is quite consistent with the XRD measurements.

4.4.4 Electrical transport measurements under pressure

1T-$TiTe_2$ is expected to show metallic behavior due to the finite band overlap of the d orbitals of Ti atom with p orbitals of the Te atoms at ambient conditions [29]. The oxidation state of typical CdI_2 structures such as TiX_2 is given by $Ti^{4+}(X^{2-})_2$ (X=S, Se, and Te), here the amount of electron transfer from orbitals p to d is zero [30]. However the overlap of the p orbitals with the d orbitals can lead to the transfer of n electrons per metal, then the oxidation formula can be changed into $Ti^{(4-n)+}(X^{(2-(n/2))-})_2$ [30]. In the energy band diagram, the transition-metal Ti d orbitals are located just above the top of the p orbitals of Te chalcogen [30]. These two orbitals can be overlapped either via the chemical or physical methods. Chemically, it can be achieved by decreasing the electronegativity of chalcogen X. As the electronegativity of Te is less than both Se and S, the top portions of the p orbital bands are raised. Hence, the overlap of p-d bands is more in Te than in Se and S atoms which leads to the behavior of $TiTe_2$, $TiSe_2$ and TiS_2 as metal, semimetal, and semiconductor, respectively. Physically, the overlap of the p-d

orbitals can be increased by reducing the Ti-X bond distance, which can be experimentally achieved using hydrostatic pressure.

In this chapter, we have investigated the pressure-dependent resistance measurements of a polycrystalline 1T-$TiTe_2$ sample at room temperature. The pressure dependence of the electrical resistance (R) and its first derivative (dR/dP) at room temperature for 1T-$TiTe_2$ are illustrated in Fig. 12. The resistance value is ~ 3.7 Ω for the lowest measured pressure (~0.8 GPa). For the 1T-$TiTe_2$ sample (single crystal), Koike *et al*. [31] and de Boer *et al*. [32] reported that the resistivity at room temperature is of the order of 10^{-4} Ω cm (at low temperature it of the order of 10^{-5} Ω cm). Then the resistance of a sample with a few microns thickness will be of the order of 1 Ω. In our

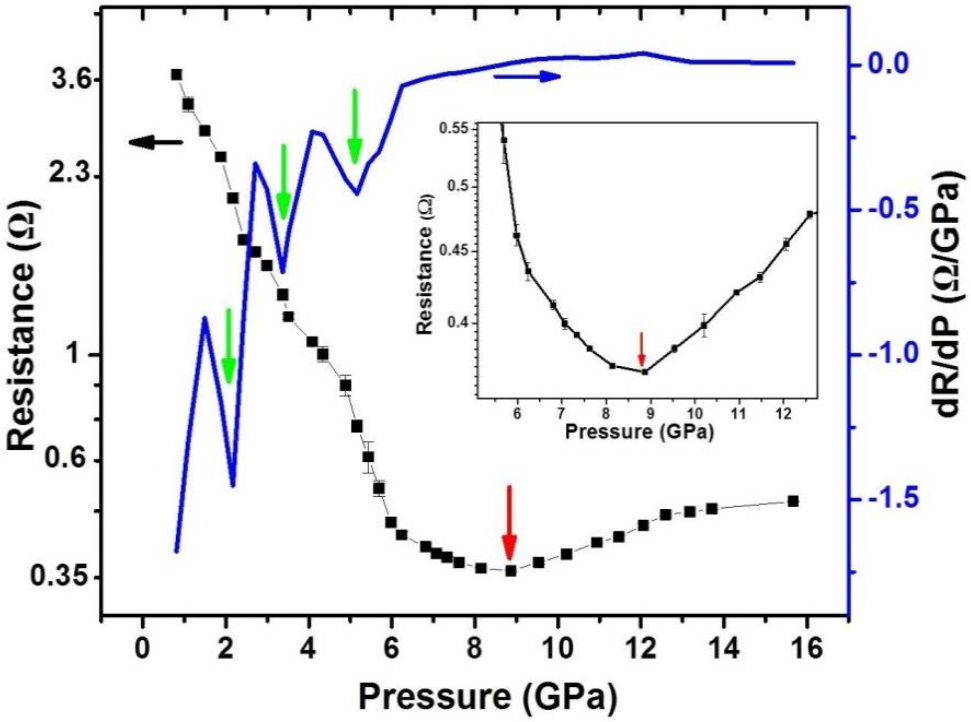

FIG. 12. Pressure-dependent electrical resistance of $TiTe_2$ (black square and a line corresponding to the left y axis) and its first derivative (blue line corresponding to the right *y* axis). The red arrow at ~ 8.8 GPa indicates the structural transition. The solid green arrows at 2.1 GPa and 3.4 GPa indicate the isostructural electronic transitions in the trigonal ($P\bar{3}m1$) phase. The inset highlights the resistance minimum in the vicinity of the structural transition.

measurements, it is 3.7 Ω at 0.8 GPa. So, its order of magnitude is more or less consistent with the literature [31,32]. Because of the soft polycrystalline nature of the

sample (small pressure can change the sample thickness by a huge amount), we have not measured the thickness of the sample at ambient pressure, and the low-pressure resistance measurements have no meaning (in the low-pressure region the inter-grain contribution is large compared to the sample contribution). We have measured the resistance above a sufficient pressure (P > 0.8 GPa) although at this pressure the inter-grain contribution is there, but will definitely be small compared to the sample resistance. Therefore, we believe that the obtained resistance of the polycrystalline 1T-$TiTe_2$ sample provides a real trend, without being affected by the wire-contact resistance or contribution of the inter-grain barriers.

As the pressure increases, the resistance of the $TiTe_2$ sample quickly drops from ~ 3.7 Ω at ~ 0.8 GPa to ~ 0.37 Ω at ~ 8.8 GPa. As we further increase the pressure from 8.8 GPa the resistance starts to increase slowly with pressure (clearly seen in the inset of the Fig. 12) and at ~ 12.6 GPa reaches a value of ~ 0.48 Ω which is 30 % more than that at ~ 8.8 GPa. Above ~ 12.6 GPa the resistance increases at a slower rate and the 0.51 Ω resistance at ~ 16 GPa (the highest measured pressure of our experiment) is roughly 38 % more than at ~ 8.8 GPa. The increase in resistance may be caused by sample size shrinkage. Fritscht *et al*. [33] suggested that the increase in resistance by the sample size shrinkage is about one third of the compressibility, which in the present case should be less than 10 % below ~ 8.8 GPa and 13 % at 16 GPa based on the bulk modulus measurements of our XRD experiment. Thus, our result suggests that, as the pressure increases, $TiTe_2$ becomes more and more metallic only up to 8.8 GPa and the unusual increase of the resistance above ~ 8.8 GPa should mainly result from the accompanying change in the crystal structure which is consistent with the structural transition from trigonal ($P\bar{3}m1$) to monoclinic ($C2/m$) as confirmed by XRD and Raman measurements at ~ 8 GPa. This type of change in crystal symmetry along with abnormal resistance increase with pressure was also observed in V_2O_3 [34]. It is also reported that the pressure-induced structural phase transitions of Bi_2Te_3 and As_2Te_3 induce a series of changes in the electrical resistivity [35,36].

In the low-pressure regime (below 8.8 GPa), the pressure-dependent resistance curve shows three distinct slope changes at ~ 2.1 GPa, ~ 3.4 GPa and ~ 5.1 GPa which are identified by the minima of the P vs. dR/dP curve. These inflection points cannot be associated with structural phase transitions since high-pressure XRD and Raman

measurements reveal the structural stability of the ambient-pressure $P\bar{3}m1$ structure up to ~ 8 GPa and are associated with isostructural electronic transitions. The first two points (~ 2.1 GPa and ~ 3.4 GPa) are consistent with our XRD and Raman measurements (~ 2 GPa and ~ 4 GPa). Here, we would like to mention that anomalies in pressure-dependent transport (resistivity) measurements at room temperature were observed in BiTeBr during the TQPT at 2.1 GPa [23]. The third transition point at ~ 5.1 GPa is not seen in XRD and Raman measurement. We have seen from XRD that the strains build up in the pressure range of 4 – 8 GPa followed by a structural phase transition at ~ 8.8 GPa. In addition, we observe the broad nature of the minimum at ~ 5.1 GPa of the dR/dP curve. Hence, the anomaly at ~ 5.1 GPa may be the signature of the precursor effect for the structural transition. We observe a considerable hysteresis between the pressure-increasing, and the pressure-decreasing cycle, which confirms the first-order nature of the transition at ~ 8.8 GPa. The irreversibility of the resistance upon decompression is noted, and which may happen for various reasons. (i) One of the most important reason is that we might not have given sufficient time for releasing [for example, see supplementary of Ref. 37]. The other reasons are (ii) irreversible changes in the shape and size of the materials upon decompression, and (iii) the high-pressure structural transition may not be completely reversible. Here the structure is entirely reversible, inferred from the high-pressure XRD and Raman data, and hence this possible reason is ruled out. But, the first two possibilities are not entirely ruled out and could play an important role in the observed irreversibility of the resistance. More importantly, the isostructural and structural transition observed in resistance studies is consistent with multiple techniques such as XRD, and Raman measurements over the similar pressure regions which further ascertain the transitions are intrinsic. The small difference in transition pressure observed with respect to XRD and Raman could be mainly due to the sensitiveness of these techniques, error in pressure measurement, and the degree of hydrostatic conditions produced by PTM used in these experiments.

4.4.5 First principles calculations

The experimental observations in the present work demonstrate a series of transitions at ~2 GPa, ~4 GPa and at ~8 GPa, wherein the first two transitions were isostructural, while the last one was found to be a first-order structural phase transition. In addition, the system is found to evolve into an increased 3D nature from an

anisotropic 2D form, which occurs within the pressure range of 4-8 GPa. To have a better understanding of these isostructural transitions, we have performed first-principles electronic structure calculations. We have optimized the ground state, and the optimized parameters are in good agreement with those of the present experimental work. We first intend to investigate the quasi-3D nature of 1T-$TiTe_2$ via charge density redistribution.

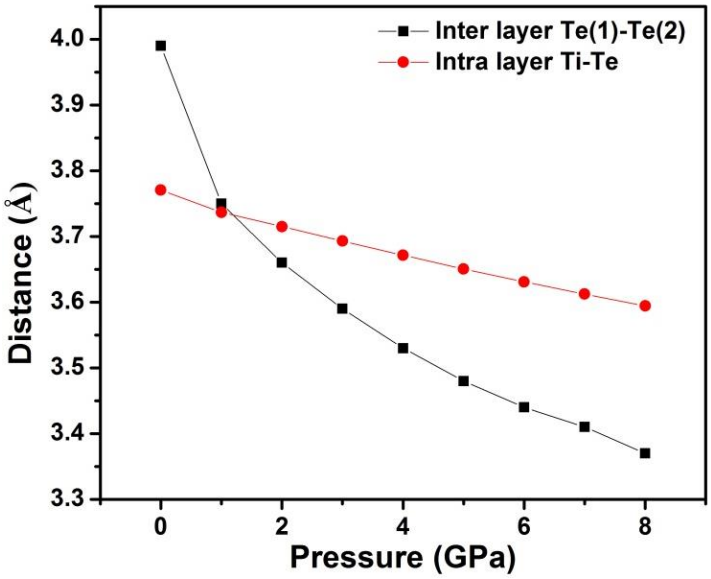

FIG. 13. Pressure dependence of the interlayer Te(1)-Te(2) and intralayer Ti-Te distance.

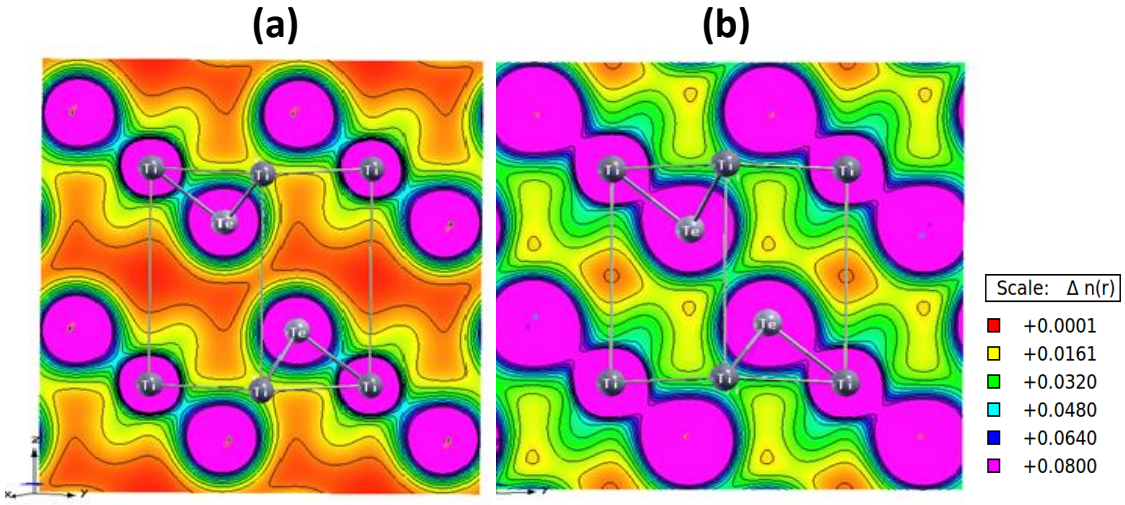

FIG. 14. (a) Pressure-dependent charge density redistribution of (111) plane at 0 GPa and (b) 8 GPa. The relative scale of the charge density is given in the color code.

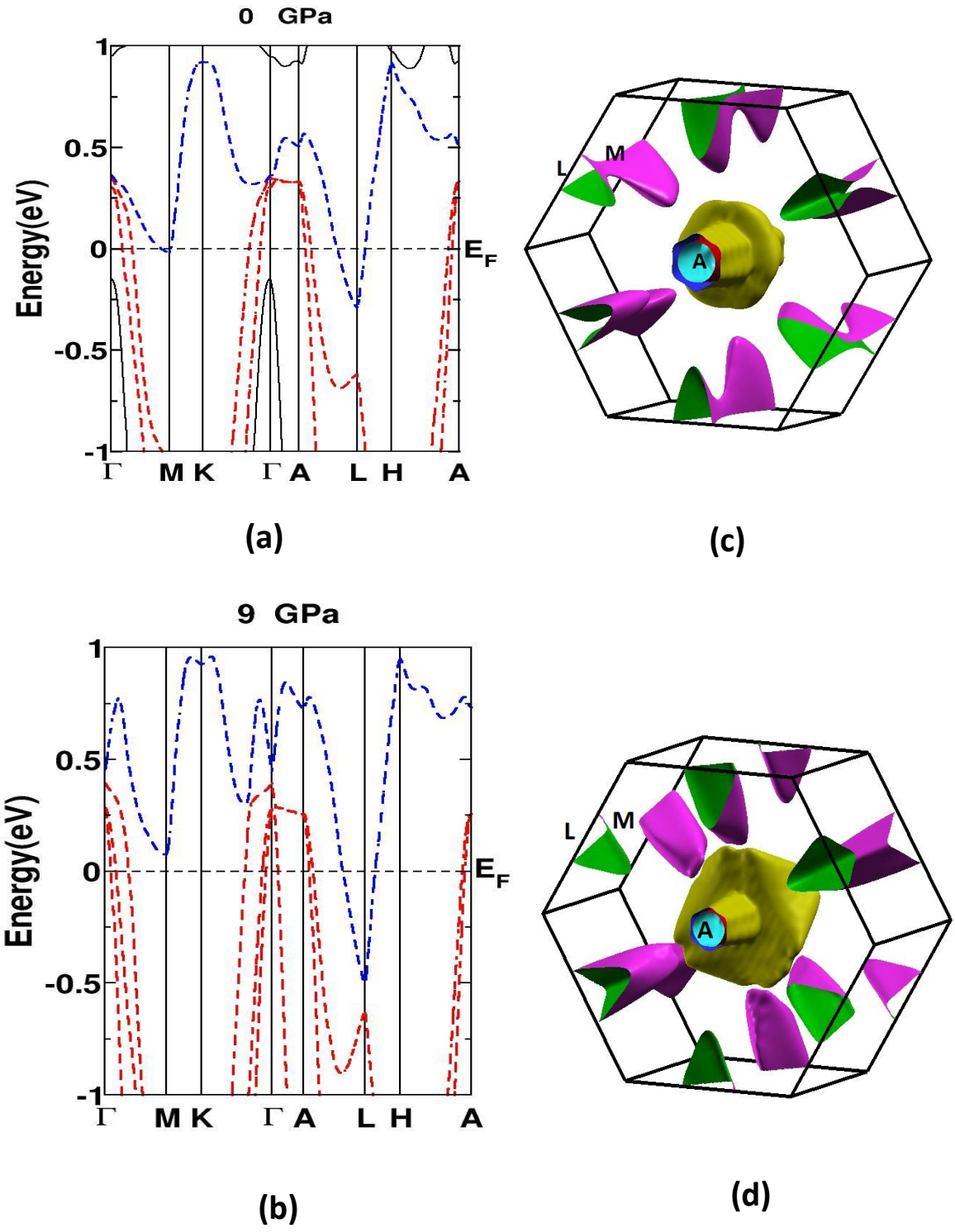

FIG. 15. (a), (b) Band structure and (c),(d) Fermi surface of 1T-$TiTe_2$ at ambient and 9 GPa. Hole-like bands are given in red color and electron-like bands are given in blue color.

Here, we have analyzed the interlayer Te(1) – Te(2) bonding, intralayer Ti – Te bonding and charge density plots. Bond lengths of both interlayer Te(1) – Te(2) and

intralayer Ti – Te are plotted as a function of pressure as shown in Fig. 13. Due to the layered nature, the interlayer Te(1) – Te(2) bond length is higher than the intralayer Te-Ti bond length at ambient conditions. Under the application of pressure above 2 GPa the intralayer Ti – Te bond length is more than the interlayer Te – Te bonding, which might result in the reduction of 2D character and increased overlap of orbitals between p and d.

Likewise, the bond length between Te(1) and Te(2) decreases with compression, which will increase the charge flow between these two layers and is clearly seen in charge density plots (Fig. 14). Figures 14(a) and (b) represent the charge density plots [(111) plane] both at ambient and 8 GPa respectively. At ambient, we observed a more ionic nature between the interlayer Te(1) and Te(2). With pressure, this ionic nature is found to decrease, and the covalent nature is found to increase. In Fig. 13, we have shown the intralayer Ti – Te bonding as a function of pressure and we observe a large overlap between intralayer Ti- Te, which will cause more charge flow between them. In addition to this, the layer thickness is found to decrease with pressure, and the Te-Ti-Te angle is found to increase with pressure.

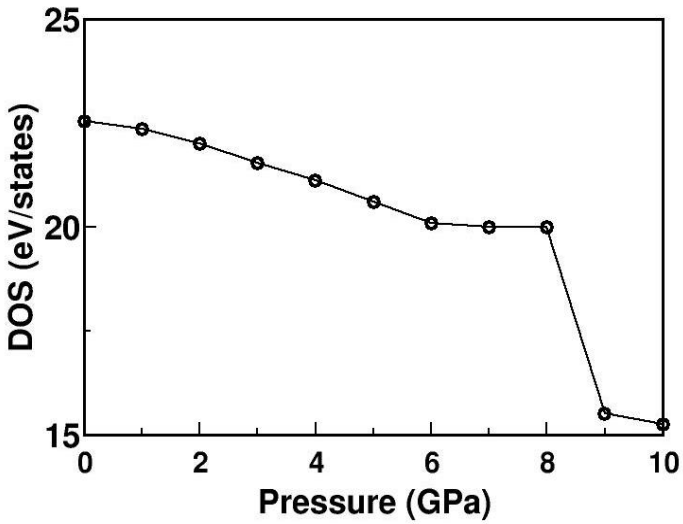

FIG. 16 Variation of the DOS at Fermi level for 1T-$TiTe_2$ as a function of pressure.

We have systematically analyzed the band structure and Fermi surface of 1T-$TiTe_2$ in more detail for each pressure. The calculated band structure and Fermi surface at ambient and 9 GPa are given in Figs. 15. From the figures, it is quite evident that the

nature of the band structure changes as a function of pressure at a small pressure itself. Since the band nature is changing little far from the Fermi level, the Fermi surface plots do not show a significant difference at 2 GPa. Still, we can see the extent of overlap increasing along M-L as a function of pressure. A similar scenario is observed in the case of 4 GPa. Detailed analysis at higher pressure (at 9 GPa) reveals a change in band nature near the Fermi level which causes corresponding changes in Fermi surface, as seen in Fig. 15(d). At ambient, three bands are crossing the Fermi level, of which, two are hole-like pockets, and one is an electron-like pocket. From 2 GPa onwards one can see an additional hole like pocket added to it. The fourth band (electron like pocket) which crosses the Fermi level along the M to L high symmetry direction produces a connected Fermi surface in the lower pressure range. In the case of the high pressure state, the fourth band alignment got lifted up at M point, and it crosses the Fermi level only around the L point, which is clearly seen from the Fermi surface. The changes in the band topology of electronic Fermi surfaces are called ETT or Lifshitz transition (discussed in Chapter 1) [38]. Here, the overall band and Fermi surface topology changes are observed around 9 GPa, which is very close to the experimental value of 8 GPa suggesting an ETT. In addition to that non-monotonic variation of the density of states (DOS) [39] at the Fermi level supports the presence of ETT around 9 GPa, and the same is given in Fig. 16.

4.5 Discussion

The recent theoretical calculation showed that 1T-$TiTe_2$ undergoes a series of topological transitions under hydrostatic isothermal compression [4]. 1T-$TiTe_2$ is shown to have four consecutive band inversions at the A, L, Γ and A points corresponding to the theoretical pressure points of 0.88 GPa, 3.40 GPa, 10.7 GPa, and ~ 26.4 GPa, respectively [4]. This transition pressure values are calculated from the comparisons of the experimental EOS with the theoretically predicted value [4] and details are mentioned below.

According to DFT calculations, the converged lattice parameters for $TiTe_2$ at ambient pressure is a = 3.81 Å and c =6 .92 Å, [4] whereas the experimental value is a = 3.78 Å and c = 6.50 Å [10,11]. The difference between the lattice parameter of a from both theory and experiment is -0.03 Å. The lattice parameter of predicted critical

transition pressure points for 1T-$TiTe_2$ are *a* = 3.78 Å, 3.72 Å, 3.60 Å and 3.45 Å. After the correction (-0.03 Å), the transition pressure points are *a* = 3.75 Å, 3.69 Å, 3.57 Å, and 3.42 Å [4]. For the comparison of theoretically predicted pressure values with experimental values, we have fitted the pressure vs. lattice parameter *a* with Murnaghan EOS using EOSfit7 software (see Fig. 17) considering only the experimental data points below the structural phase transition pressure 8 GPa. The fit yields a_0 = 3.7753 Å, linear modulus B_{a0} = 129.25 GPa, and its pressure derivative B_{a0}' = 13.305. Following the fitted curve, the pressure values corresponding to the lattice parameters 3.75 Å, 3.69 Å, 3.57 Å, and 3.42 Å are respectively ~0.88 GPa, ~3.40 GPa, 10.7 GPa and 26.4 GPa.

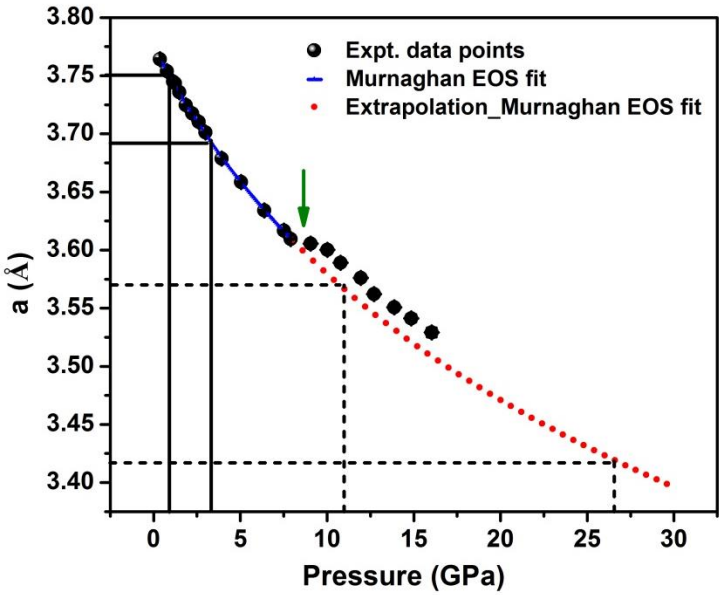

FIG. 17 Murnaghan EOS fit for the pressure P versus lattice parameter *a* of 1T-$TiTe_2$. The solid green arrow at ~8.0 GPa indicates the structural phase transition. The black solid line represents the interpolated transition points, and the dotted line represents the extrapolated transition points for 1T-$TiTe_2$ phase.

Due to the first band inversions at the A point (~0.88 GPa), the system possesses non-trivial TQPT due to the changes in the parity and consequently the topological invariant changed to Z_2 = 1. This is followed by another band inversion (~ 3.40 GPa), which takes place at the L point of the Brillouin zone. This leads the system to become a trivial metallic phase because the net parity change is the same with respect to the ambient condition (Z_2 = 0) [4]. Furthermore, there is another band

inversion (~ 10.7 GPa) at the Γ point, which changes the overall parity and hence the topological invariant (Z_2) changes from 0 to 1, leading to a second non-trivial TQPT. Finally, the band inversion (~ 26.4 GPa) at the A point in the BZ makes the system switch back to the trivial metallic phase (Z_2 = 0). Interestingly, it is suggested that if there are no phase transitions this cycle of multiple oscillations of topological transition should continue [4].

The experimentally observed multiple isostructural (1T phase) electronic transition signatures are quite consistent with the above proposed model. Hence, we attribute the isostructural anomalies at ~ 2 GPa from XRD, Raman, and resistance to the non-trivial TQPT as a consequence of the predicted band inversion at the A point of the BZ [4]. In this electronic transition, conduction band characters (dominated by Te-p orbitals) are exchanged with valence band characters (dominated by Ti-d orbitals) at A points of the electronic band structure [4]. Similarly, the anomalies at ~ 4 GPa may be due to the trivial metal as a consequence of band inversion at the L point of the BZ. Here, conduction band characters (dominated by Ti-d orbitals) are switched with valence band characters (dominated by Te-p orbitals) at the L points of the electronic band structure [4]. The charge density fluctuations that have occurred during band inversion at the A and L points of the BZ leads to anomalies in *c/a* ratio at ~ 2 GPa and ~ 4 GPa, respectively. The charge redistribution modulates the electronic structure and consequently the phonon life time is affected, which is reflected as the unusual electron-phonon coupling at ~ 2 GPa and ~ 4 GPa in Raman linewidth. A small difference exists between the theoretical (0.88 GPa and 3.40 GPa) and experimental (2 GPa and 4 GPa) pressure values. The transition pressure from the result of DFT theory may or may not quantitatively match with the experimental values. This difference comes due to the various approximations used in the theoretical approach. Particularly for the high-pressure experiments, the mismatches between the transition pressure values are reported in the literature and details are discussed with illustrative examples in Chapter 3 (section 3.5). Here, more importantly, we have seen two isostructural electronic transitions at~2.0 GPa, and ~4 GPa within the stability of the trigonal structure of $TiTe_2$ and the transition pressure values quite closely agrees with the theoretical predictions (~0.88 GPa and 3.40 GPa) [4].

Like TQPT, the anomalous changes in Raman linewidth, pressure coefficient of phonon modes, *c*/*a* ratio, and resistivity are indicators for ETT and have been reported for many compounds [25,28,35,40,41]. Though TQPT and ETT are the two completely different phenomena, experimental signatures (indirect) of the XRD and Raman are quite similar. The common method to distinguish between them (TQPT and ETT) is through electronic band structure, Fermi surface, and topological invariant Z_2 calculation. The ambient 3D topological insulators such as Bi_2Se_3, Bi_2Te_3, and Sb_2Te_3 show ETT under a hydrostatic pressure regime of ~3-5 GPa [28,35]. In some cases such as black phosphorous and Sb_2Se_3, ETT, and TQPT occur together at the same pressure region [42,43]. Our result closely (qualitatively) agrees with the theoretical prediction of TQPT. Also, the possibility of an ETT occurrence for 1T-$TiTe_2$ under pressure is discussed above (theoretical sections). The detailed band topology calculations suggest that there is no possibility of ETT at ~ 2 GPa and ~4 GPa for 1T-$TiTe_2$. Further, the theoretically observed anomaly around 9 GPa (close to experimental value ~8 GPa), as evidenced by both the Fermi surface topology change and DOS plots suggests the ETT. Hence, the anomalies at ~8 GPa are not only associated with the structural transition; they might also be a coexistence of structural phase transition and ETT.

The DFT-based first principles theoretical calculations support the stability of structural symmetry ($P\bar{3}m1$) of 1T-$TiTe_2$ up to 30 GPa (hydrostatic pressure) [4,13]. But, our experimental results contradict these theoretical proposals and show the structural transformation of 1T-$TiTe_2$ from trigonal ($P\bar{3}m1$) to monoclinic ($C2/m$) at ~ 8 GPa under hydrostatic pressure. One point to note here is that the experiment shows the coexistence of two phases consisting of both the ground-state structure ($P\bar{3}m1$) and the high-pressure structure ($C2/m$) from 8 GPa to 16 GPa (highest pressure reached in this study); still the transformation remains incompletes. It is to be mentioned that present calculations [4,13] (including our theoretical work) may not validate such a coexistence of two phases and that could be one of the reasons why theory could not capture the structural transition at 8 GPa. It is noteworthy that this kind of coexistence of two phases over large pressure regions has been observed in the prototype system $IrTe_2$ [18].

This pressure-induced structural transition may be limiting the detection of two other theoretically predicted electronic transitions at higher pressure regions ~ 10.7 GPa

and ~ 26.4 GPa (beyond the pressure range explored in this work) in the $P\bar{3}m1$ phase. Moreover, as the pressure increases, the $TiTe_2$ sample becomes more and more metallic, which is consistent with the overall intensity reduction of the phonon modes in Raman measurement. This pressure-enhanced metallization could mainly be due to the following two physical reasons. (1) The pressure decreases the interlayer Te(1)-Te(2) contact distance, and van der Waals interactions and hence bridges the two layers at ~ 4 GPa onwards. (2) In the intralayer, electron transfer from the p orbitals of the Te atom to d orbitals of the Ti atom increases under pressure. This is confirmed by our first-principles calculations, which shows that the applied hydrostatic pressure bridges the interlayer Te(1) and Te(2) via the charge density redistributions which results in the conversion of an anisotropic 2D to isotropic 3D behavior at the pressure range from 4 GPa to 8 GPa (1T phase).

Raman anomalies in the 1T-$TiTe_2$ compound can be addressed by considering the anharmonic approximations [42] in the phonon dispersion calculations as a function of pressure which is computationally expensive and beyond the scope of the present work. In addition, for this purpose, the insight of the experimentally observed additional mode (zone-folded mode M) may be needed, and hence non-adiabatic phonon renormalization computational studies can be taken as a separate future work. In consideration of our multiple experimental signatures such as charge density fluctuations, transport anomalies, and unusual electron-phonon coupling at ~2 GPa and ~4 GPa with the close agreement of the theoretically proposed the model [4], we attribute these to topologically non-trivial and trivial transitions at ~2 GPa and ~4 GPa respectively. Also, we would like to recall and emphasize that similar indirect experimental signatures (Raman, XRD and electrical transport) combined with first-principles calculations have been used to claim the topologically non-trivial (or band inversion) properties in various systems such as BiTeI, Sb_2Se_3, BiTeBr and black phosphorous [22,23,42,43]. Hence, we hope our experimental signatures of anomalies in phonon linewidth, *c*/*a* ratio and transport for 1T-$TiTe_2$ will stimulate research interest towards this material on the aspect of TQPT using a more sophisticated direct tool such as Shubnikov de Haas oscillation under pressure and provide further insight.

4.6 Conclusions

In conclusion, systematic pressure-dependent synchrotron XRD, Raman and electrical resistance studies were carried out on 1T-$TiTe_2$ samples up to ~ 16 GPa. We observed a first-order structural phase transition at ~ 8 GPa from trigonal ($P\bar{3}m1$) to monoclinic ($C2/m$) symmetry. The pressure-dependent *c/a* ratio and electrical resistance show anomalies at ~ 2 GPa and ~ 4 GPa in the 1T phase which suggest charge density fluctuations upon compression. This is consistent with the phonon linewidth anomalies at ~ 2 GPa and ~ 4 GPa indicating unusual electron-phonon coupling arising from the electronic structure changes under pressure. These multiple experimental signatures of the two isostructural electronic transitions at ~ 2 GPa and ~ 4 GPa are closely consistent with the theoretical predictions and hence may be due to non-trivial TQPT and trivial metallic transition, respectively. The 2D layered crystal of $TiTe_2$ (at ambient condition) switched into a quasi 3D network above 4 GPa via shortening of the interlayer Te(1) – Te(2) contact distances by external hydrostatic pressure inducing strains, which could be the precursor for the structural transition observed at ~8 GPa. The pressure evolution of the calculated band structure and Fermi surface shows that there is an occurrence of an ETT at ~9 GPa (close to experimental value ~8 GPa) in the 1T phase. We hope our experimental finding will stimulate researchers to further explore the 1T-$TiTe_2$ compound from the aspect of quantum oscillation measurement such as the Shubnikov de Haas effect under pressure.

4.7 Bibliography

1. T. E. Kidd, T. Miller, M. Y. Chou, and T.C. Chiang, Phys. Rev. Lett. **88**, 226402 (2002).
2. A. F. Kusmartseva, B. Sipos, H. Berger, L. Forro´, and E. Tutisˇ, Phys. Rev. Lett. **103**, 236401 (2009).
3. J. Khan, C. M. Nolen, D. Teweldebrhan, D. Wickramaratne, R. K. Lake, and A. A. Balandin, Appl. Phys. Lett. **100**, 043109 (2012).
4. Q. Zhang, Y. Cheng, and U. Schwingenschlogl, Phys. Rev. B **88**, 155317 (2013).
5. J. C. Chervin, B. Canny and M. Mancinelli, High. Press. Res. **21**, 305 (2001).

6. S. J. Clark, M. D. Segall, C. J. Pickard, P. J. Hasnip, M. I. J. Probert, K. Refson, and M. C. Payne, Z. Kristallogr. **220**, 567 (2005).
7. P. Blaha, K. Schwarz, G. K. H. Madsen, D. Kvasnicka, and J. Luitz, "WIEN2k, An augmented plane wave þ local orbitals program for calculating crystal properties," edited by K. Schwarz (Techn. Universitat Wien, Austria, 2001).
8. T. H. Fischer and J. Almlof, J. Phys. Chem. **96**, 9768 (1992).
9. J. P. Perdew, K. Burke, and M. Ernzerhof, Phys. Rev. Lett. **77**, 3865 (1996).
10. C. Riekel, M. Thomas, and R. Schollhorn, Phys. Status Solidi A **50**, K231 (1978).
11. Y. Arnaud and M. Chevreton, J. Solid State Chem. **39**, 230 (1981).
12. H. Ding and B. Xu, J. Chem. Phys. **137**, 224509 (2012).
13. R. C. Xiao, W. J. Lu, D. F. Shao, J. Y. Li, M. J. Wei, H. Y. Lv, P. Tong, X. B. Zhu and Y. P. Sun, J. Mater. Chem. C **5**, 4167 (2017).
14. M. Hangyo, S. I. Nakashima and A. Mitsuishi, Ferroelectrics **52,** 151(1983).
15. P. Goli, J. Khan, D. Wickramaratne, R. K. Lake, and A.A. Balandin, Nano Lett. **12**, 5941 (2012).
16. R. Samnakay, D. Wickramaratne, T. R. Pope, R. K. Lake, T. T. Salguero, and A. A. Balandin, Nano Lett., **15**, 2965 (2015).
17. O. R. Albertini, R. Zhao, R. L. McCann, S. Feng, M.Terrones, J. K. Freericks, J. A. Robinson, and A. Y. Liu, Phys. Rev. B **93**,214109 (2016).
18. J. M. Leger, A. S. Pereira, J. Haines, S. Jobic, R. Brec, J. Phys. Chem. Solids **61**, 27 (2000).
19. M. Hiue, Y. Akahama, M. Kobayashi and H. Kawamura, Rev. High Pressure Sci. Technol. **7**, 344 (1998).
20. J. R. Carvajal, Phys. B **192**, 55 (1993).
21. A. Boultif and D. Lour, J. Appl. Cryst. **24**, 987 (1991).
22. X. Xi, C. Ma, Z. Liu, Z. Chen,W. Ku, H. Berger, C. Martin, D. B. Tanner, and G. L. Carr, Phys.Rev.Lett. **111**, 155701 (2013).
23. A. Ohmura, Y. Higuchi, T. Ochiai, M. Kanou, F. Ishikawa, S. Nakano, A. Nakayama,Y. Yamada, and T. Sasagawa, Phys. Rev. B **95**,125203 (2017).

24. Z. Zhao, H. Zhang, H. Yuan, S. Wang, Y. Lin, Q. Zeng, G. Xu, Z. Liu, G. K. Solanki, K. D. Patel, Y. Cui, H. Y. Hwang, and W. L. Mao, Nat. Commun. **6**, 7312 (2015).
25. R.Vilaplana, D. S. P´erez, O. Gomis, F. J. Manj´on, J. Gonz´alez, A. Segura, A .Mu˜ noz, P. R. Hern´andez, E. P. Gonz´alez, V.M. Borr´as, V. M. Sanjose, C. Drasar, and V. Kucek, Phys. Rev. B **84**, 184110 (2011).
26. S. Klotz, J.C. Chervin, P. Munsch, and G.L. Marchand, J. Phys. D: Appl. Phys. **42**, 075413 (2009).
27. Yu. S. Ponosov, T. V. Kuznetsova, O. E. Tereshchenko, K. A. Kokh, and E. V. Chulkov, JETP Letters **98**, 557 (2013).
28. F. J. Manjo´n, R. Vilaplana, O. Gomis, E. P. Gonza´lez , D. S. Pe´rez, V. M. Borra´s, A. Segura, J. Gonza´lez, P. R. Herna´ndez, A. Mun˜oz, C. Drasar, V. Kucek, and V. M. Sanjose, Phys. Status Solidi B **250**, 669 (2013).
29. M. L. Doublet, N. G. Planas, P. H. T. Philipsen, R. Brec, and S. Jobic, J. Chem. Phys. **108**, 648 (1998).
30. E. Canadell, S. Jobic, R. Brec, J. Rouxel, and M.H. Whangbo, Journal of solid state chemistry **9**, 189 (1992).
31. Y. Koike, M. Okamura, T. Nakanomyo and T. Fukase, J. Phys. Soc. Jpn, **52**, 597 (1983).
32. D. K. G. de Boer, C. F. van Bruggen, G. W. Bus, R. Coehoorn, C. Haas, G. A. Sawatzky, H. W. Myron, D. Norman, and H. Padmore, Phys. Rev. B **29**, 6797 (1984).
33. G. Fritscht, W. Dyckhoff, W. Pollich, and E. Liischer, J. Phys. F: Met. Phys. **15**, 1537 (1985).
34. Y. Ding, C. C. Chen, Q. Zeng, H.S. Kim, M. J. Han, M. Balasubramanian, R. Gordon, F. Li, L. Bai, D. Popov, S. M. Heald, T. Gog, H.K. Mao, and M. van Veenendaal, Phys. Rev. Lett. **112**, 056401 (2014).
35. J. Zhang, C. Liu, X. Zhang, F. Ke, Y. Han, G. Peng, Y. Ma, and C. Gao, Appl. Phys. Lett **103** , 052102 (2013).
36. J. Zhao, L. Yang, Z. Yu, Y. Wang, C. Li, K. Yang, Z. Liu, and Y. Wang, Inorg. Chem. **5**, 3907 (2016).

37. E. Greenberg, B. Hen, Samar Layek, I. Pozin, R. Friedman, V. Shelukhin, Y. Rosenberg, M. Karpovski, M. P. Pasternak, E. Sterer, Y. Dagan, G. Kh. Rozenberg, and A. Palevski, Phys. Rev. B **95**, 064514 (2017).
38. I. M. Lifshitz, Sov. Phys. JETP **11**, 1130 (1960).
39. S. Ram, V. Kanchana, G. Vaitheeswaran, A. Svane, S. B. Dugdale, and N. E. Christensen, Phys. Rev. B **85**,174531 (2012).
40. Y. A. Sorb, V. Rajaji, P. S. Malavi, U. Subbarao, P. Halappa, S. C. Peter, S. Karmakar, and C. Narayana, J.Phys. Condens. Matter **28**,015602 (2016).
41. V. Rajaji, P. S. Malavi, S. S. R. K. C. Yamijala, Y. A. Sorb, U. Dutta, S. N. Guin, B. Joseph, S. K. Pati, S. Karmakar, K. Biswas, and C. Narayana, Appl. Phys. Lett. **109**, 171903 (2016).
42. A. Bera, K. Pal, D. V. S. Muthu,S. Sen, P. Guptasarma, U. V. Waghmare, and A. K. Sood, Phys. Rev. Lett. **110**, 107401 (2013).
43. S. N. Gupta, A. Singh, K. Pal, B. Chakraborti, D. V. S. Muthu, U. V. Waghmare, and A. K. Sood, Phys. Rev. B **96**, 094104 (2017).

Part II

Pressure induced electronic and structural phase transitions

Chapter 5

Pressure induced band inversion, electronic and structural phase transitions in InTe

The author's main contribution in this chapter is the core research idea, perfroming the high pressure Raman and synchrotron XRD measurements on InTe sample and analyzing the data. To execute this research problem, we have collaborated with Prof. Sebastian C. Peter's group, JNCASR, Bangalore for sample synthesis and Prof. Umesh V. Waghmare's group, JNCASR, Bangalore for the first principles theoretical calculations.

V. Rajaji, Koushik Pal, Saurav Ch.Sarma, B. Joseph, Sebastian C. Peter, Umesh V. Waghmare, and Chandrabhas Narayana, *"Pressure induced band inversion, electronic and structural phase transitions in InTe: A combined Experimental and theoretical study" Phys. Rev. B **97**, 155158 (2018)*

5.1 Introduction

Pressure is a powerful tool to alter the interatomic bond distances, forces, density, electronic structure, and, consequently material intrinsic characteristics. Pressure effects on an anisotropic crystal structure (i.e., anisotropic bonding exists in different crystallographic directions) have received increasing attention in recent years due to their abilities to induce the exotic electronic and topological changes in materials with strong spin-orbit coupling (SOC) [1-4]. For example, a typical transition-metal dichalcogenide (TMD) with formula MX_2 (M= transition metal and X = S, Se, and Te) compounds show strong covalent bonding in the *ab* directions (in plane) and weak van der Waals bonding along the *c* direction (out of plane) [2-3]. As a consequence of structural anisotropy, the properties of the TMD materials also show anisotropy. For instance, the $NbSe_2$ compound shows an anisotropic transport property under pressure [5]. Some TMD systems such as $MoSe_2$ and MoS_2 show large structural anisotropy during hydrostatic compression, leading to a semiconductor-to-metal transition at high pressure [2,3]. Binary layered chalcogenide based strong SOC compounds A_2B_3 (A= Bi, Sb and B = Se, Te, S) exhibit electronic topological transition (ETT) at high pressure [6-10]. Theory predicts that InSb, InSe, monolayer of TlS, and TlSe compounds are pressure induced topological insulators (TIs) [11-13]. The above illustrated examples show the importance of pressure effects on the anisotropic and strong SOC materials for tuning the various interesting properties in it. Motivated by these observations, we have investigated the possibility of pressure induced electronic and topological phase transitions in the binary layered semiconductor InTe, which is a TlSe prototype with strong SOC.

Recall that the TQPT is a non-adiabatic process in which the topological invariant quantity Z_2 changes from 0 to 1, as a consequence of continuous tuning of the SOC strength [14] (discussed in section in 1.7.2.3 in Chapter 1). The band inversion at the time-reversal invariant momenta (TRIM) points of the Brillouin zone and parity exchange (odd/even) between the valence-band maximum (VBM) and conduction-band minimum (CBM) are the necessary conditions for the TQPT [12,14-18]. Band inversion in the electronic structure of the material often gives rise to increased density of states (DOS) in the valence and conduction bands, and subsequent increase in electrical conductivity, Seebeck coefficient, and hence the enhancement of thermoelectric performance of the material [19].

Indium telluride (InTe) and other III-VI layered semiconductors have received extensive attention due to their potential application for photovoltaic and photo conducting devices [20,21]. InTe crystallizes in the TlSe-type structure (*B*37, space group (SG): *I*4/*mcm*, Z = 8) at ambient conditions with mixed valent formula $In^{1+}In^{3+}Te_2^{2-}$. The trivalent indium In^{3+} ions are tetrahedrally coordinated by four Te^{2-} ions, whereas monovalent In^{1+} ions are surrounded by eight Te^{2-} ions [22]. Recently, it was shown [23] that in InTe, the lone pairs of $5s^2$ electrons of the In^{1+} act as rattlers, leading to intrinsic ultralow lattice thermal conductivity (0.4 $Wm^{-1}K^{-1}$) through a strong anharmonic phonon-phonon interaction, giving a figure of merit (ZT) of 0.9 at 600 K. Some studies have been carried out in the aspect of high-pressure structural phase transitions in InTe [22,24-26]. A synchrotron x-ray diffraction (XRD) study has revealed that InTe undergoes a pressure induced structural transition from tetragonal (*B*37, SG: *I*4/*mcm*, Z = 8) to a face-centered- cubic phase (*B*1, SG: $Fm\bar{3}m$, Z = 4) at ~6.1 GPa and then to a primitive cubic phase (*B*2, SG: $Pm\bar{3}m$, Z = 1) at 14 GPa [25]. The structural transition (*B*37 phase to *B*1 phase) is proceeded by a semiconductor-to-metal transition at ~5 GPa due to the modification of In^{1+} and In^{3+} to In^{2+} [26]. Furthermore, the recent high-pressure transport measurement shows an unusual thermoelectric nature under pressure [25]. However, there are no studies yet to understand the behavior of the phonons of InTe during the structural phase transitions. Raman spectroscopy is a sensitive local probe, which has been extensively used for studying the structural, electronic, and topological changes in materials [6-10,27,28]. Hence, it will be important to probe the pressure-dependent behavior of InTe using Raman scattering measurements and complement it with the first-principles theoretical calculations to gain insights into the systematics of the phase transitions and also reveal indications regarding any isostructural electronic transitions.

In this chapter, we have systematically investigated the pressure-dependent behavior of InTe through Raman scattering measurements and the first-principles calculations along with the high-pressure XRD measurements up to ~5.7 GPa. An isostructural electronic transition has been observed from the unusual electron-phonon coupling of the Raman modes (A_{1g} and E_g) at ~ 3.6 GPa which is associated with the metallization, evident from the calculated electronic structure of InTe. Interestingly, our calculations reveal pressure induced band inversions in InTe at an even number of points

in the Brillouin zone near 1.0-1.4 GPa. Furthermore, the high-pressure Raman results provide signatures of pressure induced structural phase transitions ($B37 \rightarrow B1 \rightarrow B2$) in agreement with previous XRD studies [25].

5.2 Experimental details

Stoichiometric amounts of In powder (99.5%) and Te shot (99.99%) were mixed and sealed in evacuated quartz tubes, which were slowly heated to 700 ^{o}C within 8 h, held for 3 days and then cooled to room temperature in 10 h. Phase identity and purity of the sample (at ambient conditions) were determined by powder XRD experiments, which were carried out using synchrotron radiation with the wavelength λ = 0.4957 Å, at the Xpress beam line of the Elettra Synchrotron, Trieste. The Rietveld refinement of the obtained powder XRD pattern of the sample confirms the pure tetragonal phase of InTe.

Raman spectroscopy measurements were conducted on a custom-built Raman spectrometer equipped with four-level solid-state frequency-doubled Nd:YAG laser of wavelength λ = 532 nm, Horiba Jobin Yvon monochromator (550 mm focal length), and liquid-nitrogen-cooled CCD detector [29]. The spectral resolution was ~1 cm^{-1} for the grating of 1800 grooves per mm. The pressure was generated using a Mao-Bell-type diamond anvil cell (DAC) with culet diameter size of 400 μm. The procedures of gasket preparation, PTM and pressure calibration is the same as discussed in Chapters 2 and 3 (section 3.2). Typical accumulation time for each Raman spectrum was about 10 minutes for each pressure point. The high-pressure powder XRD experiments were performed at the Xpress beam line of the Elettra Synchrotron, Trieste, Italy with a wavelength λ = 0.4957 Å using a Mao-Bell DAC. The synchrotron XRD measurement and analysis details are the same as discussed in Chapter 3 (section 3.2).

5.3 Computational methods

First-principles density functional theoretical (DFT) calculation details are the same as discussed in Chapter 3 (section 3.3). In addition, expansion of wave functions and charge density in the plane-wave basis set was truncated with energy cut-offs of 60 and 240 Ry, respectively. Brillouin zone integrations were sampled on an 8x8x8 uniform mesh of k-points, smearing the discontinuity in the occupation numbers of the electrons with the Fermi-Dirac distribution function with a width (k_BT) of 0.003 Ry.

5.4 Results

5.4.1 Raman scattering measurements

5.4.1.1 Tetragonal phase of InTe under pressure

InTe adopts a tetragonal structure (D_{4h}^{18}) at ambient conditions with In^{3+}(1) and In^{1+}(2) atoms occupying, respectively, 4*a* and 4*b* sites and Te^{2-} atoms occupying 8*h* sites. The layered structure of InTe is different from the usual TMD structure, as it adopts an $In^{1+}In^{3+}Te^{2-}$ configuration with one In^{3+} atom and four Te^{2-} atoms forming a tetrahedral with In^{3+} at the center [see Fig. 1(a)]. This covalently bonded In^{3+}-Te^{2-} tetrahedra is connected by common horizontal edges and forms a linear chain along the crystallographic *c* axis [see Fig. 1(b)] [22,23]. The In^{1+} atom is arranged in between the two tetrahedral layers via weak electrostatic force along the *a* and *b* axes.

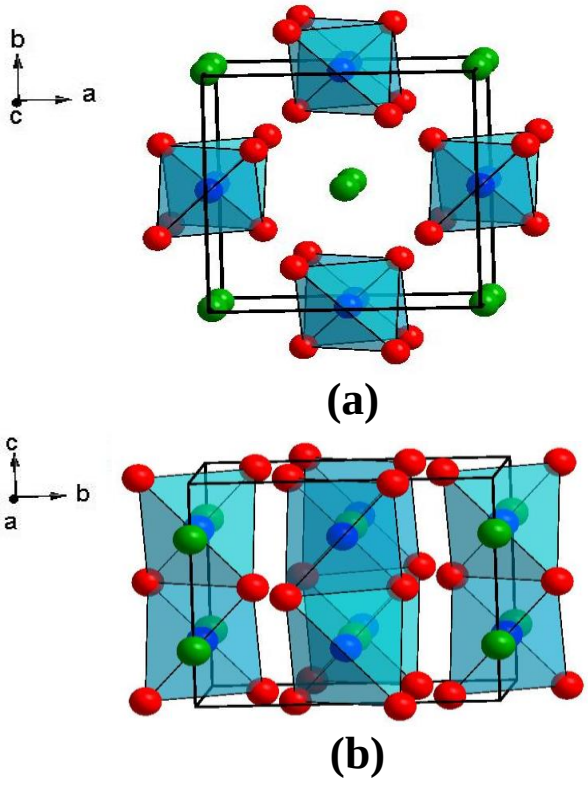

FIG. 1 The unit cell of InTe along the (a) *ab* projection and (b) *bc* projection. Here, the green, blue and red color spheres represent the In^{1+}, In^{3+}, and Te^{2-} ions, respectively.

As the primitive unit cell of InTe has eight atoms, according to the group theoretical analysis for the centrosymmetric tetragonal structure of the InTe shows 24 zone-center phonon modes at the Γ point:

$$\Gamma = A_{1g}+2A_{2g} + B_{1g} +2B_{2g} +3E_g +B_{lu}+3A_{2u}+4E_u$$

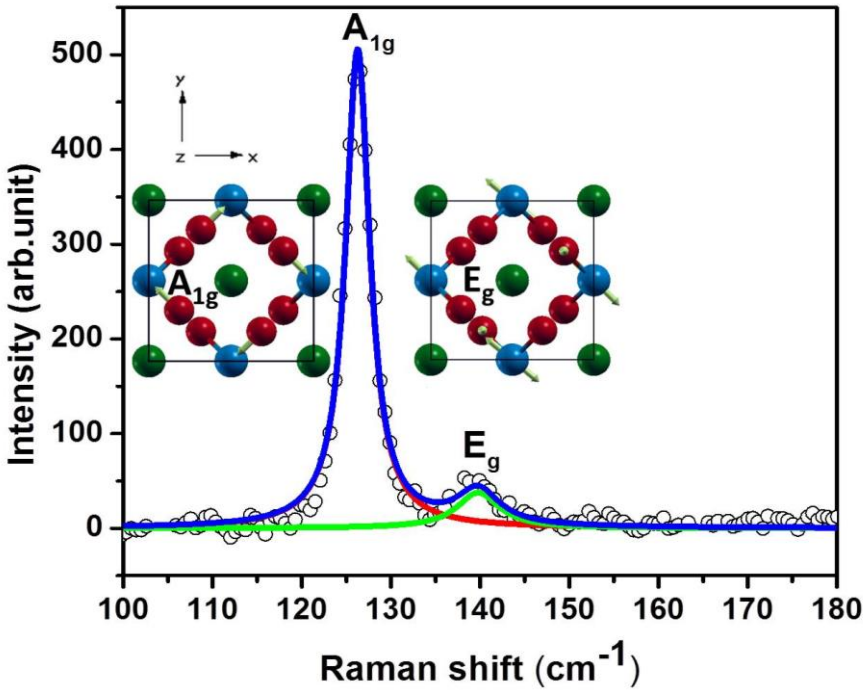

FIG. 2. Raman spectrum of InTe at ambient conditions. Visualization of the atomic displacement patterns for the A_{1g} and E_g modes are given in the inset. For the A_{1g} mode, only Te (red) atoms move in the *xy*-plane as indicated by the arrows, whereas for the E_g mode, In $^{3+}$ (blue) and Te (red) atoms vibrate along the *xy*-plane and *z*-direction respectively. In both of these modes, the In^{1+} (green) atoms sitting in the hollow cage of the crystal structure do not exhibit any displacement.

Here, the subscripts g and u represent Raman-active *gerade* and IR-active *ungerade* modes, respectively. There are 12 Raman-active modes (A_{1g} +$2A_{2g}$ + B_{1g} + $2B_{2g}$ + $3E_g$) and nine IR-active modes (B_{lu}+$2A_{2u}$+$3E_u$). Even though twelve Raman optical modes are theoretically predicted, experimentally we could see only two modes above 100 cm^{-1} (see Fig. 2). An earlier polarization-dependent Raman study on InTe single crystals by Nizametdinova identified the phonon symmetries of the observed modes as E_g (46 cm^{-1}, 139 cm^{-1}), A_{1g} (126 cm^{-1}), and B_{1g} (86 cm^{-1}) [30]. Our Raman spectrum (above 100 cm^{-1}) matches well with this report. Based on the work of

Nizametdinova [30], the observed phonon modes at ~ 126 and ~ 139 cm^{-1} are assigned to A_{1g} and E_g symmetry, respectively. We would like to further mention that our phonon assignment matches well with the previously reported ambient Raman studies of InTe by Torres *et al* [20].

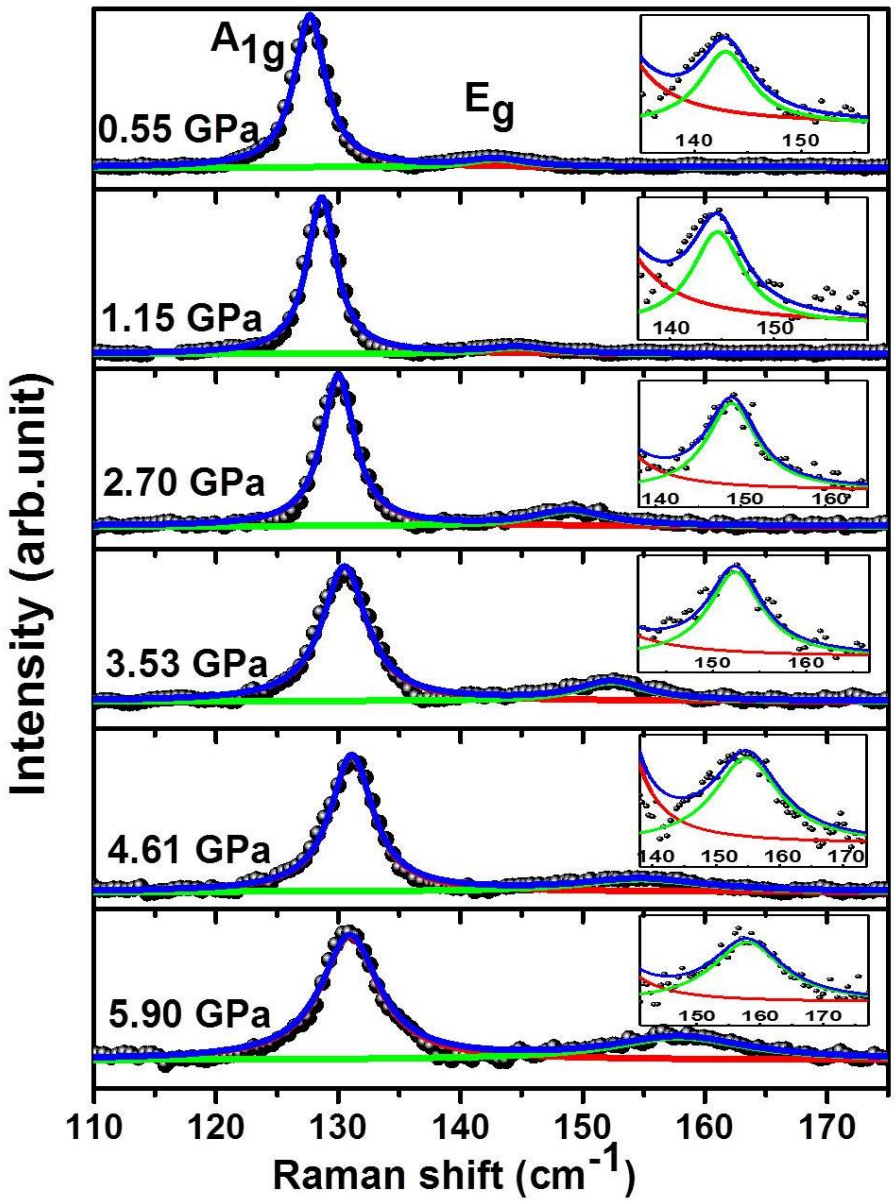

FIG. 3. Pressure evolutions of Raman spectrum of InTe (tetragonal phase) at selected pressure values (below 6 GPa). The inset shows the zoomed-in view of the E_g mode fitting for the sake of clarity. The red, green, and blue color curves represent the fitting of the A_{1g} mode, E_g mode, and cumulative peak, respectively.

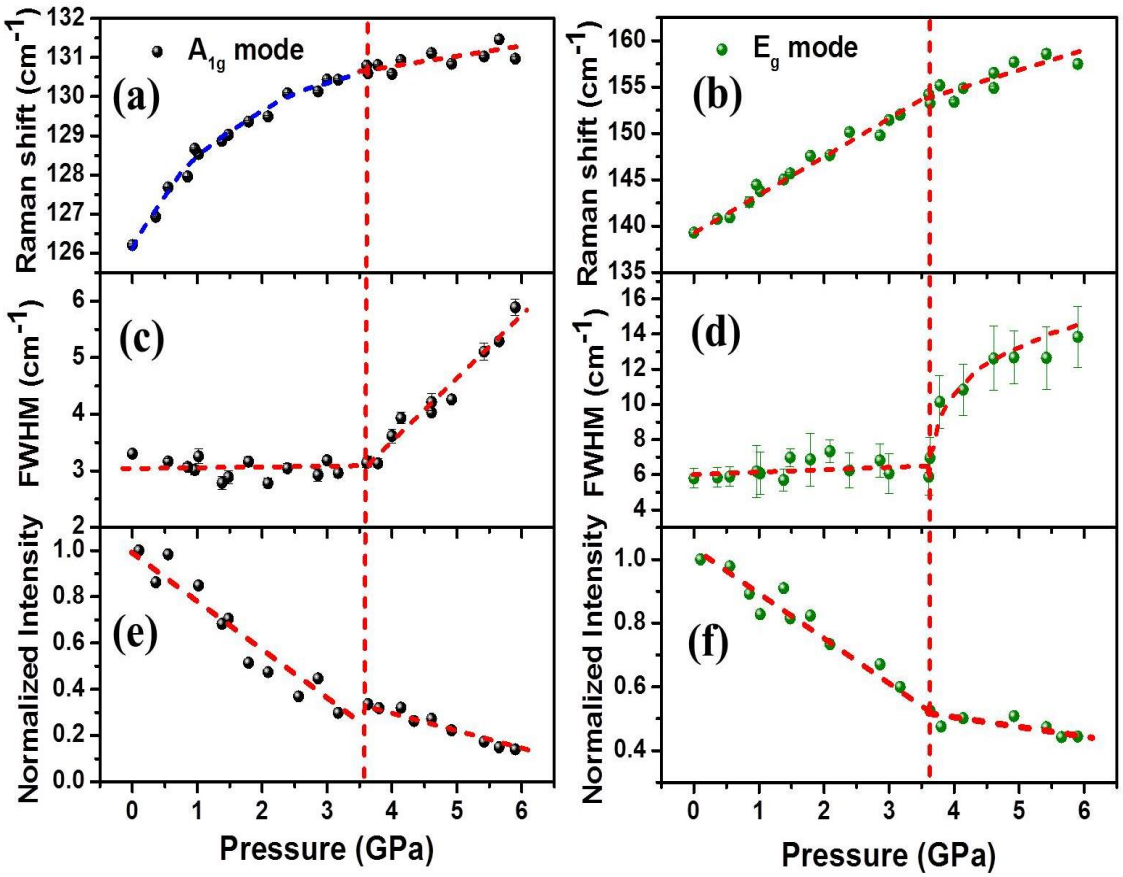

FIG. 4. Pressure dependence of Raman shift of (a) A_{1g} and (b) E_g modes. FWHM of (c) A_{1g} and (d) E_g modes. The normalized intensity of (e) A_{1g} and (f) E_g modes. The red dotted lines in (a) and (b) represent the linear equation fit, whereas the blue dotted line in (a) represents the second-order (quadratic) equation fit. The red dotted lines in (c) - (f) represent a guide to an eye. The vertical dotted line at ~3.6 GPa represents the isostructural electronic transition in InTe.

The customized Raman set up used for the present high pressure study can detect the signal only from 100 cm^{-1} due to the specific edge filter [29], thus limiting the observation of low frequency modes [E_g (46 cm^{-1}) and B_{1g} (86 cm^{-1})] [30]. Further, the possible reason for the detection of the lower number of Raman modes than the predicted ones could be due to their lower scattering cross sections. The experimental detection is limited by the signal-to-noise (S/N) ratio of the spectrometer used, and hence it is practically impossible to detect modes with lower scattering cross sections. Detecting a lower number of Raman active modes than expected is commonly observed in Raman spectroscopy [9,10,27]. Atomic displacement patterns for the A_{1g} and E_g modes are shown in the inset of Fig. 2. The Lorentzian function was used to fit the Raman modes and extracted frequencies, linewidths, and intensities. Lattice dynamical properties are

known to play an important role in the electronic or topological transitions of a material [4,6-10,28,31]. Hence to understand the pressure-dependent electronic and topological properties of InTe, it is very essential to study the behavior of the phonon modes of the *B*37 phase. First, we present a detailed analysis of phonons as a function of pressure for the tetragonal phase of InTe. Figure 3 represents the pressure evolution of InTe up to ~6.0 GPa.

The pressure dependence of the phonon frequencies for A_{1g} and E_g modes is as shown in Figs. 4(a) and 4(b). The phonon mode frequencies A_{1g} and E_g are monotonically increasing up to ~6.0 GPa with a small change in the slope at ~3.6 GPa. The pressure dependent behavior of the E_g mode is fitted using a linear equation, whereas the A_{1g} mode is fitted by second order from ambient to ~ 3.6 GPa and linear equation between ~3.6 to ~6.0 GPa [7-9]. Table I shows the pressure coefficients and Gruneisen parameter, and it can be observed that pressure coefficient (a_1) of the A_{1g} mode (2.3 cm^{-1} GPa^{-1}) is smaller than the E_g mode (3.9 cm^{-1} GPa^{-1}). Recall that the intralayer consists of a covalently bonded Te^{2-}-In^{3+}-Te^{2-}-In^{3+} chain of atoms, whereas the interlayers are separated by means of weak electrostatic interactions [23,24] between the negatively charged $In^{3+}Te_4^{2-}$ tetrahedra and In^{1+} atom. Hence, it is natural to expect that the pressure coefficient of the E_g mode will be greater than the A_{1g} mode, which is consistent with our experimental observation.

Figures 4(c) and 4(d) shows the experimental pressure dependent linewidth behavior of the A_{1g} and E_g phonon modes. The linewidth of both modes (A_{1g} and E_g) shows hardly any changes up to 3.6 GPa, but above this pressure, there is a sudden increase. Generally, the spectral linewidth (or FWHM) will increase with respect to the applied hydrostatic pressure. But here the observed anomalies in their linewidth at ~3.6 GPa are unusual and indicate that the origin is due to electron-phonon coupling. The linewidth behavior of both modes (A_{1g} and E_g) is almost similar and suggests that phonon modes interact strongly with the electronic states which are being modulated by pressure beyond ~3.6 GPa. The intensity of the A_{1g} and E_g modes is monotonically decreased under pressure with a sudden change in its slope at ~3.6 GPa [Figs. 4(e) and 4(f)]. The observed Raman results are reproducible in multiple runs. Since InTe undergoes a first-order structural transition only at ~6 GPa [25], the observed anomaly in our experiment cannot be due to a structural transition. Thus, the observed phonon anomalies

(frequencies, linewidths, and intensities) at ~3.6 GPa clearly suggest an isostructural electronic transition.

TABLE I. Experimental Raman mode frequencies and pressure coefficients of the A_{1g} and E_g modes at both room pressure and ~3.6 GPa as obtained from fits to the data using $\omega(P) = \omega(P_0) + a_1 \cdot (P - P_0) + a_2 . (P - P_0)^2$ and $\omega(P) = \omega(P_0) + a_1 . (P - P_0)$ respectively. The Gruneisen parameters γ are calculated by using the relation $\gamma = (\frac{B}{\omega(P0)} \times \frac{\partial \omega}{\partial P})$, where B represents the isothermal bulk modulus (B = 20.60 GPa).

Raman mode	Pressure regions (GPa)	Mode frequency $\omega(P_0)$ (cm^{-1})	a_1 (cm^{-1} GPa^{-1})	a_2 (cm^{-1} GPa^{-2})	γ
A_{1g}	0 - 3.6	126.3±0.1[a]	2.3±0.2[a]	-0.3±0.0[a]	0.38
A_{1g}	3.6 - 6.0	130.2±0.3[b]	0.2±0.0[b]	-	0.03
E_g	0 - 3.6	139.7±0.3[a]	3.9±0.2[a]	-	0.58
E_g	3.6 - 6.0	145.9±2.0[b]	2.1±0.5[b]	-	0.30

[a] Estimated at ambient pressure (P_0 = 1atm), [b] Estimated at P_0 = 3.6 GPa

5.4.1.2 Structural phase transitions in InTe under pressure

To explore the Raman signatures of the pressure induced structural transitions in InTe, a high- pressure Raman scattering experiment was carried out up to ~18.7 GPa, the maximum pressure reached in this study. Figures 5(a) and 5(b) represent the pressure evolution of the Raman spectrum and the pressure-dependent Raman frequencies of InTe up to ~18.7 GPa, respectively. Upon increasing pressure, two major changes are noticed at ~6 and ~15 GPa. The disappearance of the E_g mode and the discontinuity of the A_{1g} mode [Fig. 5(b)] at ~ 6 GPa indicates the structural transition from tetragonal (*B*37) to six-fold coordinated NaCl-type cubic phase (*B*1, SG: $Fm\bar{3}m$, Z = 4) [24,25]. Though the transition occurs near ~6 GPa, the very small intensity of the A_{1g} peak was still observed in 6-7.5 GPa, which suggests the coexistence of the *B*37 phase in the *B*1 cubic phase region. This happens commonly when it is a displacive pressure induced phase transition. Recently, more accurate synchrotron XRD results by Jacobsen *et al*. showed a pressure induced structural transition from NaCl type to eightfold-coordinated CsCl type (*B*2, SG: $Pm\bar{3}m$, Z = 1) at around 14 GPa [25].

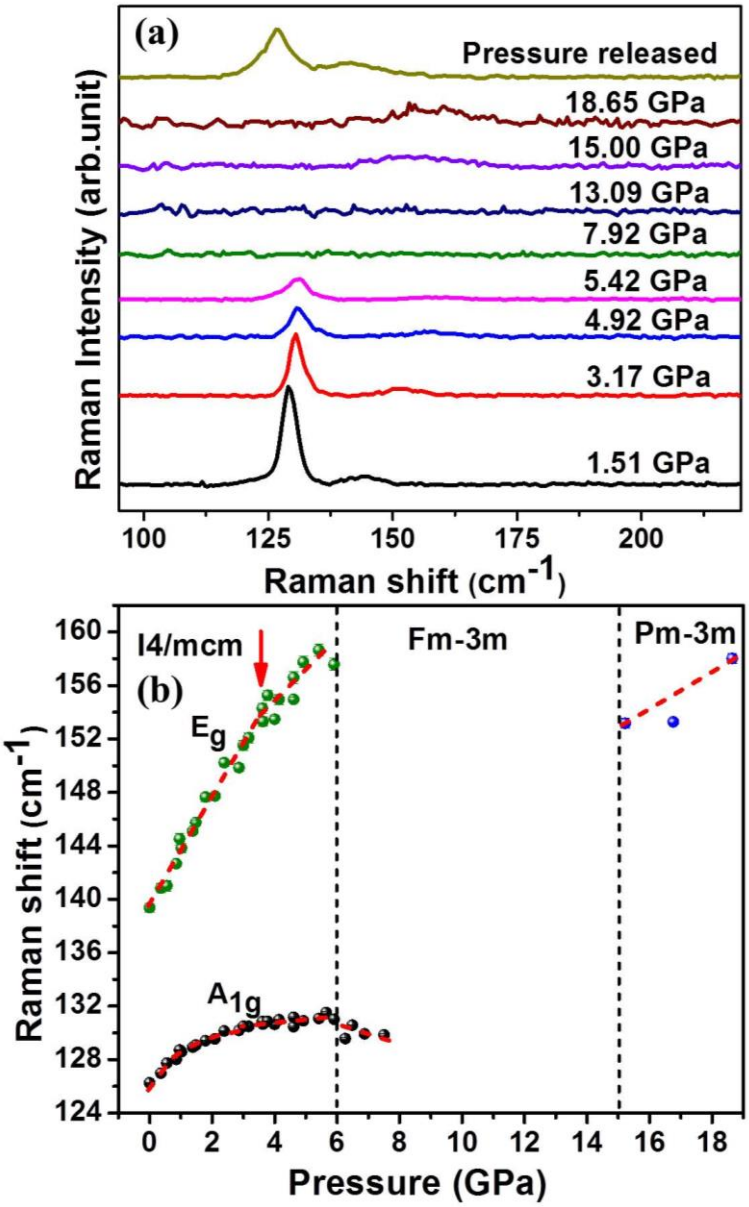

FIG. 5. (a) Pressure evolution of Raman spectrum of InTe at selected pressure values and (b) pressure vs. Raman shift of InTe up to ~18.65 GPa. The vertical dotted lines at ~6 and ~15 GPa represent the structural transition from *B*37 to *B*1 type and *B*1 to *B*2 type respectively. The red dotted line represents a guide to the eye. The solid red arrow at ~3.6 GPa indicates the isostructural electronic transition.

Since factor group analysis for cubic phases of InTe (*B*1 and *B*2) predicts no Raman active modes, it is expected to be impossible to identify the transition point for the NaCl to CsCl-type structural transition using Raman spectroscopy. However, upon increasing pressure, at ~15 GPa, a new mode starts to appear at ~153 cm^{-1}, which is in the *B*2 phase region, as suggested by the XRD measurements [25]. Our observations suggest that

broader linewidth of this new peak may be due to a defect induced mode in the *B*2 type phase, which has been observed in binary semiconductors [32]. There is another possible reason for the observation of broad peaks in Raman spectra of cubic structures, namely, the appearance of the second-order Raman spectra [33]. We observe that the pressure induced structural transition sequences (*B*37→ *B*1 →*B*2) from Raman scattering agree well with results obtained by previous XRD reports and are reversible [22,24,25].

5.4.2 Synchrotron XRD measurements

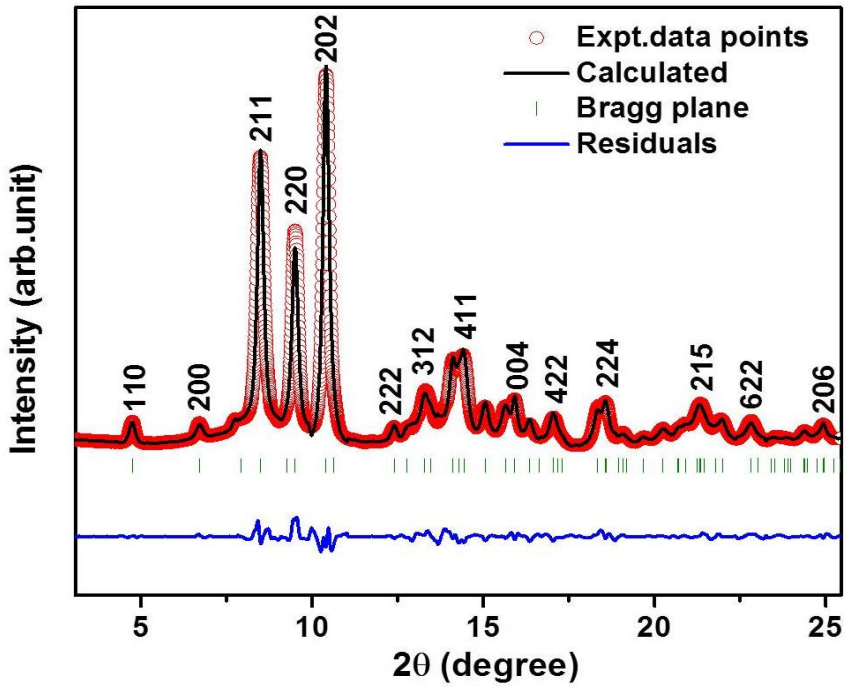

FIG. 6 Rietveld refinement of synchrotron XRD pattern of InTe at ambient conditions (outside DAC). The wavelength of synchrotron XRD used in the experiment is λ = 0.4957 Å.

Earlier XRD studies of the InTe compound under pressure established the structural phase transitions (*B*37→ *B*1 →*B*2) in this system [22,24,25]. However, there was less attention paid to the pressure dependence of the lattice parameters at the low-pressure regime. In order to shed light on the isostructural transition as well as the anisotropic compressibility of the *a* and *c* axes of the tetragonal phase (*B*37) of InTe, we have undertaken systematic high-pressure synchrotron XRD measurements up to ~5.7 GPa only. The ambient XRD pattern (outside DAC) is recorded from a rotating capillary tube (filled with InTe sample) method. The obtained ambient 2D image is converted into a 1D pattern using fit2D software.

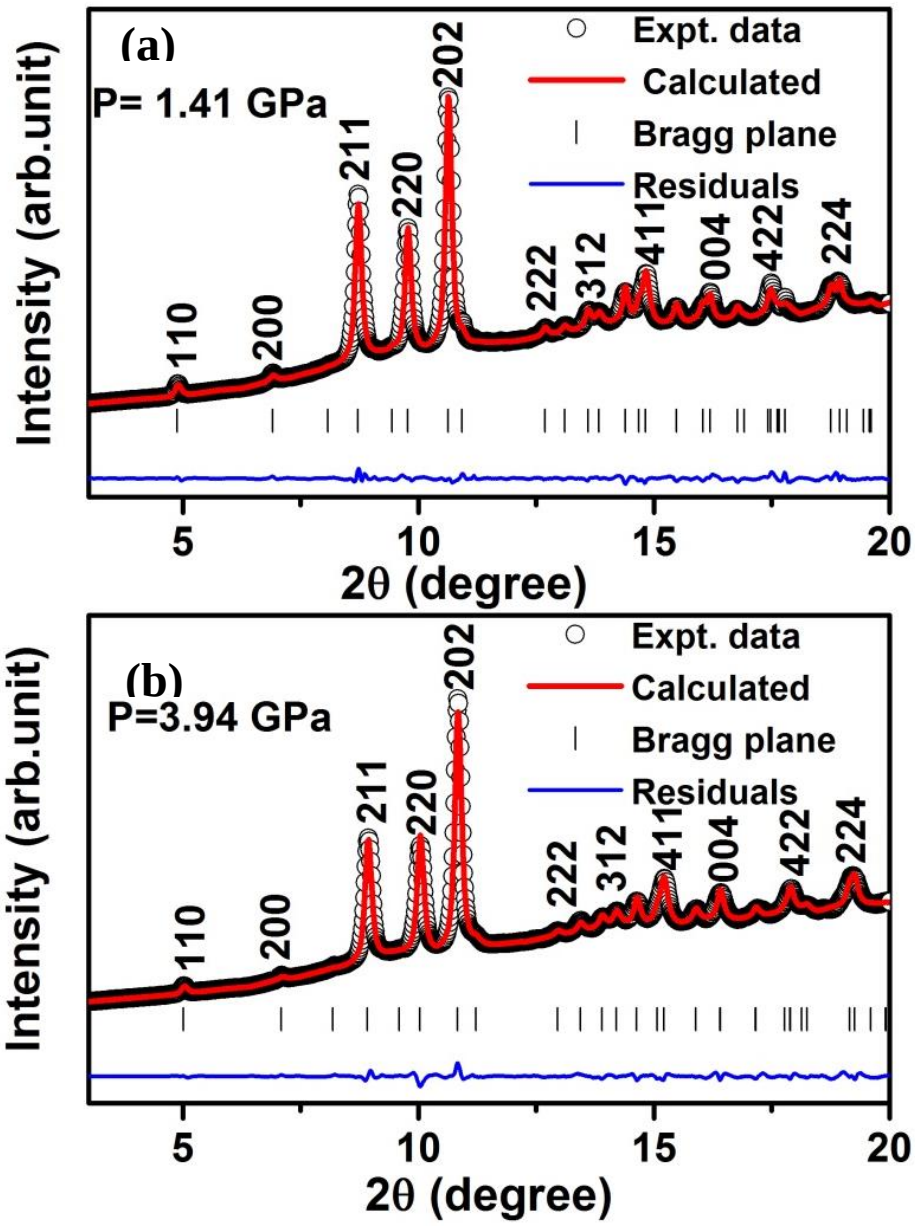

FIG. 7. (a) Le Bail fit to the synchrotron XRD patterns of InTe at ~1.41 GPa (b) 3.94 GPa. The wavelength λ = 0.4957 Å was used for the pressure dependent synchrotron XRD measurements.

The Rietveld refinement of the synchrotron XRD pattern at ambient condition is shown in Fig. 6. The calculated unit-cell parameters are $a = b = 8.4589$ Å, $c = 7.1578$ Å and volume $V = 512.17$ Å^3 and the atomic fractional coordinates of In^{3+}(1), In^{1+}(2), and Te^{2-}(3) are (0, 0, 0.25), (0, 0.5, 0.25), and (0.181, 0.681, 0) respectively, which agree well with the literature [34]. The fitting parameters associated with Fig. 6 are R_p=7.13, R_{wp}=8.00 and chi-square (χ^2) = 0.721. The synchrotron XRD patterns of the

polycrystalline InTe sample show tetragonal phase stability up to ~5.7 GPa, which is in good agreement with our Raman results and recent XRD work [25]. Due to the presence of the texture effect in the obtained XRD patterns, we could not do the full Rietveld refinement. However, we have analyzed the synchrotron XRD patterns for each pressure value by the Le Bail refinement method using Fullprof software [35]. The representative Le Bail fit of the synchrotron patterns at P = 1.41 GPa and P = 3.94 GPa is shown in Figs. 7(a) and 7(b), respectively. The Le Bail refinement method can give the accurate unit-cell parameters (*a*, *b*, *c*, and *V*) within the permitted error bar and their associated fitting parameters are not truly significant. Hence, we did not mention the fitting parameters in Figs. 7(a) and 7(b).

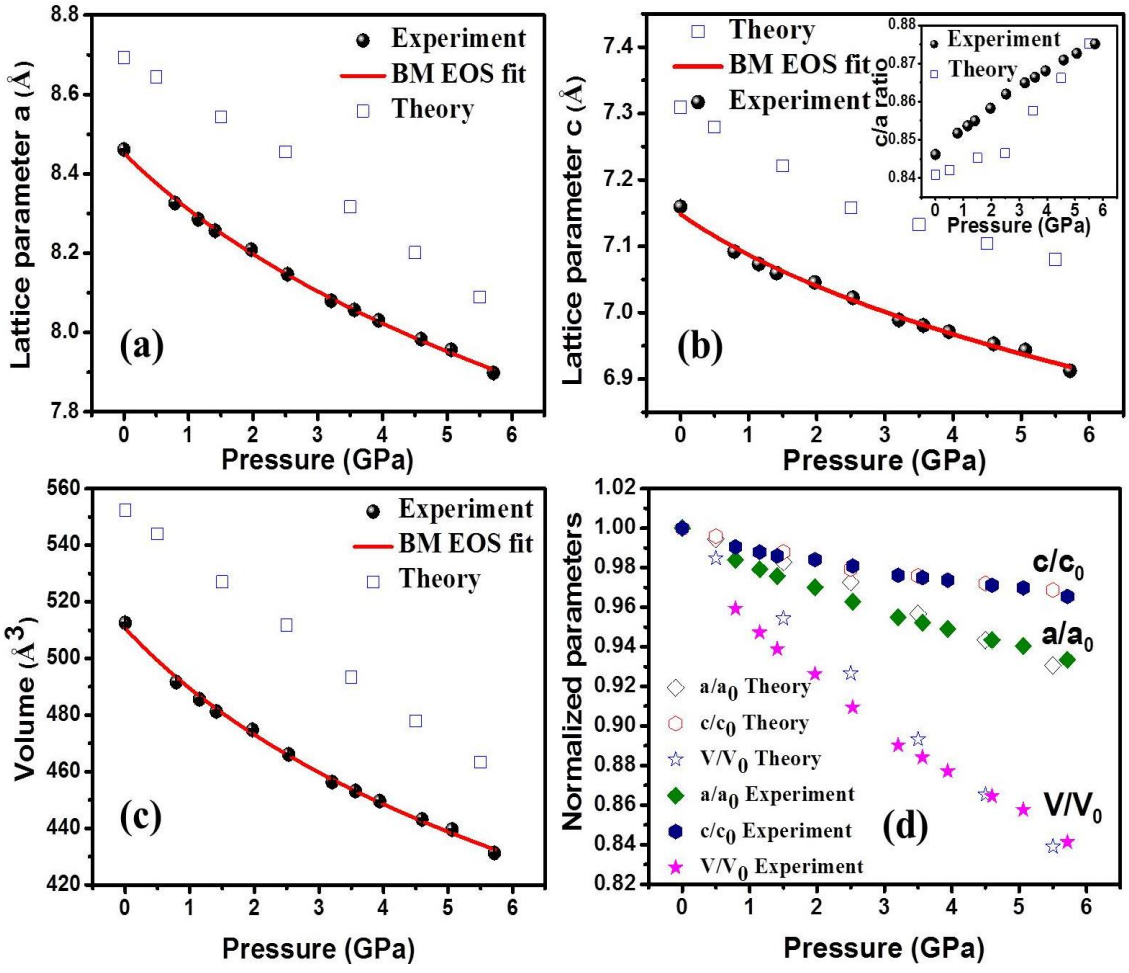

FIG. 8. Experimental and DFT calculated lattice parameters (a) *a*, (b) *c*, (c) *V* and (d) relative unit-cell parameters (a/a_0, c/c_0, and V/V_0) as a function of applied hydrostatic pressure. Here , a_0, c_0, and V_0 are the values of lattice constants (*a*, and *c*) and volume at 0 GPa. The inset of (b) shows the pressure vs. *c/a* ratio. The red solid line represents the third order Birch-Murnaghan equation-of-state fit for the tetragonal phase of InTe.

The pressure dependence of the comparison between the experimental and theoretical lattice parameters (*a* and *c*) of InTe is shown in Figs. 8(a) and 8(b). Figure 8(d) represents the pressure versus relative unit-cell dimensions (a/a_0, c/c_0) and V/V_0 ratio. Also, Fig. 8(d) clearly illustrates the anisotropic compressibility along the *a* and *c* axes. The pressure vs. *a* and *c* of the experimental data is fitted by the third-order Birch Murnaghan equation of state (BM EOS) [36] (discussed in Chapter 1) using EosFit7 software [see Figs. 8(a) and 8(b)]. The fit yields the linear compressibility of lattice parameter *a* , $K_a = K_b = 19.19 \times 10^{-3}$ GPa^{-1}, and that of *b*, $K_c = 10.08 \times 10^{-3}$ GPa^{-1}. Hence, the *c* axis is stiffer than *a* axis, which is consistent with our Raman spectroscopic results and, quantitatively, the *a* axis (and *b* axis) is about 1.9 times more compressible than the *c* axis. Also, the *c/a* ratio increases monotonically with pressure, as shown in the inset of Fig. 8(b). Further, Chattopadhyay *et al.* [22] have shown a decreasing *c/a* ratio (*c* axis is more compressible than *a* axis) in the tetragonal phase of InTe under pressure, which is counter-intuitive with respect to bonding present in the crystal structure and is in contradiction with our results. We like to emphasize here that the axial compressibility (*c/a* ratio) is directly linked to the specific bonding (along *a*, *b*, and *c* axes) in the crystal structure and our results of anisotropic compressibility [*a* (or *b*) and *c* axes] and Raman pressure coefficients of the A_{1g} and E_g modes are consistent with each other and are in line with that expected from the crystal structure bonding in InTe. It is noteworthy that, cell parameters *a*, *c*, and *c/a* ratio do not show any anomalies within the experimental resolution. The experimental pressure-dependent volume is fitted by third-order BM EOS using the equation and the fit yields $B_0 = 20.60$ GPa, $V_0 = 510.69$ Å^3, and derivative of bulk modulus $B_0' = 6.24$, and the obtained values are matching well with the earlier report [25].

5.4.3 Theoretical calculations

To understand the observed isostructural anomaly at ~ 3.6 GPa, first-principles calculations were carried out for the tetragonal phase (*B*37) of InTe as a function of pressure. Our estimates of the optimized lattice constants of InTe are $a = 8.69$ Å and $c = 7.30$ Å, which are overestimated compared to their experimental values [34] ($a = 8.45$ Å and $c = 7.15$ Å), as is typical of GGA-DFT calculations. Variation in the calculated lattice constants (*a* and *c*) with pressure [shown in Figs. 8(a) and 8(b)], agrees with our experiments. The calculated lattice constants are slightly overestimated (~2.7% for *a* and

~2 % for *c*) with respect to their experimental values, but are within the typical errors of DFT calculations using the GGA exchange-correlation functional. As a result of the overestimation of the *a* and *c* lattice constants, the calculated volume [Fig. 8(c)] of the unit cell is also overestimated (by ~7%). More importantly, the calculated pressure dependence of the relative unit-cell parameters a/a_0, c/c_0 and V/V_0 [Fig. 8(d)] agrees remarkably well with their experimental counterparts. Here a_0, c_0, and V_0 are being the lattice constants and volume at 0 GPa. These results suggest that our DFT calculations are in good agreement with experiment.

The calculated *c/a* ratio [see inset of Fig. 8(b)] increases with pressure, also in overall agreement with the experimentally measured *c/a* ratio. Notably, a small deviation in the *c/a* ratio trend is observed between the experiment (like convex shape) and theoretical (like concave shape) values [see inset of Figure 8(b)]. The origin of the concave (DFT calculations) vs. convex (experiment) nature of the *c/a* curve as a function of pressure [see inset of Fig. 8 (b)] can be traced to the pressure dependence of lattice constant *a*. As the DFT-GGA errors in *a* and *c* are slightly different, their calculated response to pressure also has errors. The pressure dependence of the calculated lattice constant *a* is weaker (convex) than that of the measured one[see Fig. 8(a)]. As a result, the calculated *c/a* ratio exhibits a concave dependence whereas the experimental *c/a* ratio shows a convex dependence with the applied pressure, though the difference between them is small.

The electronic structure of InTe calculated with inclusion of the spin-orbit interaction in the Hamiltonian reveals an indirect band gap of 0.04 eV at the optimized lattice constants, which is close to its experimental value [37] of 0.03 eV. The electronic structure of InTe exhibits valleys at the M and Z points at the boundary of the Brillouin zone with similar energies. The VBM at the M valley has slightly higher energy than the VBM at the Z valley [see Fig. 9(a)], whereas the CBM at the Z valley is slightly lower in energy than the CBM at the M valley. With increasing hydrostatic pressure, CBM and VBM in both the valleys come closer to each other and cross, resulting in inversion of CBM and VBM at the M and Z points in the electronic structure of InTe. Band inversions in InTe take place near the pressure region P_c = 1.0-1.4 GPa. Particularly, our calculations reveal that the critical pressures (P_C^M and P_C^Z) of band inversions at the M and Z points are different. This is due to the fact that the band gaps separating the VBM and CBM at the M and Z-

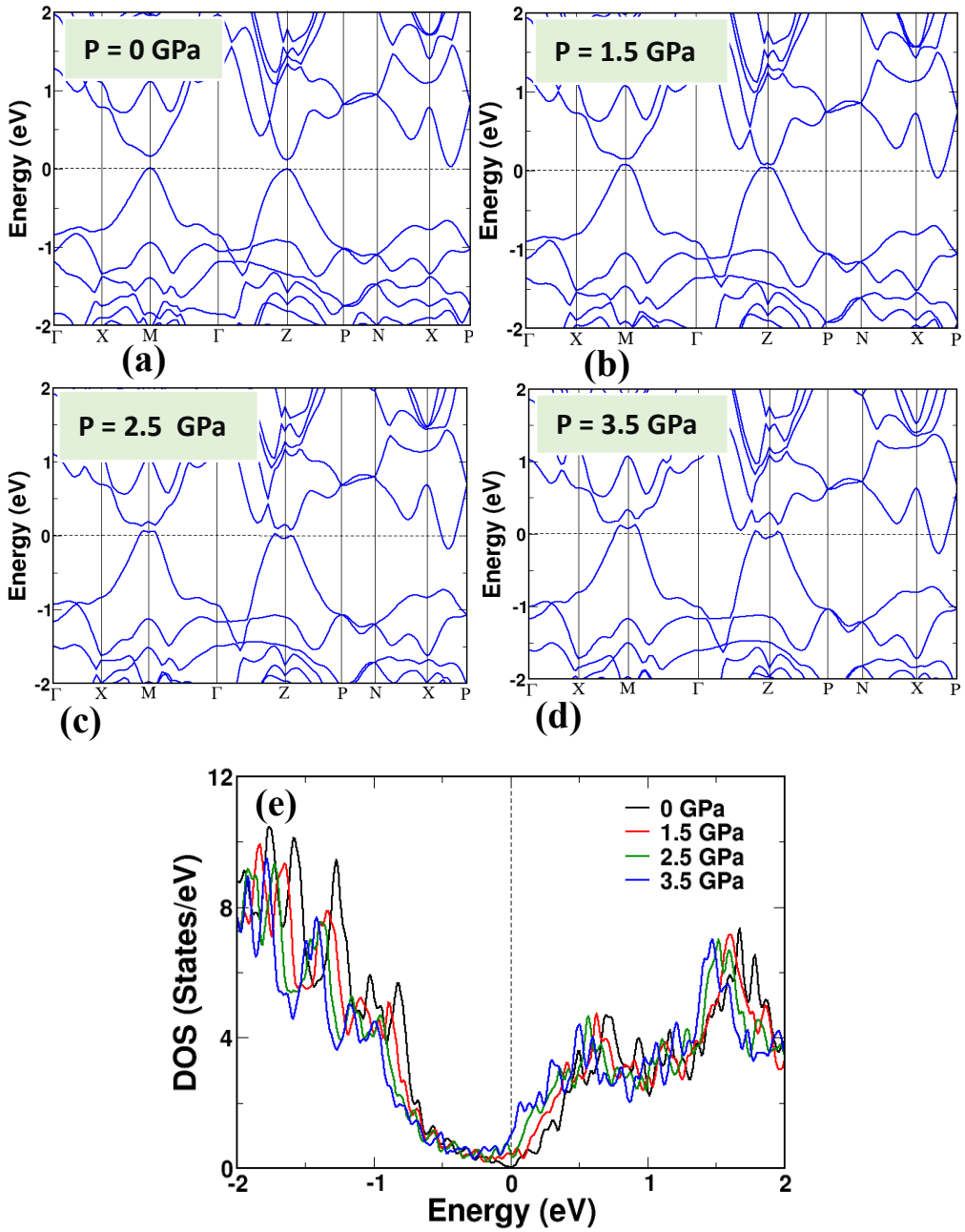

Fig. 9. (a)-(d) Electronic structure and (e) electronic density of states of InTe are calculated with SOC at different hydrostatic pressures. Band inversion takes place at the Z and M points in the Brillouin zone as a function of pressure near P_C^Z = 1 GPa and P_C^M = 1.4 GPa respectively. After the band inversion, the topmost valence band and the bottom conduction band begin to cross the Fermi energy and thereby induce an onset of a semiconductor-to-metal transition in InTe.

points are different [see Figs. 10(a) and 10(c)]. At the Z point, the band inversion occurs in between 0.9 and 1.1 GPa [i.e., 0.9 GPa < P_C^Z < 1.1 GPa, hence P_C^Z ~ 1 GPa], which is evident in the iso-surfaces of charge densities [see Fig. 10(b)] associated with VBM

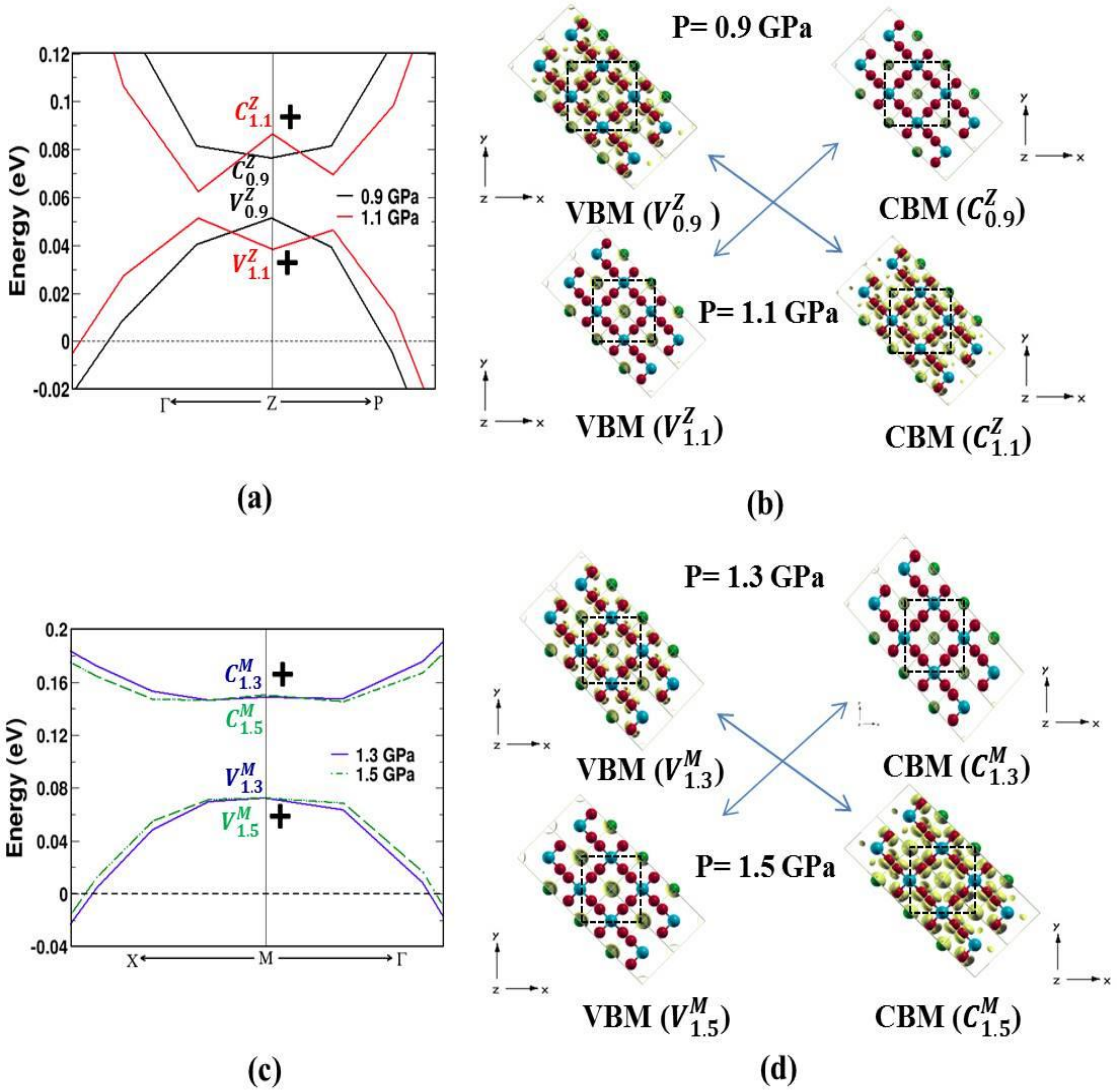

FIG. 10. Electronic structures of InTe around (a) Z, and (c) M points showing the band inversion between the top valence and lowest conduction bands as a function of hydrostatic pressures. The positive signs marked at VBM and CBM denote their parity at the Z and M points. As both of the bands have the same parity, band inversion does not change the bulk electronic topology of InTe. Iso-surfaces of charge densities (b, d) associated with valence and conduction bands (before and after the band inversion) at the Z point ($V^Z_{0.9}$,$V^Z_{1.1}$,$C^Z_{0.9}$, $C^Z_{1.1}$) and the M point ($V^M_{1.3}$, $V^M_{1.5}$, $C^M_{1.3}$, $C^M_{1.5}$) reveal that the band inversion at Z takes place in between 0.9 GPa and 1.1 GPa (i.e., 0.9 GPa < P^Z_C < 1.1 GPa, hence P^Z_C ~ 1 GPa), whereas the band inversion at the M point occurs in between 1.3 GPa and 1.5 GPa (i.e., 1.3 GPa <P^M_C< 1.5 GPa, P^M_C ~ 1.4 GPa). The black dashed box indicates the conventional tetragonal unit cell of InTe.

(denoted with V, i.e., $V^{Z}_{0.9}$, $V^{Z}_{1.1}$) and CBM (denoted with C, i.e., $C^{Z}_{0.9}$, $C^{Z}_{1.1}$) at 0.9 and 1.1 GPa. On the other hand, the band gap separating the VBM and CBM at the M point [see Fig. 10(c)] is slightly higher than the gap between them at the Z point [see Fig. 10(a)]. Hence, higher pressure is required to induce the band inversion at the M point. Looking at the iso-surfaces of charge densities associated with VBM ($V^{M}_{1.3}$, $V^{M}_{1.5}$) and CBM ($C^{M}_{1.3}$, $C^{M}_{1.5}$) at the M point [see Fig. 10(d)] at 1.3 and 1.5 GPa, it is clear that band inversion at the M point occurs in between 1.3 and 1.5 GPa (i.e., 1.3 GPa < P^{M}_{C} < 1.5 GPa, hence P^{M}_{C} ~ 1.4 GPa). As the Fermi level [marked with the dashed horizontal line in Figs. 10(a) and 10(c)] crosses the top valence band around the M and Z points in the Brillouin zone before the critical pressures of band inversions, the system no longer remains semiconducting; rather, it becomes semi-metallic [see the DOS at P=1.5 GPa in Fig. 9(e)].

Figures 10(a)-10(d) shows the band inversions at the Z and M points and their associated isosurfaces of charge densities before and after the critical pressures of band inversions. Band inversion in InTe gives rise to 'M' and 'W'-shaped double-well features in the top of the valence and bottom of the conduction bands at the M and Z points in the Brillouin zone [e.g., see Fig. 10(a)], which are typical signatures of an inverted band structure [19]. In InTe, although band gaps at M and Z remain finite after band inversion, electronic bands close to these points, and along other directions (e.g., X-P) cross the Fermi level, making InTe an ordinary semimetal. This semiconductor to semimetal transition is concomitant with the band inversions at the Z (P^{Z}_{C} = 1 GPa) and M (P^{M}_{C} = 1.4 GPa) points.

5.5 Discussion

The band inversion is the typical indicator of the topological quantum phase transition (TQPT) in material [6,38,39], this motivated us to check the bulk electronic topology of InTe as a function of pressure. Symmetry analysis shows that the parity of the electronic wave functions for VBM and CBM at the M and Z points is even. Hence, we expect the band inversion not to change the topology of the bulk electronic structure. To confirm this symmetry based argument, we determined the Z_2 topological index using a robust and more accurate method as implemented in the Z2Pack code [40]. The calculated Z_2 topological invariant (υ_0) of InTe remains zero before and after the band

inversion, confirming no change in the electronic topology, and establishing the trivial band topology of InTe that remains unchanged through P = P_C^Z and P = P_C^M. Although the onset of a metallic state in InTe begins with band inversion near P ~1 GPa, the complete metallization occurs only at P ≥ 3.5 GPa, where both valence and conduction bands cross the Fermi level along several directions in the Brillouin zone, and DOS increases significantly across the Fermi level [see the DOS at P = 3.5 GPa in Fig. 9(e)]. The DOS above the Fermi level at ~3.5 GPa are mostly contributed by 5s orbitals of In^{3+} and 5p orbital of In^{1+} ions. These band inversions (P_C^Z= 1 GPa and P_C^M = 1.4 GPa) and the complete metallization (P = 3.5 GPa) occur well below the critical pressure (~6 GPa) of the structural phase transition (*B*37 to *B*1 structure).

Experimentally, we do not find any anomalies (within the experimental resolution) associated with a beginning of the predicted band inversion around ~1.0-1.4 GPa. This band inversion causes a small change in the electronic band structure, whereas the subsequent metallization introduces drastic change in it. In principle, a long-wavelength optical phonon linewidth can measure the band inversion via the electron-phonon coupling mechanism and has been reported for many compounds [4,6,38,41]. Generally, the Raman linewidth has the significant contribution from electron-phonon interactions and anharmonic phonon-phonon interactions. The phonon-phonon coupling is independent of an electronic carrier density, and hence it does not contain any information about the band inversion. In our case, as seen from Fig. 4(a), the quadratic nature of the A_{1g} mode [i.e., the nonlinear (second order) pressure coefficient of the A_{1g} mode] as a function of pressure up to ~3.6 GPa indicates strong anharmonic phonon-phonon coupling existing in the system. Further, recently calculated [23] phonon dispersion of the InTe at the experimental lattice constants revealed an almost flat negative-frequency branch along the Γ-X-M-Γ direction in the Brillouin zone, which also supports the existence of strong anharmonic phonon-phonon interactions in InTe. The negative-frequency modes [the phonon frequency value from the calculated phonon dispersion curve is negative (i.e., imaginary)] in InTe mainly involves displacement of In^{+1} cations along the *z*-direction, which was shown to scatter a heat-carrying acoustic phonon through anharmonic phonon-phonon interactions, and thereby giving rise to ultralow lattice thermal conductivity of InTe [23]. Hence, the presence of strong anharmonic phonon-phonon interactions at low pressure ranges may be limiting the

detection of the small electronic change (electron-phonon coupling) caused by band inversion at ~1.0-1.4 GPa [41]. Further, this work may be the typical example, where strong phonon-phonon coupling presents; it is quite difficult to use Raman linewidth as an indirect signature for detecting the band inversion.

Upon complete metallization, the interaction between electrons and phonons is initiated, and the strength of electron-phonon coupling is expected to increase, which probably causes the sudden jump in the FWHM of the A_{1g} and E_g modes seen in our experiment near P = 3.6 GPa [see Figs. 4(c) and 4(d)]. Although the phonon-phonon interaction is significant in InTe (at ambient conditions) due to the presence of unstable phonon modes, the renormalization of phonon frequencies is relatively weak, hence the change in FWHM of observed Raman active modes is mainly due to electron-phonon interaction. There are several observations of a decreasing trend in the intensity of a first-order Raman mode under pressure [42,43]. However, here we have clearly observed a sudden change in the decreasing trend of the phonon modes' (A_{1g} and E_g) intensity [see Figs. 4(e) and 4(f)] at ~3.6GPa, which may be caused by electronic changes in InTe. The calculated DOS of InTe at around 3.5 GPa reveals metallization and we have observed anomalies in the frequency and linewidth of both modes (A_{1g} and E_g) around this pressure. Metallization due to the increased DOS increases the number of conduction electrons which would screen the incident electromagnetic light. Consequently, this will effect the Raman scattering cross section in the case of InTe. It could be one of the plausible reasons for the sudden decrease in the inelastically scattered light (Raman) intensity in InTe at high-pressure metallic regions. Earlier transport measurements showed that the coexistence of the structural transition (*B*37 to *B*1) and semiconductor-to-metal transition is due to the complete transformation of In^{3+} and In^{1+} to In^{2+} [26]. Here, our results suggest that the metallization occurs in the tetragonal phase (*B*37) itself at ~3.6 GPa and this may act as a precursor for the structural transition to cubic phase (*B*1) at P ~ 6 GPa. Mention must be made that this type of pressure induced metallization without changing the oxidation state of Tl (Tl^{1+} and Tl^{3+}) was observed in the prototype compound TlSe (*B*37 phase) at ~2.7 GPa [44].

The obtained band inversion in InTe compound is unique, and to the best of our knowledge, there is no such observation in the literature. In InTe compound, the same parity (+) was observed in both the VBM (mostly contributed by 5p orbitals of Te^{2-}) and

CBM (mostly contributed by 5p orbitals of In^{1+}). In fact, this is a major constraint for the TQPT in InTe. So, tuning of the orbital contributions through suitable doping or substitution in either one of the parity may lead to the possibility of TQPT in this InTe. For instance, chemical substitutions induced TQPT was observed in $TlBi(S_{1-x}Se_x)_2$ [45], $Pb_{1-x}Sn_xSe$ [46], $Bi_{1-x}Sb_x$ [47] systems without any structural transformations. Hence, we hope our result will motivate researchers to look for the possibility of modulating the parity change in InTe by altering its chemical identity (orbital characters) through suitable doping or substitution to get the non-trivial topological phase in this material. Since an even number of band inversions in a crystal with mirror symmetry generally gives rise to the topological crystalline insulating (TCI) phase (e.g., in SnTe [48] or PbTe [49]), here the possibility of having the TCI phase is not completely ruled out. So, we speculate that this kind of band inversion will lead to a significant amount of further research and detailed studies of possible topological phase transitions in InTe. Also, due to its metallization properties in a relatively low-pressure range, InTe can be used as pressure-conducting switches and pressure sensors.

5.6 Conclusions

In summary, we have explored the lattice dynamical properties of InTe under hydrostatic compression up to ~19 GPa. Our Raman spectroscopic experiment reveals pressure induced structural transitions ($B37 \rightarrow B1 \rightarrow B2$) in InTe which shows agreement with the earlier XRD experiments. Further, an isostructural electronic transition is seen from the anomalies in the FWHM of phonon modes (E_g and A_{1g}) at a relatively low pressure around 3.6 GPa. DFT calculations show that the observed anomalies are associated with a pressure induced metallization near 3.6 GPa. The pressure coefficient of the A_{1g} and E_g modes is well correlated with the variation in lattice parameters *a* and *c* under pressure. Though InTe exhibits band inversion as a function of hydrostatic pressure, there is no change in its electronic topology ($Z_2 = 0$) since it retains the same parity. Tuning of the parity with obtained band inversions in InTe may be achieved either via doping or substitutions that can open the door to considerable development of the topological phase transitions in this system.

5.7 Bibliography

1. M. S. Bahramy, B. J. Yang, R. Arita, and N. Nagaosa, Nat. Commun. **3**, 679 (2012).
2. Z. Zhao, H. Zhang, H. Yuan, S. Wang, Y. Lin, Q. Zeng, G. Xu, Z. Liu, G. K. Solanki, K. D. Patel, Y. Cui, H. Y. Hwang, and W. L. Mao, Nat. Commun. **6**, 7312 (2015).
3. A. P. Nayak, S. Bhattacharyya, J. Zhu, J. Liu, X. Wu, T. Pandey, C. Jin, A. K. Singh, D. Akinwande, and J. F. Lin, Nat. Commun. **5**, 3731 (2014).
4. V. Rajaji , U. Dutta, P. C. Sreeparvathy, S. C. Sarma, Y. A. Sorb, B. Joseph, S. Sahoo, S. C. Peter, V. Kanchana, and C. Narayana, Phys. Rev. B **97**,085107 (2018).
5. R. F. Frindt, R. B. Murray, G. D. Pitt, and A. D. Yoffe, J. Phys. C **5**, L154 (1972).
6. A. Bera, K. Pal, D. V. S. Muthu, S. Sen, P. Guptasarma, U. V. Waghmare, and A. K. Sood, Phys. Rev. Lett. **110**, 107401 (2013).
7. O. Gomis, R. Vilaplana, F. J. Manj´on, P. Rodr´ıguez-Hern´andez, E. P´erez-Gonz´alez, A. Mu˜noz, V. Kucek, and C. Drasar, Phys. Rev. B **84**, 174305 (2011).
8. R. Vilaplana, O. Gomis, F. J. Manj´on, A. Segura, E. P´erez-Gonz´alez, P. Rodr´ıguez-Hern´andez, A. Mu˜noz, J. Gonz´alez, V. Mar´ın-Borr´as, V. Mu˜noz-Sanjos´e, C. Drasar, and V. Kucek, Phys. Rev. B **84**, 104112 (2011).
9. R. Vilaplana, D. Santamar´ıa-P´erez, O. Gomis, F. J. Manj´on, J. Gonz´alez, A. Segura, A. Mu˜noz, P. Rodr´ıguez-Hern´andez, E. P´erez-Gonz´alez, V. Mar´ın-Borr´as, V. Mu˜noz- Sanjose, C. Drasar, and V. Kucek, Phys. Rev. B **84**, 184110 (2011).
10. Y. A. Sorb, V. Rajaji, P. S. Malavi, U. Subbarao, P. Halappa, S. C. Peter, S. Karmakar, and C. Narayana, J. Phys.: Condens. Matter **28**, 015602 (2016).
11. W. Feng, W. Zhu, H. H. Weitering,G. M. Stocks, Y. Yao, and D. Xiao, Phys. Rev. B **85**, 195114 (2012).
12. Y. Ma, Y. Dai, L.Yu, C. Niu, and B. Huang, New J. Phys. **15**, 073008 (2013).
13. C. Niu, P. M. Buhl, G. Bihlmayer, D. Wortmann, S. Blügel, and Y. Mokrousov, Nano Lett. **15**, 6071 (2015).
14. M. Z. Hassan, and C. L. Kane, Rev. Mod. Phys. **82**, 3045 (2010).

15. L. Fu, C. L. Kane, and E. J. Mele, Phys. Rev. Lett. **98**, 106803 (2007).
16. X. Xi, C. Ma, Z. Liu, Z. Chen, W. Ku, H. Berger, C. Martin, D. B. Tanner, and G. L. Carr, Phys. Rev. Lett. **111**, 155701 (2013).
17. A. Ohmura, Y. Higuchi, T. Ochiai, M. Kanou, F. Ishikawa, S. Nakano, A. Nakayama, Y. Yamada, and T. Sasagawa, Phys. Rev. B **95**,125203 (2017).
18. W. Feng, and Y. Yao, Science China Physics, Mech. Astron. **55**, 2199 (2012).
19. K. Pal, S. Anand, and U. V. Waghmare, J. Mater. Chem. C **3**, 12130 (2015).
20. M. Z. Torres, J. L. Pena, Y. P. Mascarenhas , R. C. Rodríguez, M. M. Lira, and O. Calzadilla, Superficies Vacio **13**, 69 (2001).
21. J. J. Wang, F. F.. Cao, L. Jiang, Y. G. Guo, W. P. Hu, and L. J. Wan, J. Am. Chem. Soc. **131**, 15602 (2009).
22. T. Chattopadhyay, R. P. Santandrea, and H. G. Von Schnering, J. Phys. Chem. Solids **46**, 351 (1985).
23. M. K. Jana, K. Pal, U. V. Waghmare, and K. Biswas, Angew. Chem., Int. Ed. **55**, 7792 (2016).
24. T. Chattopadhyay, R. P. Santandrea, and H. G. Von Schnering, Physica **139**, 353(1986).
25. M. K. Jacobsen, Y. Meng, R. S. Kumar, and A. L. Cornelius, J. Phys. Chem. Solids **74**, 723 (2013).
26. S. Pal, D. N. Bose, S. Asokan, and E. S. R. Gopal, Solid State Commun. **180**, 753 (1991).
27. V. Rajaji, P. S. Malavi, S. S. Yamijala,Y. A. Sorb, U. Dutta, S. N. Guin, B. Joseph, S. K. Pati, S. Karmakar, K. Biswas, and C. Narayana, Appl. Phys. Lett. **109**, 171903 (2016).
28. A. Bera, A. Singh, DVS Muthu, U. V. Waghmare, and A. K. Sood, J. Phys. Condens.: Matter **29,** 105403 (2017).
29. G.V. P. Kumar, and C. Narayana , Curr. Sci. **93**, 778 (2007).
30. M. A. Nizametdinova, Phys. Status Solidi B **97**, K9 (1980).
31. A. Bera, K. Pal, DVS Muthu, U. V. Waghmare, and A. K. Sood, J. Phys.: Condens. Matter **28**, 105401 (2016).
32. I. Efthimiopoulos, J. Zhang, M. Kucway, C. Park, R. C. Ewing, and Y. Wang, Sci. Rep. **3**, 2665 (2013).
33. A. C. Ho, R. C. Hanson and A. Chizmeshya, Phys. Rev. B **55**, 14818 (1997).

34. J. H. C. Hogg, H. H. Sutherland, Acta Cryst. B **B32**, 2689 (1976).
35. J. R. Carvajal, Phys. B **192**, 55 (1993).
36. F. D. Murnaghan, Proc. Nat. Acad. Sci. U.S.A. **30**, 244 (1944).
37. M. Parlak, C. Ercelebi, I. Gunal, H. Ozkan, and N. M. Gasan, Cryst. Res. Technol. **31**, 673 (1996).
38. S. N. Gupta, A. Singh, K. Pal, B. Chakraborti, D. V. S. Muthu, U. V. Waghmare, and A. K. Sood, Phys. Rev. B **96**, 094104 (2017).
39. K. Pal and U. V. Waghmare, Appl. Phys. Lett. **105**, 062105 (2014).
40. D. Gresch, G. Autès, O. V. Yazyev, M. Troyer, D. Vanderbilt, B. A. Bernevig, and A. A. Soluyanov, Phys. Rev. B **95**, 075146 (2017).
41. K. Saha, K. Légaré, and I. Garate, Phys. Rev. Lett. **115**, 176405 (2015).
42. D. Olego and M. Cardona, Phys. Rev. B **25**, 1151 (1982).
43. G. Lucazeau, J. Raman Spectrosc. **34**, 478 (2003).
44. M. K. Rabinal, S. Asokan, M. O. Godazaev, N. T. Mamedov, and E. S. R. Gopal, Phys. Status Solidi B **167**, K97 (1991).
45. S. Y. Xu, Y. Xia, L. A. Wray, S. Jia, F. Meier, J. H. Dil, J. Osterwalder, B. Slomski, A. Bansil, H. Lin, R. J. Cava, and M. Z. Hasan, Science **332**, 560 (2011).
46. P. Dziawa, B. J. Kowalski, K. Dybko, R. Buczko, A. Szczerbakow, M. Szot, E. Łusakowska, T. Balasubramanian, B. M. Wojek, M. H. Berntsen, O. Tjernberg, and T. Story, Nat. Mater. **11**, 1023 (2012).
47. D. Hsieh, D. Qian, L. Wray, Y. Xia, Y. Hor, R. J. Cava, and M. Z. Hasan, Nature (London) **452**, 970 (2008).
48. T. H. Hsieh, H. Lin, J. Liu, W. Duan, A. Bansil, and Liang Fu, Nat. Commun. **3**, 982 (2012).
49. P. Barone,T. Rauch, D. Di Sante, J. Henk, I. Mertig, and S. Picozzi, Phys. Rev. B **88**, 045207 (2013).

Chapter 6

Pressure induced structural, electronic topological and semiconductor to metal transition in $AgBiSe_2$

The author's main contribution in this chapter is the core research idea, performing the high pressure Raman and synchrotron XRD measurements on $AgBiSe_2$ sample and analyzing the data. To execute this research problem, we have collaborated with Prof. Kanishka Biswas's group, JNCASR, Bangalore for sample synthesis, Prof. Swapan K. Pati's group, JNCASR, Bangalore for the first principles theoretical calculations and Dr. S. Karmakar's group, BARC, Mumbai for electrical transport measurements.

V. Rajaji, Pallavi S. Malavi, Sharma S. R. K. C. Yamijala, Y. A. Sorb, Utpal Dutta, Satya N. Guin, B. Joseph, Swapan K. Pati, S. Karmakar, Kanishka Biswas, and Chandrabhas Narayana, "*Pressure induced structural, electronic topological, and semiconductor to metal transition in $AgBiSe_2$*" , *Appl. Phys. Lett*. **109**, 171903 (2016).

6.1 Introduction

The semiconducting narrow band gap chalcogenide based compounds with strong spin orbit coupling (SOC) has recently received increasing attention on account of their high thermoelectric and topological insulating properties [1,2]. For instance, binary semiconducting layered chalcogenides, *viz*., Bi_2Se_3, Bi_2Te_3 and Sb_2Te_3 have been shown as examples of a 3D topological insulators at ambient conditions which might have potential applications in spintronics and quantum computing applications [2-4]. Ternary semiconducting class of I-V-VI_2 (where I= Cu, Ag or alkali metal; V= Sb, Bi; VI = Se, Te, S) compounds exhibit intrinsic ultralow thermal conductivity due to bond anharmonicity caused by ns^2 lone pair of group V cation [5-7]. This makes them to exhibit high thermoelectric figure of merit (ZT). Further, under high pressure conditions, semiconducting materials with strong SOC exhibit exotic features which are discussed in Chapter 1 (section 1.9). In particular, ETT is one of the technologically important phenomena due to its ability of enhancement in thermoelectric (TE) power [8,9]. Recall that ETT is mainly caused by the drastic changes in the topology of electronic Fermi surface and the most direct tool to detect is the angle resolved photoemission spectroscopy (ARPES) (like TQPT) which shows the changes in the electronic band structure of the materials. But, there is no sophisticated technique to implement ARPES study under high pressure. Since ETT causes significant changes in transport properties, it can be identified indirectly through changes in the resistivity and TE power measurements [8,10,11]. ETT can also be detected by Raman line width studies due to electron-phonon coupling [12-16]. In addition, observed pressure induced ETT can be simulated by chemical substitutions by varying cationic radius ratios to achieve the same at ambient conditions. Besides, the pressure induced semiconductor to metal transition is another interesting phenomenon which is caused by the charge density redistribution during overlapping of atomic orbitals. Electrical resistivity and Raman line width study are influenced by the semiconductor to metal transition [17,18].

$AgBiSe_2$ is a narrow band gap (~ 0.6 eV) semiconductor which crystallizes in ordered hexagonal structure (SG $P\bar{3}m1$, Z=3) at ambient conditions and shows intriguing temperature dependent structural order-disorder phase transition behavior [19,20]. Bulk form of $AgBiSe_2$ exhibits the high ZT of ~ 1 due to intrinsic low lattice thermal conductivity caused by bond anharmonicity [19] and it shows n-type conduction when

doped with Nb and halogen [19,20]. Nanocrystalline $AgBiSe_2$ shows p-n-p type conduction switching during structural phase transition [21].

The presence of strong SOC in $AgBiSe_2$ and its symmetrical equivalence ($\bar{3}m1$) with binary layered chalcogenide α-Bi_2Se_3 has motivated us to see if $AgBiSe_2$ too exhibit the identical behavior under high pressure. For instance, α-Bi_2Se_3 (SG: $R\bar{3}m$, Z=1) is a narrow band gap, strong SOC, 3D topological insulator and shows exotic properties under pressure [11,14]. Hence it would be very interesting to study the chemically similar narrow band gap semiconductor $AgBiSe_2$ in order to explore its pressure induced structural and electronic transitions. To the best of our knowledge, this is the first high pressure study on this class of compounds, namely, $AgBiSe_2$. In addition to the fundamental interest, knowledge of $AgBiSe_2$ characteristics under pressure may be also useful for fabrication of thermoelectric device operating in a mechanically strained environment.

In this chapter, we have investigated pressure dependent synchrotron powder X-ray diffraction (XRD), electrical resistivity and Raman scattering measurements up to a maximum pressure of around 21 GPa on $AgBiSe_2$. The XRD and Raman scattering results clearly show that $AgBiSe_2$ undergoes pressure induced structural transition from hexagonal $P\bar{3}m1$ (α-$AgBiSe_2$) to rhombohedral $R\bar{3}m$ (β-$AgBiSe_2$) at ~ 0.7 GPa. Furthermore, electrical transport and phonon line width anomalies provides evidence that β-$AgBiSe_2$ undergoes pressure induced ETT and semiconductor to metal transition at ~2.8 and ~7 - 8.9 GPa respectively. Raman scattering measurement also indicate that the β-$AgBiSe_2$ stable up to ~20.7 GPa. The first principles calculations based on density functional theory were performed to understand ETT and the atomic level origin of semiconductor to metal transition under pressure.

6.2 Experimental details

Elemental silver (Ag, 99.999%, metal basis), elemental bismuth (Bi, 99.9999%, metal basis), elemental selenium (Se, 99.999%, metal basis) were purchased from Alfa Aesar and used as starting materials. Polycrystalline $AgBiSe_2$ (~1 g) was synthesized by elemental melting reaction, mixing appropriate ratios of high-purity elemental Ag, Bi and Se in a quartz tube. The tube was flame sealed under high vacuum (~10^{-5} Torr) and slowly heated to 673 K over a period of 12 h, then heated up to 1123 K in 4 h, soaked for

10 h, and subsequently slow cooled to room temperature over a period of 12 hrs [20]. Powder XRD for the synthesized $AgBiSe_2$ sample were recorded using laboratory Bruker D8 diffractometer with Cu K_α (λ = 1.5406 Å). The obtained ambient X-ray diffraction pattern of α-$AgBiSe_2$ is matching well with the JCPDS pattern (no: 29-1441) and also confirms that there is no secondary phase up to its detection limit.

The pressure was generated by Mao Bell type diamond anvil cell (DAC) with diamonds of culet size 400 μm for the synchrotron XRD and Raman scattering measurements. High pressure powder XRD measurement was carried out up to 12 GPa at the XRD1 beam line of the ELETTRA synchrotron radiation, using a monochromatic beam of wavelength 0.7000 Å. The other synchrotron XRD measurement and analysis details are the same as mentioned in Chapter 3 (section 3.2). In addition, the typical exposure time for data accumulation was 20 minutes. The procedures of gasket preparation, PTM and pressure calibration is the same as mentioned in Chapters 2 and 3 (section 3.2). Raman spectroscopy measurements were conducted on a custom-built Raman spectrometer which are discussed in Chapter 2. The power of the sample kept well below 0.5 mW in order to avoid the light induced damage of the sample. The data acquisition for each Raman spectrum was about 45 minutes.

The experimental details of resistivity measurements are the same as discussed in Chapter 4 (section 4.2). In addition, the pressure dependence of resistivity at room temperature and at low temperature down to 170 K have been performed on a pressed pellet of $AgBiSe_2$ sample (of diameter~50 μm and ~20 μm thick) up to ~12 GPa using a miniature DAC mounted in an optical cryostat.

6.3 Computational methods

We have optimized $AgBiSe_2$ ($R\bar{3}m$ phase) at various pressures and we have calculated the corresponding band structures, density of states (DOS) and projected DOS (pDOS) using density functional theory (DFT) within the generalized gradient approximation and with SOC, as implemented in the QUANTUM ESPRESSO (QE) code [22]. Perdew-Burke-Ernzerhof (PBE) exchange-correlation functional [23] and ultrasoft relativistic pseudo-potentials [24] are considered throughout these calculations. For geometry optimizations, a 6×6×6 Monkhorst-Pack k-grid, 60 Ry energy cutoff, 480 Ry charge cutoff and 0.04 Ry Marzari-Vanderbilt cold smearing are used. K-grid has been

increased from 6×6×6 to 10×10×10 grid during DOS and pDOS calculations, and for band structure calculations, a minimum of 30 k-points are used between any two high symmetry points.

For geometry optimization, first we took the experimental lattice constants (at zero pressure) and optimized them using non-relativistic 'variable-cell-relax' calculations. These optimized lattice parameters and atomic coordinates (at zero pressure) are used to obtain the optimized structures at various values of pressure. For a particular pressure value, optimized lattice parameters and atomic coordinates from non-relativistic calculations have been directly used to calculate the band structure, DOS and pDOS, considering additionally the SOC. We considered the systems to be fully optimized when the forces acting on all the atoms are less than 10^{-4} Ry/Bohr. For finding the Raman modes, we have used Perdew-Zunger exchange-correlation functional along with norm-conserving pseudo-potentials. Stricter convergence criteria (10^{-5} Ry/Bohr force cutoff) and larger k-grids (10×10×10) have been used while performing the normal mode calculations (to get rid of the negative frequencies). 80 Ry energy cut off and 320 Ry charge cutoff are used during these calculations.

6.4 Results and discussion

6.4.1 Synchrotron XRD measurements under pressure

The α-$AgBiSe_2$ compound crystallizes in hexagonal structure with space group $P\bar{3}m1$ and the triple primitive hexagonal unit cell as shown in Fig. 1(a), which also shows the Rietveld fitting of synchrotron XRD pattern at ~0.12 GPa. The calculated lattice parameter values for the α-$AgBiSe_2$ is a = 4.1886 Å, c = 19.6540 Å and V = 298.61 Å^3. Since the texture affects the obtained XRD pattern strongly, the refined atomic fractional coordinates are considered unreliable. Hence, only the lattice parameters were extracted with the permitted error. The representative XRD patterns of $AgBiSe_2$ at various pressures are shown in Fig. 2. It is evident from Fig. 1(b), at 0.7 GPa α-$AgBiSe_2$ undergoes a structural phase transition from hexagonal (SG: $P\bar{3}m1$, Z = 3) to rhombohedral (S.G: $R\bar{3}m$, Z = 1) called here as β-$AgBiSe_2$, which is structurally identical to the 3D topological insulator Bi_2Se_3 [14].

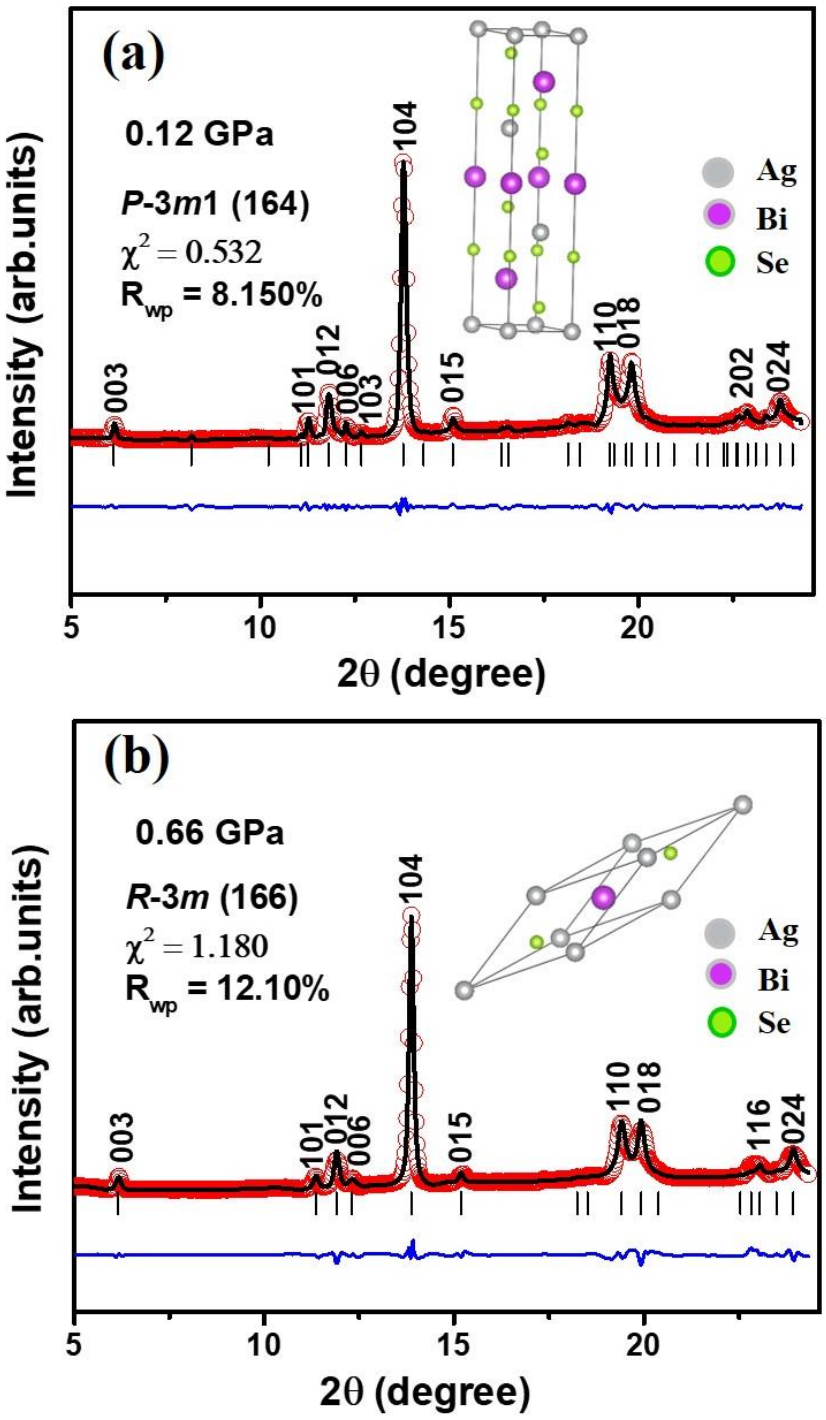

FIG. 1. Rietveld fit to the synchrotron XRD pattern for (a) α-$AgBiSe_2$ and (b) β-$AgBiSe_2$.

In this centro-symmetric hexagonal (β-$AgBiSe_2$) structure, both Ag and Bi/Se can act as inversion centers and Ag, Bi, and Se are located at the (0, 0, 0), (0.5, 0.5, 0.5), and (0.26, 0.26, 0.26) sites, respectively. The β-$AgBiSe_2$ contains four atoms in the unit cell and each Ag/Bi layer is stacked between two Se layers as shown in Fig. 1(b). At ~0.66 GPa, one Bragg reflection (103) disappears and the remaining reflection satisfies the condition (-h+k+l = 3n) of rhombohedral symmetry ($R\bar{3}m$) which is the clear indication of the symmetry change. Mention must be made that this $AgBiSe_2$ compound exhibits similar symmetry change induced by high temperature [25]. Even though $P\bar{3}m1$ is not a subgroup of $R\bar{3}m$, the volume change from α phase to β phase is around 1.14 % only. Hence the obtained transition can probably be due to second order transition.

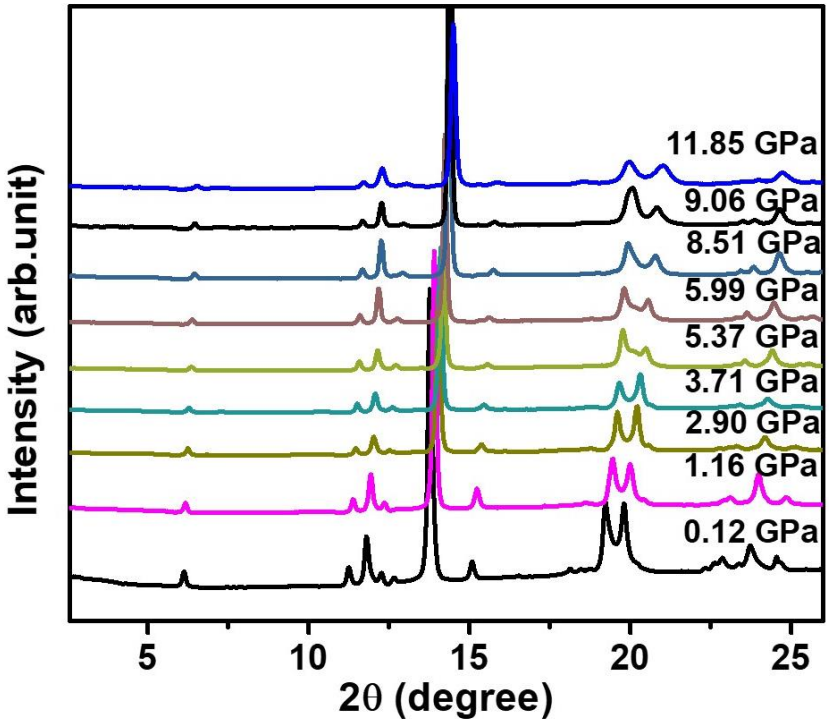

FIG. 2. Representative synchrotron powder XRD patterns of $AgBiSe_2$ at various selected pressure up to 11.85 GPa.

The pressure dependence of *c/a* ratio and volume of $AgBiSe_2$ are shown in Figs. 3 and 4. It is clear from Fig. 3, there is a maximum at 0.7 GPa between the hexagonal (α-$AgBiSe_2$) and rhombohedral (β-$AgBiSe_2$) evidence the structural transition. The systematic decrease in *c/a* ratio is observed in high pressure phase β-$AgBiSe_2$, which directly indicates that the compressibility of *c* axis is larger than *a* axis. The pressure-volume curves for β-$AgBiSe_2$ phase were fitted using a third-order Birch-Murnaghan

equation of state (BM-EOS) (discussed in Chapter 1) as shown in Fig. 4. The BM-EOS fit yields the bulk modulus, B_0 = 50.79 GPa, its pressure derivative, B_0' = 7.79, and volume V_0 = 295.83 $Å^3$ at zero pressure. Table I summarizes the structural and EOS fit parameters of α-$AgBiSe_2$ and β-$AgBiSe_2$.

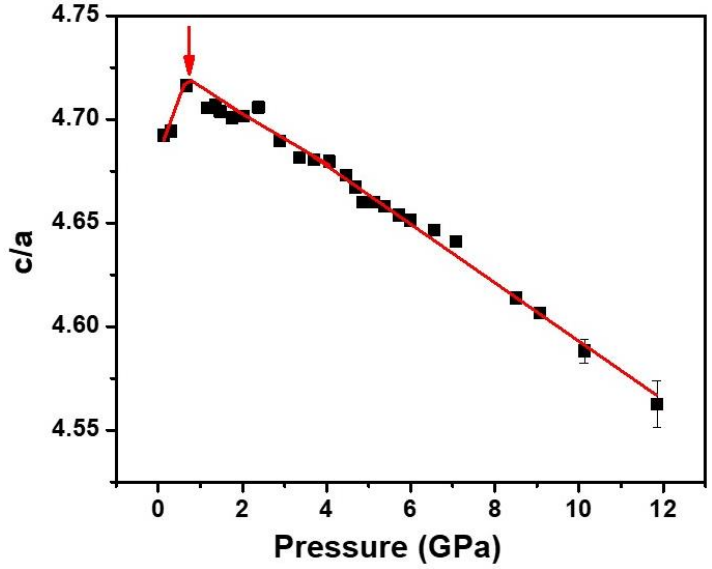

FIG. 3. Pressure variation of lattice parameter ratio (c/a). The red solid line and arrow represents the guide to eye and structural transition respectively.

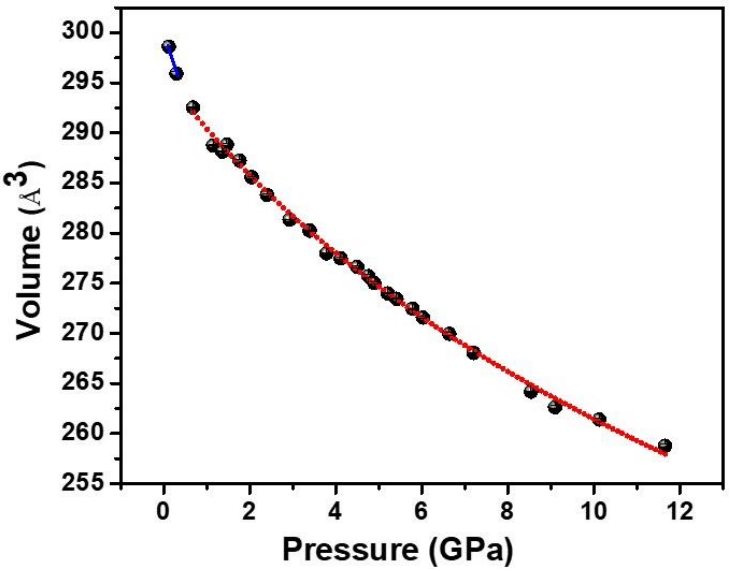

FIG. 4. Pressure variation of structural volume in $AgBiSe_2$. The red dotted line represents the third order BM-EOS fit to the experimental data.

TABLE I. The unit cell and equation of state fit *(B*, B_o and V_0) parameters for $AgBiSe_2$ compound.

	Phase	
	***α*-$AgBiSe_2$**	***β*-$AgBiSe_2$**
Space group	$P\bar{3}m1$ (164)	$R\bar{3}m$ (166)
Z	3	1
a (Å)	4.1886	6.9489
c(Å)	19.6540	
α (˚)	90	34.81
V(Å^3)	298.61	97.62
B (GPa)		50.79
B_0		7.79
V_0(Å^3)		295.83

6.4.2 Electrical resistivity measurements under pressure

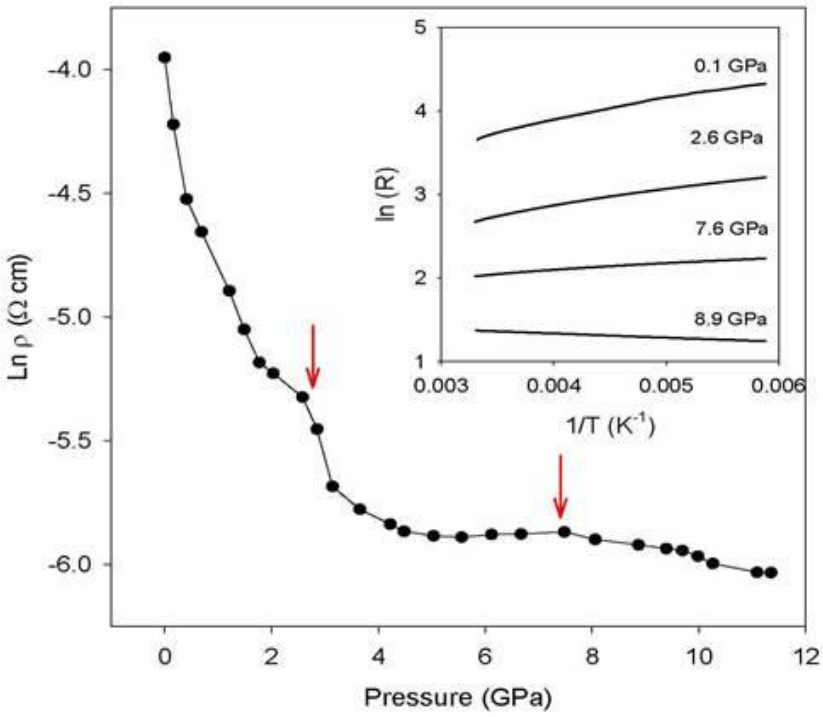

FIG. 5. Pressure dependent electrical resistivity of $AgBiSe_2$ at room temperature condition. The solid red arrow indicates the presence of an ETT at ~2.8 GPa and semiconductor to metal transition above 7.0 GPa. The inset shows the Arrhenius plot of $AgBiSe_2$ at various selected pressure values.

The pressure dependent electrical resistivity of $AgBiSe_2$ up to 11.5 GPa at room temperature is shown in Fig. 5. The inset shows the Arrhenius plot (1/T vs ln(R)) of the sample in the range 170-300K for a few representative pressures. The value of resistivity is 19.225 mΩ cm at ambient conditions and obtained results have found to be in good agreement with Lin Pan *et al* [19]. It is evident from Fig. 5, as the pressure increases, resistivity of the sample decreases up to 2.8 GPa, with a sudden drop occurring and shows a similar trend to that reported for 3D topological insulator Bi_2Se_3 and Bi_2Te_3. By comparing these results, the observed anomaly at 2.8 GPa in our case can be attributed to an ETT [10,11]. The observed inflection point in first derivative of resistivity with respect to pressure (dρ/dP) graph clearly shows an ETT transition at ~ 2.8 GPa as shown in Fig. 6. ETT occurs, when the external perturbations like pressure, chemical doping, temperature, *etc*, in metals or degenerate semiconductors, leading to the crossing of van Hove singularity (band extremum in the DOS) through the Fermi level and consequently strong redistribution of electrons takes place near to Fermi surface [11,26] Hence, Fermi surface can undergo different types of topological transition (changes) like appearance and disappearance of void, formation and disruption of a neck, depending on the type of critical point passing through the Fermi surface [27] (discussed detail in section in 1.7.2.2 Chapter 1).

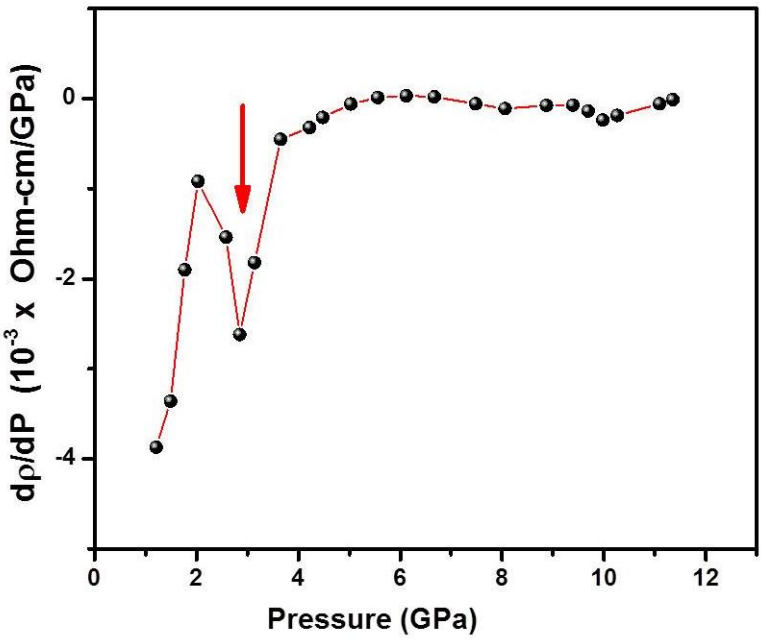

FIG. 6. Pressure dependence of first derivative of resistivity for *β*- $AgBiSe_2$. The solid red arrow indicates the ETT transition at ~ 2.8 GPa

Figure 5 shows the systematic decrease in the overall resistance of the sample at high pressure and the system undergoes metallization in the pressure above 7 GPa where the resistance slope changes from an activation type to the metallic character (see inset of Fig. 5). Visual observation indicated that the lateral dimension of the sample remains unaltered up to the highest pressure of this investigation, confirming the pressure-induced decrease in sample resistivity. To understand the origin of observed metallization, it is necessary to have detailed knowledge of the band structural evolution under pressure.

6.4.3 Raman scattering measurements under pressure

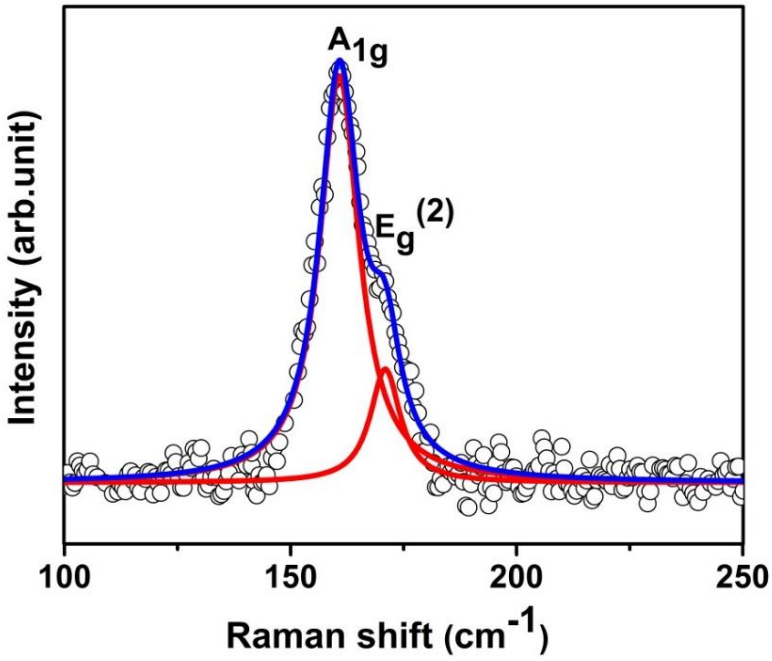

FIG. 7. Raman spectrum of α-$AgBiSe_2$ at ambient conditions.

Raman spectroscopic studies were undertaken to substantiate the above observations. The factor group analysis for the α-$AgBiSe_2$ structure predicts ten Raman active phonon modes at the Γ point of the Brillouin zone, $\Gamma = 5\ A_{1g} + 5\ E_g$. To the best of our knowledge, there is no systematic Raman study available for $AgBiSe_2$ compound. Hence, we have calculated Raman spectra of α-$AgBiSe_2$ based on density functional perturbation theory and tentatively assigned the Raman modes as shown in the Table II. We observed two Raman active modes namely A_{1g} and $E_g^{(2)}$ above 100 cm^{-1} in our experiment (see Fig. 7) which are matching well with that observed in Ref. 21. The phonon modes are fitted using Lorentzian line shape function. The doubly degenerate

$E_g^{(2)}$ mode is related to shear vibration along the *a*-*b* plane and A_{1g} mode can be related to out of plane vibrations along the *c* axis [see Figs. 8(a), (b), and (c)]. The detailed comparison of the assignment between the experiments and theory is shown in Table II. Figure 9 shows the pressure evolution of Raman spectra up to 20.7 GPa. Upon increasing pressure, new phonon mode occurs at 0.7 GPa and this is consistent with the XRD results that $AgBiSe_2$ undergoes a structural transition from hexagonal ($P\bar{3}m1$) to rhombohedral ($R\bar{3}m$). The newly appeared phonon mode in β-$AgBiSe_2$ phase is assigned to $E_g^{(1)}$ symmetry based on structurally similar compound α-Bi_2Se_3 and $PdCoO_2$ [14,28].

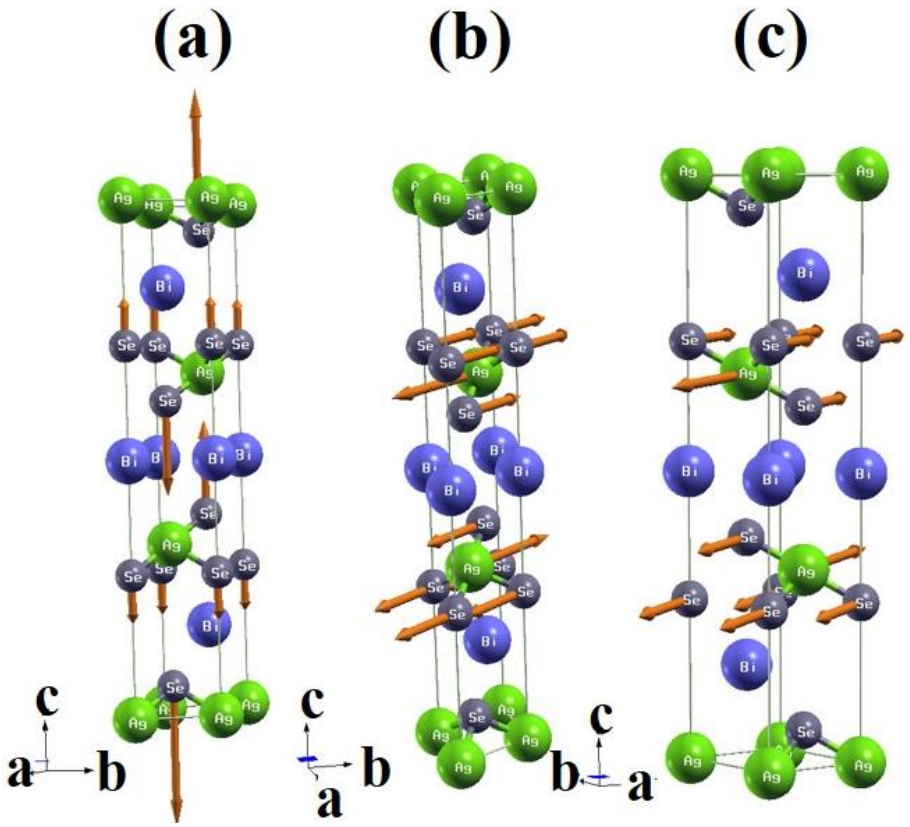

FIG. 8. Schematic of displacement patterns for phonon modes at the Γ point of α-$AgBiSe_2$ (a) A_{1g} modes and (b) and (c) doubly degenerated $E_g^{(2)}$ modes involve displacements along the *c* axis and in the *a*–*b* plane respectively.

TABLE II. Tentative assignment for Raman modes of *α*-$AgBiSe_2$.

Phase	Raman mode assignment	Experimental frequency ω (cm^{-1})	Theoretical frequency ω (cm^{-1})
α-$AgBiSe_2$	A_{1g}	160.8 ± 0.10	202.28
	$E_g^{(2)}$	171.1 ± 0.07	212.57

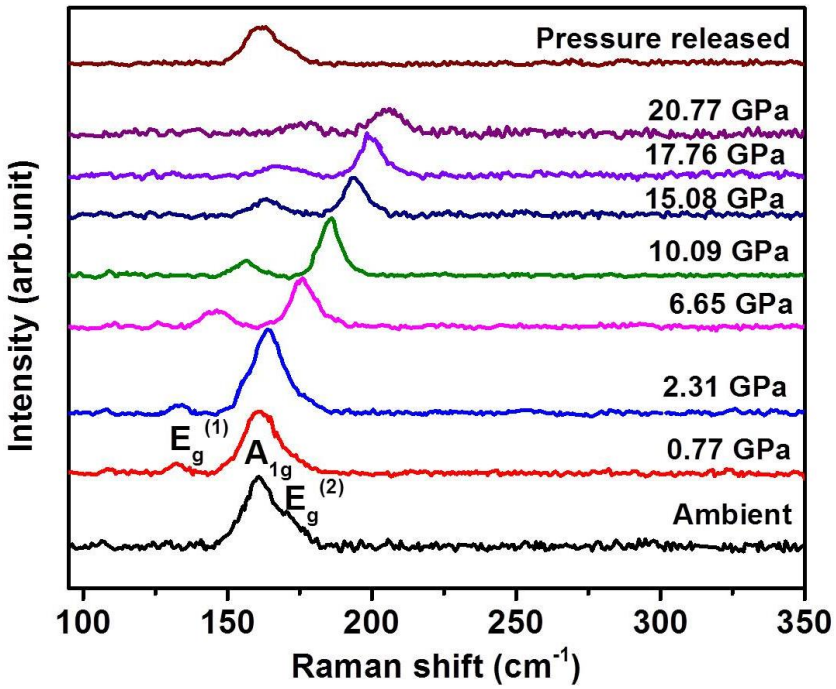

FIG. 9. Pressure evolution of Raman spectra of $AgBiSe_2$ for selected pressure values.

The pressure dependence of the frequency of phonon modes for $AgBiSe_2$ is shown in Fig. 10(a). Upon increasing pressure, $E_g^{(2)}$ mode hardens and it disappears at 1.19 GPa. The phonon mode A_{1g} initially softens up to 0.7 GPa and thereafter it hardens up to ~ 20.7 GPa which is the maximum pressure reached in Raman study, with a small change in slope at around 7 GPa. Similarly, the newly appeared phonon mode $E_g^{(1)}$ hardens with pressure up to ~ 20.7 GPa, with a slope change at around 7 GPa. The pressure dependent behavior of $E_g^{(2)}$, A_{1g} and $E_g^{(1)}$ modes are fitted by a linear equation and the calculated pressure coefficients are summarized in Table III. The pressure coefficient a_1 of A_{1g} mode is -2.52 (± 0.35) cm^{-1}/GPa and 2.64 (± 0.05) cm^{-1}/GPa for

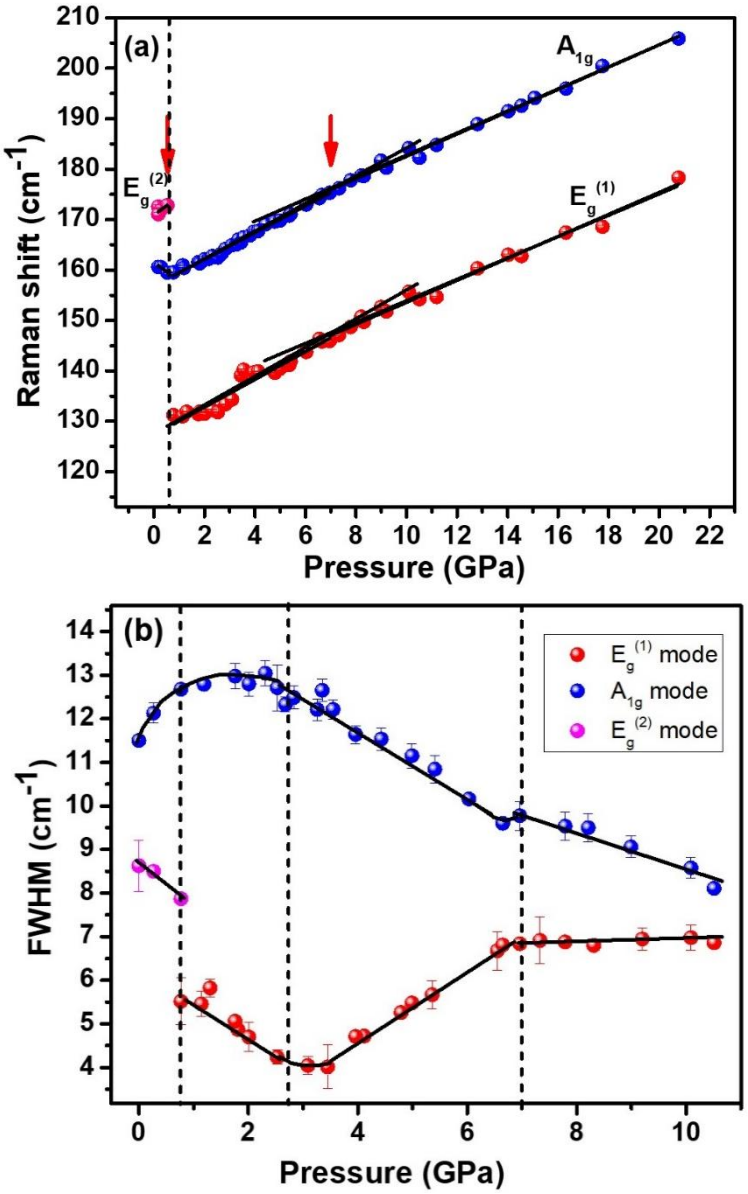

FIG. 10. (a) Pressure versus Raman frequency of A_{1g}, $E_g^{(1)}$ and $E_g^{(2)}$ modes of $AgBiSe_2$ up to 20.7 GPa. The black solid line denotes the linear fit to experimental data points. A vertical dotted line at 0.7 GPa denotes symmetry change from hexagonal ($P\bar{3}m1$) to rhombohedral ($R\bar{3}m$). A red downward vertical arrow at 7 GPa denotes semiconductor to metal transition. (b) Pressure versus FWHM of A_{1g}, $E_g^{(1)}$ and $E_g^{(2)}$ modes of $AgBiSe_2$ up to 10.5 GPa. The black solid line represents the guide to an eye. The vertical dotted line represents the structural, ETT and semiconductor to metal transition at ~0.7 GPa, ~2.8 GPa and ~7.0 GPa respectively.

α-$AgBiSe_2$ and β-$AgBiSe_2$ respectively. Above 7 GPa, both the modes show a change in pressure dependence with a_1 values of 2.21 (± 0.05) and 2.18 (± 0.07) for $E_g^{(1)}$ and A_{1g} modes, respectively. The clear change in the slope of A_{1g} mode around 0.7 GPa with absence of frequency discontinuity during the structural transition, along with

appearance ($E_g^{(1)}$) and disappearance ($E_g^{(2)}$) of modes confirms it is weakly first order in nature. This is consistent with a very low volume change (~1.14 %) across this transition as seen from XRD measurements. Here the high frequency modes, A_{1g} (symmetric out of plane stretching) is related to the inter-layer vibration and $E_g^{(1)}$ (symmetric in plane bending) is related to the intra-layer vibration [14]. Both these modes ($E_g^{(1)}$ and A_{1g}) shows similar pressure coefficient up to the highest pressure in β-$AgBiSe_2$ suggesting that both the inter-layer and the intra-layer properties show very little anisotropy similar to α-Bi_2Se_3 and related family of chalcogenides [14]. In addition, the covalent nature of the intra-layer bonds is similar in all these compounds due to similar pressure coefficients shown by β-$AgBiSe_2$ and other chalcogenides like α-Bi_2Se_3 [14]. It should be noted that XRD doesn't show any change at 7 GPa, while the resistivity shows a semiconductor to metal transition above this pressure. The Raman spectrum of $AgBiSe_2$ is perfectly reversible under pressure and were reproducible over three runs.

TABLE III. Pressure dependence behavior of various Raman-mode frequencies of $AgBiSe_2$. The pressure coefficients for α-$AgBiSe_2$ and β-$AgBiSe_2$ were fitted using linear equation $\omega(P) = \omega(P_0) + a_1.(P - P_0)$. The superscripts a, b and c are represents the estimation of values at P_0 = 1atm, P_0 = 0.7 GPa and P_0 =7.0 GPa respectively.

Phase	**Raman mode**	**Mode frequency $\omega(P_0)$ (cm^{-1})**	**a_1 (cm^{-1} GPa^{-1})**
α-$AgBiSe_2$	A_{1g}	160.8 ± 0.1 [a]	-2.52 ± 0.35[a]
	$E_g^{(2)}$	171.1 ± 0.1 [a]	3.06 ± 0.24 [a]
β-$AgBiSe_2$	$E_g^{(1)}$	127.3 ± 0.7 [b]	2.75 ± 0.17 [b]
	$E_g^{(1)}$	131.8 ± 0.8 [c]	2.18 ± 0.07 [c]
	A_{1g}	156.8 ± 0.2 [b]	2.64 ± 0.05 [b]
	A_{1g}	160.4 ± 0.6 [c]	2.21 ± 0.05 [c]

At ambient conditions, the line width of A_{1g} and $E_g^{(2)}$ modes are 11.5 cm^{-1} and 8.6 cm^{-1} respectively. The large line width of first order A_{1g} mode can possibly be due to strong phonon-phonon interaction leading to anharmonic decay, which decreases the phonon lifetime as shown in Fig. 10(b) [29]. The line width of A_{1g} mode increases up to

~ 2.8 GPa and turns around and decreases up to 10.5 GPa with a noticeable change in slope at ~ 7 GPa [see Fig. 10(b)]. In contrast, the line width of $E_g^{(1)}$ mode decreases with pressure up to 2.8 GPa and sudden reverses by broadening up to 7 GPa where it again shows a slope change in the FWHM. The anomalies in line width of A_{1g} and $E_g^{(1)}$ phonon mode at 2.8 GPa and 7 GPa is consistent with the observations in the resistivity measurements. The Raman changes at 2.8 GPa confirms the pressure induced ETT through electron-phonon coupling in β-$AgBiSe_2$ as was observed in other binary chalcogenide based materials with strong SOC [12-14].

It will be quite interesting to compare the line width behavior of β-$AgBiSe_2$ with α-Bi_2Se_3. In α-Bi_2Se_3, the line width of both $E_g^{(2)}$ and $A_g^{(2)}$ modes decrease with pressure and the possible reason for this decrease was interpreted as Fermi resonance lifting [14]. It is well known that, whenever the first order Raman frequencies coincide with the two phonons [Longitudinal Acoustic (LA) and Transverse Acoustic (TA)] (LA+TA) density of states causes Fermi resonance [29]. As a result of this strong phonon-phonon coupling, large line width observed in first order Raman peak. However, upon applying pressure, the first order Raman frequency increases whereas that of combination mode (LA+TA) decreases. Consequently, the Fermi resonance gradually disappears causing a decrease in line width, which is well studied in conventional semiconductors [29]. Hence, the observed decrease in line width of A_{1g} mode in β-$AgBiSe_2$ may probably be due to the lifting of Fermi resonance. The systematic decrease in the electrical resistivity values (Fig. 5) with pressure may be due to the weakening of phonon-phonon coupling in β-$AgBiSe_2$. It is very difficult to say, but the anomalous behavior of E_g mode can also be related to electron-phonon coupling, similar to that of Zn during ETT [30].

There is an abrupt change observed in the pressure coefficient of Raman frequency and line width of the A_{1g} and $E_g^{(1)}$ modes above ~ 7 GPa and this can be attributed to the semiconductor to metal transition. There is a small difference in the semiconductor to metal transition pressure values observed in the Raman and resistivity measurements. This could be mainly due to different PTM used in these experiments. Due to change in the electronic structure across this transition, the electron-phonon coupling is effected leading to change in the life time as well as the frequency of both A_{1g} and $E_{1g}^{(1)}$ modes.

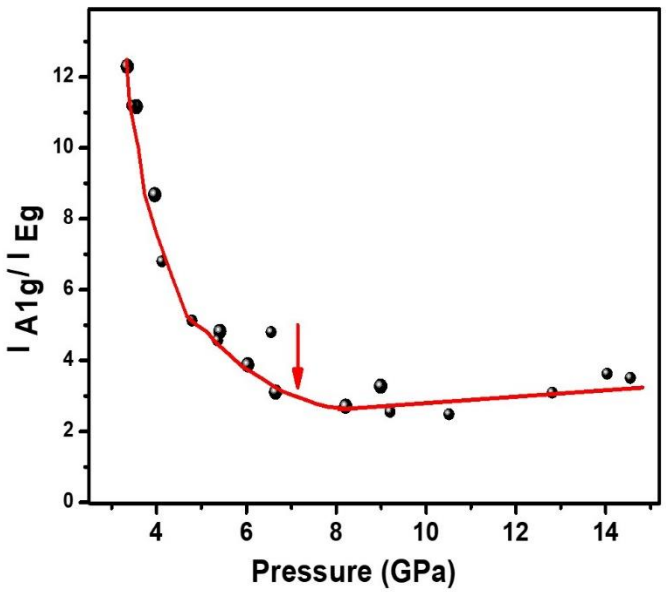

FIG. 11. Pressure dependent intensity ratio $\boldsymbol{I_{A_{1g}}/I_{E_g^{(1)}}}$ of β-$AgBiSe_2$. The solid red line and arrow represents the guide to eye and semiconductor to metal transition respectively.

Figure 11 shows the pressure versus relative intensity ratio ($\boldsymbol{I_{A_{1g}}/I_{E_g^{(1)}}}$) of β-$AgBiSe_2$. Here, the intensity of the A_{1g} mode significantly reduces and becomes almost saturate after the metallization (around ~7 GPa). After ~ 7 GPa, the optical penetration depth of β-$AgBiSe_2$ decreases due to metallic state, as a consequence, the scattering volume and Raman intensity of the sample decreases on account of metallic nature of the sample. Hence the Raman scattering, like resistivity, is able to elucidate the ETT and semiconductor to metal transition and is a useful probe to study the subtle changes induced by electronic state in an isostructural electronic transition, which goes undetected in XRD measurements.

6.4.4 Theoretical calculations

To understand the reason behind the experimentally observed pressure induced semiconductor to metal transition in β-$AgBiSe_2$, we have performed the first principle calculations. At first, we have studied the changes in band structure (along the Γ-Z-F- Γ-L path) and PDOS at various pressures (between 0 GPa to 20 GPa), please note that we have considered the rhombohedral structure (β-$AgBiSe_2$) at 0 GPa. The band structure plot for various pressure values are given in the Fig. 12 (a)-(d). Clearly, at zero pressure, the system behaves as a semiconductor with an indirect band gap of ~0.26 eV as shown in Fig. 12(a). However, at the Γ-point, there is a direct band-gap of ~0.64 eV. In Fig. 13-

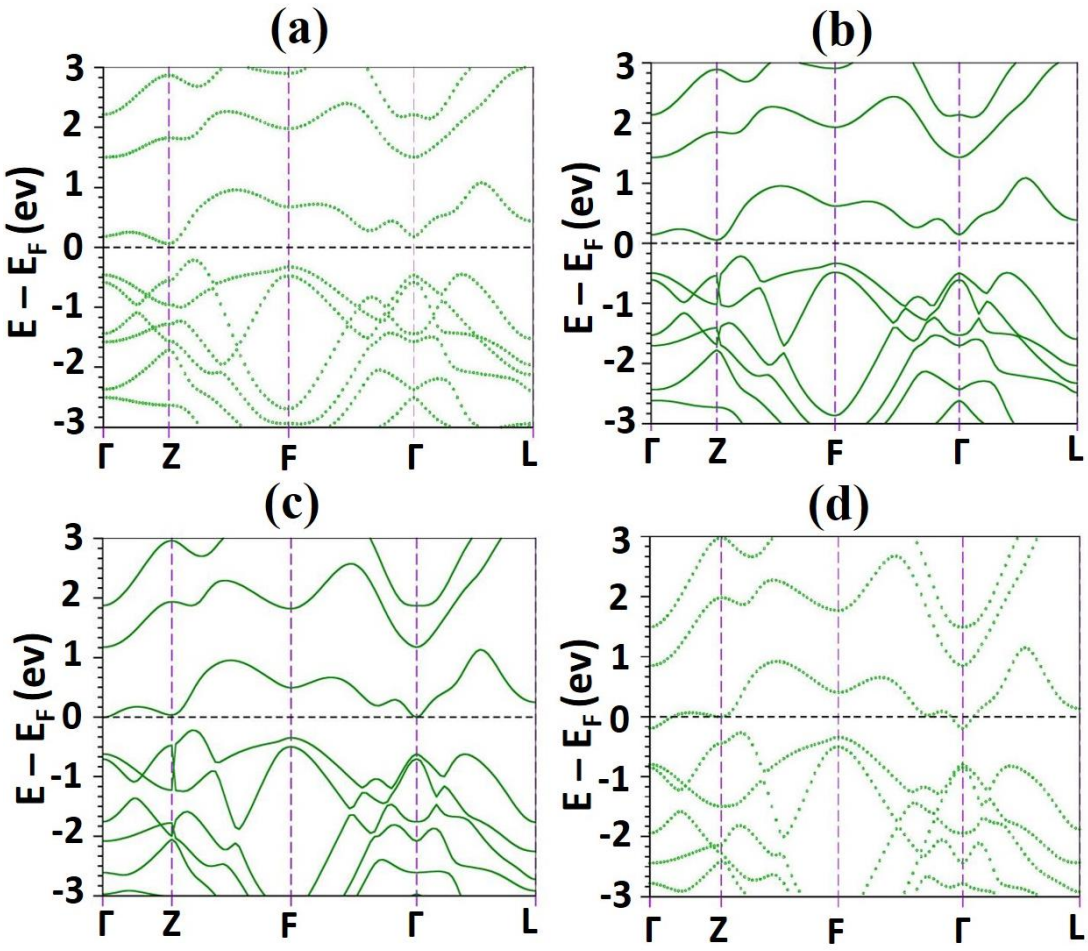

FIG. 12. Band structure of β-$AgBiSe_2$ at pressure (a) 0 GPa, (b) 2.4 GPa, (c) 11 GPa and and 20 GPa The dotted and connected representations has no specific significance.

(a) and (b), we have given the PDOS plots at 0 GPa and 20 GPa pressures. With the increase in pressure, bands near the Fermi level shifts down in energy, suggesting an increased stability for the electrons occupying these bands. Such a change can be explained based on the expected decrease in bond distances between atoms (implying an increased bonding nature, and hence, stability), albeit with an increment in the (isotropic) pressure. Interestingly, conduction band slowly shifts down with pressure and at ~ 11.0 GPa [see Fig. 12 (c)] it touches the Fermi-level at Γ-point and at higher pressures it is dispersed across the Fermi level, reminiscent of metallic band. Also, from the PDOS plots at 0 GPa and 20 GPa pressures (Figs. 13(a) and (b)), it is clear that there is a strong redistribution of DOS near the Fermi level, where, the major redistribution is in the energy states corresponding to p-orbitals of both Se and Bi atoms.

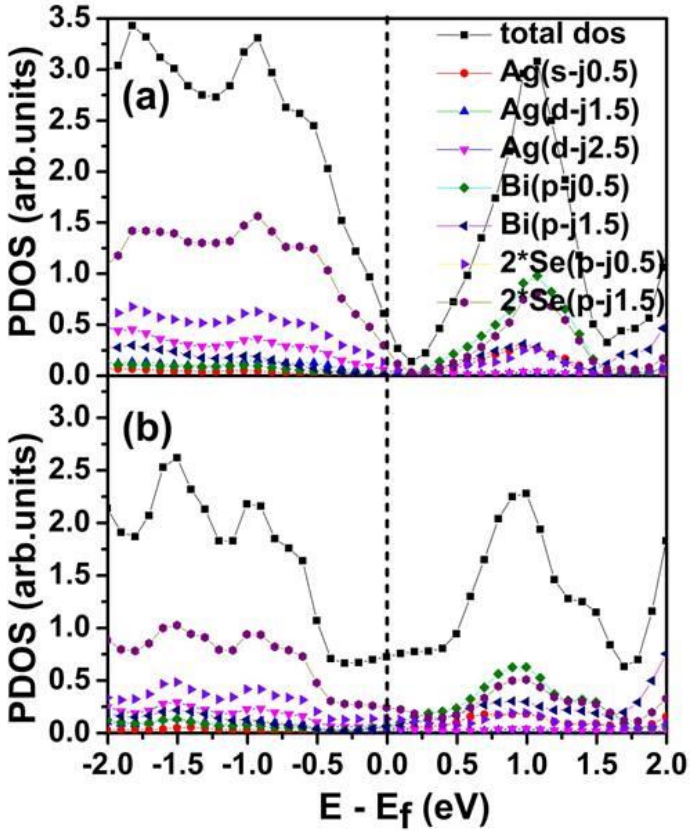

FIG. 13. PDOS of β-$AgBiSe_2$ at pressure (a) 0 GPa and (b) 20 GPa.

Although we find changes in band structure with a change in pressure, such changes are very subtle till 11.0 GPa and we find notable changes only above this pressure. Indeed, several earlier studies [11, 31-33] have already noticed such subtle changes in the band extremum with pressure correspond to the change in transport properties. As major changes in the band structure near the Fermi level are mainly due to the conduction band, we have plotted the second derivative of change in the conduction band energy with respect to the Fermi-level as a function of pressure (see Fig. 14) to look clearly whether there is change in slope or kink in conduction band energy as a function of wave vector (k). The second derivative of energy would correspond to the electrical conductivity, which is a second-order transport quantity. Figure 14 shows major changes in the regions between 2 to 2.5 GPa and between 11 to 12 GPa. Any changes in the topology of Fermi surface will directly affect the electronic DOS near to the Fermi level and have strong influences on the bands lying very close to the Fermi level. Hence, the inflection point observed at 2 GPa possibly be due to an ETT. Another inflection point

observed at 11.5 GPa signifies the overlap of conduction band with Fermi level, where the system starts behaving like metal. The DFT level of theory may not quantitatively match with experimental data. In fact, since this happens for high pressure, it is due to some nonlinear response, which the DFT fails to capture. It is hard to compare the second order experimental response functions with the data from DFT level of theory. The various illustrative examples of mismatches between the transition pressure values (between the experiments and theory) are discussed in Chapter 3 (section 3.5). Here, more importantly, our calculations confirm the presence of ETT and semiconductor to metal transition in β-$AgBiSe_2$ quite accurately using DFT, albeit, qualitatively.

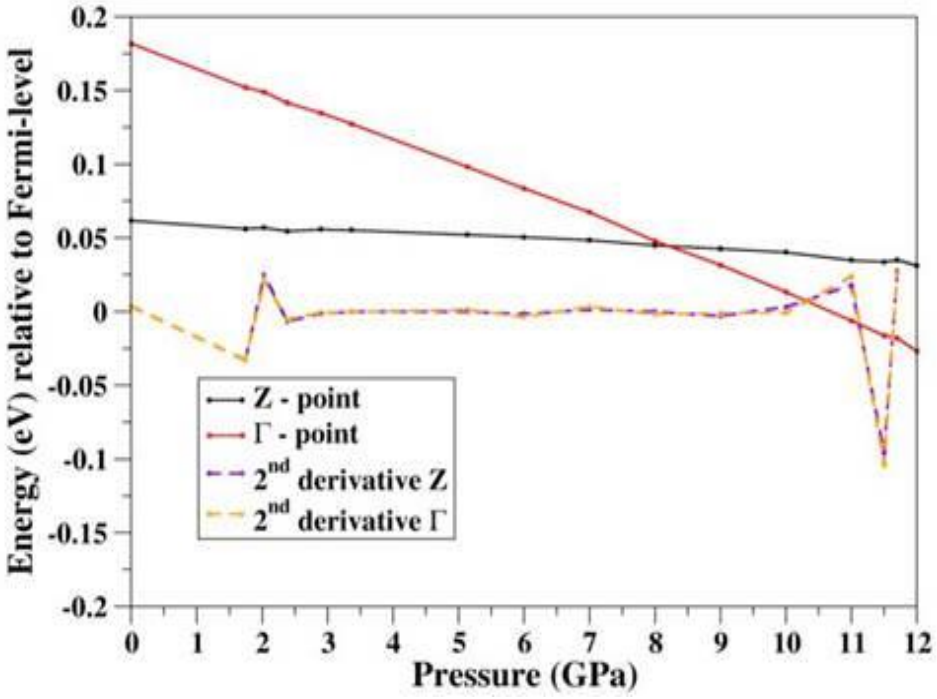

FIG. 14. Variation of the conduction band position and its numerical second derivative at Γ and Z points with pressure.

The empirical results demonstrate that significant enhancement of TE power has been observed in some materials during an ETT phenomenon [8,9,34]. For instance, ~44 % increase in TE power has been observed in p-type $Sb_{1.5}Bi_{0.5}Te_3$ in the vicinity of an ETT at ~1.5 GPa [34]. Hence, it is to worth carry out the TE power measurement at high pressure on $AgBiSe_2$. Since the chemical pressure (chemical doping and substitutions) is analogous to the external pressure, it is experimentally possible to bring ETT at ambient conditions by proper alloying. Metallization under pressure can be used as the basis of

pressure conducting (insulating) switches and sensors [17,18]. Hence our comprehensive studies propose that $AgBiSe_2$ can be used for multilevel physics device with pressure sensors, pressure switches and high thermoelectric performance at high pressure.

6.5. Conclusions

In summary, a combination of synchrotron XRD and Raman scattering measurement confirms that $AgBiSe_2$ undergoes the pressure induced weakly first order structural phase transition from hexagonal ($P\bar{3}m1$) to rhombohedral ($R\bar{3}m$) at ~0.7 GPa. Furthermore, $E_g^{(1)}$ and A_{1g} phonon mode frequency and line width anomaly due to electron-phonon coupling changes along with the electrical transport measurement provides evidence for a pressure induced ETT at ~ 2.8 GPa and a semiconductor to metal transition above 7 GPa. First principles calculations corroborate the experimentally observed semiconductor to metal transition and suggest that the strong redistribution of electronic DOS mainly contributed by p orbitals of Bi and Se atoms lying near to Fermi level causes the metallization in β-$AgBiSe_2$. We are sure that our results will stimulate further research interest in $AgBiSe_2$ on the aspect of thermoelectric measurement at high pressure.

6.6 Bibliography

1. K. F. Hsu, S. Loo, F. Guo, W. Chen, J. S. Dyck, C. Uher, T. Hogan, E. K. Polychroniadis and M. G. Kanatzidis, Science **303**, 818 (2004).
2. H. Zhang, C. X. Liu, X. L. Qi, X. Dai, Z. Fang and S. C. Zhang, Nat. Phys. **5**, 438 (2009).
3. M. Z. Hassan and C. L. Kane, Rev. Mod. Phys. **82**, 3045 (2010).
4. J. E. Moore, Nature **464**, 194 (2010).
5. M. D. Nielsen, V. Ozolins and J. P. Heremans, Energy Environ. Sci. **6**, 570 (2013).
6. S. N. Guin, A. Chatterjee, D. S. Negi, R. Datta and K. Biswas, Energy Environ. Sci. **6**, 2603 (2013).
7. S. N. Guin and K. Biswas, Chem. Mater. **25**, 3225 (2013).
8. S.V. Ovsyannikov, V.V. Shchennikov, G.V. Vorontsov, A.Y. Manakov, A.Y. Likhacheva and V.A. Kulbachinskii, J. Appl. Phys. **104**, 053713 (2008).

9. N. V. Chandra Shekar, D. A. Polvani, J. F. Meng and J. V. Badding, Phys. B **358,** 14 (2005).
10. J. Zhang, C. Liu, X. Zhang, F. Ke, Y. Han, G. Peng, Y. Ma and C. Gao, Appl. Phys. Lett. **103**, 052102 (2013).
11. J. Zhang, Y. Han, C. Liu, X. Zhang, F. Ke, G. Peng, Y. Ma and C. Gao, Appl. Phys. Lett. **105**, 062102 (2014).
12. O. Gomis, R. Vilaplana, F. J. Manj´on, P. Rodr´ıguez-Hern´andez, E. P´erez-Gonz´alez, A. Mu˜noz, V. Kucek and C. Drasar, Phys. Rev. B **84**, 174305 (2011).
13. R. Vilaplana, O. Gomis, F. J. Manj´on, A. Segura, E. P´erez-Gonz´alez, P. Rodr´ıguez- Hern´andez, A. Mu˜noz, J. Gonz´alez, V. Mar´ın-Borr´as, V. Mu˜noz-Sanjos´e, C. Drasar and V. Kucek, Phys. Rev. B **84**, 104112 (2011).
14. R. Vilaplana, D. Santamar´ıa-P´erez, O. Gomis, F. J. Manj´on, J. Gonz´alez, A. Segura, A. Mu˜noz, P. Rodr´ıguez-Hern´andez, E. P´erez-Gonz´alez, V. Mar´ın-Borr´as, V. Mu˜noz- Sanjose, C. Drasar and V. Kucek, Phys. Rev. B **84**, 184110 (2011).
15. G. K. Pradhan, A. Bera, P. Kumar, D. Muthu and A. Sood, Solid State Commun. **152**, 284 (2012).
16. Y. A. Sorb, V. Rajaji, P. S. Malavi, U. Subbarao, P. Halappa, S. C. Peter, S. Karmakar and C. Narayana, J. Phys. Condens. Matter **28**, 015602 (2016).
17. Z. Zhao, H. Zhang, H. Yuan, S. Wang, Y. Lin, Q. Zeng, G. Xu, Z. Liu, G. K. Solanki, K. D. Patel, Y. Cui, H. Y. Hwang and W. L. Mao, Nature Commun. **6**, 7312 (2015).
18. A. P. Nayak, S. Bhattacharyya, J. Zhu, J. Liu, X. Wu, T. Pandey, C. Jin, A. K. Singh, D. Akinwande and J. F. Lin, Nature Commun. **5**, 3731 (2014).
19. L. Pan, D. Bérardan and N. Dragoe, J. Am. Chem. Soc. **135**, 4914 (2013).
20. S. N. Guin, V. Srihari and K. Biswas J. Mater. Chem. A **3**, 648 (2015).
21. C. Xiao, X. Qin, J. Zhang, R. An, J. Xu, K. Li, B. Cao, J. Yang, B. Ye and Y. Xie, J. Am. Chem. Soc. **134**, 18460 (2012).
22. P. Giannozzi, S. Baroni, N. Bonini, M. Calandra, R. Car, C. Cavazzoni, D. Ceresoli, G.L. Chiarotti, M. Cococcioni, I. Dabo, A. D. Corso, S. de Gironcoli, S. Fabris, G. Fratesi, R. Gebauer, U. Gerstmann, C. Gougoussis, A. Kokalj, M. Lazzeri, L. Martin-Samos, N. Marzari, F. Mauri, R.

Mazzarello, S. Paolini, A. Pasquarello, L. Paulatto, C. Sbraccia, S. Scandolo, G. Sclauzero, A.P. Seitsonen, A. Smogunov, P. Umari and R.M. Wentzcovitch, J. Phys. Condens. Matter **21**, 395502 (2009).

23. J. P. Perdew, K. Burke and M. Ernzerhof, Phys. Rev. Lett. **77**, 3865 (1996).
24. See http:// www.quantum-Espresso.org / for "ultrasoft relativistic pseudo-potentials"(last accessed March 29, 2016).
25. S. Geller and J. H. Wernick, Acta Cryst. **12**, 46 (1959).
26. Y. M. Blanter, M. I. Kaganov, A.V. Pantsulaya, and A. A. Varlamov, Phys. Rep. **245**, 159 (1994).
27. I. M. Lifshitz, Sov. Phys. JETP **11**, 1130 (1960).
28. H. Takatsu, S. Yonezawa, S. Mouri, S. Nakatsuji, K. Tanaka and Y. Maeno, J. Phys. Soc. Jpn. **76**, 104701 (2007).
29. M. Cardona, High Press. Res. **24**, 17 (2004).
30. H. Olijnyk, A. P. Jephcoat, D. L. Novikov and N. E. Christensen, Phys. Rev. B **62**, 5508 (2000).
31. F. J. Manjón, R. Vilaplana, O. Gomis, E. Pérez-González, D. Santamaría-Pérez, V. Marín-Borrás, A. Segura, J. González, P. Rodríguez-Hernández, A. Muñoz, C. Drasar, V. Kucek, and V. Muñoz-Sanjosé, Phys. Stat. Sol. **250**, 669 (2013).
32. J. S. Tse, Z. Li, K. Uehara, Y. Ma, and R. Ahuja, Phys. Rev. B **69**, 132101 (2004).
33. A. B. Garg, A. K. Verma, V. Vijayakumar, R. S. Rao, and B. K. Godwal, J. Phys. Condens. Matter **18**, 8523 (2006).
34. D. A. Polvani, J.F. Meng, N.V. Chandra Shekar, J. Sharp and J.V. Badding, Chem. Mater. **13,** 2068 (2001).

Chapter 7

Pressure induced electronic topological transition in Sb_2S_3

The author's main contribution in this chapter is to perform the high pressure Raman scattering measurements on Sb_2S_3 sample and analyze the data. To execute this research problem, we have collaborated with Prof. Sebastian C. Peter's group, JNCASR, Bangalore for sample synthesis and Dr. S. Karmakar's group, BARC, Mumbai for electrical transport measurements.

Y. A. Sorb, V. Rajaji, P. S Malavi, U. Subbarao, P. Halappa, S. C Peter, S. Karmakar and C. Narayana, *"Pressure-induced electronic topological transition in Sb_2S_3" J. Phys.: Condens. Matter* **28**, 015602 (2016).

7.1 Introduction

The metal chalcogenide semiconductors belonging to the A_2B_3 (A = Bi, Sb, As; B = S, Se, Te) series have been of great interest owing to their exceptional thermoelectric properties and technological applications [1-3]. For instance, Bi_2Se_3, Bi_2Te_3 and Sb_2Te_3 compounds in the above series are extensively studied in the view point of topological insulators since they possess a single Dirac cone at the Γ point of the Brillouin zone [4-8]. These compounds adopt rhombohedral structure (SG: $R\bar{3}m$, Z = 3) at ambient pressure and upon pressurizing them, they exhibit novel phenomena such as structural phase transitions [9-11], ETT or Lifshitz transition [9-13], insulator to metal transitions [14] and superconductivity [14,15]. These materials undergo a series of pressure-induced structural phase transitions from the ambient rhombohedral to a disordered body-centered cubic through monoclinic structure. Motivated by the increasing interest in these materials, much research has been stimulated in the compounds involving heavy elements such as Bi, Sb, Te, *etc* [16-19].

Another class of compounds (wide band gap semiconductors) formed in the A_2B_3 series are Sb_2Se_3 (E_g = 1 eV), Bi_2S_3 (E_g = 1.3 eV) and Sb_2S_3 (E_g = 1.7-1.8 eV) [20]. Unlike Bi_2Te_3, Sb_2Te_3 and Bi_2Se_3, these compounds adopt orthorhombic structure (SG: *Pnma*, Z = 4, U_2S_3-type) at ambient pressure [12, 21]. Among the above three wide bandgap semiconductors, Sb_2Se_3 has recently been received wide attention from the view point of pressure-induced topological quantum phase transition (TPQT), insulator-metal transition, electronic topological transition (ETT), superconductivity and structural phase transition [14, 22, 23]. Similarly, high-pressure structural and vibrational properties of Bi_2S_3 studied up to ~65 GPa show that the ambient *Pnma* structure remains stable up to 50 GPa and suffer from structural disorder upon further pressurization [12]. An important finding observed in this study is the possibility of ETT at around 4-6 GPa due to the topological modification of the Bi_2S_3 electronic structure [12]. A significant characteristic feature of the compounds in the A_2B_3 chalcogenide series is the existence of ETT below 6 GPa [9-14].

Among the metal chalcogenide compounds in the A_2B_3 series, Sb_2S_3 has not received much attention as compared to other compounds that may probably be due to its wide band gap which make it unlikely to be topological properties. However, it has

good photovoltaic properties, high thermoelectric power and broad spectrum response [24]. It has been used in various applications such as television cameras with photo-conducting targets, thermoelectric cooling devices, electronic and optoelectronic devices, solar energy conversion and visible light-responsive photo catalysis [24]. It has been experimentally found that there is a correlation between pressure-induced ETT and thermopower enhancement [3]. For instance, the thermoelectric studies on $Sb_{1.5}Bi_{0.5}Te_3$ by Polvani *et al.* observed that there is an increase in thermopower with increasing pressure (up to 2 GPa) similar to that already observed in metallic lithium–magnesium alloys in which the thermopower enhancement is in the account of ETT [25]. An alternative way to achieve high pressure for technological applications is by engineering the materials via appropriate alloying to tune the chemical pressure near the ETT region to design better thermoelectric materials. In this chapter, we present high-pressure vibrational properties and ETT in Sb_2S_3 using both high-pressure Raman and resistivity studies.

7.2 Experimental details

The pure phase of Sb_2S_3 was synthesized by combining 0.7168 g of antimony in the form of shots (99.99%, Alfa Aesar) and 0.2832 g of sulfur in powder form (99.99% Alfa Aesar), were placed in a 9 mm diameter quartz tube, under an inert (argon) atmosphere inside a glove box, which was flame-sealed under vacuum of 10^{-3} Torr, to prevent oxidation during heating and 10^{-3} Torr was achieved with the help of rotary pump. The tube was then placed in a vertically aligned tube furnace and heated to 120 ^oC over the period of 2 h to allow proper homogenization. Subsequently, the temperature was increased to 600 ^oC and kept for 2 d. Finally, the system was allowed to cool to room temperature in 10 h. No reaction with the quartz tube was observed. A light grey polycrystalline Sb_2S_3 was formed and it was found to be stable in moist air for several months. The weight losses of the final material were found to be less than 1%. Phase identity and purity of the sample was determined by powder X-ray diffraction study (XRD), which was carried out with a Bruker D8 Discover diffractometer using Cu-*K*α radiation (λ = 1.5406 Å) over the angular range $20^0 \leq 2\theta \leq 80^0$, at room temperature, calibrated against corundum standard. The experimental powder patterns of Sb_2S_3 and the XRD pattern simulated from the reported data were found to be in good agreement

[26]. Also, we have noticed that the sample was not oxidized up to the level of X-ray detection. XRD do not show any secondary phase formation.

The sample was then used for high pressure Raman and resistivity studies. High pressure Raman studies were carried out using a Mao-Bell type Diamond Anvil Cell (DAC). Raman measurements were carried out by a custom-built micro-Raman spectrometer [27] and details are discussed in Chapters 2 and 5 (section 5.2). Also, the procedures of gasket preparation, PTM and pressure calibration is the same as discussed in Chapters 2 and 3 (section 3.2). The data accumulation time for each spectrum is about 30 minutes, and the power at the sample kept <0.5 mW to prevent heating and oxidation of the sample.

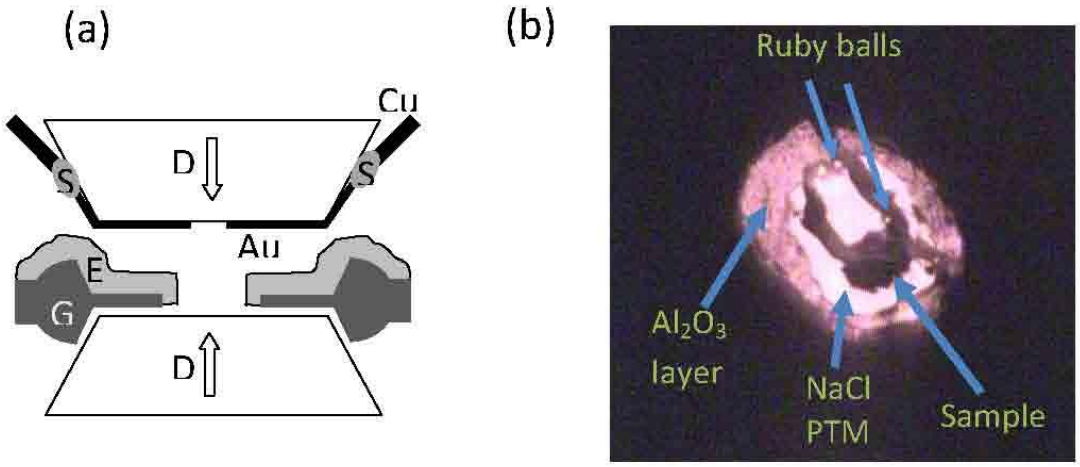

FIG. 1 (a) Schematics of opposed diamond anvils for resistance measurements, and (b) Photograph of the sample mounted inside DAC for resistance measurements in quasi-four probe arrangement. Sample is mounted inside the electrically insulated (Al_2O_3 layered) gasket hole along with NaCl pressure transmitting medium and ruby spheres (as pressure calibrant).

The pressure dependence of resistivity at room temperature was measured on Sb_2S_3 up to ~10 GPa using a miniature DAC and an optical cryostat [28] and details are discussed in Chapter 4 (section 4.2). In addition, we would to mention other specific details related to transport measurements. Figure 1(a) and (b) shows the schematics as well as actual photograph of the sample mounted inside the DAC respectively, for resistivity measurements. Powered (polycrystalline) sample was first pelletized with

static pressure up to 2-3 kbar. This makes the sample appropriate for resistance measurements (making good intergrain connectivity). Such a moderate pressure (2-3 kbar) helps in binding the grains, without affecting the interatomic separation (or sample density) in an irreversible manner. A tiny fleck of such pelletized sample was mounted inside the electrically-insulated (Al_2O_3 layered) gasket hole [see Fig. 1(b)]. We would like to mention that it is difficult to measure the density of the tiny fleck picked up for the experiment, but we believe that the density of the sample is close to 99% of theoretical density. Resistance was measured on a pressed pellet of Sb_2S_3 (diameter ~50 μm and ~20μm thick) using 10 μm thin gold electrical leads, that remains in good contact with the sample when pressure was applied through the solid PTM (NaCl). Resistance measured at 2 GPa is 85 kΩ and that at 8 GPa is ~160 KΩ. These measurements were carried with current at 1μA. The resistance bridge having specified current range for such high-resistance measurement was 3.16 nA to 3.16 μA. We verify that for the currents of 3.16 nA, 10 nA, 31.6 nA, 100 nA, 316 nA, 1.0 μA and 3.16 μA, the current-to-voltage data is linear at all pressures but does not generate any *I-V* data at every pressure. This is used to determine the error bar of resistivity which is in the range ~ 25-110 Ωcm based on the assumption that the shape of the sample is unchanged up to the highest pressures (from our visual inspection).

7.3 Results and discussion

7.3.1 Raman scattering measurements

The orthorhombic (SG: *Pnma*, point group symmetry: D_{2h}) unit cell of the Sb_2S_3 consists of 20 atoms, which have 60 phonon active modes at the Γ point of the Brillouin zone [29]. Since *Pnma* is a centrosymmetric space group, both Raman and infrared (IR) modes of Sb_2S_3 are mutually exclusive [29-30].

$$\Gamma_{vib} = 30\,\Gamma_{Raman} + 22\,\Gamma_{IR} + 3\,\Gamma_{acoustic} + 5_{\ silent}$$

Where $\Gamma_{acoustic} = B_{1u} + B_{2u} + B_{3u}$ are acoustic modes, $\Gamma_{Raman} = 10\,A_g + 5\,B_{1g} + 10\,B_{2g} + 5B_{3g}$ are Raman active modes, $\Gamma_{IR} = 4\,B_{1u} + 9\,B_{2u} + 9\,B_{3u}$ are IR active modes and $\Gamma_{silent} = 5A_u$ are silent modes.

In Sb_2S_3 lattice, the Sb and S atoms are at the Wyckoff positions 4*c*, with the site symmetry C_s having four-fold multiplicity. The motion of Sb and S atoms is within *xz*

plane for the B_{2g}, B_{1u} and B_{3u} modes and are along *y*-axis for B_{1g}, B_{3g} and B_{2u} modes [29]. Our present study shows that there are six Raman active modes at ambient pressure. There is no systematic experimental study available to assign these phonon modes. However, Sereni *et al.* carried out polarization-dependent Raman scattering experiments on Sb_2S_3, where they have used backscattering geometry $x(yy)\bar{x}$ and 90º geometry with parallel polarization $\bar{x}(yy)z$ and observe the A_g modes. But in the case of 90º geometry $\bar{x}(yy)z$ with cross polarization there is a spurious contribution from the B_{1g} modes in their A_g spectrum [30]. However, the authors could not distinguish between B_{1g}, B_{2g}, and B_{3g} modes from the A_g owing to the lack of information about the intensities of phonon modes. For the present study, we could resolve six Raman active modes at ambient pressure (300 K) as shown in lower spectrum of Fig. 2 (a). The peaks at 195 , 208 and

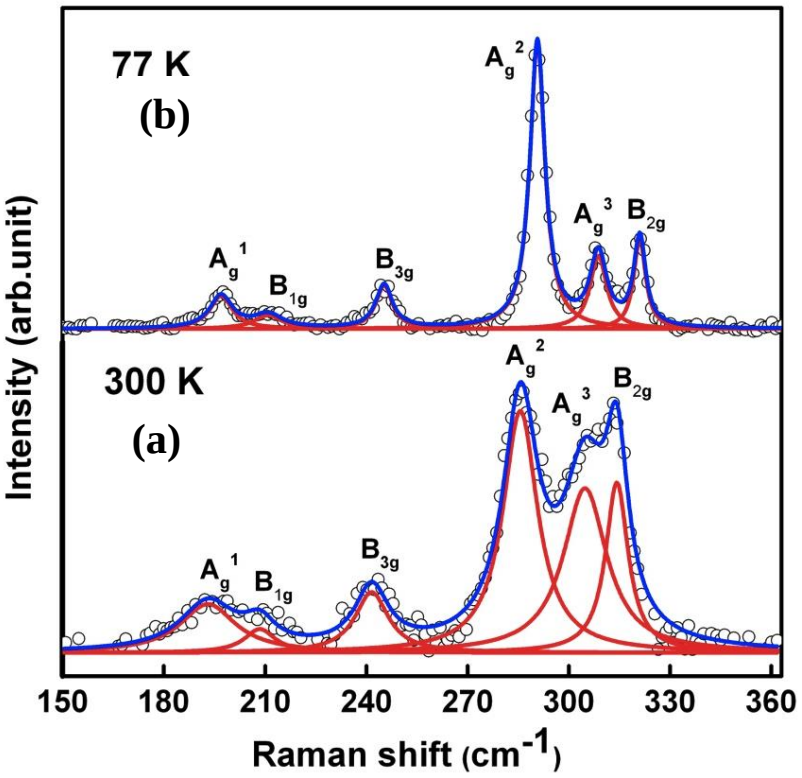

FIG. 2. Raman spectra of Sb_2S_3. The lower (a) and upper (b) spectra represent the Raman spectra collected at 300 K and 77 K respectively.

241 cm^{-1} appear to be very weak due to poor background. However, the spectrum is well resolved at low temperature (77K) is shown in upper spectrum of Fig.2 (b). The experimentally observed phonon modes of Sb_2S_3 have been assigned based on the lattice dynamics calculation by Liu *et al.* and the observed phonon mode frequencies are shown in Table I [29]. The phonon modes at 77 K are hardened (increase in frequency) with

respect to the 300 K as shown in Fig. 2 as expected due to the compression of lattice upon reducing the temperature. For convenience, we represent the three different A_g modes by a superscript which ascending order of numbers to signify the increasing frequency of modes.

Table I. Mode assignment of experimentally observed Raman spectra of Sb_2S_3 at ambient conditions

Raman shift (cm^{-1})	Raman modes
195	A_g^1
208	B_{1g}
241	B_{3g}
286	A_g^2
308	A_g^3
314	B_{2g}

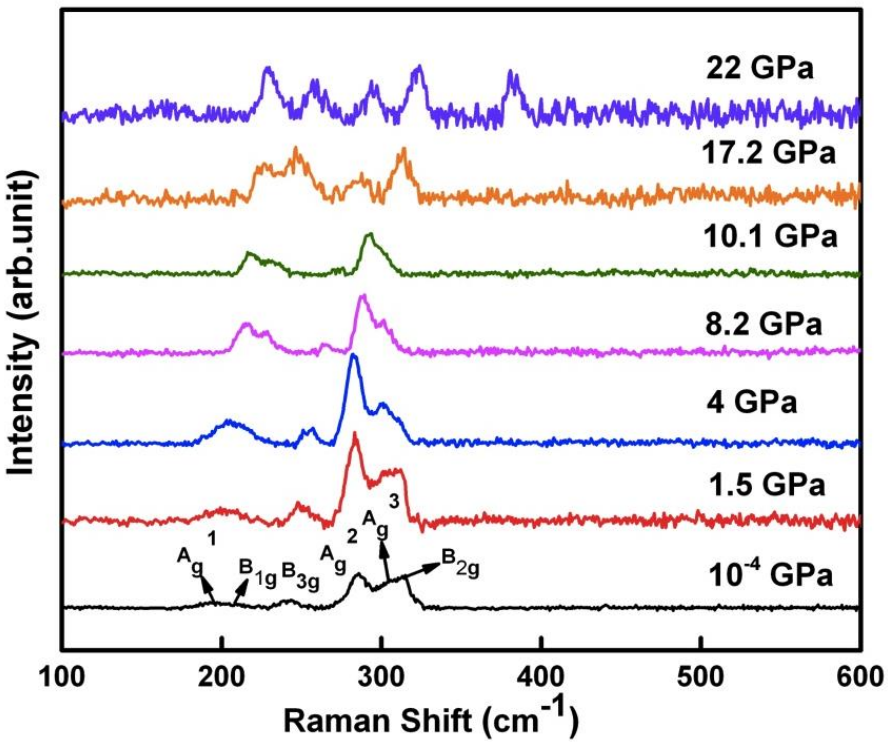

FIG. 3. Raman spectra of Sb_2S_3 at various pressures. The observed phonon modes of Sb_2S_3 are assigned at ambient pressure (10^{-4} GPa).

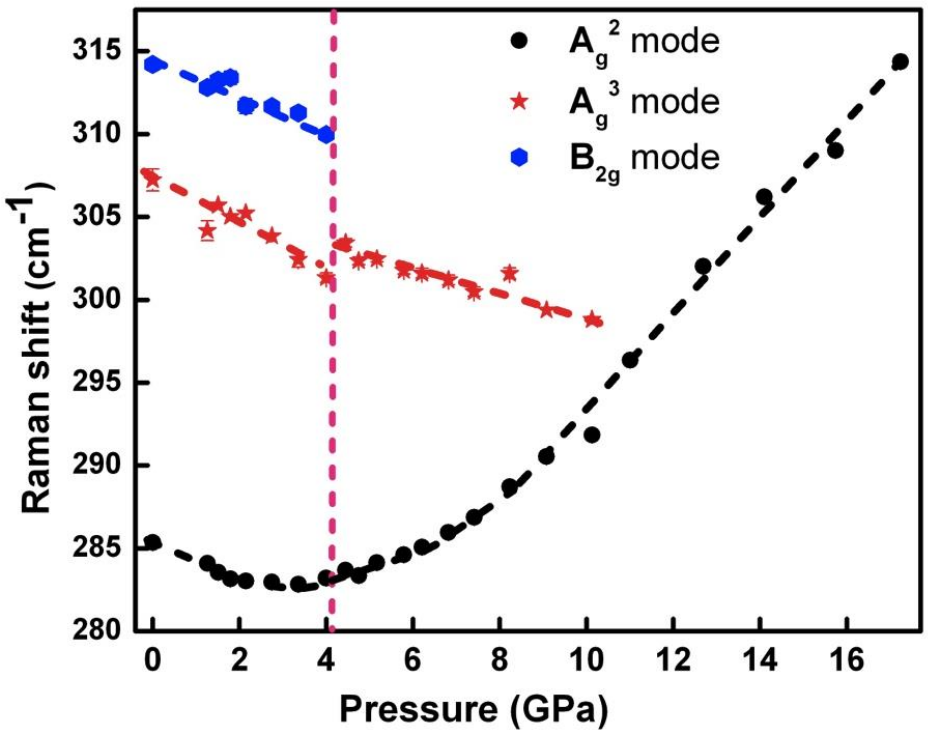

FIG. 4. P vs. Raman shift of Ag^2, Ag^3 and B_{2g} modes of Sb_2S_3. A vertical dotted line at 4 GPa is to indicate an ETT. The dotted lines drawn to each phonon modes are for guidance to the eye.

High-pressure Raman studies have been carried out on Sb_2S_3 up to 22 GPa and the representative Raman spectra at various pressures are shown in Fig.3. It is evident from Fig.3 that apart from the observed phonon modes; the appearance of additional Raman modes above 20 GPa consistently in all runs, suggests that the compound may be undergoing structural phase transition. Although, both Sb_2Se_3 and Bi_2S_3 compounds adopt identical crystal structure with Sb_2S_3, so far there is no structural phase transition observed below 50 GPa in these compounds [12, 21]. However, high pressure XRD studies are required to confirm our observation. In the present work, our interest is focused on high-pressure vibrational properties and also pressure-induced ETT in Sb_2S_3 rather than its structural transitions under high pressure. All the phonon modes are fitted with Lorentzian line shape function. Due to the poor signal-to-noise ratio, line width analysis of A_g^1, B_{1g} and B_{3g} modes is highly unreliable. Hence, out of six experimentally observed Raman modes, we have fitted only three high intense modes namely A_g^2, A_g^3 and B_{2g} at different pressures. Pressure dependence of A_g^2 (286 cm^{-1}), A_g^3 (305 cm^{-1}) and

B_{2g} (314 cm^{-1}) phonon modes are shown in Fig.4. Figure 4 shows the softening of all the phonon modes below 4 GPa, which is not generally expected. The intensity of B_{2g} (314 cm^{-1}) mode decreases with pressure and at around 4 GPa the mode is not resolvable from the A_g^3 (305 cm^{-1}) mode. The frequency of A_g^3 (305 cm^{-1}) mode continues to soften below 4 GPa and we observe a discontinuity in frequency at 4 GPa. The behavior of A_g^2 mode is quite different as compared to the other modes. The A_g^2 mode softens with pressure, reaching a minimum at around 4 GPa and thereafter the mode hardens upon increasing the pressure. These observations hint a phase transition (at 4 GPa) and the transition observed is reproducible over many runs. Raman mode frequencies and pressure coefficients in Sb_2S_3 were are calculated by fitting P versus $\omega(P)$ to linear equation, $\omega(P) = \omega(P_0) + a_1 \times (P-P_0)$ for the modes A_g^3 and B_{2g} and to quadratic equation, $\omega(P) = \omega(P_0) + a_1 \times (P-P_0) + a_2 \times (P-P_0)^2$ for A_g^2 mode, where a_0, a_1 and P_0 are pressure coefficients and pressure at 1 atm respectively (see Table II). We have used the above expressions and notations based on the high pressure studies of Bi_2Te_3 [9], Sb_2Te_3 [10] and Bi_2Se_3 [11]. It is evident from Table II that there is a significant change in pressure coefficient values for the A_g^2 and A_g^3 modes below and above 4 GPa. The changes in the pressure coefficient values of A_g^2 and A_g^3 phonon modes at 4 GPa can be attributed to ETT as observed and concluded in the similar A_2B_3 series earlier [9-11].

Table II. Raman-mode frequencies and pressure coefficients in Sb_2S_3 at ambient pressure and 4 GPa which is obtained by fitting *P* vs. $\omega(P)$ using $\omega(P) = \omega(P0) + a_1 \times (P-P_0)$ for A_g^3 and E_2^g modes and $\omega(P) = \omega(P_0) + a_1 \times (P-P_0) + a_2 \times (P-P_0)^2$ for A_g^2 mode, where a_0, a_1 and P_0 are pressure coefficients and ambient pressure.

Raman mode	$\omega(P_0)$ **(cm^{-1})**	a_1 **(cm^{-1} GPa^{-1})**	a_2 **(cm^{-1} GPa^{-2})**
A_g^2	286.32[a]	-2.11	0.35
	278.41[b]	-0.01	0.12
A_g^3	308.16[a]	-1.63	-
	306.73[b]	-0.84	-
E_{2g}	314.25[a]	-0.96	

[a]Estimated at ambient pressure (P_0 = 1atm), [b] Estimated at P_0 = 4 GPa

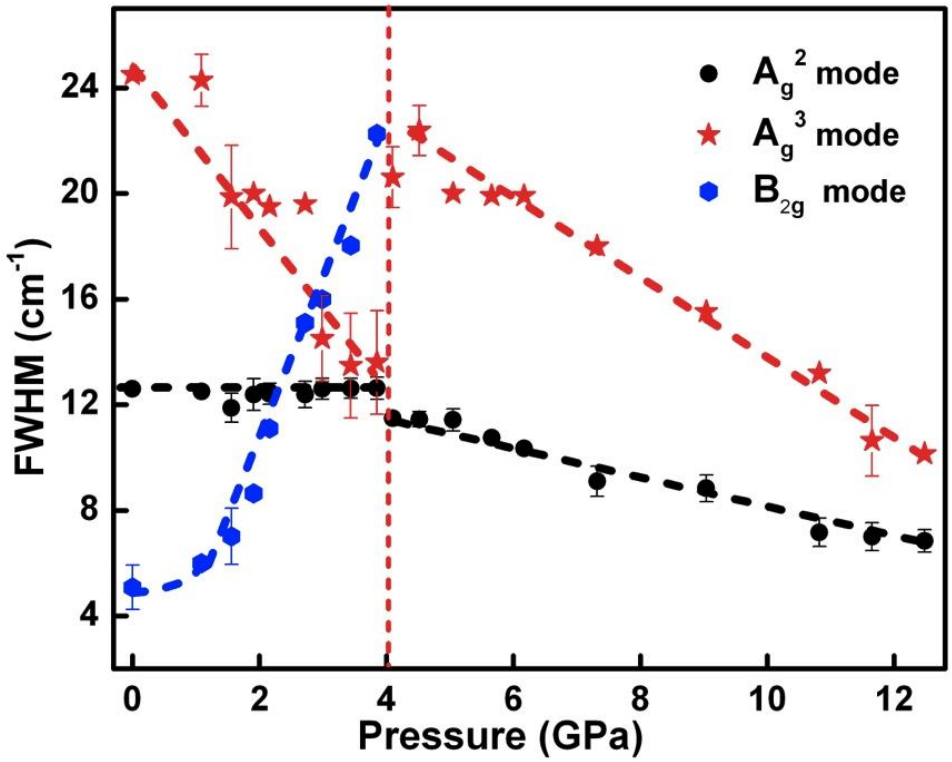

FIG. 5. P vs. FWHM of A_g^2, A_g^3 and B_{2g} modes of Sb_2S_3. A vertical dotted line at 4 GPa is to indicate an ETT. The dotted lines drawn to each phonon modes are for guidance to the eye.

The pressure dependence of the full width at half maximum (FWHM) of A_g^2, A_g^3 and B_{2g} modes of Sb_2S_3 is shown in Fig.5. It is evident from Fig.5 that the line width of the B_{2g} (314 cm^{-1}) mode increases substantially with pressure up to 4 GPa before it merges with A_g^3 mode and becomes difficult to resolve. There is a sharp anomaly in the line width of A_g^3 (305 cm^{-1}) mode noticed at ~ 4 GPa. The line width of A_g^2 mode is almost independent of pressure up to ~4 GPa and thereafter it decreases with pressure. The large line width of Sb_2S_3 phonon modes can be explained by assuming the anharmonic decay into two phonons of lower frequency as a result of strong phonon-phonon interaction, which is possible, when the frequencies of the first order phonon modes coincide with the high density of two-phonon density of states [9, 31].

High pressure XRD studies reported on Sb_2S_3 showed that there is no structural phase transition up to 10 GPa [32], which suggests that the observed softening of phonon modes and anomalous behavior of their line widths at 4 GPa are not due to any structural phase transition. However, the above mentioned changes can be attributed to an isostructural phase transition. Further, an interchange of lattice parameters *a* and *c* at

around 1.2 GPa was observed by Lundegaard *et al.* which motivated us to plot pressure dependence of *a/c* ratio and we noticed a minimum at around 5 GPa from *P* versus *a/c* as shown in Fig.6 [32]. The asymmetric behavior of *P* versus *a/c* ratio is already well documented in similar compounds of metal chalcogenide A_2B_3 series and is attributed to an isostructural transition [10-14]. An ETT causes anomalous signature in mechanical, electrical and thermodynamic properties and which affects the vibrational properties [33,34]. Based on this, we suggest that the anomaly at around 4 GPa in Sb_2S_3 can be ascribed to a second order isostructural phase transition which is the ETT in comparison with a similar transition observed in the A_2B_3 series [9-14].

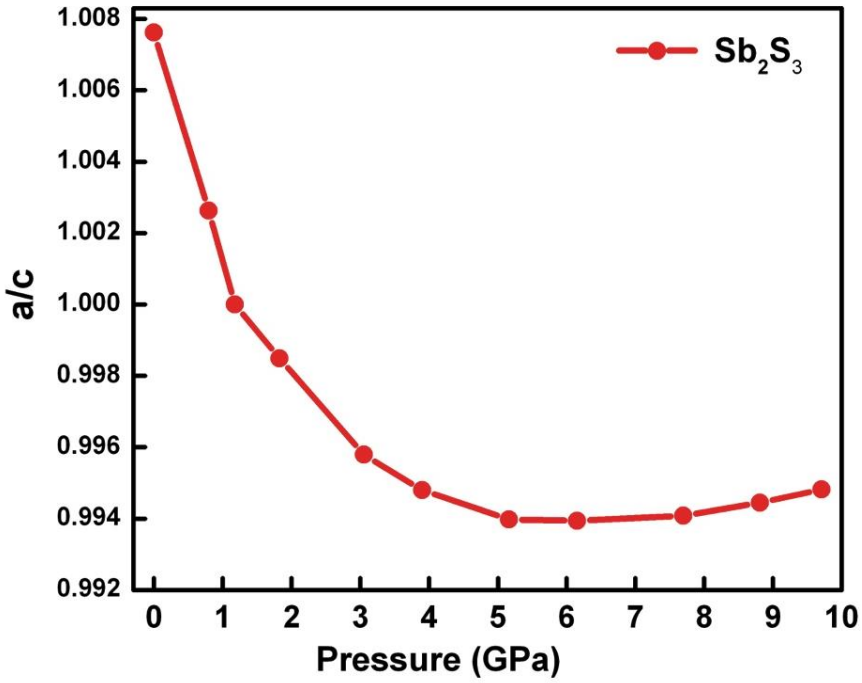

FIG. 6. *P* vs. *a/c* ratio of Sb_2S_3 up to 10 GPa (Adapted from L. F. Lundegaard *et al.* [32]).

7.3.2 Electrical resistivity measurements

In order to confirm it is the ETT, electrical transport measurement were carried out, since they are a versatile tool to detect the subtle changes which occur during ETT. The pressure dependent electrical resistivity (ρ) of Sb_2S_3 at room temperature is shown in Fig.7. A non-monotonic increase of resistivity is observed below 1.4 GPa and two points of inflections are noticed at 1.4 GPa (maximum) and 2.4 GPa (minimum) respectively. Subsequently, the resistivity increases monotonically with pressure up to 4

GPa and it is saturating on further pressurizing the sample. The reproducibility of our result in two separate runs confirms the anomalous pressure dependence in the observed

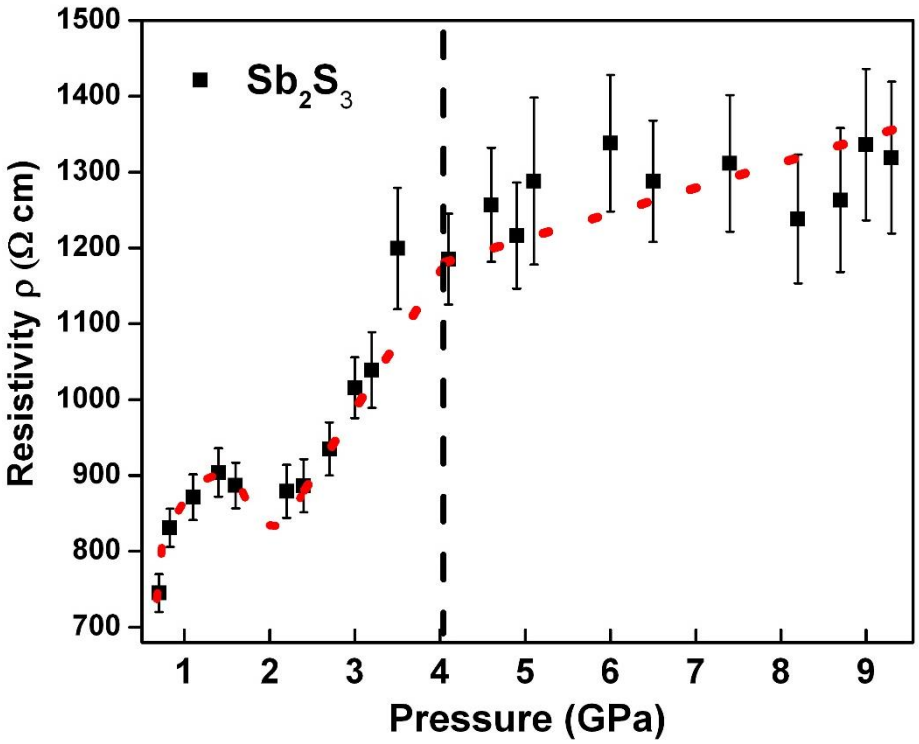

FIG. 7. P vs. electrical resistivity of Sb_2S_3 with error bars. A vertical dashed line at 4 GPa is to indicate the ETT. The dashed red lines drawn to the resistivity data is for guidance to the eye.

resistance behavior. The sharp maximum and minimum of resistivity values at 1.4 GPa and 2.4 GPa is around the same pressure where there is an interchange of the lattice parameter *a* and *c* in the XRD studies (around 1.2 GPa). We ascribe the anomalies around 1.4 GPa and 2.4 GPa to the change in band structure due to the interchange of lattice parameters. Theoretical calculations would throw light on this transition. As is evident from Fig. 7, the resistivity stays around 1300 Ω cm after ~4 GPa and the saturation of resistivity values (around 1300 Ω cm) after ~4 GPa is a clear indication of ETT. The observed weak signature of resistivity at 4 GPa may probably be due to the large resistivity value of the system at ambient pressure. This sort of subtle change in the resistivity values at high pressure has already been documented in Bi_2Te_3 [35]. Our observation of change in the slope of pressure versus resistivity plot at 4 GPa supports our proposed presence of an anomaly of electronic states during ETT, which could

possibly be due to electron-phonon coupling seen in Raman experiments, that modifies the band structure of this compound.

Table III. Comparison of pressure induced ETT of different metal chalcogenides in A_2B_3 series.

Compound	E_g (eV)	Space group	Transition pressure (GPa)
Bi_2Se_3	0.3	$R\bar{3}m$	3-5 [11]
Bi_2Te_3	0.12	$R\bar{3}m$	3.2 or 4 [9,13]
Sb_2Te_3	0.28	$R\bar{3}m$	3-3.5 [10]
Sb_2Se_3	1.00	*Pnma*	2.5 [14]
Bi_2S_3	1.3	*Pnma*	4[12]
Sb_2S_3	1.7-1.8	*Pnma*	4[a]

[a]present work.

We have tabulated the ETT reported to date in the A_2B_3 series in Table III. Now, it is quite interesting to compare why Sb_2Se_3 is a probable non-trivial topological insulator whereas Sb_2S_3 a band insulator at high pressure, even though both of them have same crystal symmetry. The reason is that the compounds formed by elements with atomic number greater than 50 are naturally among the prime candidates of topological insulators as a result of strong intrinsic spin orbit coupling, which must be strong enough to have considerable effect to modify electronic structure. It is well known that the spin-orbit coupling strength is proportional to Z^4 (where Z is the atomic number; Z = 51 for Sb, 34 for Se and 16 for S) [22]. Consequently, the spin-orbit coupling is not strong enough at ambient pressure to generate the band inversion in both Sb_2Se_3 and Sb_2S_3 compounds. However, these band insulators can probably be transformed in to a non-trivial topological insulator by applying pressure owing to the enhancement of the crystal-field splitting, resulting a crossover of conduction and valence bands which leads to TQPT [22] (discussed in Chapter 1). Since the band gap of Sb_2S_3 (E_g = 1.7-1.8 eV) is quite large as compared to the energy scale of spin-orbit coupling, the spin-orbit coupling in this material is not strong enough to change the phase [36]. Therefore, the observed changes at 4 GPa in Sb_2S_3 cannot be attributable to TPQT whereas it is a consequence of

an isostructural ETT. Since the ETT is a consequence of topology of the Fermi surface, however, the experimental observation of ETT in the relatively large band gap material, Sb_2S_3 is unusual. Theoretical calculations are a must to understand this and should motivate work in this direction.

7.4 Conclusions

The high-pressure Raman and electrical resistivity studies were used to investigate the vibrational properties and ETT in Sb_2S_3. Sharp changes observed in the phonon frequencies A_g^2, A_g^3 and B_{2g} and their line widths at 4 GPa are may be due to the strong electron-phonon coupling. The electrical transport measurements at high pressures shows a change in slope at 4 GPa due to the electron-phonon coupling leading to the changes in the electronic band structure. It is exactly around the pressure (~5 GPa) where a minimum is seen in *P* versus *a/c* ratio. All this evidences (the phonon anomalies, change in resistivity and the minimum in *a/c* ratio) indicate that the observed transitions at 4 GPa is a result of an isostructural ETT. We also observe a plausible structural phase transition above 20 GPa. These results should motivate further theoretical as well as experimental work to understand the presence of ETT in a large band insulator and also the structural phase transition of Sb_2S_3 under high pressure.

7.5 Bibliography

1. E. S. Itskevich, L. M. Kashirskaya, and V. F. Kraidenov, Semiconductors **31**, 276 (1996).
2. S. V. Ovsyannikov, V. V. Shchennikov, G. V. Vorontsov, A. Y. Manakov, A. Y. Likhacheva, and V. A. Kulbachinskii, J. Appl. Phys. **104**, 053713 (2008).
3. N. V. Chandra Shekar, D. A. Polvani, J. F. Meng, and J. V. Badding, Physica B **358**, 14 (2005).
4. W. Liu, X. Peng, C. Tang, L. Sun, K. Zhang, and J. Zhong, Phys. Rev. B **84**, 245105 (2011).
5. Y. L. Chen, J. G. Analytis, J.H. Chu, Z. K. Liu, S.-K. Mo, X. L. Qi, H. J. Zhang, D. H. Lu, X. Dai, Z. Fang, S. C. Zhang, I. R. Fisher, Z. Hussain, and Z.-X. Shen, Science **325**, 178 (2009).
6. Y. H. Wang, D. Hsieh, D. Pilon, L. Fu, D. R. Gardner, Y. S. Lee, and N. Gedik, Phys. Rev. Lett. **107**, 207602 (2011).

7. D. Hsieh, Y. Xia, D. Qian, L. Wray, F. Meier, J. H. Dil, J. Osterwalder, L. Patthey, A. V. Fedorov, H. Lin, A. Bansil, D. Grauer, Y. S. Hor, R. J. Cava, and M. Z. Hasan, Phys. Rev. Lett. **103**, 146401 (2009).
8. H. J. Zhang, C. X. Liu, X. L. Qi, X. Dai, Z. Fang, and S. C. Zhang, Nat. Phys. **5**, 438 (2009).
9. R. Vilaplana, O. Gomis, F. J. Manjón, A. Segura, E. Pérez-González, P. Rodríguez-Hernández, A. Muñoz, J. González, V. Marín-Borrás, V. Muñoz-Sanjosé, C. Drasar, and V. Kucek, Phys. Rev. B **84**, 104112 (2011).
10. O. Gomis, R. Vilaplana, F. J. Manjón, P. Rodríguez-Hernández, E. Pérez-González, A. Muñoz, V. Kucek, and C. Drasar, Phys. Rev. B **84**, 174305 (2011).
11. R. Vilaplana, D. Santamaría-Pérez, O. Gomis, F. J. Manjón, J. González, A. Segura, A. Muñoz, P. Rodríguez-Hernández, E. Pérez-González, V. Marín-Borrás, V. Muñoz-Sanjose, C. Drasar, and V. Kucek, Phys. Rev. B **84**, 184110 (2011).
12. I. Efthimiopoulos, J. Kemichick, X. Zhou, S. V Khare, D. Ikuta, and Y. Wang, J. Phys. Chem. A **118**, 1713 (2014).
13. A. Polian, M. Gauthier, S. M. Souza, D. M. Trichês, J. Cardoso de Lima, and T. A. Grandi, Phys. Rev. B **83**, 113106 (2011).
14. P. P. Kong, F. Sun, L. Y. Xing, J. Zhu, S. J. Zhang, W. M. Li, Q. Q. Liu, X. C. Wang, S. M. Feng, X. H. Yu, L. Zhu, R. C. Yu, W. G. Yang, G. Y. Shen, Y. S. Zhao, R. Ahuja, H. K. Mao, and C. Q. Jin, Sci. Rep. **4**, 6679 (2014).
15. J. L. Zhang, S. J. Zhang, H. M. Weng, W. Zhang, L. X. Yang, Q. Q. Liu, S. M. Feng, X. C. Wang, R. C. Yu, and L. Z. Cao, Proc. Natl. Acad. Sci. USA **108**, 24 (2011).
16. M. Bahramy, B.J. Yang, R. Arita, and N. Nagaosa, Nat. Commun. **3**, 679 (2012).
17. T. R. Devidas, N. V. Chandra Shekar, C. S. Sundar, P. Chithaiah, Y. A. Sorb, V. S. Bhadram, N. Chandrabhas, K. Pal, U. V. Waghmare, and C. N. R. Rao, J. Phys: Condens. Mater. **26**, 275502 (2014).
18. X. Xi, C. Ma, Z. Liu, Z. Chen, W. Ku, H. Berger, C. Martin, D. B. Tanner, and G. L. Carr, Phys. Rev. Lett. **111**, 155701 (2013).

19. H. Lin, L. A. Wray, Y. Xia, S. Xu, S. Jia, R. J. Cava, A. Bansil, and M. Z. Hasan, Nat. Mater. **9**, 546 (2010).
20. S. J. Moon, Y. Itzhaik, J. H. Yum, S. M. Zakeeruddin, G. Hodes, and M. Gratzel, J. Phys. Chem. Lett. **1**, 1524 (2010).
21. I. Efthimiopoulos, J. Zhang, M. Kucway, C. Park, R. C. Ewing, and Y. Wang, Sci. Rep. **3**, 2665 (2013).
22. W. Li, X.Y. Wei, J.X. Zhu, C. S. Ting, and Y. Chen, Phys. Rev. B **89**, 035101 (2014).
23. A. Bera, K. Pal, D. V. S. Muthu, S. Sen, P. Guptasarma, U. V. Waghmare, and A. K. Sood, Phys. Rev. Lett. **110**, 107401 (2013).
24. X. Shuai and W. Shen: Nanoscale Res. Lett. **7**, 199 (2012).
25. D. A. Polvani, J. F. Meng, N. V. C. Shekar, J. Sharp, and J. V. Badding, Chem. Mater. **13**, 2068 (2001).
26. A. Kyono and M. Kimata, Am. Mineral. **89**, 932 (2004).
27. G. V. P. Kumar, and C. Narayana, Curr. Sci. **93,** 778 (2007)
28. S. Karmakar, High Press. Res. **33,** 381(2013).
29. Y. Liu, K. T. E. Chua, T. C. Sum, and C. K. Gan, Phys. Chem. Chem. Phys. **16**, 345 (2014).
30. P. Sereni, M. Musso, P. Knollb, P. Blaha, K. Schwarz, and G. Schmidt, AIP Conf. Proc. **1267,** 131 (2010).
31. M. Cardona, High Press. Res. **24,** 17 (2004).
32. L. F. Lundegaard, R. Miletich, T. Balic-Zunic, and E. Makvicky, Phys. Chem. Miner. **30**, 463 (2003).
33. F. J. Manjón, R. Vilaplana, O. Gomis, E. Pérez-González, D. Santamaría-Pérez, V. Marín-Borrás, A. Segura, J. González, P. Rodríguez-Hernández, A. Muñoz, C. Drasar, V. Kucek, and V. Muñoz-Sanjosé, Phys. Status Solidi B **250**, 669 (2013).
34. L. Dagens, J. Phys. F. Met. Phys. **8,** 2093(1978)
35. J. Zhang, C. Liu, X. Zhang, F. Ke, Y. Han, G. Peng, Y. Ma, C. Gao, Y. Ma, and C. Gao, Appl. Phys. Lett. **103**, 052102 (2013).
36. J. E. Moore, Nature **464,** 194 (2010).

Chapter 8

Summary and outlook

In addition to the well-known electronic states of matter such as an insulator, semiconductor, and metal, recent theoretical and experimental investigations have established topological insulators (TIs). In a highly simplified picture, the newly discovered TI can be viewed as a plastic material covered with metallic wires which make the surface conducting and the bulk insulating. The subject of topology (topological phase transitions and topological phases of matter) has been awarded the Nobel Prize in Physics (2016), which undoubtedly explains the richness of this subject and its upcoming technological significances in the society. The present thesis mainly discusses the importance of Raman scattering as a tool to investigate the pressure induced electronic transitions namely topological quantum phase transitions (TQPT), electronic topological transitions (ETT), and metallization in condensed matter systems at room temperature. A summary of the important idea, results, and the inference of this thesis and possible future directions are highlighted below.

During the TQPT process, we expect charge density fluctuations as well as changes in the electron-phonon coupling in materials. Raman scattering is an effective tool to investigate the electron-phonon coupling changes. Therefore, we have extensively used Raman scattering in this thesis to study the topological phase transitions in strong spin-orbit coupling (SOC) materials. Note that the Raman scattering is a qualitative microscopic tool and any changes (or transitions) such as magnetic and electronic transitions, metallization, and structural phase transitions will be reflected in its frequency, lifetime (full-width at half maxima) and intensity. From this point of view, to confirm that it is indeed an electronic transition (say topological transitions), we need to use multiple experimental tools which will carefully rule out the possibility of any other transitions and the results should be confirmed (or supplemented) with the first principles theoretical calculations.

The combined high-pressure Raman and first principle theoretical investigations on $TlBiS_2$ reveals (through phonon anomalies) that the applied hydrostatic pressure systematically tunes the electronic states of $TlBiS_2$ from a normal semiconductor at ambient conditions to a TI ~0.5 GPa and then to a topological crystalline insulator (TCI) at ~1.8 GPa. The explored two consecutive topological transitions in rhombohedral $TlBiS_2$ under hydrostatic pressure is unique, because one material adopts three different types of electronic states and to the best of our knowledge, till date, this work is the first

experimental report in this field. The present study would lead to the following two essential directions in this system. 1) To stimulate the interest in the possibility of making multifunctional devices, and 2) to perform the quantum oscillations measurements which could provide further insight.

The 2D layered transition metal chalcogenide (TMD) *1T*-$TiTe_2$ undergoes a pressure-induced TQPT at ~ 2 GPa and then again switches back to trivial metallic phase at ~ 4 GPa. Also, the flat *c/a* ratio gives evidence to the isotropic 3D behavior (between ~ 4 – 8 GPa) and a structural transition from trigonal (SG: $P\bar{3}m1$) to monoclinic (SG: $C2/m$) phase is observed at ~8 GPa. Recently, this work has been reproduced by another group [1]. The present study would lead to the following three important directions in this system. 1) It will be interesting to look for the Shubnikov de Haas oscillations which will give the Fermi surface modifications during the TQPT. 2) The explored TQPT is at relatively low-pressure regions, which can be achieved by alternative chemical methods (doping or substitution) and bring it (transition pressure) down to ambient conditions. But the chemical route should not violate the parities of the VBM and CBM of the bands and the overall crystal structure. Therefore, attempt for the developing of synthetic strategy (chemical method) would be interesting and can possibly lead to a lot of exciting outcomes. 3) More recently we have explored the similar pressure induced TQPTs in a prototype compound 1T-$TiSe_2$ [2]. These results suggest that crystal structure and similar chemistry (Se and Te) controls the topological properties in this family. Hence, they behave similarly under pressure. Therefore, a model calculation to generalize the observation of TQPT in TiX_2 (X = Te and Se) would be an interesting future direction to this work.

The pressure-induced metallization has been evidenced in Raman modes at ~ 3.6 GPa in the InTe compound. Also, Raman signatures confirm a pressure induced a structural transition from tetragonal (SG: $I4/mcm$) to face-centered cubic (SG: $Fm\bar{3}m$) phase at ~ 6.0 GPa and then to a primitive cubic (SG: $Pm\bar{3}m$) phase at ~ 14 GPa. Interestingly a pressure induced band inversion at ~ 1.0 – 1.2 GPa has been evidenced in our first principles calculations and a mechanism for the observed metallization in InTe has been given. It will be an interesting idea to look for the possibility of modulating the parity change in InTe by altering its chemical identity (orbital characters) through suitable doping or substitution to get a non-trivial topological phase in this material (both

theory and experiments). We believe that our present experimental results on InTe would serve as a benchmark to initiate these calculations.

The pressure-induced structural phase transitions, ETT and metallization, have been explored for the first time in the $AgBiSe_2$ compound. Interestingly $AgBiSe_2$ adopts a rhombohedral phase ($R\bar{3}m$) at ~0.6 GPa which is like the crystal structures of 3D topological insulators such as Bi_2Se_3, Bi_2Te_3 and Sb_2Te_3, $TlBiSe_2$, and $TlBiTe_2$ compounds. However, we did not see any TI properties in the rhombohedral phase of the $AgBiSe_2$ compound under high pressure. Now, here we would like to correlate the high-pressure studies of $AgBiSe_2$ with $TlBiS_2$ compounds. Even though both the compounds β-$AgBiSe_2$ ($R\bar{3}m$) and $TlBiS_2$ adopt a similar crystal structure ($R\bar{3}m$) and have strong SOC, but topological insulating properties are present in $TlBiS_2$ and not in $AgBiSe_2$. Our results on $TlBiS_2$ and $AgBiSe_2$ taken together clearly illustrate us that the TQPT process is not a straight forward approach, even if you have the same crystal structure and significantly strong SOC strengths. Therefore, the theoretical predictions (which are relatively faster and easier than experiments through well-known methodologies) could play a crucial role in exploring the possibility of TQPT in various systems. Then the suitable predicted compounds shall get the attention of the experimentalist and quick experiments can be performed like in our case (Raman scattering) to validate the predictions. But, there are some roadblocks in the theoretical calculations as well. Most of the calculations reported in the literature are abstract, by which we imply that the assumed crystal structure (for the calculations) is arbitrary (any possible theoretical minimum energy ground state). However, experimentally the compounds only adopt a specific crystal symmetry (most common ground state) and should be possible to synthesis in more common routes (as a pure phase). One more critical point to be added to the reported theoretical prediction is, in theoretical approaches one can apply all kinds of strains such us uniaxial, biaxial and hydrostatic (both compression and tension). But, it is important to note that the hydrostatic pressure (compression) is the most common, controlled and experimentally easily accessible strain using simple DAC of the order of GPa. Hence, we believe that hydrostatic pressure calculations are more important for practical aspects. The crystal structure and the kind of strain reported in the theoretical predictions should be of concern for an experimentalist before they embark on the experiments on the predicted topological transition in materials. To complete the pressure

induced topological transitions part, we would like to add a few more generalized questions through this thesis work such as: (1) Is there any generalized connection (correlation) between the crystal symmetry and TI properties? (2) Is strong SOC strength a sufficient condition to drive the TQPT?, *etc*. To answer these exciting and more important fundamental questions, we need to do a lot of exciting experiments on many compounds (both predicted and experimentally claimed materials) which will initiate the right questions to the theoretical researchers and may provide a potential answer to the few questions raised above.

The Raman signatures of anomalies in phonon line widths, and frequencies, evidence a pressure induced ETT in Sb_2S_3 (E_g ~ 1.7-1.8 eV) at ~4.0 GPa. It is a very interesting results, because the observation of ETT in a wide bandgap semiconductor is ~~a~~ rare case. These results have been reproduced by another group [3]. Generally, the A_2B_3 (A = Bi, Sb, and B = S, Se, Te) metal chalcogenide family crystallizes into two space groups. One is rhombohedral (SG $R\bar{3}m$, Z = 3) and another is orthorhombic (SG *Pnma*, Z = 1). Moreover, in A_2B_3 family, the compounds which adopt rhombohedral structure are 3D TIs at ambient conditions (e.g. Bi_2Se_3, Bi_2Te_3, Sb_2Te_3), whereas the compounds which adopt orthorhombic structure are the semiconductors (e.g. Bi_2S_3 and Sb_2S_3). However, when the pressure is applied to A_2B_3 compounds, both the structural types undergo pressure induced ETT around ~3 – 5 GPa, because of the changes in the topology of Fermi surface. This may indicate a unified picture suggesting the existence of a pressure-induced mechanism for ETT in this A_2B_3 family. Therefore, an interesting future prospect for this work could be a systematic set of theoretical investigations of all the A_2B_3 compounds to study the pressure evolutions of the band structure and Fermi surface and provide a possible unified picture.

Finally, this thesis illustrates that Raman scattering is a potential tool to study the pressure induced topological transitions through electron-phonon coupling changes in strong SOC materials. This thesis discovered the multiple pressure induced topological phase transitions in $TlBiS_2$ and 1T-$TiTe_2$ compounds. Raman scattering (non-contact probe) is commonly used as a probe to study conventional structural and electronic transitions, 2D materials such as graphene, TMDs, *etc*. Now, in this list, the exotic topological transitions can also be included (as inferred from major results of the present thesis). Thus, we conclude that this thesis is an outcome of high-pressure investigations

of various strong SOC materials which could be a benchmark for exploring the pressure induced topological phase transitions using Raman scattering.

8.1 Bibliography

1. M. Zhang, X. Wang, A. Rahman, Q. Zeng, D. Huang, R. Dai, Z. Wang, Z. Zhang, Appl. Phys. Lett. **112**, 041907 (2018).
2. V. Rajaji, S. Janaky, Saurav Ch. Sarma, Sebastian C. Peter, and Chandrabhas Narayana (Accepted in J. Phys.: Condens. Matter – doi: 10.1088/1361-648X/ab01bb).
3. I. Efthimiopoulos, C. Buchan, and Y. Wang, Sci. Rep. **6**, 24246 (2016).

Miscellaneous work

1. **V. Rajaji,** S. Janaky, Saurav Ch. Sarma, Sebastian C. Peter, and Chandrabhas Narayana, "Pressure induced topological and structural phase transitions in 1T-$TiSe_2$: A Raman study" *(In press - **J. Phys.: Condens. Matter**- doi: 10.1088/1361-648X/ab01bb).*
2. R. S. Joshya, **V. Rajaji**, Chandrabhas Narayana, A. Mascarenhas, and R. N. Kini,"Anharmonicity in light scattering by optical phonons in $GaAs_{1-x}Bi_x$", *J. Appl. Phys.* ***119****, 205706 (2016).*
3. Sebastian C. Peter, M. Kanagaraj, Amit Pawbake, Saurav Ch. Sarma**, V. Rajaji**, Chandrabhas Narayana, and Marie-Aude Measson "Structural, magnetotransport and Hall coefficient studies in ternary Bi_2Te_2Se, Sb_2Te_2Se and Bi_2Te_2S tetradymite topological insulating compounds" *(Under review in Mater. Res. Express).*
4. B. Vishal, H. Sharona, U. Bhat, A. Paul, M. B. Sreedhara, **V. Rajaji**, Saurav C Sarma, Chandrabhas Narayana, Sebastian C Peter, Ranjan Datta "Growth of epitaxial ReS_2 thin film by pulsed laser deposition" *(Under review in Journal of Crystal Growth).*
5. Soumyabrata Roy, Vamseedhara Vemuri, Dababrata Bagchi, Saurav C Sarma, Vinitha Ahuja, **V. Rajaji**, Chandrabhas Narayana, and Sebastian C Peter "Deconvoluting Activity Descriptors in Phase-Size-Strain Modulated POMOF Derived Ultrasmall WC & MoC Nanocrystals for Enhanced Hydrogen Evolution" (*Under review in ACS Nano*).
6. **V. Rajaji,** Subhajit Roychowdhury, B. Joseph, K. Biswas and C. Narayana, " Pressure driven isostructural electronic transition in 3D topological insulator $TlBiSe_2$" *(Manuscript under preparation).*